FOSSIL ENERGY PROGRAM ANNUAL PROGRESS REPORT

APRIL 2000 – MARCH 2001

© PhotoDisc, Inc.

© PhotoDisc, Inc.

OAK RIDGE NATIONAL LABORATORY

ORNL/TM-2001/895

Fossil Energy Program Annual Progress Report for April 2000 Through March 2001

Roddie R. Judkins
Program Manager

Paul T. Carlson
Technical Assistant

July 2001

Prepared for the
DOE Office of Fossil Energy
(AA, AB, AC, AW, AZ, SA)

Prepared by the
OAK RIDGE NATIONAL LABORATORY
Oak Ridge, Tennessee 37831-6285
managed by
UT-BATTELLE, LLC
for the
U.S. DEPARTMENT OF ENERGY
under Contract DE-AC05-00OR22725

CONTENTS

CONTENTS

CONTENTS

We would like to thank the ORNL Creative Media Solutions group for its assistance in this project. Vickie Conner, in Graphics Services, designed the cover; Sandra Lyttle, in Publishing Services, formatted the papers and created the PDF file.

ABBREVIATIONS AND ACRONYMS

ABF	aerosol beam focusing
ACRS	acoustic cavity resonance detector
AIChE	American Institute of Chemical Engineers
AIMSI	Advanced Integrated Management Services, Inc.
ANL	Argonne National Laboratory
APCVD	atmospheric pressure chemical vapor deposition
API	American Petroleum Institute
AR	Advanced Research
AR&TD	Advanced Research and Technology Development
ARM	Advanced Research Materials
ASTM	American Society for Testing and Materials
BCC	background-corrected count
BTEXH	benzene, toluene, ethylbenzene, xylenes, and hexanoic acid
CAPP	Canadian Association of Petroleum Producers
CCD	charge-coupled device
CCI	Community College Institute (DOE)
CCT	Clean Coal Technology
CEA	Completion Engineering Association
CFB	circulating fluidized bed
CRADA	cooperative research and development agreement
CSIC	Consejo Superior de Investigaciones Cientificas
CTE	coefficient of thermal expansion
CVD	chemical vapor deposition
CVI	chemical vapor infiltration
D&D	decommissioning and dismantlement
DEA	Drilling Engineering Association
DIPPR®	Design Institute for Physical Property Data
DOE	U.S. Department of Energy
DSC	differential scanning calorimeter
E&P	exploration and production
EBC	environmental barrier coating
ECAS	Environmental Compliance Assistance System
EDS	energy-dispersive spectroscopy
EDX	energy-dispersive X-ray
EIS	environmental impact statement
EPMA	electron probe microanalysis
FEG-SEM	field-emission gun scanning electron microscopy
FIB	focused ion beam
FID	flame ionization detector
GDP	gross domestic product
GRI	Gas Research Institute

HVOF	high-velocity oxy-fuel
ICP/AES	inductively couples plasma atomic emission spectroscopy
INEEL	Idaho Engineering and Environmental Laboratory
JEA	Jacksonville Electric Authority
LIPS	laser-induced plasma emission spectroscopy
MSDS	Material Safety Data Sheet
NEPA	National Environmental Policy Agency
NETL	National Energy Technology Laboratory (DOE)
NGOTP	Natural Gas and Oil Technology Partnership
NIPER	National Institute for Petroleum and Energy Research
NPTO	National Petroleum Technology Office
NROM	naturally occurring radioactive material
ODS	oxide-dispersion strengthened
ORNL	Oak Ridge National Laboratory
OSHA	Occupational Safety and Health Administration
PAH	polyaromatic hydrocarbons
PDF	probability density function
PEG	polyethylene glycol
PERF	Petroleum and Environmental Research Forum
PERF	Petroleum Environmental Research Forum
PM	powder metallurgical
PS	plasma spray
RE	reactive element
SEM	scanning electron microscopy
SEM/EDX	scanning electron microscope/energy-dispersive X-ray
SPR	Strategic Petroleum Reserve
SRS	Savannah River Site
STEM	scanning transmission electron microscopy
TPH	total petroleum hydrocarbons
USGS	U.S. Geological Survey
UV	ultraviolet
VLE	vapor-liquid equilibrium
XRD	X-ray diffraction
XRF	X-ray fluorescence
YAG	yttrium aluminum garnet
YSZ	yttria-stabilized zirconia

FOSSIL ENERGY PROGRAM ANNUAL PROGRESS REPORT FOR APRIL 2000 THROUGH MARCH 2001[1]

Roddie R. Judkins, Program Manager
Paul T. Carlson, Technical Assistant

INTRODUCTION

This report covers progress made at Oak Ridge National Laboratory (ORNL) on research and development projects that contribute to the advancement of fossil energy technologies. Projects on the ORNL Fossil Energy Program are supported by the U.S. Department of Energy (DOE) Office of Fossil Energy, the DOE National Energy Technology Laboratory (NETL), the DOE Fossil Energy Clean Coal Technology (CCT) Program, the DOE National Petroleum Technology Office, and the DOE Fossil Energy Office of Strategic Petroleum Reserve (SPR).

The ORNL Fossil Energy Program research and development activities cover the areas of coal, clean coal technology, gas, petroleum, and support to the SPR. An important part of the Fossil Energy Program is technical management of all activities on the DOE Fossil Energy Advanced Research (AR) Materials Program. The AR Materials Program involves research at other DOE and government laboratories, at universities, and at industrial organizations.

---

[1] Research sponsored by the U.S. Department of Energy, Office of Fossil Energy, under contract DE-AC05-00OR22725 with UT-Batttelle, LLC.

ATMOSPHERIC PRESSURE CVD OF YSZ USING STAGNATION FLOW FOR THERMAL BARRIER COATINGS

T. M. Besmann and J. C. McLaughlin
Metals and Ceramics Division, Oak Ridge National Laboratory

V. Varanasi and T. J. Anderson
Chemical Engineering Department, University of Florida

T. L. Starr
Chemical Engineering Department, University of Louisville

INTRODUCTION

Thermal barrier coatings, or TBC’s, have become excellent materials for improving the performance, longevity, and overall costs of gas turbine engines (GTE’s) (Haynes 1997). These ceramic coatings, made of yttria-stabilized zirconia (YSZ), improve GTE’s by reducing the turbine blade temperature and preventing failure (Haynes 1997). A schematic of the TBC system is shown in Fig. 1.

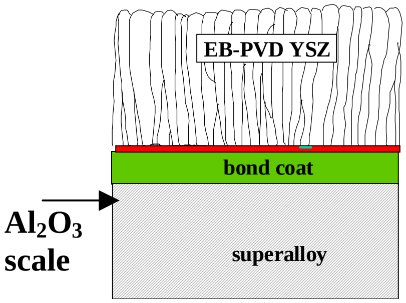

Fig. 1: Schematic of TBC.
(After J. A. Haynes)

The nickel- or cobalt-superalloy turbine blade is protected by three coating layers: an oxidation-resistant aluminum-rich bond coat, a thermally-insulating YSZ top coat, and an α-alumina scale interface (Haynes 1997). The aluminum-rich bond coat is an alloy of MCrAlY (M = Ni or Co), and is coated onto the blade by plasma spraying (Haynes 1997). The YSZ top coat is typically zirconia (ZrO_2) stabilized by six- to eight-weight (3.5- to 5.5-mole percent) yttria (Y_2O_3), and is deposited onto the bond coat by electron-beam, physical vapor deposition (EB-PVD) (Haynes 1997).

There are several advantages to using a YSZ top coat for the superalloy blade. The decrease in blade temperature of as much as 167°C, improves blade by three to four fold. This top coat can even improve fuel consumption by more than one percent. In addition, less air-cooling will be required, thus increasing the GTE efficiency and reliability (Haynes 1997).

There are two methods of YSZ fabrication currently employed for the top coat: (1) plasma spraying and (2) EB-PVD (Haynes 1997). Plasma spraying tends to allow the formation of a rough top coat-scale interface, whereas EB-PVD allows the formation of a columnar microstructure of the top coat, and a much smoother top coat-scale interface. Since this EB-PVD coating has the desirable columnar microstructure, there tends to be less of a thermal mismatch between the YSZ top coat and the underlying bond coat and scale interface. Spallation, or stripping, of the top coat or scale interface is the key issue in determining which technique is used. Since the EB-PVD technique allows for better chemical adhesion of the top coat and scale interface, this technique is preferred over plasma spraying (Haynes 1997).

EB-PVD, however, is very costly. An alternate approach is atmospheric pressure, chemical vapor deposition (APCVD) of the YSZ top coat. This is potentially a much cheaper technique, in which transport and kinetic control can help to fabricate tailored YSZ coatings. The goal is to obtain the 100 to 250 μm YSZ coatings, with the same microstructure as EBPVD, but at a much lower cost.

EXPERIMENTAL DESIGN AND RESULTS

The APCVD experimental design is based on several factors. Fist, low cost and effective precursors, or metal sources, must be chosen. Second, a controlled oxygen source must be used to effectively oxidize the precursors on a substrate. Third, a substrate must be chosen that will not be chemically etched by the gases and also simulate the scale interface. Finally, a flow system and reactor design must be developed to make the coating diffusion controlled.

For the zirconium and yttrium metal sources, $ZrCl_4$ and $Y(tmhd)_3$ were chosen. $Y(tmhd)_3$ was chosen due to its closely matched vapor pressure to that of $ZrCl_4$ (both sublime at ~300°C), its high thermal stability (up to 500^{o}C), and its success as a precursor for YSZ thin films and $YBa_2Cu_3O_7$ superconductors. In addition, the reverse water gas shift reaction will be used to control the oxygen source. Thus the overall reaction sequence is:

$$H_2(g) + CO_2(g) = CO(g) + H_2O(g) \tag{1}$$

$$ZrCl_4(g) + 2\ H_2O(g) \rightarrow ZrO_2(s) + 4\ HCl(g) \tag{2}$$

$$2Y(tmhd)_3(g) + 3H_2O(g) \rightarrow Y_2O_3(s) + 6H(tmhd) \tag{3}$$

To compliment this choice of precursors and oxygen source, a stagnation flow design was employed because it allows the determination of the rate-limiting processes and promotes efficient deposition. Stagnation flow offers design flexibility by controlling residence time, prevents pre-reaction of inorganic or organometallic precursors, provides for high deposition rates, and promotes deposition uniformity.

Furthermore, stagnation flow allows growth rates to be diffusion controlled as opposed to kinetically controlled.

In a stagnation flow reactor the gas mixture, with a laminar flow profile, approaches a gas-distributing nozzle in a cylindrical flow tube reactor (Fig. 2). The gas-distributing nozzle “breaks up” the laminar flow profile of the gas stream (at B) which enters the region above the substrate (at C). In this region, the velocity, temperature, and reactant concentration gradients of the forced-convective gas stream are independent of the substrate diameter. As the gases approach the substrate, heterogeneous reactions occur on the substrate to form the coating (at D). The coating thickness is independent of the substrate diameter and grows in the axial direction. Moreover, the coating thickness depends solely on the gas flow and the substrate-nozzle spacing.

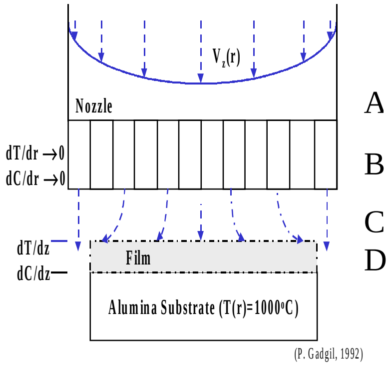

(P. Gadgil, 1992)

Fig. 2: Schematic of stagnation-point flow reactor. *(After P. N. Gadgil)*

A reactor and flow system have been developed for the deposition of zirconia alone as a first step (Fig. 3). Flow of $HCl_{(g)}$ (Air Liquide) into a packed bed of $Zr_{(s)}$ chips (Strem) produces $ZrCl_{4(g)}$. The oxygen source is provided by a 1:1 molar mixture of $H_{2(g)}$ and $CO_{2(g)}$ (Air Liquide). Argon gas (Air Liquide) is preheated and used as a carrier and diluent gas. The gas streams mix and flow through the reactor (maintained at 200°C by a heating jacket of silicone oil) toward the alumina substrate (Coors). The alumina substrate (inductively heated using a radio frequency coil and a graphite susceptor) was maintained at 1200°C. Waste gases were exhausted to a fume hood. The deposition time was typically two hours.

X-ray diffraction (Cu K-α,θ-2θ) revealed that the deposition of zirconia (baddelyite) was successful. Scanning electron microscopy (Hitachi S800) showed the coatings were 10 to 12 µm thick. The results can be seen in Fig. 4.

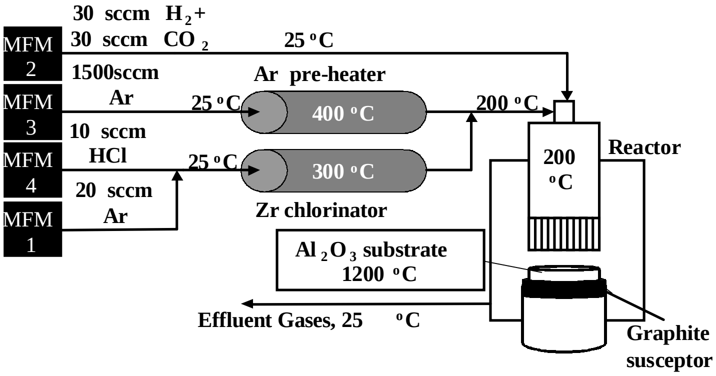

Fig. 3: Flow schematic of APCVD reactor (without Y addition).

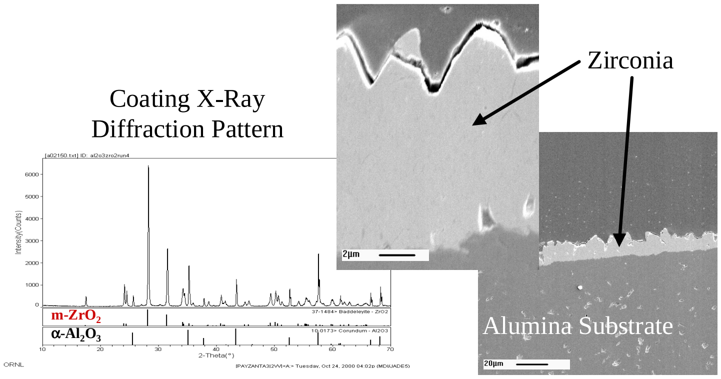

Fig. 4: Results of XRD and SEM.

FUTURE WORK

A kinetic study of zirconia deposition is the next step in the development and optimization of he APCVD system. The kinetic study will focus on deposition rates, homogeneously nucleated materials, and effluent gases.

In addition to the zirconia kinetic study, yttrium must be added to this deposition apparatus. A preliminary design for the yttrium source delivered to the reactor is shown in Fig. 5. The yttrium precursor, $Y(tmhd)_3$, will be dissolved in an organic solvent, such as a mixture of isopropyl alcohol, tetrahydrofurane, and triglyme (J. Zhang 1992). This solution will be siphoned into a syringe pump (KD Scientific). The syringe pump will then deliver this solution to an ultrasonic nozzle (Sonics) for quick volatilization. These volatilized reactants will then mix with the other gases mentioned above and be delivered to the substrate for deposition. Further process optimization and kinetic work will follow.

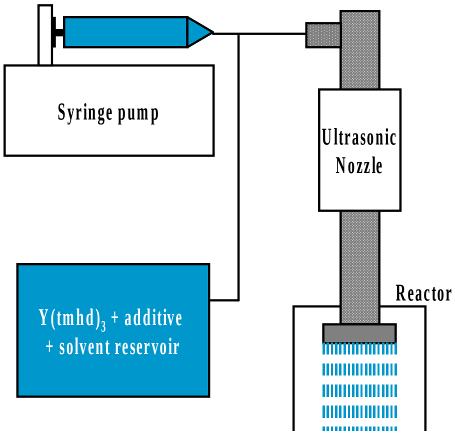

Fig. 5: Design for introducing yttria precursor *(After S. Matsuno).*

SUMMARY

The need to reduce the cost of TBC fabrication is necessary for the commercialization of these coatings for gas turbine engines. APCVD offers a cost effective, non-“line-of-sight,” uniform deposition technique that can either replace or supplement EB-PVD coatings. A stagnation flow reactor was used to deposit zirconia. Results of XRD and SEM show that zirconia coatings were successfully obtained with a thickness of 10 to 12 µm. Ytrrium source addition and kinetic studies are planned for understanding process parameters and control.

REFERENCES

Gadgil, P. N. “Single Wafer Processing in Stagnation Point Flow CVD Reactor: Prospects, Constraints and Reactor Design.” *Journal of Electronic Materials*, Volume 22, Number 2: 1992.

Haynes, J. A. *Oxidation and Degeneration of Thermal Barrier Coating System*. University of Alabama at Birmingham. Birmingham, Alabama: 1997.

Matsuno, S., F. Uchikawa, and S. Utsunomiya. “Etalorganic Chemical Vapor Deposition Using a Single Solution Source for high J_C $Y_1Ba_2Cu_3O_{7-X}$ Superconducting Films.” *Applied Physics Letters*. Volume 60, Number 19, pp. 2427–2429: 1992.

Jiming Zhang, Robin A. Gardiner, Peter S. Kirlin, Robert W. Boerstler, and John Steinbeck. “Single liquid source plasma-enhanced metalorganic chemical vapor deposition of high-quality $YBa_2Cu_3O_{7-x}$ thin films.” *Applied Physics Letters:* Volume 61, Number 24, 1992.

EVALUATION OF IRON-ALUMINIDE CVD COATINGS FOR HIGH TEMPERATURE CORROSION PROTECTION

B. A. Pint, Y. Zhang,* P. F. Tortorelli, J. A. Haynes and I. G. Wright

Metals and Ceramics Division
Oak Ridge National Laboratory
Oak Ridge, TN 37831-6156

***Center for Manufacturing Research**
Tennessee Technological University
Cookeville, TN 38505-0001

INTRODUCTION

A current interest is to increase the temperature capabilities of ferritic and austenitic alloys for power generation applications. However, these alloys owe their oxidation resistance to the formation of Cr- containing oxides which become less protective at higher temperatures and in steam or exhaust environments.[1-2] Iron aluminides are well-known to have excellent oxidation and sulfidation resistance due to the formation of an external, protective alumina scale.[3-7] An additional benefit of forming an alumina scale, compared to chromia or silica scales, is its resistance to carburization[8] and to vaporization in exhaust environments.[9] Thus, an aluminide coating could improve the oxidation resistance of ferritic and austenitic steels and enable their use at higher temperatures and/or in environments where they may not have adequate oxidation resistance.

In order to gain confidence in the performance of such coatings, more fundamental information is needed on their potential applications and benefits. Of particular interest is their performance in water vapor- and/or sulfur-bearing gases at high temperature and the prediction of coating lifetime as a function of its Al content. Chemical vapor deposited (CVD) Fe-Al coatings[10] are being investigated to provide some of this information. With a well-controlled laboratory CVD procedure, the coatings can be made uniform in composition, purity and microstructure over the entire substrate. One ferritic and one austenitic substrate were selected to examine differences in the two types of substrates. Two issues of particular concern are modeling the effect of time and temperature on the loss of Al from the coating into the substrate and understanding possible compatibility problems between candidate substrates and Fe-Al coatings which can have substantially different coefficients of thermal expansion (CTE).[11-12] The present work has focused on characterizing as-fabricated coatings and cyclic oxidation and sulfidation experiments. Acyclic test could expose any potential problems with CTE mismatch in the coating system or a problem with protective oxide scale adhesion.

EXPERIMENTAL PROCEDURE

The substrates used in this study were a ferritic alloy, Fe-9Cr-1Mo, and an austenitic stainless steel, 304L (nominally Fe-18Cr-9Ni). The CVD coating apparatus and method have been described previously.[10] A standard exposure of 6h at 900°C was used. Because the coatings contain significantly less Al than a typical Fe_3Al alloy such as FAS or FAL (28at.%Al), model Fe-Al alloys containing 15at.%(8wt.%) and 20at.%(11wt.%) were cast for comparison in oxidation tests and CTE measurements. All of the specimens were polished to a 0.3mm alumina finish either prior to coating or prior to exposure. As a final treatment, all specimens were ultrasonically cleaned in acetone and methanol.

High temperature exposures were conducted at 800°C. The cyclic oxidation testing in air with 10±0.5vol.%H_2O was done in an automated test rig with a cycle consisting of 1h at temperature and 10min cooling at room temperature. Both ends of the vertical reaction tube were closed and the water vapor was controlled in the carrier gas by a water injection system described elsewhere.[2] Cyclic testing in H_2S-H_2O-H_2-Ar (P_{S_2}=10^{-6}atm; P_{O_2}=10^{-22}atm) was done manually in a Cahn microbalance with a cycle time of approximately 25h and a cooling time of >1h. Before and after exposure, selected specimens were examined by light microscopy, field emission gun, scanning electron microscopy (SEM) equipped with energy dispersive x-ray analysis (EDXA), x-ray diffraction (XRD), and electron probe microanalysis (EPMA) using wavelength dispersive x-ray analysis. The surface product of cross-sectioned specimens was protected by Cu-plating the specimen prior to mounting in epoxy. Thermal expansion measurements were performed on specimens (3-4mm diameter, 1cm or 2.5cm long) of several alloys up to 1300°C on a Theta Industries dual push rod differential dilatometer.

RESULTS AND DISCUSSION

AS-DEPOSITED COATING CHARACTERIZATION

Figure 1 shows a cross-section of the as-deposited aluminide coating on Fe-9Cr-1Mo. From the atomic number contrast of the back-scattered electron image, there appears to be a ≈3mm thick outer layer and a ≈60mm thick inner layer. Figure 2 shows a composition profile from the outer surface into the substrate. The outer layer contains ≈20at.%Al but a gradual decrease in the Al content was observed back to a depth of ≈50mm, which is slightly less than expected from the image in Fig. 1.

Figure 3 is a EPMA back-scattered electron image of a cross-section of the as-deposited coating on 304L. In this case, the presence of Ni in the substrate results in a more complicated microstructure. The outer layer is slightly thicker than with the ferritic substrate, ≈5mm. The composition profile in the coating, Figure 4, indicates that this layer is rich in Ni (>20at.%) and contains more Al (≈35at.%) than the outer layer on Fe-9Cr-1Mo. However, the inner layer on 304L is only ≈35mm thick. This difference is attributed to slower diffusion in the austenitic substrate which also affects its oxidation behavior.[13-14] Again, the inner layer on 304L contains more Al than on Fe-9Cr-1Mo and appears to have a more abrupt change in composition at the interface with the substrate.

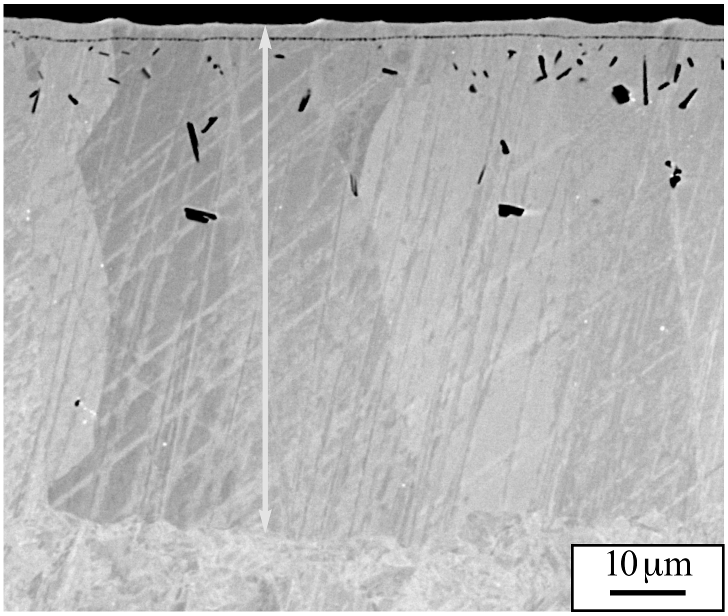

Fig. 1. EPMA back-scattered electron image of the as-deposited aluminide coating on Fe-9Cr-1Mo.

The coatings also were characterized by XRD. Figure 5 shows one peak associated with (211) in the a structure or (422) in the DO_3 (Fe_3Al) structure. For the coatings on both substrates, the two peaks are due to the Ka_1 and Ka_2 Cu radiation. For comparison, diffraction data for cast alloys with different Al contents also are plotted. These peaks show a shift with increasing Al content. They do not show a split peak because a faster scan rate was used. Results for the coating on 304L appear to show a slightly higher Al content as the peak shift is greater than for the coating on Fe-9Cr-1Mo. However, this could also be attributed to an effect of Ni in the coating, which is not present in the other substrate. It is possible that the location and shape of this peak may be a non-destructive means of evaluating the Al content in the coating.

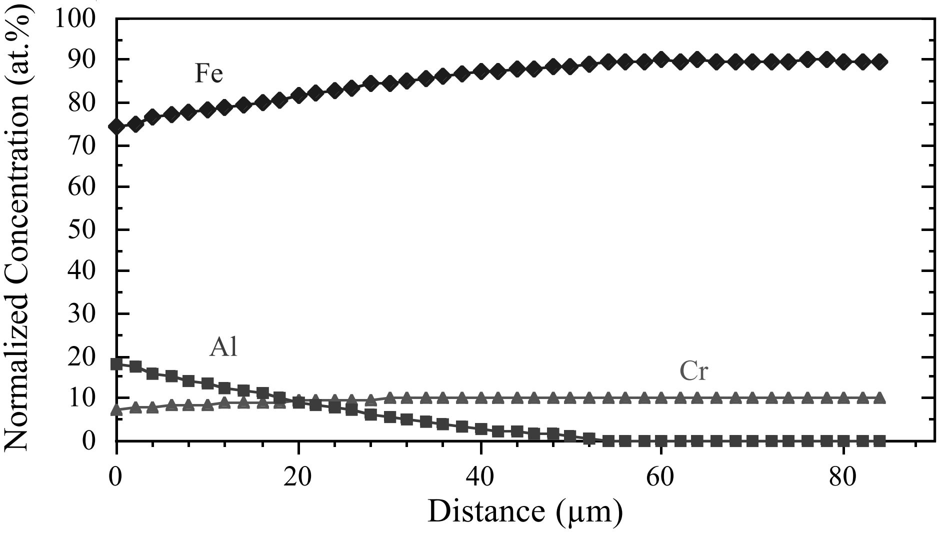

Fig. 2. Fe, Al and Cr profiles in the as-deposited coating on Fe-9Cr-1Mo using EPMA.

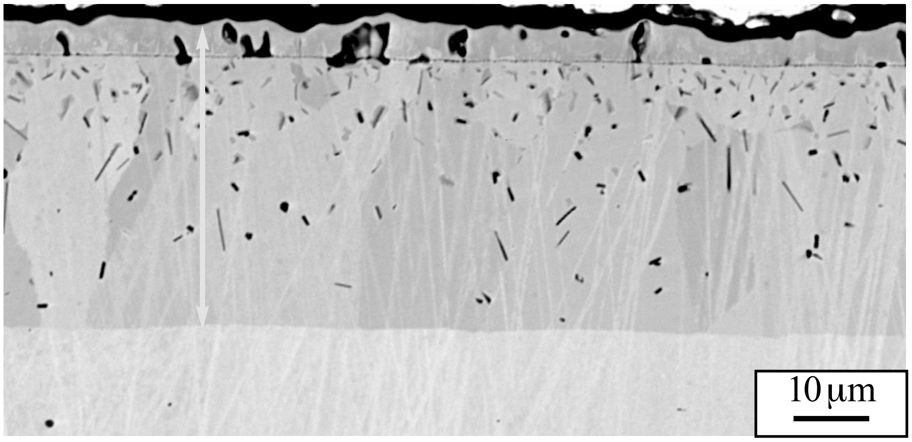

Fig. 3. EPMA back-scattered electron image of the as-deposited aluminide coating on 304L.

CHARACTERIZATION OF COATED 304L

Initial exposures at 800°C in air, air+10vol.%H_2O and H_2S-H_2O-H_2-Ar showed promising mass change results for the CVD coatings.[10] Characterization of the reaction products has been completed that further elucidates the coating benefit. Figure 6 shows metallographic polished cross-sections on 304L with and without the coating and the effect of water vapor after a 24h exposure at 800°C. Figures 6a and 6b show the thin reaction product formed in air with and without the CVD coating, respectively. At 800°C, 304L would not require a coating for service in air. However, when 10%H_2O was added to the environment, the reaction product was significantly thicker without a coating, Figure 6c. The coated specimen showed no significant change with the addition of water vapor, Figure 6d. This same specimen also was characterized using EPMA, Figure 7. Figure 7a is a back-scattered electron image similar to the light microscopy image in Figure 6d. X-ray maps of O, Ni and Al are shown in Figures 7b-7d. The O map shows a continuous surface oxide with little oxygen penetration into the coating, Figure 7b. The Ni and Al maps show Ni-Al precipitates in the coating and an enrichment of both elements near the coatings

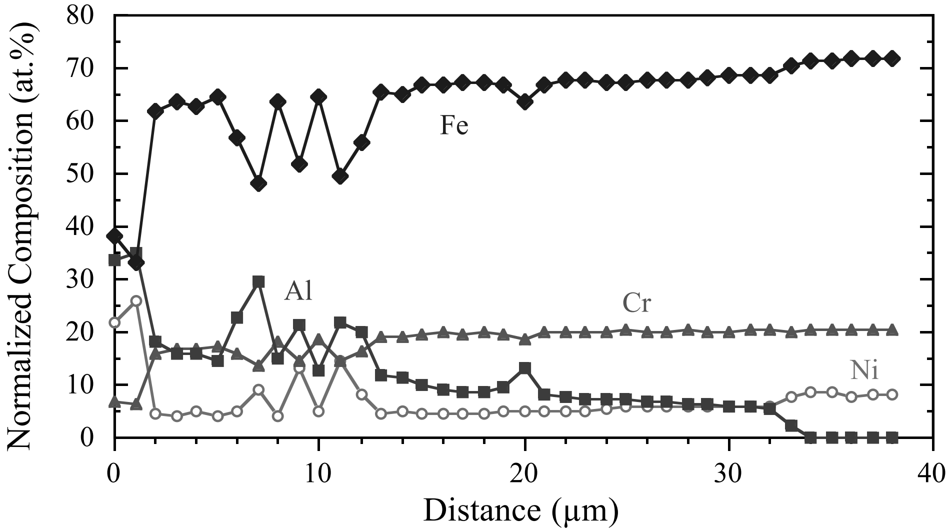

Fig. 4. Fe, Al Cr and Ni profiles in the as-deposited coating on 304L using EPMA.

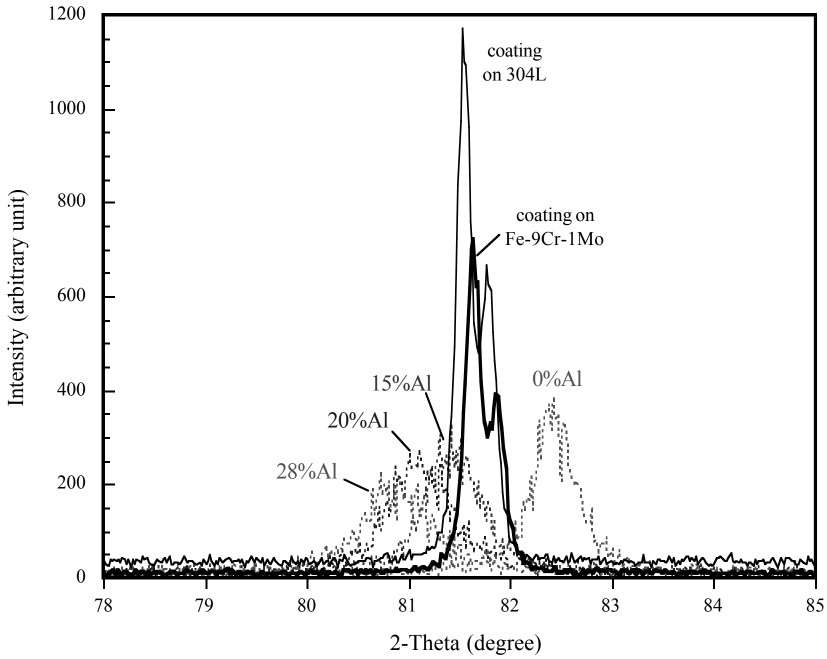

Fig. 5. X-ray diffraction results for cast alloys and coatings on Fe-9Cr-1Mo and 304L. At this location, there are two peaks for the coating and a single peak for the cast alloys which shifts with Al

surface. Figure 8 shows a composition profile in the coating after the 24h, 800°C exposure in air+10%H_2O. Compared to the as-deposited composition, Figure 4, the Ni and Al contents in the outer coating layer actually appear higher with less Al in the inner layer. This change could be associated with a preference for intermetallic phase formation but these differences also may be a location dependence effect or due to a coating to coating variation. More work is necessary to confirm this change in composition with exposure. However, it does appear clear from these results that, with an aluminide

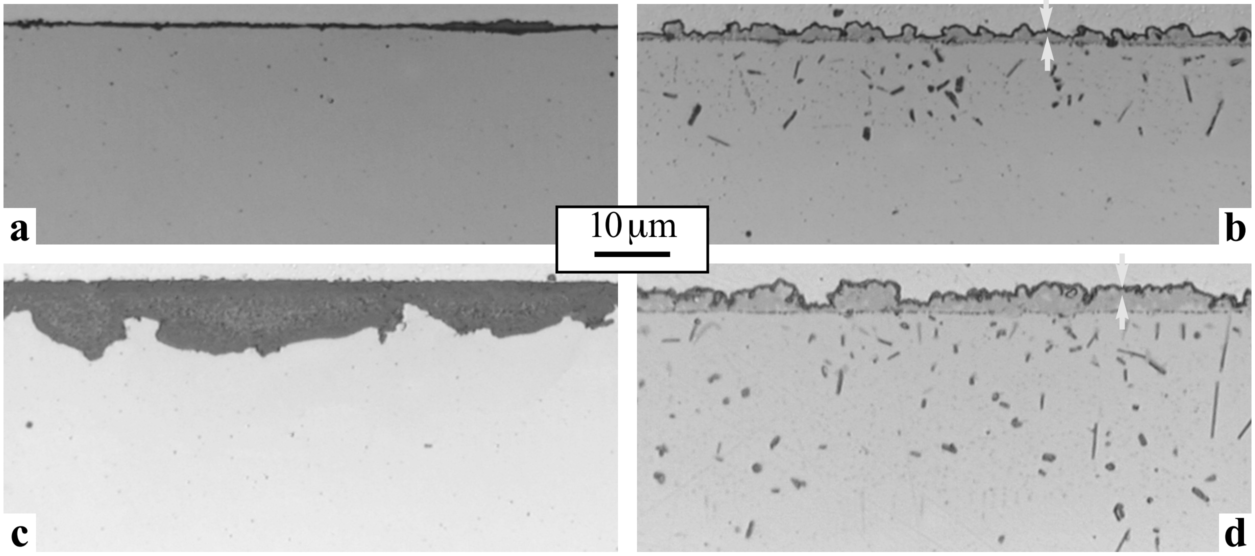

Fig. 6. Light microscopy images of cross-sections of 304L after 24h at 800°C uncoated in (a) air and (c) air+10%H_2O and with an aluminide coating in (b) air and (d) air+10%H_2O. Without a coating, 304L was strongly attacked by water vapor. Arrows point to the thin oxide layer in (b) and (d).

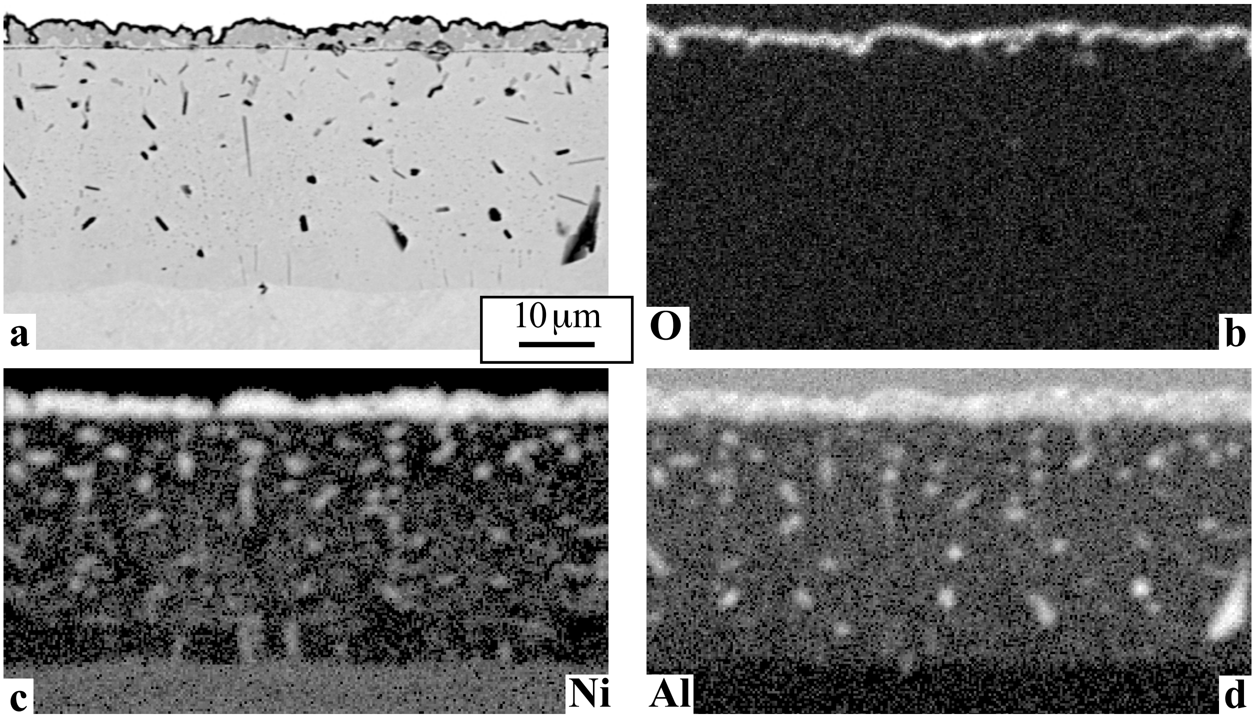

Fig 7. (a) EPMA back-scattered electron cross-sectional electron image of coated 304L after 24h at 800°C in air+10%H_2O. X-ray maps of the same region showing (b) O, (c) Ni and (d) Al. Oxygen was only detected in the surface oxide and not within the coating.

coating, 304L is much more resistant to environments containing water vapor.

CHARACTERIZATION OF COATED Fe-9Cr-1Mo

Figure 9 shows metallographically polished cross-sections on Fe-9Cr-1Mo with and without the

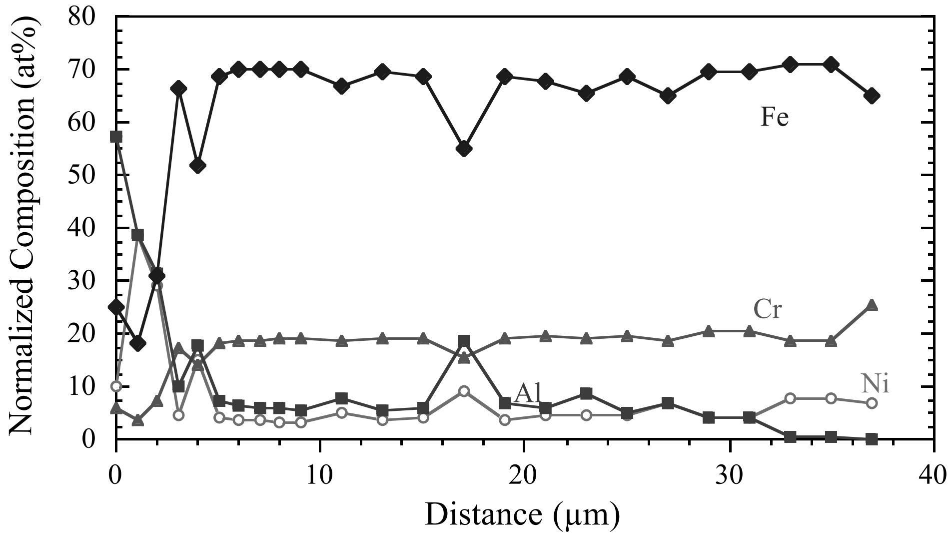

Fig. 8. Fe, Al Cr and Ni profiles in the coating on 304L after 24h at 800°C in air+10%H_2O using EPMA.

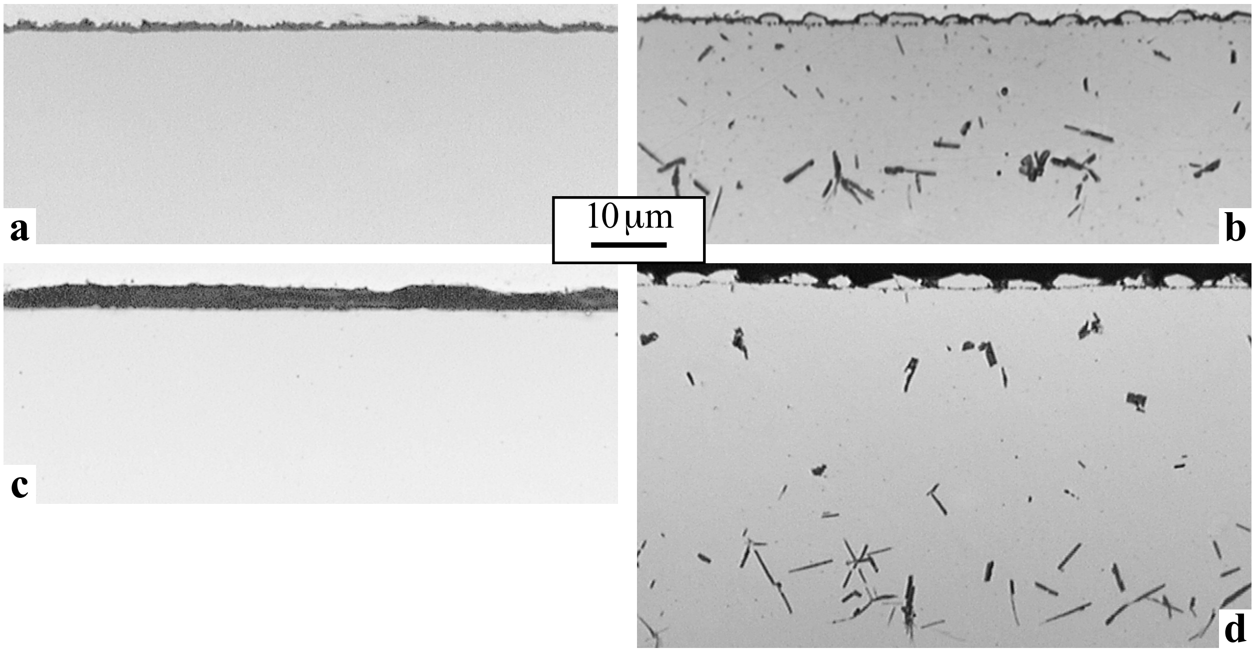

Fig. 9. Light microscopy images of cross-sections of uncoated Fe-9Cr-1Mo after 24h at 800°C in (a) air and (c) air+10%H_2O and with an aluminide coating in (b) air and (d) air+10%H_2O. Without a coating, Fe-9Cr-1Mo showed a much thicker oxide when exposed to water vapor.

coating and the effect of water vapor on the amount of reaction after 24h at 800°C. As was the case of 304L, dry air oxidation at 800°C resulted in a thin, protective reaction layer on uncoated Fe-9Cr-1Mo, Figure 9a. A similar thin oxide was formed on the coated substrate, Figure 9b. Uncoated Fe-9Cr-1Mo also was adversely affected by the addition of 10%H_2O, Figure 9c. The reaction layer appears thinner than that observed on 304L, Figure 6c. However, the cross-section did not include one of the large FeO nodules which formed on the specimen during this test. With the CVD coating, no accelerated attack was observed with the addition of water vapor. The coated specimen exposed for 24h to air+10%H_2O also was examined by EPMA. Figure 10 shows a back-scattered electron image and the corresponding O, Cr and Al x-ray maps from the same area. The Al and O maps show a continuous Al_2O_3 external oxide and no oxygen penetration into the coating or substrate. There are a few Cr-rich precipitates in the coating and in the substrate, Figure 10c. The acicular particles concentrated near the substrate-coating interface are rich in Al, Figure 10d. Figure 11 shows a concentration profile through the exposed coating shown in Figure 10. The Al content in the coating has decreased to less than 10at.% except at the surface. The two peaks in the Al profile correspond to the Al-rich precipitates shown in Figure 10d. More particles appeared to form during the 24h, 800°C exposure and, like the coating on 304L, this coating showed a tendency toward intermetallic (Fe_3Al) phase formation. While the coating performed well in this test, the low Al content observed after completion suggests that the coating lifetime may be limited when made using these conditions.

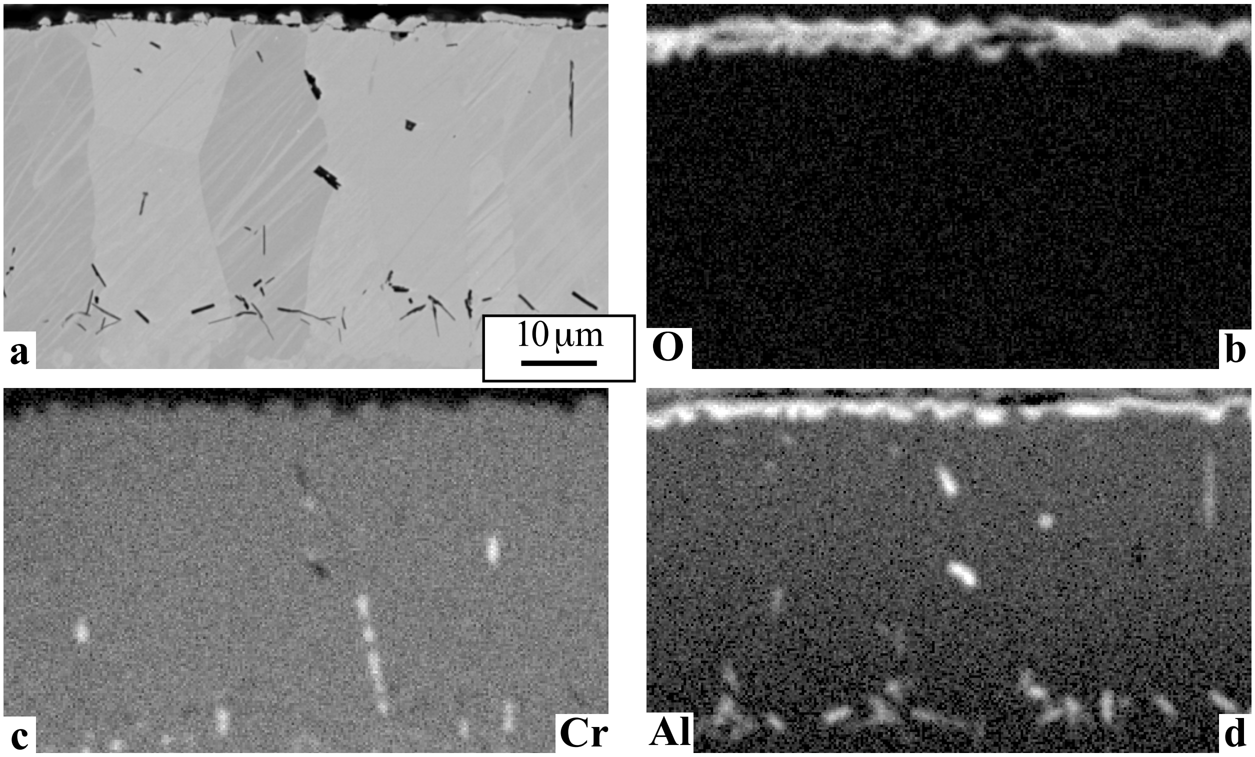

Fig. 10. (a) EPMA back-scattered electron cross-sectional electron image of coated Fe-9Cr-1Mo after 24h at 800°C in air+10%H_2O. X-ray maps of the same region showing (b) O, (c) Ni and (d) Al. Oxygen was only detected in the surface oxide and not within the coating.

CYCLIC OXIDATION AND SULFIDATION RESULTS

Based on the positive results observed in 24h isothermal tests,[10] cyclic experiments were conducted on similar coatings at 800°C. There are two purposes to a cyclic test. First, upon cooling after a cycle, any damage to the external alumina scale must be repaired in order to maintain the benefit during additional cycles. The coating must contain sufficient Al to reform the surface oxide or accelerated attack

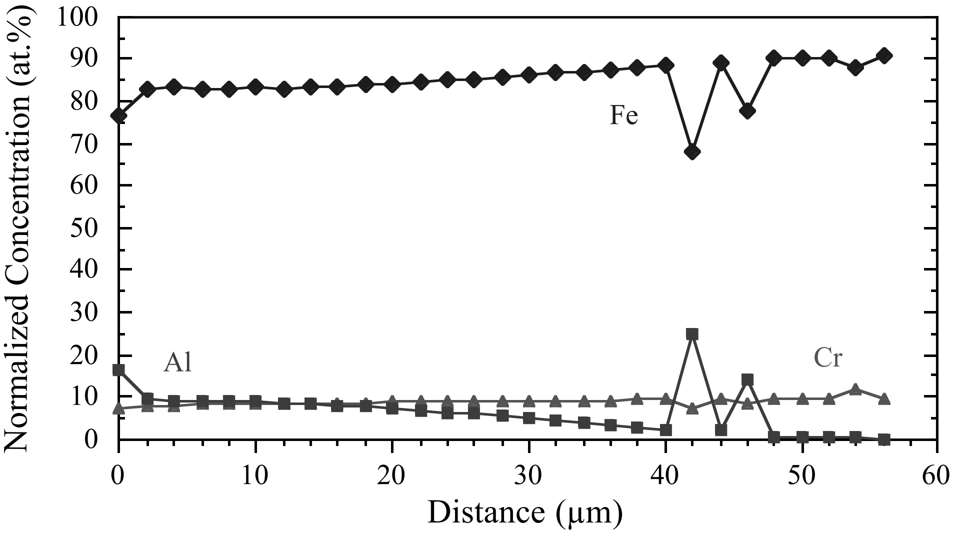

Fig. 11. Fe, Al and Cr profiles in the coating on Fe-9Cr-1Mo after 24h at 800°C in air+10%H_2O using EPMA.

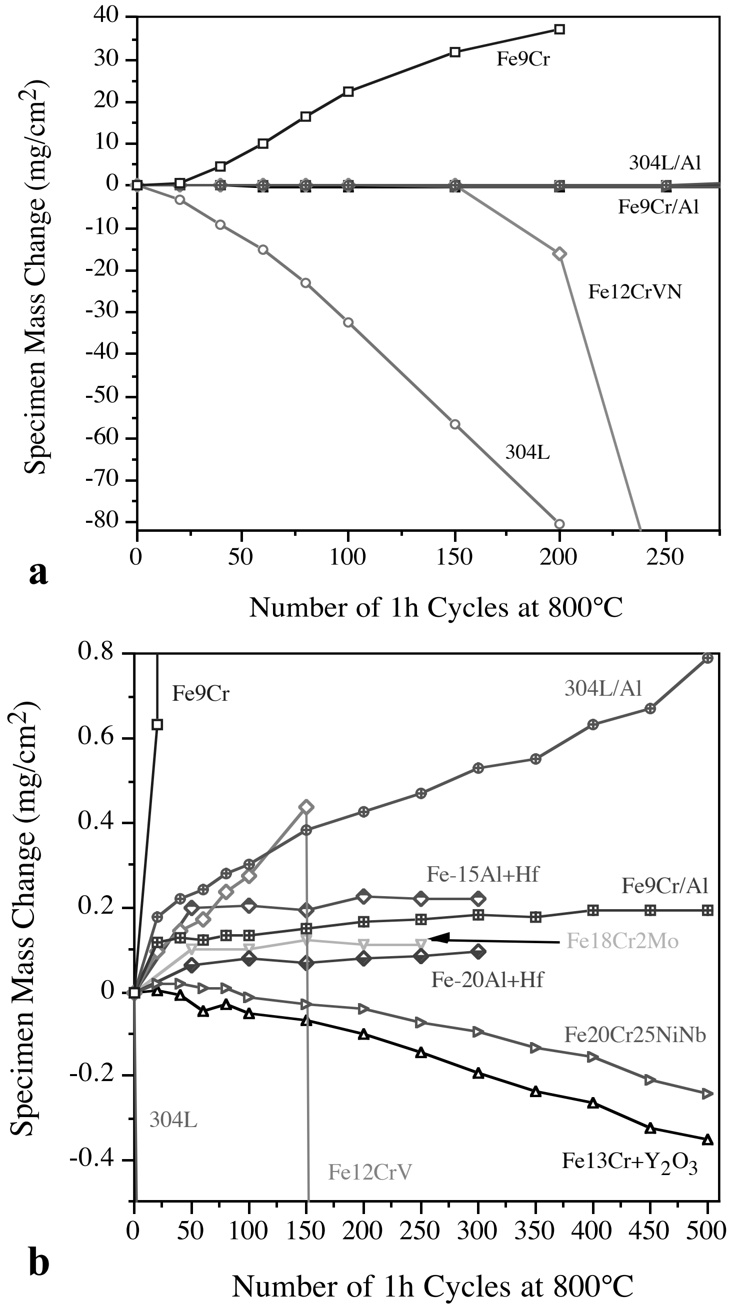

Fig. 12. Specimen mass changes during 1h cycles at 800°C in air+10%H_2O.

may occur. Second, any problem due to the CTE mismatch between the coating and substrate are exacerbated during thermal cycling.

Figure 12 shows results for 1h cycles conducted in air+10%H_2O. Besides the coated and uncoated 304L and Fe-9Cr-1Mo specimens, several other compositions also were included. Figure 12a shows the benefit of coating both materials. For uncoated Fe-9Cr-1Mo, a high mass gain results from FeO_x formation. This type of rapid attack would not be anticipated in a dry air environment. In contrast, uncoated 304L showed high mass losses during a 200 cycle exposure. The thick oxide formed in the

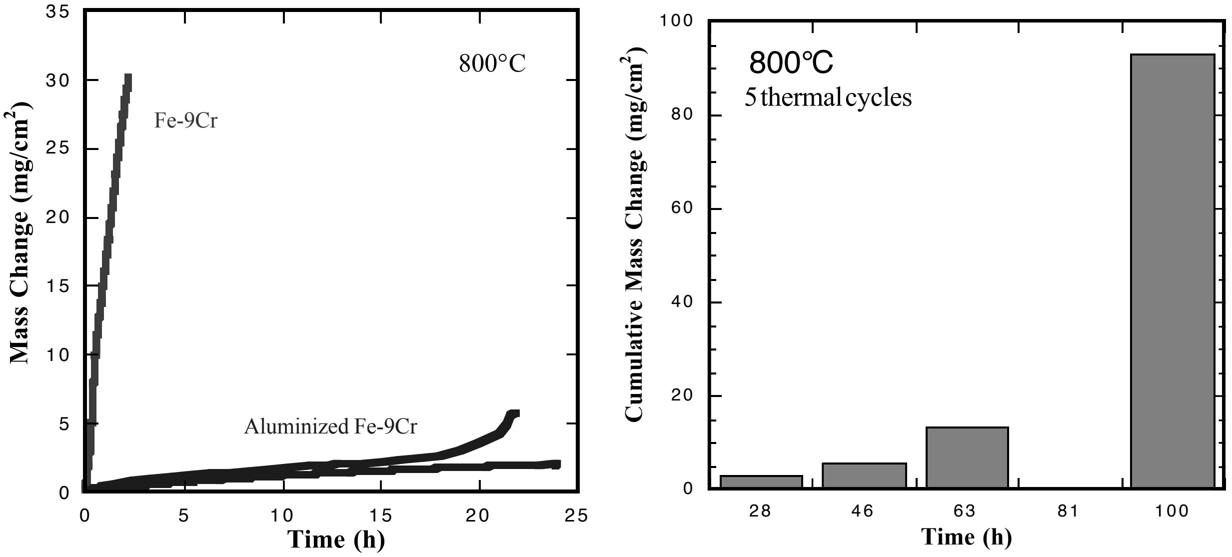

Fig. 13. For coating on Fe-9Cr-1Mo exposed to a sulfidizing environment at 800°C, (a) shows the mass gain during the first 24h for two coated specimens compared to the uncoated material. In (b), the cumulative mass gain is shown for each of 5 cycles to a total of 100h. By the 5th cycle, the specimen was strongly attacked.

presence of water vapor (e.g. Figure 6c) apparently continued to spall as a result of the thermal cycling.

Figure 12b shows results for the same test but with a smaller mass change range than Figure 12a that shows the benefit of the aluminide coatings on these materials. Small mass gains were noted for the coated substrates with little or no spallation noted for the coated Fe-9Cr-1Mo specimen. The mass gain was slightly higher for 304L and this specimen appeared to show some spallation at the specimen edges. These

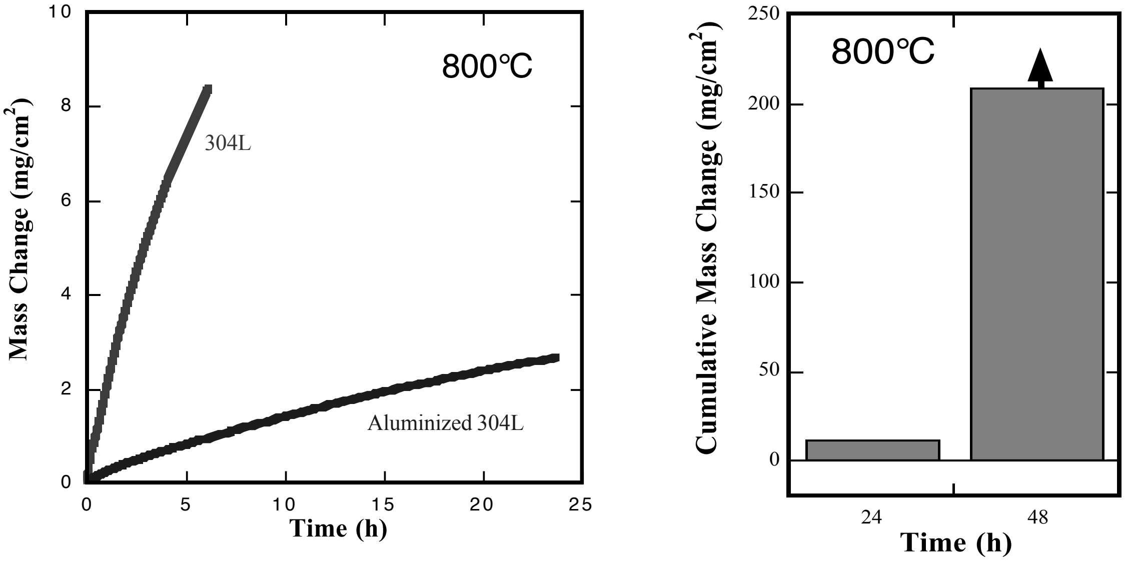

Fig. 14. For coating on 304L exposed to a sulfidizing environment at 800°C, (a) shows the mass gain during the first 24h for a coated specimens compared to the uncoated material. In (b), the cumulative mass gain shows that after a second 24h exposure, the specimen was completely consumed.

specimens have not yet been characterized by metallography or SEM.

For comparison, a Fe-12Cr with VN (manufactured by ABB Alstrom) showed good oxidation resistance in this environment for 150 cycles but then was heavily attacked, likely due to Cr depletion. This improvement in behavior is expected in alloys with higher Cr contents, and better performance of the higher Cr content alloys was noted, Figure 12b. Specimens of NF709 (Fe-20Cr-25Ni) and Fe-18Cr-2Mo showed low mass changes during this test due to their higher Cr contents. The slight mass loss for NF709 is associated with the evaporation of $Cr(OH)_x$. Similar performance was noted for an oxide dispersion strengthened (ODS) Fe-13Cr-3W specimen. In this case, the excellent oxidation resistance is attributed to the fine subgrain structure of the ODS material which allows for rapid, short-circuit Cr diffusion in the substrate. The benefit of short-circuit diffusion has been observed for both chromia- and alumina-forming substrates.[15-19]

Cyclic exposures also was performed in a sulfidizing H_2S-H_2O-H_2-Ar environment. In this case, the equipment was not automated and ≈20-25h cycles were used instead of 1h cycles. However, the mass gain was monitored continuously by a microbalance. In the case of Fe-9Cr-1Mo, the improved performance of the specimen with an aluminized coating was excellent during the first 24h, Figure 13a. However, in subsequent cycles, the mass gain increased dramatically, Figure 13b. (No mass gain was measured during the 4th cycle due to an equipment problem.) By the end of the 5th cycle, the large mass gain represents almost 50% of the specimen thickness consumed. Thus the coating did not continue to provide protection in this system. The coating performance degraded even more rapidly for 304L, Figure 14. The first 24h showed good performance, Figure 14a, but the second 24h resulted in essentially complete consumption of the specimen, Figure 14b. The relatively poor performance for the coatings could be attributed to their low Al contents. Additional characterization of the coated specimens run for only 24h is being performed

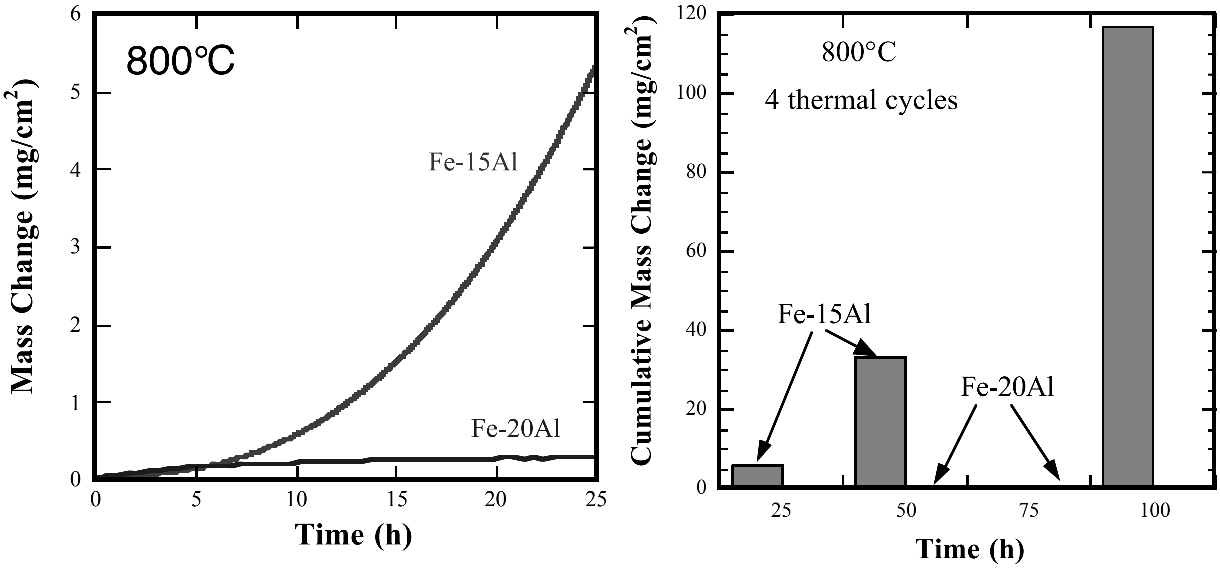

Fig. 15. For cast Fe-15Al and Fe-20Al exposed to a sulfidizing environment at 800°C, (a) shows the mass gain during the first 24h and (b) shows the cumulative mass gain during subsequent cycles. Increasing the Al content to 20at% resulted in a total mass change after 4 cycles of less than

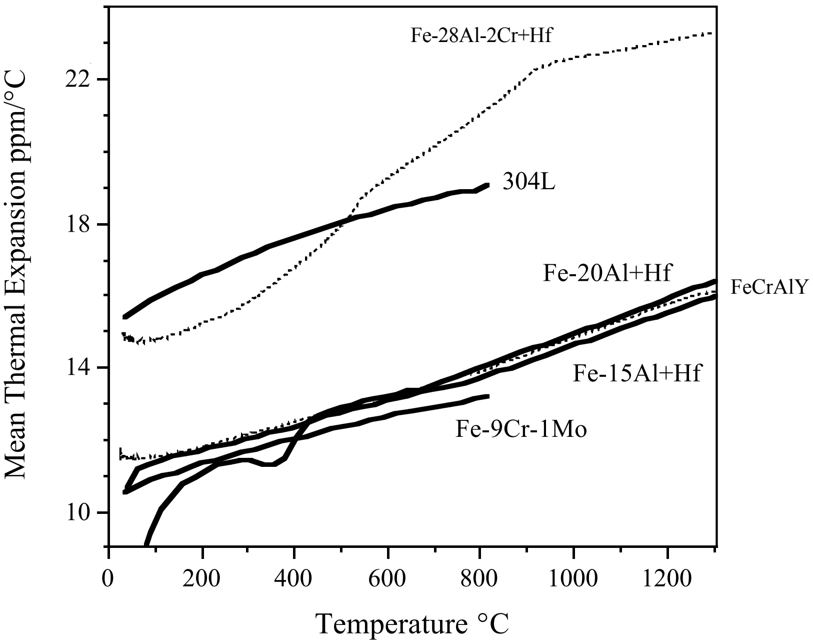

Fig. 16. Mean coefficient of thermal expansion as a function of temperature for various FeCrAl and Fe-Al substrates.

to determine the Al contents and possibly provide more information on the cause of failure.

Previous work by DeVan and Tortorelli suggested that 18at.% Al was required for good sulfidation resistance of iron aluminides.[4] While the initial coating may contain that level of Al at the surface (Figures 2 and 4), after 24h at 800°C the Al contents were much lower on average (Figures 8 and 11). In addition, the enrichment of Ni in the outer layer of the coating on 304L may lead to the formation of NiS_x which melts at <700°C. In order to explore the possible problems with low Al contents, cast alloys with 15 and 20at.%Al were exposed under the same conditions as the coatings. Figure 15a shows the higher mass gain observed for Fe-15Al compared to Fe-20Al. As with the coated substrates, Fe-15Al was fully consumed after 4 cycles totaling 101h at 800°C. As expected from the previous work,[4] Fe-20Al showed much better sulfidation resistance in this test. Thermal cycling did not appear to affect the excellent performance during the first cycle, Figure 15a, and the total mass gain after 4 cycles was less than 0.2mg/cm^2.

CTE MEASUREMENTS

While the sulfidation tests show higher Al contents are desirable, previous work on Fe_3Al-type materials showed that their high CTE led to increased scale spallation compared to other Fe-base alloys.[10-12] This problem was first noted by Smialek and co-workers for Fe-40at.%Al.[20] While the CTE has been determined for FAL and FAS and ODS FAS, less information on CTE is available for lower Al contents. Therefore, Fe-15Al and Fe-20Al were examined to determine the effect of Al on the CTE of ferritic alloys. Figure 16 shows the CTE determined for these 2 cast materials along with that for FAS and FeCrAlY determined in a previous study and literature values for 304L and Fe-9Cr-1Mo.[21-22] These results indicate that the CTE for ferritic materials is essentially independent of Al content. By maintaining

Al contents below Fe_3Al (≈20at.%), good oxidation performance and a good CTE match with Fe-9Cr-1Mo could be achieved. However, since 304L has a higher CTE, it may be that a fully DO_3 structure may be more compatible. The higher CTE of 304L may be why the current coatings (with low Al and thus low CTE) did not perform as well in 1h cyclic testing as did the coating on Fe-9Cr-1Mo, Figure 12b. Future work will try to optimize coating composition and performance based on matching the substrate and coating CTE and sufficient Al to maintain corrosion resistance.

SUMMARY

Coatings made by CVD aluminizing offer a potential method for synthesizing model corrosion-resistant coatings for oxidizing and sulfidizing environments. Present results show that CVD aluminized coatings have excellent resistance to environments containing water vapor but do not appear to have sufficient Al for long-term resistance to low oxygen, high sulfur environments. The different CTE of ferritic and austenitic substrates suggest different strategies for the optimum Al content in each case. The high CTE of 304L may be more compatible with Fe_3Al coatings while the ferritic substrates should avoid the intermetallic phase formation.

ACKNOWLEDGMENTS

The authors would like to thank K. Cooley, S. Waters, M. Howell, G. Garner and L. D. Chitwood at ORNL for assistance with the experimental work.

REFERENCES

1. G. C. Wood, I. G. Wright, T. Hodgkiess, D. P. Whittle, "A Comparison of the Oxidation of Fe-Cr, Ni-Cr and Co-Cr Alloys in Oxygen and Water Vapor," *Werk. Korr.*, 21 (1970) 900-10.
2. B. A. Pint and J. M. Rakowski, "Effect of Water Vapor on the Oxidation Resistance of Stainless Steels," NACE Paper 00-259, Houston, TX, presented at NACE Corrosion 2000, Orlando, FL, March 2000.
3. P. F. Tortorelli and J. H. DeVan, "Behavior of Iron Aluminides in Oxidizing and Oxidizing/ Sulfidizing Environments," *Mat. Sci. and Eng.*, A153 (1992) 573-7.
4. J. H. DeVan and P. F. Tortorelli, "The Oxidation-Sulfidation Behavior of Iron Alloys Containing 16-40at.% Aluminum," *Corr. Sci.*, 35 (1993) 1065-71.
5. K. Natesan and R. N. Johnson, "Corrosion Performance of Fe-Cr-Al and Fe Aluminide Alloys in Complex Gas Environments," in *Heat Resistant Materials II*, K Natesan, P. Ganesan and G. Lai, Eds., ASM Int.,Materials Park, OH, 1996, pp.591-9.
6. P. F. Tortorelli and K. Natesan, Mater. Sci. and Eng. A258 (1998) 115.
7. B. A. Pint, P. F. Tortorelli and I .G. Wright, "Long-Term Oxidation Performance of Ingot-Produced Fe_3Al Alloys," Mater. High Temp., 16 (1999) 1-13.
8. B. Jönsson and C. Svedberg, "Limiting Factors for Fe-Cr-Al and NiCr in Controlled Industrial Atmospheres," Mater. Sci. Forum, 251-4 (1997) 551-8.

9. E. J. Opila and N. S. Jacobson, “Volatile Hydroxide Species of Common Protective Oxides and Their Role in High Temperature Corrosion,” in *Fundamental Aspects of High Temperature Corrosion*, D. A. Shores, R. A. Rapp, and P. Y. Hou, Eds., Proc. Vol.96-26, Electrochemical Society, Pennington, NJ, 1996, pp.344-56.
10. B. A. Pint, P. F. Tortorelli, I. G. Wright, J. A. Haynes, and W. Y. Lee, “Evaluation Of Iron-Aluminide Coatings For High-Temperature Corrosion Protection,” paper 1.X in Proc. Fourteenth Annual Conf. Fossil Energy Materials, R. R. Judkins (comp.), U. S. Department of Energy, 2000.
11. I. G. Wright, B. A. Pint and P. F. Tortorelli, "The High Temperature Oxidation Behavior of ODS Fe_3Al," *Oxid. Met*., 55 (2001) 333-57.
12. B. A. Pint, K. L. More, P. F. Tortorelli, W. D. Porter and I. G. Wright, "Optimizing the Imperfect Oxidation Performance of Iron Aluminides," Mater. Sci. Forum, in press.
13. G.V. Samsonov, *Oxide Handbook*, IFI/Plenum, New York, 1973.
14. N. V. Bangaru and R. C. Krutenat, “Diffusion Coatings of Steels: Formation Mechanism and Microstructure of Aluminized Heat-Resistant Stainless Steels,” J. Vac. Sci. Technol. B, 2 (1984) 806-15.

INVESTIGATION OF ADVANCED ALLOYS FOR HEAT RECOVERY SYSTEMS

R. W. Swindeman, M. L. Santella, and P. J. Maziasz

INTRODUCTION

The objective of the research on advanced alloys is to provide databases and design criteria that will assist contractors in selecting optimum alloys for construction of components needed to contain process streams in advanced heat recovery systems. Typical components include steam line piping and superheater tubing for ultracritical steam cycles (600 to 700°C), heat exchanger tubing for advanced steam systems (650 to 800°C), foil materials for recuperators on advanced turbine systems (700 to 750°C), heat exchanger tubing for pulsed combustors (650 to 950°C), and tubesheets, plenums, and liners for hot gas cleanup systems (850 to 1000°C). The near term objective is to gather data that will permit the consideration of advanced steels for applications to 900°C in oxidizing environments or to 870°C slightly sulfidizing environments. Studies include the collection of data that will permit the consideration of third-generation advanced ferritic steels for service to 650°C, Ni-Co-Cr-Al alloys for service to 950°C, and oxide dispersion strengthened (ODS) alloys in aggressive environments to 1000°C.

BACKGROUND

In the United States, new power generation needs are being met by the use of co-generation and the installation of medium-size gas turbines. Research in the fossil power industry is largely focused on condition assessment and life extension of aging components. Research related to inspection, damage assessment, and repair is actively supported by fossil power and petrochemical industries. In both industries, replacement of components with “new” and “advanced” materials is sometimes required, and research on the performance of the advanced materials for such components is in progress. Development of advanced materials for the fossil power industry has largely performed in Japan under sponsorship of the Electric Power Research Institute (1). Alloys such as tungsten-vanadium-modified 2 1/4 Cr (T23), 9Cr (T92), and 12Cr (T122) steels have reached ASME Code status and are being used to replace T11, T22, and austenitic stainless steels such as 304H and 321H. These advanced ferritic steels are candidates for the construction of piping systems, headers, and tubing for steam service to 600°C, but more research is needed before the complex metallurgical constitution of the alloys is fully understood and their reliability for long-time service can be guaranteed. Advanced austenitic stainless steels for service above 600°C include niobium-modified 310 stainless steel (HR3C), a titanium-modified 20Cr-25Ni-Nb stainless steel (NF709), and a copper-modified 18Cr-Ni-Nb-N steel (SAVES 25). Of these steels, HR3C has attained

Code status as 310HCbN and a copper-modified stainless steel is in the Code- approval process. The steels are intended for superheater tubing, but service temperatures are limited to approximately 730°C. Similar to the advanced ferritic steels, there is much to be learned about the behavior of the complex austenitic steels in high-temperature environments. For service above 730°C, alloys containing over 30% nickel, such as HR 120 and HR 160, have been developed (2,3). Also, there is renewed interest in cobalt-containing alloys, such as alloy 617, and ODS aluminum-containing alloys for service at 1000°C and higher.

ADVANCED FERRITIC STEELS

Issues have arisen in regard to the usage of the advanced ferritic steels in high-temperature service. Recently, concerns were raised about the welding procedures. To avoid hydrogen cracking, a preheat of 204°C is required for these alloys. This temperature is above the martensite finish temperature for Grade 91, hence some of the austenite produced in the welding heat cycle could remain untransformed. It would save energy if fabricators could proceed to the post weld heat treatment (PWHT) without cooling below 204°C, but there is concern that austenite retained in the weldment at 204°C would produce fresh martensite after the PWHT. Further, filler metals used for welding Gr91 are permitted to contain up to 1% Nickel. Nickel is known to lower the critical temperature where martensite or tempered martensite begins to transform to austenite (Ac1 temperature). If the PWHT is above this temperature, some of the newly formed austenite could produce fresh martensite or softer ferrite upon cooling slowly. The influence of untempered martensite on the high-temperature performance Gr91 is unknown. To assist in the resolution of the issue, weldments of Grade 91 are being examined.

Gleeble testing of base metal (0.18% Ni) and weld metal (0.70% Ni) was performed. It was observed that the Ac1 for the base metal was near 840°C and that for weld metal was near 810°C. On cooling, the martensite start temperature (Ms) for base metal was near 400°C and that for weld metal was near 350°C. Weld metal, cooled to the preheat temperature (204°C) then returned to 740°C for a simulated PWHT treatment, contained about 18% fresh martensite after cool-down. The Ac1 and Ms data for several weld and based metal compositions were collected and used to assess the validity of models developed to correlate the Ac1 and Ms temperatures. Good correlations were observed. The maximum temperature for PWHT (Ac1) for Gr91 was determined as a function of (Ni + Mn). See Fig. 1. From this correlation, it may be seen that (Mn+Ni) content of the weld metal should not exceed 1.3% if the intended PWHT temperature is to be 780°C.

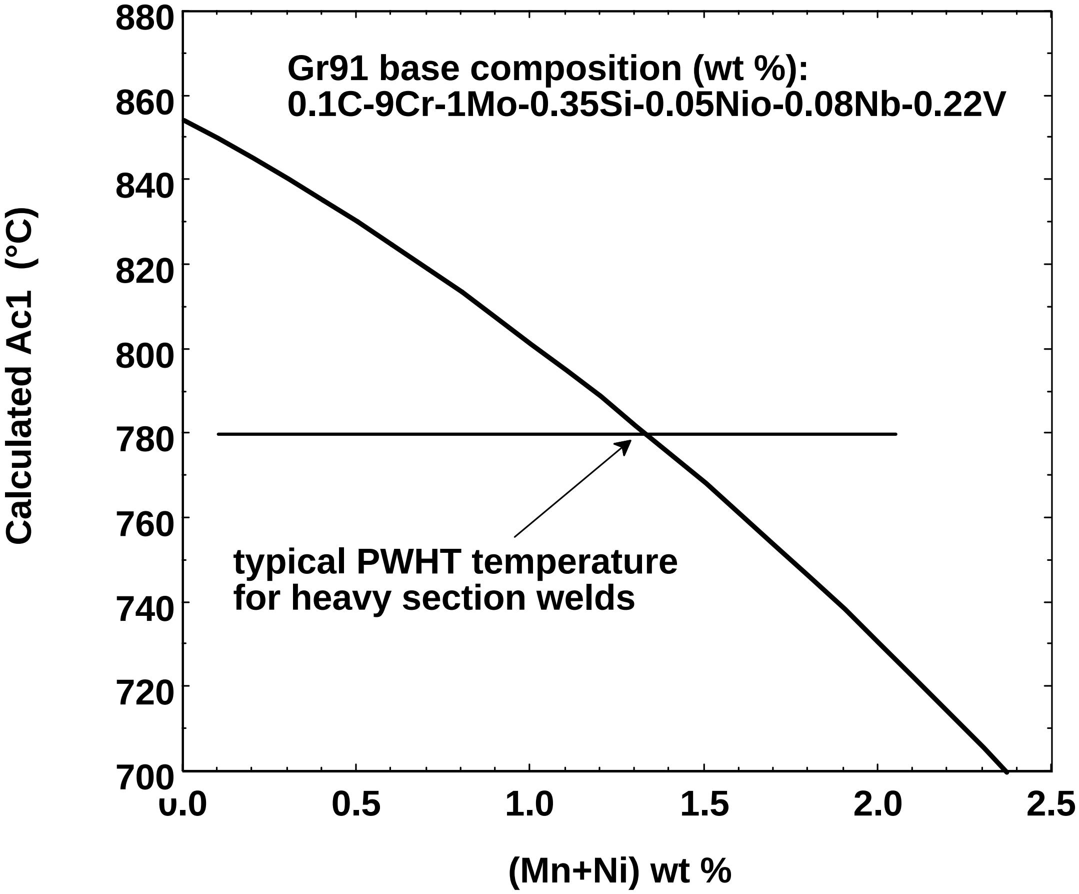

Fig. 1. Ac1 versus (Ni+Mn) for Gr91 steel.

Creep rupture testing was performed at 600°C. Weld metal samples were tested after exposure to PHWT temperatures of 740 and 780°C. These temperatures represent the extremes for the PWHT temperature. It was observed that specimens with fresh martensite were stronger than those with fully tempered martensite (drop pre-heat). See Figs. 2 and 3. The effect of the welding conditions that produce fresh martensite on weld strength reduction factors is being examined by creep-rupture testing of weldment specimens. This work is in progress.

Another issue pertains to the long-time stability of the martensitic structure in the advanced ferritics. In the case of Grade 91, evaluation after thermal aging and service exposure for up to 155,000 hours revealed a loss in strength (2). This loss was related to long-time thermal exposure, rather than in-service creep damage. The margin on life implicit in the selection of allowable stresses for design was adequate to accommodate the aging effects in Gr91 over most of the useful temperature range. This margin, in

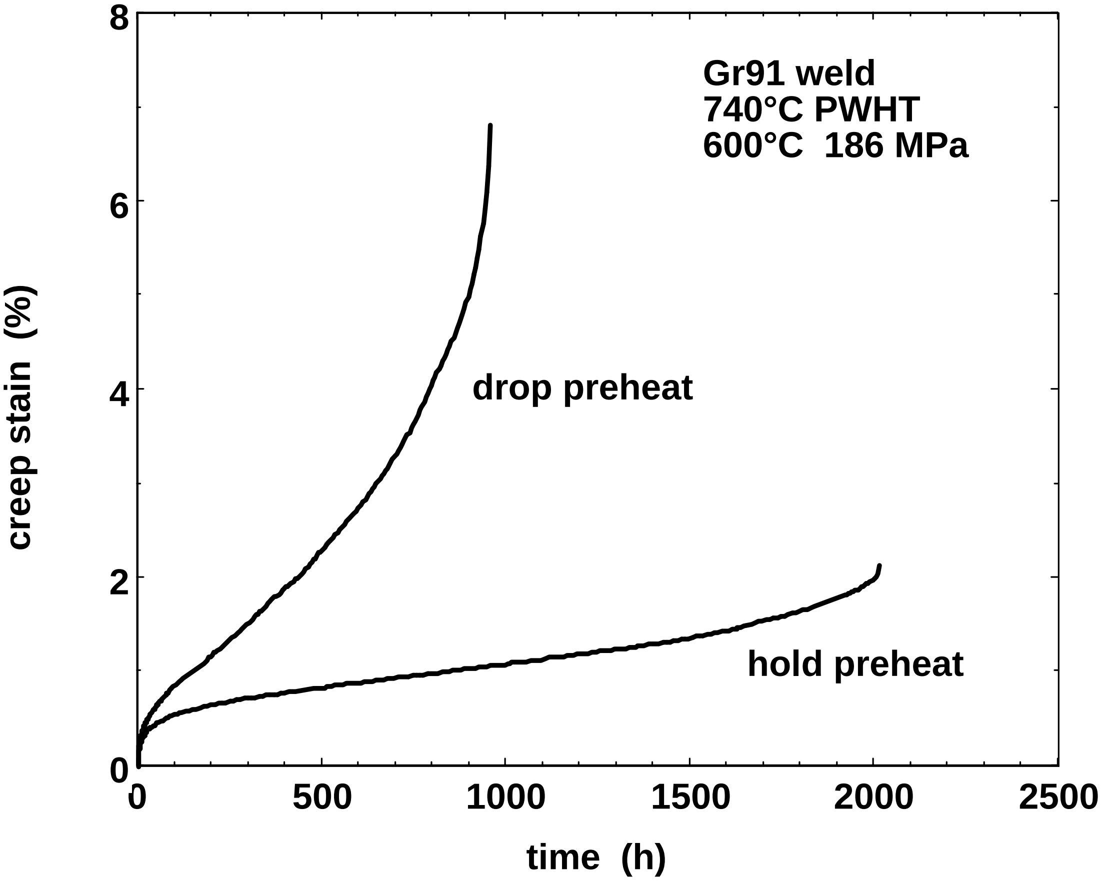

Fig. 2. Effect of fresh martensite (hold preheat) on the creep curve for Gr91 weld metal with PWHT at 740°C.

terms of strength, may be seen in Fig. 4, which compares the rupture strength of service-exposed material to the allowable stresses on the basis of the Larson Miller parameter.

New martensitic steels have been developed for advanced steam cycle applications (1). These steels contain tungsten, cobalt, and other elements for improved creep strength but are expected to undergo time-dependent degradation similar to that observed for Gr91 steel. Efforts are being to find ways to experimentally produce this degradation at an accelerated rate in order to establish temperature limits for the use of these materials. A CRADA with McDermott Technology, Inc. has been initiated to examine the topic of temperature limits.

Advanced Austenitic Stainless Steels

Most of the testing of modified 310 and 20Cr-25N-Nb steels has been completed and reported (6,7), although some additional testing to beyond 30,000 is in progress. Long-time data for 310TaN stainless

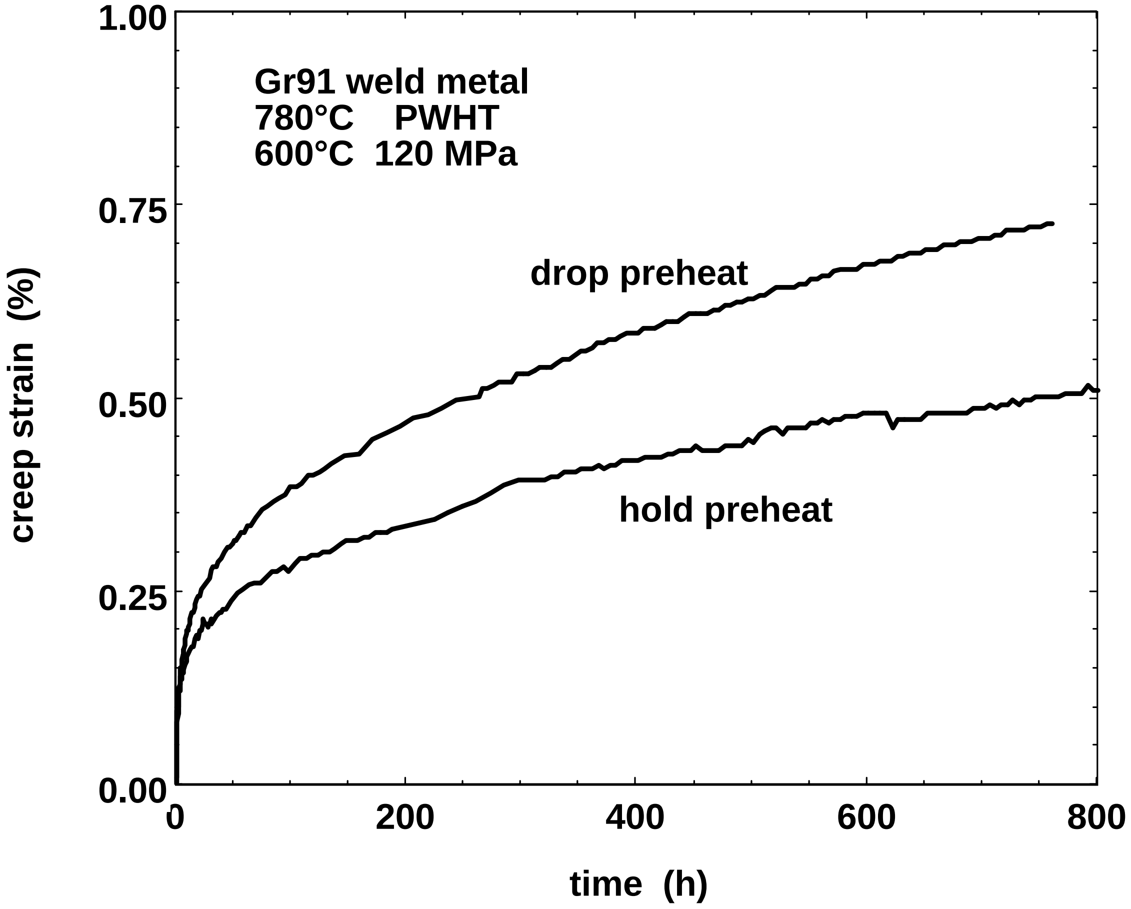

Fig. 3. Effect of fresh martensite (hold preheat) on the creep curve for Gr91 weld metal with PWHT at 780°C.

steel at 600 and 650°C indicated an improvement in strength over 310HCbN by at least 20%. Exploratory creep and stress-rupture tests were completed for 347HFG stainless steel. Data confirmed the good strength reported for this material. Testing of modified alloy 803 has begun. This work supplements a CRADA with Huntington Alloys, which seeks to improve the strength and corrosion resistance of alloy 803 in the temperature range of 650 to 800°C.

Testing of stainless steel foils was completed. This work was intended to supplement the alloy characterization and corrosion studies performed under a CRADA with Solar Turbines, Inc.

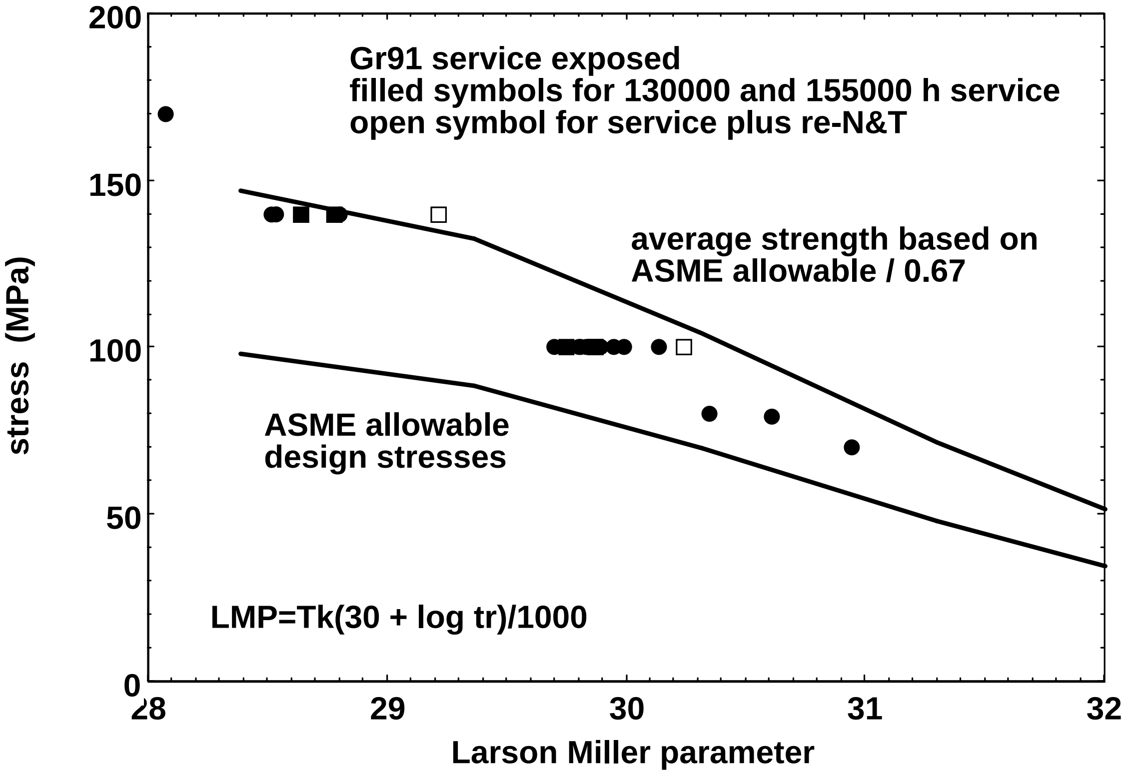

Fig. 4. Comparison of the rupture strength of service exposed Gr91 steel to the allowable stresses on the basis of the Larson Miller parameter.

PUBLICATIONS

(1) R. Viswanathan and W. T. Bakker, "Materials for Ultra Supercritical Fossil Power Plants-Boiler Materials: Part I," J. Materials Engineering and Performance, Vol. 10, February, 2001, pp. 81–95.

(2) R. W. Swindeman, P. J. Maziasz, and C. R. Brinkman, "Aging Effects on the Creep Rupture of 9Cr-1Mo-V steel," Paper IJPGC2000-15050, International Joint Power Generation Conference & Exposition, Miami Beach, Florida, July 23–26, 2000.

(7) R. W. Swindeman, "High-Temperature Performance of a Modified Type 310 Stainless Steel," pp. 121–128 in Proceedings 9th International Conference on Pressure Vessel Technology, Volume 1, Sydney Australia April 9–14, 2000.

MULTI-PHASE Cr-BASED ALLOYS FOR AGGRESSIVE HIGH TEMPERATURE ENVIRONMENTS

M. P. Brady, C. T. Liu, I. M. Anderson, P. F. Tortorelli,* J. H. Zhu, I. G. Wright, V. K. Sikka,
C. A. Walls, L. R. Walker, S. B. Waters, J. L. Wright, and C. A. Carmichael
Oak Ridge National Laboratory
Oak Ridge, TN 37831-6115

***Tennessee Technological University**
Cookeville, TN 38505-0001

INTRODUCTION

A new family of structural Cr alloys based on Cr-(6-10)Ta (at.%) is under development for high-temperature use (900–1300°C) in the oxidizing and aggressive hot corrosion environments encountered in advanced fossil energy conversion and combustion systems [1–4]. The microstructures of these alloys consist of a Cr solid solution matrix reinforced with the intermetallic Cr_2Ta Laves phase for high-temperature strength. The compositions of interest are in the range of: Cr-(6-10)Ta-(3-6)Mo-(0.5-3)Si-(0.2-1.0)Ti-(0.05-0.2)La/Ce at.%. The Mo is added for solid solution strengthening, Si (primarily) for oxidation resistance, Ti for interstitial gettering, and La or Ce for oxidation resistance and interstitial gettering.

Substantial progress has been made in developing attractive high-temperature properties. Microalloying with Si and La has yielded alloys with oxidation resistance in the range reported for commercial Cr_2O_3-forming alloys (900–1100°C, air, 1000 h duration) [1]. Immersion screenings in molten alkali salts and coal slags have also indicated promising behavior [2]. The alloys exhibit tensile fracture strengths in excess of 700 MPa at 1000°C and in excess of 400 MPa at 1200°C [1]. Cast Cr-8Ta-5Mo-0.5Ti-0.01Ce at.% was creep tested up to 1438 hours at 1000°C in humid room air under a load of 138 MPa, at which point the test was stopped due to failure of the grip rods [1]. However, room temperature fracture toughness remains the key challenge for development. Current compositions exhibit a brittle to ductile transition temperature in the range of 800–1000°C [1,2]. At room temperature, tensile fracture strengths are in excess of 700 MPa, but no plastic tensile elongation is observed and fracture toughness of the best alloys is in the range of only 12–14 MPa $m^{1/2}$ [2].

Two approaches for improved fracture toughness at room temperature were investigated: (1) ductilization of unalloyed Cr by the addition of MgO [2,5] and (2) macroalloying to improve the fracture toughness of the Cr matrix phase in Cr-Cr_2Ta alloys. This paper presents the results of microstructural analysis of Cr and Cr-MgO alloys aimed at gaining an understanding of the mechanism by which MgO additions ductilize unalloyed Cr. Promising preliminary results showing significant improvement in room-temperature fracture toughness by macroalloying of Cr_2Ta-reinforced Cr alloys with Fe are also presented.

MEASUREMENT OF ROOM-TEMPERATURE MECHANICAL PROPERTIES

Room temperature tensile properties were evaluated using dogbone tensile samples approximately 0.6–0.7 mm thick with a gage length of 12.7 mm. The samples were prepared to a surface finish of 600 grit and a crosshead speed of 2.54 mm/minute was used (strain rate of 3.33×10^{-3}/s). Subsized chevron-notched three-point bend samples approximately $3 \times 4 \times 25$ mm were used to evaluate fracture toughness at room temperature. The samples were prepared to a 600 grit surface finish and then notched using a low speed diamond saw. The crosshead speed was 0.6 mm/min. A modulus of 250 GPa was estimated for Cr-Cr_2Ta based alloys and 300 GPa for Cr-based alloys. Fracture toughness values obtained by this technique should be considered semiquantitative; details are provided in reference 6.

DUCTILIZATION OF UNALLOYED Cr BY MgO

A major contributor to the ambient brittleness of Cr is the presence of impurity nitrogen [e.g., 7–9]. Work by Scruggs and co-workers demonstrated that plastic tensile elongations up to 20% could be achieved at room temperature in Cr via the addition of MgO [10–12]. The baseline composition of these alloys was Cr-(3-6)MgO-0.5Ti wt.%. During powder processing, some of the MgO particles convert to a $MgCr_2O_4$ spinel, which was hypothesized to getter nitrogen (and other impurities) from the Cr, rendering it ductile [10–12]. A sintered and extruded ingot of Cr-6MgO-0.5Ti wt.% provided by Scruggs was found to exhibit an average plastic tensile elongation of 8.2% (3 samples) with a 600 grit surface finish and a strain rate of 3.33×10^{-3}/s, despite a nitrogen impurity level of 0.03 wt.% [2]. For unalloyed Cr (without MgO additions) to exhibit appreciable room-temperature ductility at these strain rates, high purity (<0.001–0.005 wt.% nitrogen), cold work (usually but not always), and electropolished surfaces (to eliminate local notches) are needed [7–9].

A series of Cr, Cr-0.5Ti, Cr-6MgO, and Cr-6MgO-(0-1)Ti wt.% alloys was made in order to investigate the ductilizing effect of MgO on unalloyed Cr and assess the potential of this approach to improve the room-temperature mechanical properties of the Cr_2Ta reinforced Cr alloys. Control alloys of Cr-6Y_2O_3, La_2O_3, or TiO_2 wt.% were also studied. The alloys were produced by oblique blending commercial purity 1–5 micron size powders for 24 h using zirconia balls and hot-pressing under vacuum in a graphite die at 1590°C for 2 h at a load of approximately 20 MPa (the Cr-0.5Ti alloy was made by hot isostatic pressing in a Nb can at 1600°C for 1.5 h). Selected alloys were further processed by sealing the hot-pressings in a steel can and extruding at 1300°C with a 9:1 reduction ratio. Both hot-pressing and hot-pressing/extrusion yielded fully dense material. The hardness of the hot-pressed, and hot-pressed and extruded, Cr-6MgO-(0-1)Ti wt.% alloys was in the range of 150–180 VHN, similar to the original Scruggs Cr-6MgO-0.5Ti alloy and consistent with a recrystallized structure. Chemical analysis of the Cr, Cr-Ti, Cr-MgO, and Cr-MgO-Ti alloys indicated that the nominal compositions were achieved, with nitrogen and carbon impurity levels in the range of 0.03–0.06 wt.%.

The unalloyed Cr, Cr-0.5Ti, and Cr-6Y_2O_3, La_2O_3, or TiO_2 control alloys all exhibited brittle behavior at room-temperature, with plastic tensile elongation less than ~2%. However, plastic tensile elongation in the ~3–5% range was observed for hot-pressed Cr-6MgO-(0-1) Ti alloys. It should be noted that the grain size of the Cr and Cr-0.5Ti alloys was on the order of 0.5 millimeter while the grain size of the hot-pressed alloys with oxide dispersions (e.g., MgO) was on the order of 50 microns. Subsequent extrusion more than doubled the plastic tensile elongation at room temperature, with ~10–12% elongation observed for hot-pressed and extruded Cr-6MgO-0.75Ti wt.%.

The scanning electron microscopy (SEM) technique of low-voltage EDS spectrum imaging (LV-EDS) was used to examine alloy microstuctures for the presence of nitride and other impurity phases [13]. This technique provides an attractive alternative to electron probe microanalysis (EPMA) for mapping of different phases through their characteristic X-ray spectra, although it is not as good for quantitative analysis. A low operating voltage is used relative to the EPMA, which results in an order of magnitude better spatial resolution (~150 nm for 4 kV); however, many of the X-ray lines most suitable for quantification (e.g., Cr-K) are not excited at these voltages. The much poorer spectral resolution of EDS relative to WDS also compromises quantitative compositional analysis. However, because a full spectrum, rather than the intensities of a few selected X-ray lines, are acquired at each pixel in the image, low-voltage EDS spectrum imaging provides a true phase, rather than elemental, mapping technique. In-house ORNL multivariate statistical analysis software is used to identify all spectrally-distinct phases in the image, and also robustly distinguishes phases having spectral overlaps (e.g., O-K and Cr-L) [14,15].

Acicular Cr-nitrides and Cr-carbides were detected at the grain boundary regions in unalloyed Cr (Fig. 1). Such impurity phase formation significantly contributes to the poor room-temperature ductility of Cr. The microstructure of hot-pressed Cr-6MgO is shown in Fig. 2. The alloy grain boundaries were decorated by MgO and Mg-Cr-O phases. The composition of the ternary oxide phase was determined by electron probe microanalysis (EPMA) to be 12Mg-52Cr-36O (wt.%), consistent with the $MgCr_2O_4$ spinel phase. Within the sensitivity limits of EPMA, nitrogen was not detected in the spinel phase. A similar microstructure was observed for hot-pressed Cr-6MgO-0.5Ti and Cr-6MgO-1Ti, except that Ti was present in the spinel phase (Ti segregation to the spinel phase was also observed in the Scruggs Cr-6MgO-0.5Ti alloy).

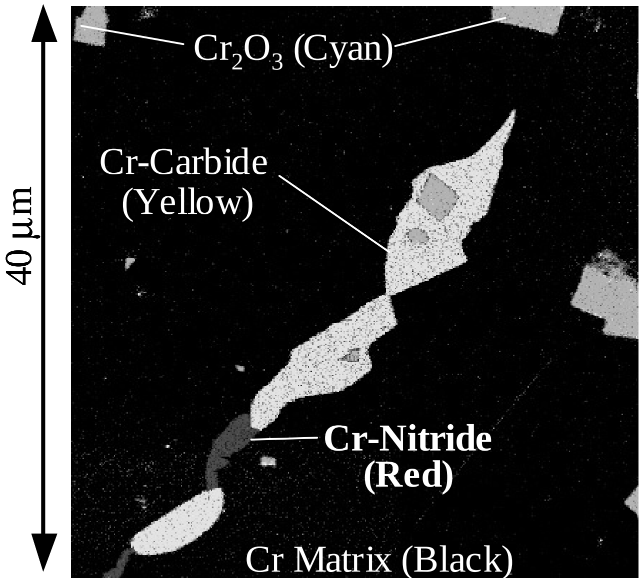

Fig. 1. Low voltage EDS spectrum image phase map of hot-pressed, unalloyed Cr.

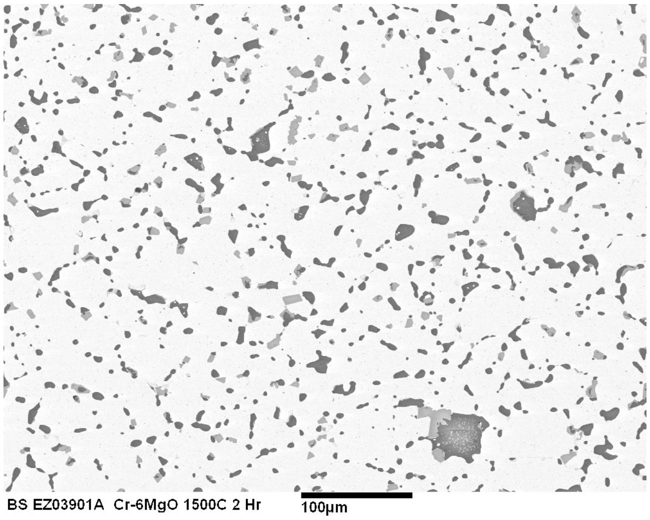

Fig. 2. SEM secondary image micrograph of hot-pressed Cr-6MgO wt.%. The light gray phase is the $MgCr_2O_4$ spinel and the dark gray phase is MgO.

An LV-EDS spectrum image phase map for Cr-6MgO is shown in Fig. 3. In addition to the Cr matrix, MgO and $MgCr_2O_4$ phases, chromium nitride and sulfide phases were also identified. The nitrides were typically located adjacent to the MgO and $MgCr_2O_4$ oxide dispersions. Qualitatively, the nitrides appeared more blocky (Fig. 3) than the acicular nitrides typically observed in unalloyed Cr (Fig. 1). Similar nitrides were also observed in hot-pressed Cr-6MgO-1Ti. Given that up to 5% plastic tensile elongation at room-temperature was exhibited in these hot-pressed Cr-MgO alloys, the observation of Cr

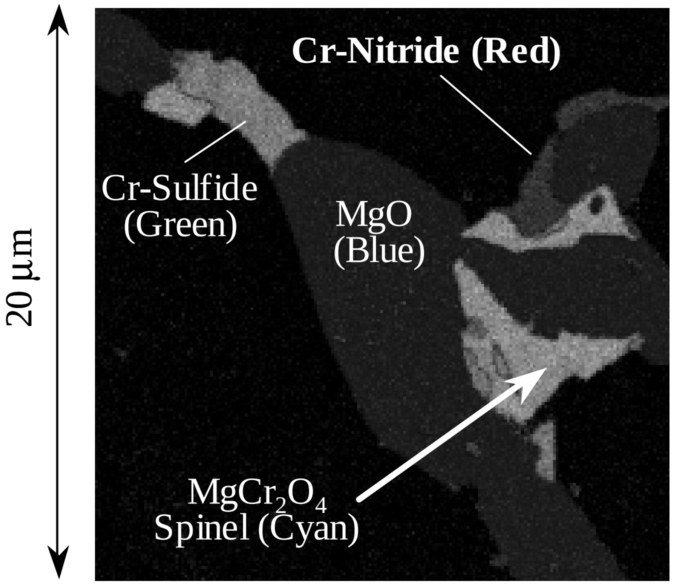

Fig. 3. Low voltage EDS spectrum image phase map of hot-pressed Cr-6MgO wt.% from Fig. 2.

nitrides was very surprising. This result suggests that the ductilization of Cr by MgO is more complicated than the spinel nitrogen gettering mechanism proposed by Scruggs [10–12].

The addition of other oxide dispersions (6 wt.% Y_2O_3, La_2O_3, or TiO_2) did not result in room-temperature tensile ductility as did MgO. Fig. 4 shows an LV-EDS spectrum image phase map for Cr-6TiO_2 wt.%. As with the Cr-MgO alloys, impurity nitride phases were observed to precipitate in a somewhat blunt morphology adjacent to the oxide dispersions. Why MgO dispersions are effective in ductilizing Cr, but others such as TiO_2 are not, is not clear and is the subject of ongoing study.

In the present work, subsequent extrusion of hot-pressed material more than doubled the observed plastic tensile elongation at room-temperature to greater than 8–10%. Analysis of the sintered and extruded Scruggs Cr-6MgO-0.5Ti alloy and a hot-pressed and extruded Cr-6MgO-0.75Ti alloy of the present study by EPMA and LV-EDS spectrum image phase mapping did not reveal the presence of nitrides despite similar levels of nitrogen impurities to the hot-pressed material shown in Figs. 1–4 (0.02–0.04 wt.%), in which nitrides were easily detected. To investigate whether the increased ductility with extrusion resulted from complete removal of the nitride precipitates (observed in hot-pressed material) by $MgCr_2O_4$ spinel phase gettering, the Scruggs Cr-6MgO-0.5Ti extrusion was analyzed by electron energy-loss spectroscopy (EELS) in the transmission electron microscope (TEM). The EELS analysis did not reveal the presence of nitrogen in either the $MgCr_2O_4$ spinel phase particles, the MgO particles, or the Cr matrix. This result strongly suggests that nitrogen gettering by the spinel phase as originally postulated by Scruggs [10–12] may not occur.

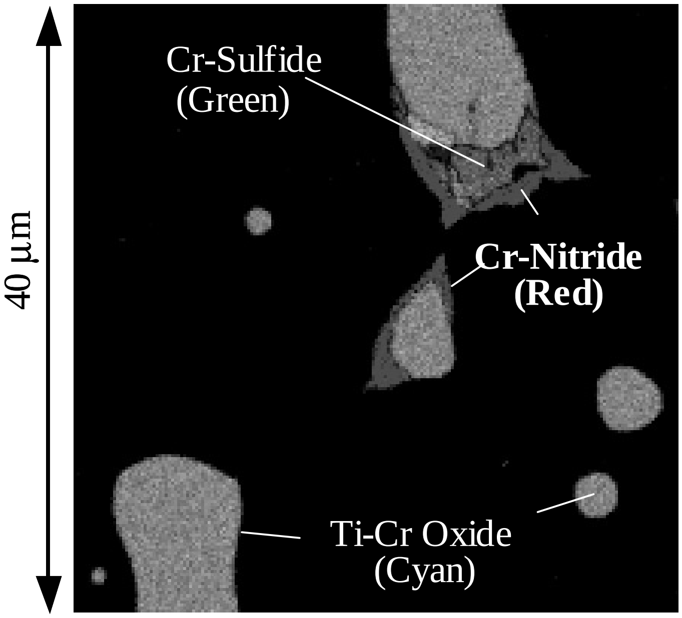

Fig. 4. Low voltage EDS spectrum image phase map of hot-pressed Cr-6TiO_2 wt.%.

The inability to detect any nitrogen or nitride anywhere in the extruded Cr-MgO alloys by SEM, EPMA, and EELS (despite confirmation by bulk chemical analysis that nitrogen was indeed present) is not understood. It is speculated that the extrusion process breaks up the nitride precipitate particles formed during the initial hot-pressing or sintering step such that they are not retained during sample preparation for SEM and TEM analysis, i.e. the inability to identify nitrides in the extruded material may be an artifact of the sample preparation. The increased ductility due to extrusion is attributed to the aligned columnar grain structure introduced by the extrusion (the tensile axis was aligned with the extrusion direction) and refinement in the size of MgO/$MgCr_2O_4$ particle agglomerations.

Attempts to introduce the ductilizing effect of MgO into the high-strength Cr_2Ta reinforced Cr alloys were not successful. Therefore, it is concluded that significant modification of the Cr matrix phase by macroalloying is needed to achieve the toughness goals of this project.

MACROALLOYING EFFECTS FOR Cr-Cr_2Ta ALLOYS

Fig. 5a shows the resultant microstructure of an initial attempt at macroalloying a Cr-Cr_2Ta base alloy with Fe. Due to patent considerations, detailed compositions are not reported here. Despite the presence of a high concentration of fine Laves phase precipitates in the primary Cr regions, a fracture toughness in the range of 14–15 MPa $m^{1/2}$ was achieved. EPMA analysis indicated that the Fe partitions in both the Cr–rich matrix (dark contrast) and the Cr_2Ta-type Laves phase (bright contrast) in Fig. 5. Adjustment of Fe/Ta levels produced a nearly 100% eutectic structure (Fig 5b). This resulted in room-

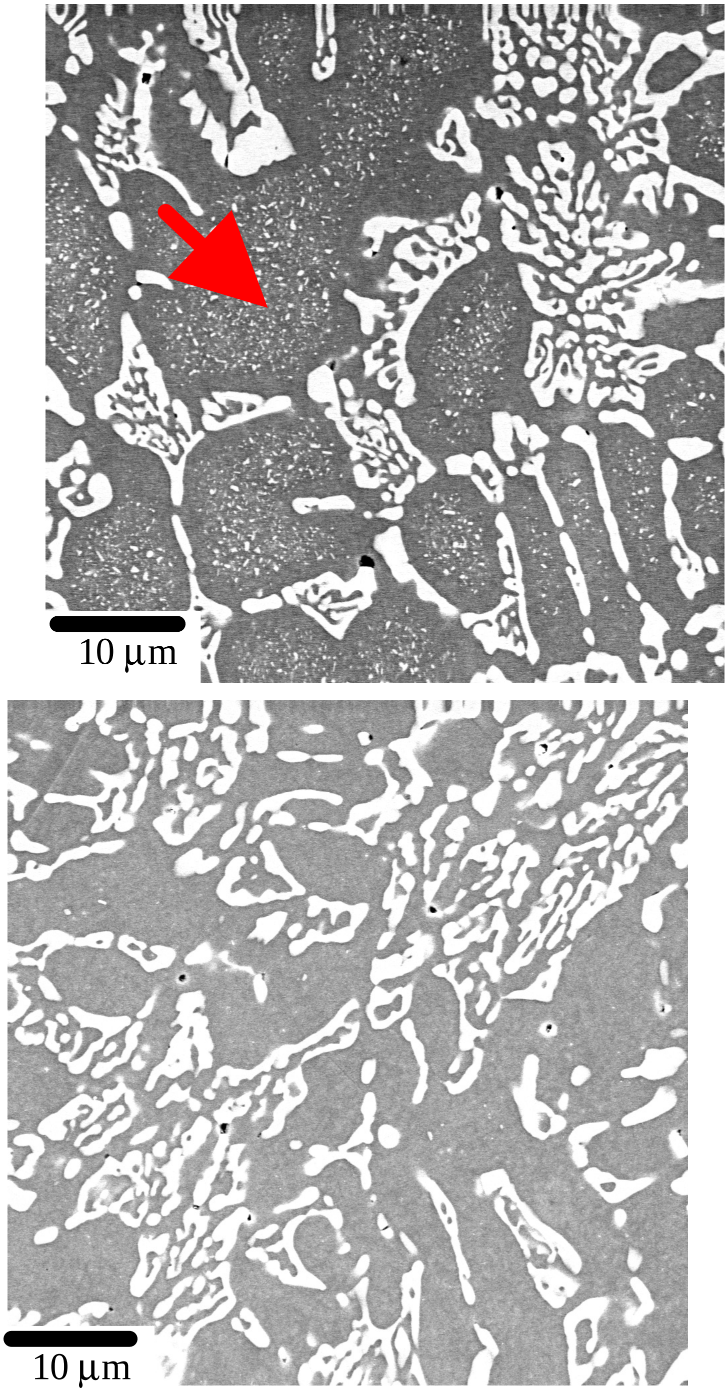

Fig. 5.SEM images of Fe modified Cr-Cr_2Ta base alloys. The light phase is the Cr_2Ta Laves phase and the dark phase is the Cr phase. A) top: hypoeutectic alloy exhibiting 14–15 Mpam $^{1/2}$ fracture toughness at room-temperature (primary Cr regions marked by arrow B) bottom: eutectic alloy exhibiting 18–20 MPam ^{½} fracture toughness at room-temperature

temperature fracture toughness in the range of 18–20 MPa $m^{1/2}$, which is significantly higher than any other Cr_2Ta reinforced Cr base alloy evaluated in this effort and meets the fracture toughness goals of this program. Detailed study and confirmation of these results, as well as full characterization of high-temperature physical, chemical, and mechanical properties, are planned.

REFERENCES

1. M. P. Brady, J. H. Zhu, C. T. Liu, P. F. Tortorelli, L. R. Walker, C. G. McKamey, J. L. Wright, C. A. Carmichael, D. J. Larson, M. K. Miller, and W. D. Porter, *Materials at High Temperatures*, vol. 16, no. 4, pp. 189–193 (1999).
2. M. P. Brady, C. T. Liu, J. R. Keiser, P. F. Tortorelli, V. K. Sikka, E. Lara-Curzio, C. A. Walls, C. G. Westmoreland, C. A. Carmichael, J. L. Wright, J. D. Vought, M. Howell, H. Longmire, K. L. Crowley, and M. L. Weaver, in Proceedings of the Fourteenth Annual Conference on Fossil Energy Materials, Knoxville, TN, April 24–26, 2000, R.R. Judkins, Compiler, ORNL TM-2000/249, paper 5.5 (2000).
3. C. T. Liu, J. H. Zhu, M. P. Brady, C. G. McKamey, and L. M. Pike, “Physical Metallurgy and Mechanical Properties of Transition-Metal Laves Phase Alloys”, *Intermetallics*, 8, 9–11, pp. 1119–1129 (2000).
4. M. P. Brady, J. H. Zhu, C. T. Liu, P. F. Tortorelli, and L. R. Walker, “Oxidation Resistance and Mechanical Properties of Laves Phase Reinforced Cr In-Situ Composites”, *Intermetallics*, 8, 9–11, pp. 1111–1118 (2000).
5. M. P. Brady, I. G. Wright, I. M. Anderson, V. K. Sikka, E. K. Ohriner, C. Walls, G. Westmoreland, and M. L. Weaver, “Ductilization of Cr via Oxide Dispersions” to be published in Proceedings of the 15th International Plansee Seminar, Editors: G. Kneringer, P. Rodhammer, H. Wildner, Plansee AG, Reutte, Austria (2001).
6. J. H. Schneibel, C. A. Carmichael, E. D. Specht, and R. Subramanian, *Intermetallics*, 5, p. 61 (1997).
7. H. L. Wain, F. Henderson, S. T. M. Johnstone, N. Louat, J. Inst. Met., 86, pp. 281–288 (1957).
8. A. H. Scully and E. A. Brandes, *Chromium*, 2nd. Edition, New York: Plenum Press (1967).
9. W. D. Klopp, “Recent Developments in Chromium and Chromium Alloys”, NASA Technical Memorandum, NASA TM X-1867 (Sept. 1969).
10. D. M. Scruggs, L. H. Van Vlack, and W. M. Spurgeon, *J. Amer. Ceram. Soc.*, 51, 9, pp. 473–481 (1968).
11. D. M. Scruggs, ‘Ductile Chromium Composition”, U.S. Patent 3, 175, 279 (Mar. 30, 1965).
12. D. M. Scruggs, *American Rocket Society Journal*, 31, 11, pp. 1527–1533 (1961).

13. I. M. Anderson, *Microscopy & Microanalysis 6* (Suppl. 2), 1048 (2000).
14. P. Trebbia and N. Bonnet, *Ultramicroscopy* 34, 165 (1990).
15. I. M. Anderson, *Proc. 14th ICEM: Electron Microscopy* 1998 1, 357 (1998).

ACKNOWLEDGEMENTS

The authors thank D. M. Scruggs for donation of a Cr-MgO alloy ingot and helpful discussions regarding his efforts in the 1960's to ductilize Cr. The authors also thank J. R. Keiser and J. H. Schneibel for their reviews of this manuscript. This research was sponsored by the U.S. Department of Energy, Fossil Energy Advanced Research Materials (ARM) Program and by the Assistant Secretary for Energy Efficiency and Renewable Energy, Office of Industrial Technologies, Advanced Industrial Materials Program. Oak Ridge National Laboratory is managed by U.T.-Battelle, LLC for the U.S. Department of Energy.

OXIDE DISPERSION-STRENGTHENED ALLOY DEVELOPMENT

I. G. Wright, C. G. McKamey, and B. A. Pint
Oak Ridge National Laboratory

INTRODUCTION

Oxide dispersion-strengthened (ODS) alloys have the potential for safe operation at temperatures significantly higher than possible with current heat-resistant alloys. Essentially, these alloys represent the maximum temperature capability of metallic alloys that can be used in tube and sheet form, and they allow operation at the lower end of the temperature range for which it is usually assumed that ceramic materials would be required. The incorporation of ODS alloys into the design of advanced heat transfer modules, for instance, would not only increase the system temperature capability but also reduce the size of any downstream ceramic heat transfer component, if even higher temperatures were required. Two prototype ferritic ODS alloy heat exchangers [1,2] have already demonstrated the ability to operate at metal temperatures of approximately 1100°C (2102°F).

ODS alloys have not attained wide usage to date because they are made by a powder metallurgy process and so are relatively expensive, and the unique microstructure necessary to develop their exceptional high-temperature strength leads to difficulties in joining, which results in restricted fabrication options. The prototype ODS heat exchangers mentioned above employed less than optimum configurations to allow the use of available joining techniques.

The goal of this program is to develop a detailed understanding of the behavior of ODS alloys in all phases of their use, including relevant properties, fabrication and joining, service performance, oxidation life prediction, mode of failure, repair, and refurbishment. These data are needed to provide designers of components requiring exceptional high-temperature strength (such as heat transfer modules) with the basis from which to consider ODS alloys in their initial component designs. The peculiar properties of these alloys do not allow their strength benefits to be fully exploited when retrofitted into existing designs based on the properties of current heat-resistant alloys. The successful outcome of this project will result in developments that allow ODS alloys to be used with confidence in a variety of applications previously not possible with metallic materials.

DISCUSSION OF CURRENT ACTIVITIES

Mechanical properties of ODS-Fe_3Al

Creep rupture lives of specimens of ODS-Fe_3Al over the temperature range 750 to 1075°C are summarized in the Larson-Miller diagram shown in Fig. 1. These data were obtained using cylindrical

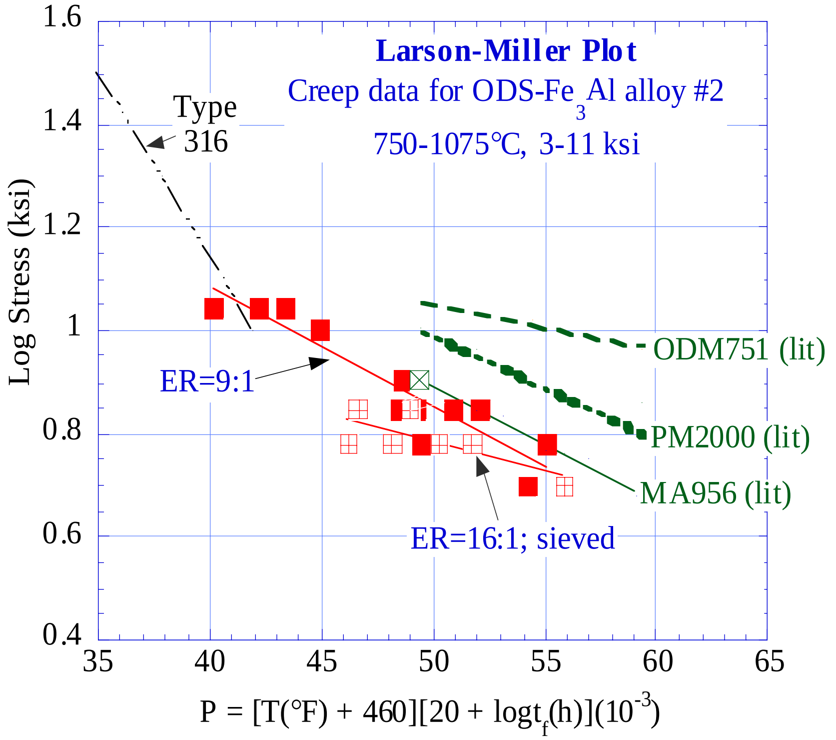

Fig. 1. Larson-Miller diagram for ODS-Fe_3Al alloys tested in tensile creep at 750–1075°C (1382–1967°F). Data for commercial ODS-FeCrAl alloys MA956, ODM751, and PM2000 are included, along with data for type 316 stainless steel, for comparison

specimens with threaded grips. Overall, the data for ODS-Fe_3Al essentially overlap the curve for the commercial ODS-FeCrAl alloy INCO MA956 [3], indicating the potential of ODS-Fe_3Al to develop the high-temperature creep properties typical of this class of alloys. In Fig. 1, two distinct data sets may be distinguished for ODS-Fe_3Al: those for Alloy 2a [original mechanically-alloyed powder, extrusion ratio (ER) 9:1], and for Alloy 2c (powder sieved to remove the >400 µm size fraction which was found to contain incompletely alloyed particles [4], and extruded with a reduction ratio of 16:1). Alloy 2c was found to undergo secondary recrystallization to form the high aspect ratio grain structure required for high-temperature creep strength at a lower temperature than did Alloy 2a (1200°C vs. 1250°C), and exhibited significantly fewer stringers of non-recrystallized material, as shown in Fig. 2. However, the cleaner microstructure of Alloy 2c resulted in lower creep rupture strengths at the lower temperatures, as shown in Fig. 1, although the slope of the curve in the Larson-Miller diagram suggested that the creep rupture strength would be similar to that for Alloy 2a at the higher temperatures.

The reason for this difference in behavior is not obvious. As shown in Figs. 2 and 3, the typical fracture cross sections of the alloys were similar, both showing the peculiar failure mode

Fig. 2. Fracture cross section of a specimen of ODS-Fe_3Al Alloy 2a after creep rupture at 1050°C (1922°F) and 55.2 MPa (8 ksi).

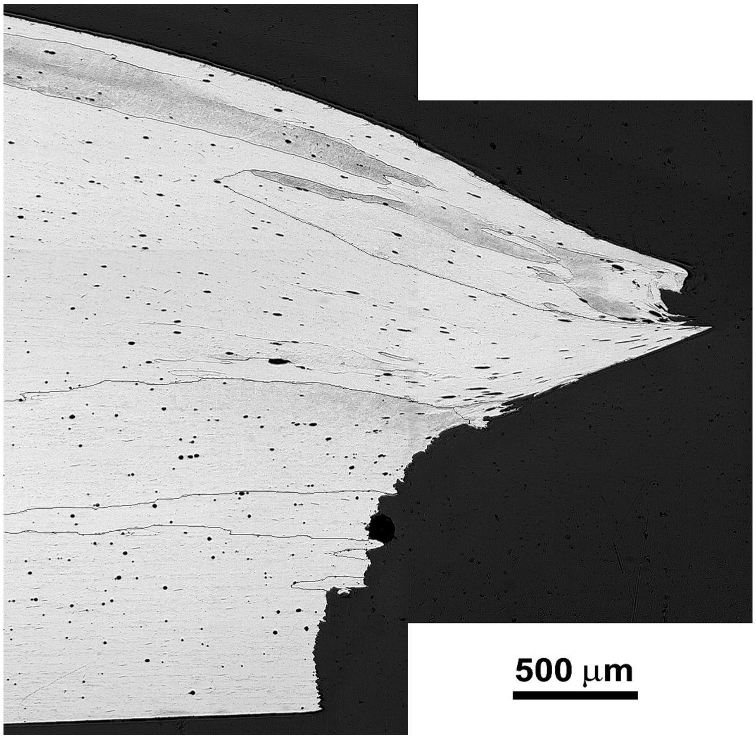

Fig. 3. Fracture cross section of a specimen of ODS-Fe_3Al Alloy 2c after creep rupture at 950°C (1742°F) and 48.3 MPa (7 ksi).

associated with this (and other) ODS alloys. The failure appeared to involve an apparent 'brittle' fracture, followed by ductile failure with obvious necking. In the case of the Alloy 2a specimen, the gauge section of which consisted of essentially two grains (Fig. 2), the 'brittle' fracture followed a path normal to the stress axis across a single grain, whereas the other grain failed in a ductile fashion. In Fig. 2, the zone of non-recrystallized material demarcates the boundary between the two main grains. According to the extensometer data, the whole failure process was very rapid; the fast loading of the second grain following the ‘brittle’ failure event led to what became essentially a tensile test of the remaining grain. As shown in Fig. 2, there was an alloy grain boundary in the second (ductile failure mode) grain that appeared to follow a very similar path to that taken by the ‘brittle’ fracture, suggesting that the initial fracture may have followed the grain boundary. There was also indication of necking at the intersection of the ‘brittle’ failure zone with the specimen surface in the location that normally would have been expected to be the failure initiation point.

The cross section of the fracture surface of Alloy 2c, shown in Fig. 3, indicates that more than two alloy grains were involved, but that the same ‘brittle’-ductile failure mode occurred. In this specimen, it appeared that failure initiated at the outer surface and followed a path normal to the stress direction with steps where the fracture path intersected alloy grain boundaries. After the fracture had traversed approximately 20 percent of the specimen thickness, the mode of failure changed, and there were signs of increasing flow in the microstructure leading to considerable necking and failure of the remaining grains.

The observed mode of failure of these ODS-Fe_3Al specimens is shown schematically in Fig. 4. In the sequence of events indicated, the time interval between $t = t_0$ and $t = t_n$ may be very long, whereas the interval between $t = t_n$ and $t = t_z$ typically is very short. While it is suggested that the failure process involves a transverse grain boundary in the alloy, it is not certain that this is always the case. Nevertheless, it is suggested that the initial failure occurs at a microstructural feature in the alloy that is oriented normal to the stress direction. This feature may simply be located in the gauge section and fortuitously aligned so that it will fail first when the stress increases to some critical value as the specimen section is reduced by creep (note that this morphology was observed for specimens that were incrementally loaded, as well as for specimens subjected to dead weight-loaded creep tests). Since the rate of creep of this alloy typically is extremely low, it may be necessary to invoke some form of embrittling mechanism, involving the presence of aligned second phase particles, the accumulation of creep voids, or the accumulation of voids resulting from the desorption of gas (which is a problem in ODS alloys [5]) at the transverse microstructural feature of interest. Once the fracture initiates, it apparently follows the easy path along the transverse/embrittled feature until it encounters a non-embrittled region, or a longitudinal grain boundary. The increase in load on the remaining cross section

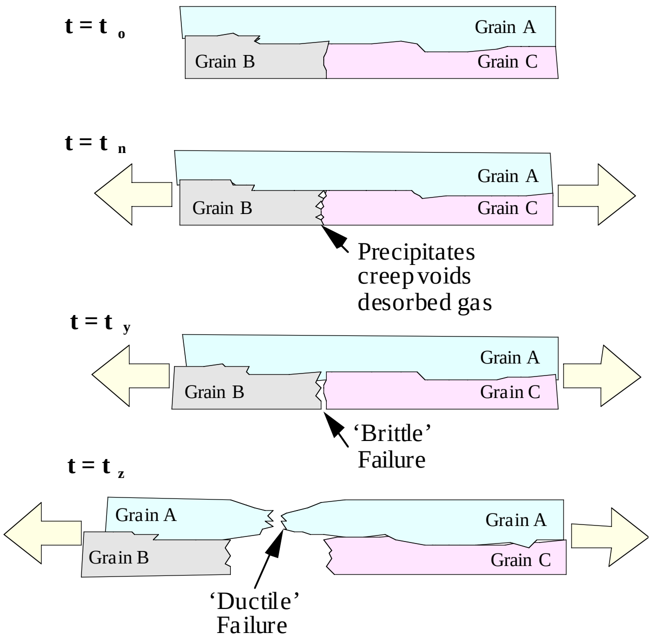

Fig. 4. Schematic diagrams of cross sections of ODS-Fe_3Al suggesting the sequence of events during creep rupture exposures.

obviously depends on the length of the initial transverse fracture: if this represents a significant fraction of the alloy thickness, the remaining cross section will quickly become overloaded and fail, as suggested in Fig. 4. Where there are several grains across the thickness of the gauge section (as in Alloy 2c) the failure process involves sequential 'brittle' and ductile failure steps, since the length of the initial 'brittle' fracture path is reduced, until the stress on the remaining cross section is sufficient to cause a 'normal' ductile failure. While this difference might suggest that the overall failure process may be slowed down, in the testing reported to date the failures were essentially as unannounced as with Alloy 2a.

Since the observed failures occurred abruptly with essentially no change in slope of the elongation-time readout, it was not possible to stop the tests immediately prior to failure to determine the changes in microstructure that presage failure. Modifications to the test equipment are being made to further explore this possibility.

The approach of sequentially-loading specimens in tensile creep (6.9 MPa/1 ksi increments every 100 h) until failure to determine the 'threshold' for creep failure was continued, with the results shown in Fig. 5 for rod-shaped specimens of Alloy 2a. Results of similar tests on joints made by friction welding of ODS-Fe_3Al rod to itself and to the high-temperature wrought Ni-based alloy Haynes 230 also are shown. These indicated that self joints in ODS-Fe_3Al that were subsequently recrystallized retained approximately 46 percent of the parent metal strength. As described previously [6], the friction welding

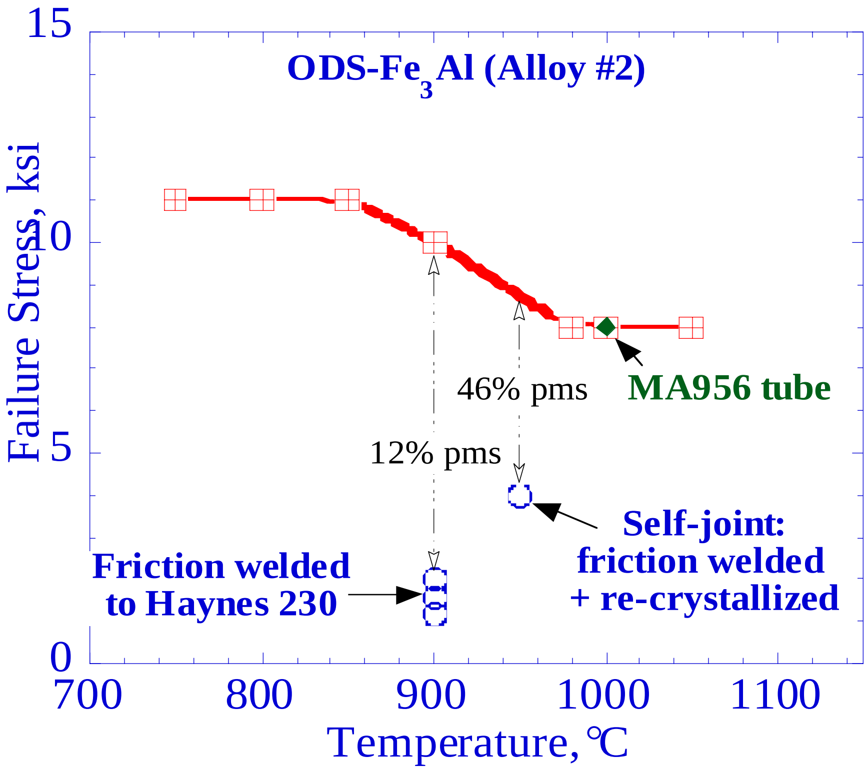

Fig. 5. Creep threshold stress for ODS-Fe_3Al (Alloy 2a) over the temperature range 750–1050°C (1382–1967°F), with data points for joined specimens (and for MA956 tubing) for comparison.

process sufficiently disturbed the local alloy microstructure that the recrystallized grains followed the flow lines in the joint, resulting in grain boundaries normal to the longitudinal axis of the rods, and consequently lowered creep rupture strength. The friction welded joints to Haynes 230 were very weak, retaining at best 20 percent of the parent metal strength. Note that the comparative data obtained for a specimen taken from the wall of a 2.5 cm–2 mm wall [1 in. OD–0.08 in. wall)] tube of MA956 exhibited an identical threshold stress to ODS-Fe_3Al at 1000°C (1832°F).

Oxidation limits for ferritic ODS alloys

Long-term oxidation tests are being conducted on ODS-Fe_3Al and the commercial ODS-FeCrAl alloys in order to generate kinetic data and information on the mode of eventual failure. Exposures are being made in air at 1000–1300°C (1832–2372°F) in 100-h cycles, using a technique that allows the total oxygen uptake of the specimens as well as the extent of scale loss by spallation to be measured. The very high temperature of 1300°C (2372°F) was included because of the need to achieve failure in a reasonable time, and Fig. 6 shows the complete oxidation behavior for seven specimens of the ODS-FeCrAl alloy

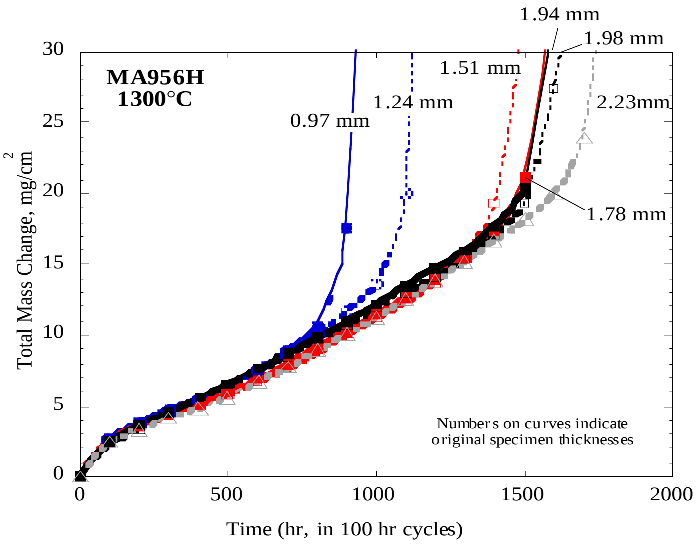

(a)

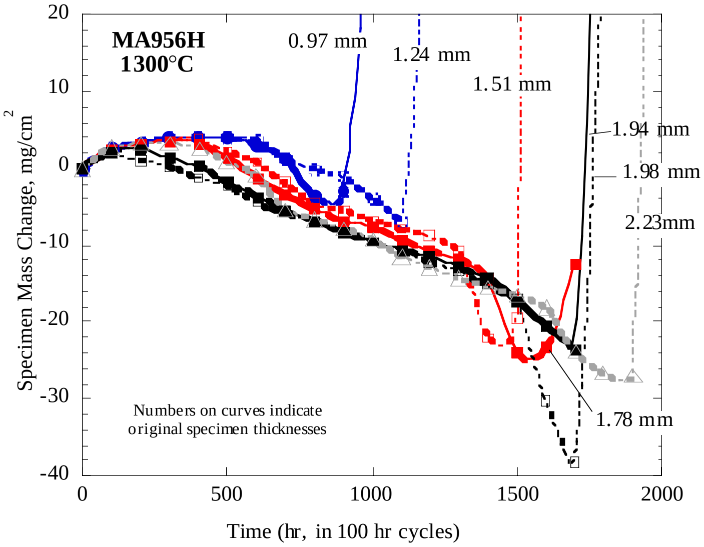

(b)

Fig. 6. Total mass gain (a) and specimen mass change (b) data for specimens of alloy MA956HT exposed in 100-h cycles in air at 1300°C.

MA956HT at this temperature. Figure 6a shows that the total mass gain curves followed a very consistent pattern, and that the onset of rapid mass gain (oxidation failure) occurred at times that increased with increasing initial specimen thickness (see Table 1). The specimen mass change curves, in Fig. 6b, indicate that scale spallation initiated at approximately 100 to 400 h, and that mass loss continued in an almost linear fashion until shortly before the failure. Given the reproducibility of the oxidation curves, the idealized oxidation behavior of this alloy at 1300°C can be represented

Table 1. Experimentally-Observed Lifetimes for MA956HT

Time to breakaway, h	Specimen Thickness, mm							
	0.97	*1.04*	*1.24*	*1.51*	*1.78*	*1.94*	*1.98*	*2.23*
1300°C	880	—	1,100	1,450	1,550	1,700	1,700	1,900
1200°C	—	4,700	—	—	—	—	—	—

as shown in Fig. 7. If any initial period of transient oxidation (Stage 1) is ignored, two major stages of essentially steady-state oxidation can be defined: Stage 2, which appeared to be essentially parabolic, and Stage 3, which appeared to be essentially linear. Assuming that the consumption of aluminum (W/A, mass per unit area) by the oxidation process can be described by:

$$W_B/A = kt^n \tag{1}$$

where k is the rate constant for the oxidation process, t is the time that the oxidation process is operating, and n is the rate law exponent, values of n were obtained for each stage by log-log slope analysis of the data for each of the seven specimens. The average values for the data set of n_2 and n_3 were 0.52 and 1.03, respectively (see Table 2), suggesting essentially parabolic and linear oxidation behavior. Further, Stage 2 terminated at an average mass gain equivalent to an oxide thickness ($\tau_{2\text{-}3}$, assuming the scale was all Al_2O_3) of 29 µm. Values of k_2 and k_3 were obtained from parabolic and linear plots of the respective segments of each data set, and the average values were determined (Table 2). These rate constants were input to an expression developed for the time to consume the available aluminum content of the specimen by oxidation at the rates indicated for Stages 2 and 3 [7–9], from which the specimen oxidation life (t_b) was derived to be [10]:

$$\begin{aligned} t_b &= \text{time spent in stage 2} + \text{time spent in stage 3} \\ &= (10^{-4}S\tau_{2-3}\rho_A/k_2)^{1/n2} + \{[(C_{B_o}-C_{B_b})\delta\rho_M - 0.02MS\tau_{2-3}\rho_A]/(200Mk_3)\}^{1/n3} \end{aligned} \tag{2}$$

where:

ρ_A is the density of alumina = 3965 $mgcm^{-3}$ (used in the absence of an actual value for a thermally-grown oxide),

ρ_M = the density of the alloy = 7200 mg/cm^3,

τ_{2-3} is the oxide thickness at the transition from Stage 2 to Stage 3 (µm), as determined from the experimental data when possible, and

C_{B_o} = the initial Al content of the alloy = 5.9 wt %,

C_{B_b} = the Al level at which a protective Al_2O_3 can no longer form (wt %),

d = the thickness of the section being oxidized (cm),

M = converts mass gain to Al consumed = 1.1246, and

S converts mass gain to mass of Al_2O_3 formed = 0.4707.

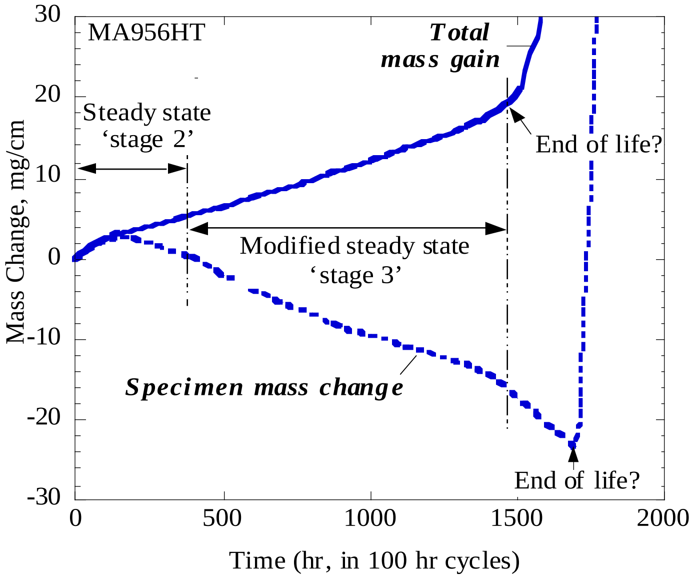

Fig. 7. Schematic diagram of oxidation kinetics of alloy MA956HT exposed in 100-h cycles in air at 1300°C (2372°F).

Table 2. Summary of Experimental Data over the Temperature Range 1000–1300°C

Temperature	n_2	k_2	τ_{2-3}	n_3	k_3
°C		mgcm^{-2}h$^{-0.5}$	µm		mgcm^{-2}h^{-1}
1300	0.52	0.236	29	1.03	12.49 _ 10^{-3}
1200	0.40	0.113	28	1.07	2.60 _10^{-3}
1100	0.52	0.066	25	0.89	0.70 _ 10^{-3}
1000	0.37	0.015	23*	—	0.13 _ 10^{-3}*

*Extrapolated.

Using values of n_2 = 0.5, and n_3 = 1.0 to signify strictly parabolic and linear oxidation behavior in Stages 2 and 3, respectively, together with the experimentally-determined values for k_2 and k_3, eqtn. 2 was found to significantly over-predict the specimen lifetimes. Since a parabolic Stage 2 appeared entirely consistent with the experimental kinetic and morphological data, it was considered that the more likely source of the underestimation of the rate of Al consumption was the assumption of a strictly linear third stage. Examination was made of the sensitivity of eqtn. 2 to changes in the value of n_3 (and the linked values of k_3), using values of k_3 calculated from plots of weight gain versus $t^{1/n3}$. As shown in Table 3, for all combinations of n_3 and k_3 for values of n_3 ranging from 1.00 to 1.10, eqtn. 2

Table 3. Sensitivity of Calculated Lifetime at 1300°C to Major Variables

n_3	k_3 (mgcm^{-2}h^{-n3})	τ_{2-3} (μm)	C_{B_b} (%)	Δt_b (%)*
1.00	**0.012490**	**29**	**1.2**	**+39**
1.03	0.009912	29	1.2	+40
1.05	0.008484	29	1.2	+41
1.07	0.007273	29	1.2	+42
1.10	0.005776	29	1.2	+42
Changes in individual variables to give best fit:				
1.00	**k_3 _ 1.5**	29	1.2	+3
n_3+ 0.06	0.012490	29	1.2	+2
1.00	0.012490	29	**2.5**	+2
1.00	0.012490	**0–40**	1.2	No closure

*t_b calculated for the specimen thicknesses shown in Table 1, and compared to the observed lifetimes.

overestimated life by approximately 41 percent, indicating that the use of a single process to describe Stage 3 resulted in a poor match to the experimental observations.

The sensitivity of the two-stage fit to the main variables was then re-examined by using the base values obtained from the experimental data (see Table 2), and allowing one of the variables n_3, k_3, τ_{2-3}, and C_{B_b} to vary. This indicated that an excellent match to the experimentally-observed lifetimes could be obtained if n_3 was increased to 1.06, or if k_3 was increased by a factor of 1.5, or if the value of C_{B_b} was increased to 2.5 percent (see Table 3). Note that the use of the experimentally-determined average value of k_3 (1.03) led to an over-prediction of lifetimes. Of these changes, the increases required in k_3 and C_{B_b} to obtain a fit to the experimental data were considered to be unrealistic, based on the range of consistency of the experimentally-observed values of k_3 among the seven specimens studied and the general acceptance that C_{B_b} for alloys of this type is less than 2.0 percent [7–9]. Since it is possible that Al consumption in Stage 3 is driven by more than one process occurring simultaneously (or sequentially), such as scale spallation at specimen ends and scale cracking and rehealing on the parallel sides, its description by a single, linear process probably is overly simplistic. A process involving localized loss of scale followed by reoxidation can lead to an essentially linear overall oxidation rate for the area of surface affected by the thickness of oxide lost in each event and the frequency of the spallation events [11,12]. At present, there is insufficient experimental evidence to provide such information. Hence, it was considered that augmentation of the Stage 3 rate exponent (to suggest a more complex process than scale spallation alone) was a reasonable modification of the model until an acceptable mechanism-based description of Stage 3 is available. The rate exponent in Stage 3 then becomes (n_3+ f_{n3}); in the case of MA956HT at 1300°C, n_3 = 1.00 and f_{n3} = 0.06. The lifetimes calculated at 1300°C as a function of specimen thickness using the 2-stage model modified by an augmentation factor are shown in Table 4 and Fig. 8.

Table 4. Oxidation Lifetimes Calculated Using a Multistage Approach

Temp°C	Model Inputs Used						2-Stage Model Predictions (h)		
	n_2	k_2* mgcm^{-2}h$^{-0.5}$	τ_{2-3} µm	n_3	f_{n3}	k_3 mgcm^{-2}h^{-1}	1.0 mm	1.5 mm	2.0 mm
1300	*0.50*	*0.236*	*29*	*1.0*	*0*	*12.49 _ 10^{-3}*	*1,258*	*1,860*	*2,462*
1300	0.50	0.236	29	1.0	0.06	12.49 _ 10^{-3}	1,005	1,388	1,761
1200	*0.40*	*0.241*	*28*	*1.0*	*0.06*	*2.60 _ 10^{-3}*	*4,286*	*5,966*	*7,605*
1200	0.50	0.113	28	1.0	0.06	2.60 _ 10^{-3}	4,312	5,992	7,631
1100	0.50	0.066	25	1.0	0.06	0.70 _ 10^{-3}	13,265	19,046	24,689
1000	*0.37*	*0.046*	*23*	*1.0*	*0.06*	*0.13 _ 10^{-3}*	*218,635*	*245,988*	*272,703*
1000	0.50	0.015	23	1.0	0.06	0.13 _ 10^{-3}	118,768	146,121	172,836

*Corresponding to indicated n_2.

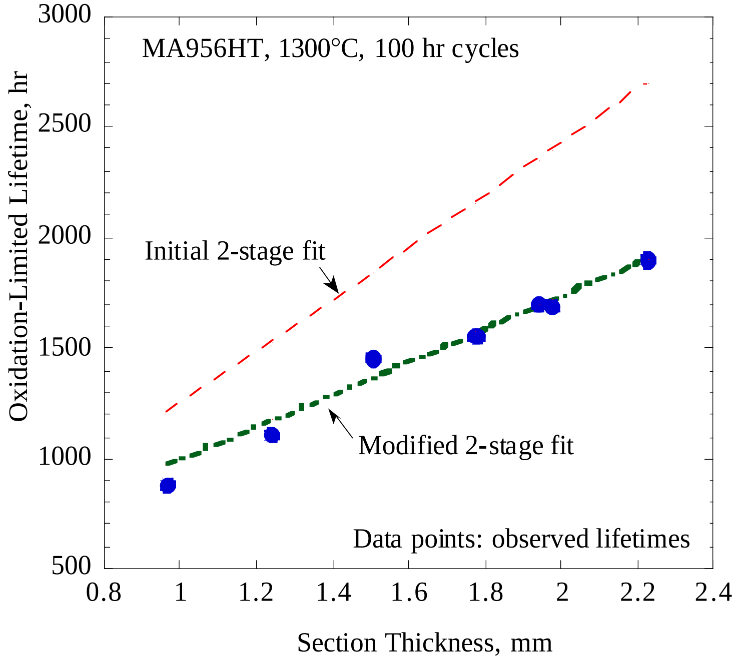

Fig. 8. Comparison of observed and predicted oxidation lifetimes for alloy MA956HT exposed in 100-h cycles in air at 1300°C (2372°F). [Initial 2-stage fit used: $n_2 = 0.5$; $n_3 = 1.0$ ($f_{n3} = 0$); k_2, k_3 = average of data set; τ_{2-3} = 29µm; C_{Bb} = 1.2%. Modified 2-stage fits used same basis, with indicated changes in f_{n3}, or C_{Bb}.]

The next step was to examine the ability of the modified 2-stage model to predict the performance of the same alloy at lower temperatures, using the experimental results shown in Fig. 9. At 1200°C, the experimental total mass change data appeared to fit similar trends as at 1300°C, although the form of the specimen mass change curve was different from that at 1300°C. Since only one data set was available where a specimen had accumulated sufficient exposure time at 1200°C, this trend will be further examined as more specimens are exposed. Nevertheless, there was a clear transition between Stages 2 and 3, Fig. 9, so that values could be calculated for n_2, k_2, n_3, and k_3, Table 2. The experimentally-determined value of n_2 for this specimen was lower (0.40) than observed at 1300°C, while the observed transition point (τ_{2-3}) was 28 µm, essentially the same as at 1300°C. In fact, the lifetimes calculated by the modified two-stage model using $n_2 = 0.4$ and the corresponding value of k_2, and by using $n_2 = 0.5$ and the corresponding k_2, were very similar (Table 4). Further, the lifetime of 4,455 h for the 1.04 mm-thick specimen predicted by the modified two-stage approach was close to the observed lifetime, 4,700 h, which was encouraging.

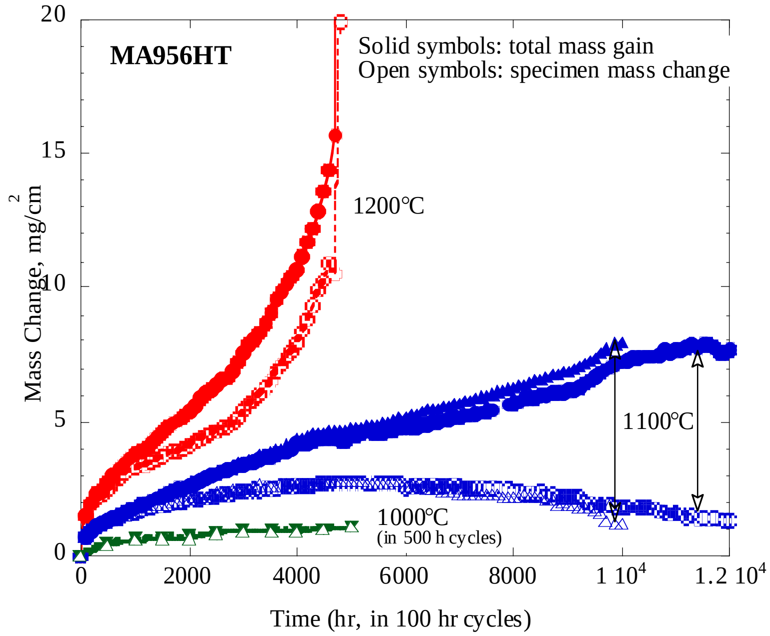

Fig. 9. Experimental data for MA956HT oxidized at 1000°C (1832°F) in 500-h cycles, and at 1100 and 1200°C (2012 and 2192°F) in 100-h cycles.

Data were available for two specimens exposed to 100h cycles at 1100°C for 10,000h or longer, as shown in Fig. 9, allowing the calculation of values for n_2, k_2, n_3, k_3, and τ_{2-3} (Table 2). However, in this case $n_3 = 0.89$, suggesting that there may not yet be sufficient experimental data to obtain an overall value for k_3. If the model is correct, these specimens may not be fully into Stage 3; spallation of oxide was observed from only the specimen edges after 10,000 h.

For a specimen exposed for 5,000 h (in 500h cycles) at 1000°C, a single, near-parabolic oxidation rate was followed throughout the exposure, Fig. 9, with no scale spallation observed. As a result, only values of n_2 and k_2 could be obtained experimentally. As shown in Table 2, the experimental value of n_2 was 0.37. A value of k_3 was obtained from an Arrhenius extrapolation using the higher-temperature k_3 values. Also, since there was an apparent trend for the values of $\tau_{2\text{–}3}$ to decrease with temperature (Table 2), the higher-temperature values were used to extrapolate a value of $\tau_{2\text{–}3}$ of 23 μm for 1000°C. At this point there is no indication that $\tau_{2\text{–}3}$ should be independent of temperature, since factors contributing to loss of scale protectiveness probably change with temperature. For instance, relaxation of stresses developed in the scale may become easier with increasing temperature, so that an argument could be made that $\tau_{2\text{–}3}$ would increase with temperature. The use of these data in the modified two-stage calculation with the experimental value of $n_2 = 0.37$ and the corresponding value of k_2 resulted in lifetimes approximately double those obtained when a value of $n_2 = 0.5$ and the corresponding k_2 was used, Table 4. Again, there was obviously no way to verify these values from the experimental data available.

Figure 10 summarizes the predictions of lifetime as a function of temperature using eqtn. 2 [with $(n_3 + f_{n3}) = 1.06$]. The current status of long exposure specimens at 1100°C is indicated. It is clear that it is vital to obtain more experimental data at 1100–1200°C for MA956HT to verify the range of applicability of the modified multistage consumption methodology to this one alloy. Significantly more work is needed to examine its extension to other alloys.

The total mass gain curves for ODS-Fe_3Al oxidized in air in 100-h cycles at 1300°C shown in Fig. 11 have a similar form to those for MA956HT, with the exception that two groups of behavior can be distinguished: while four specimens oxidized at very similar rates (similar values of k_3) and exhibited oxidation lifetimes that increased with increasing specimen thickness, two specimens oxidized with lower (and different) values of k_3 and, for a given specimen thickness, exhibited longer lives. Examination of the individual specimen mass change curves indicated different behavior than that observed for MA956HT, suggesting that the scale spallation process was different. The reason for the differences among the ODS-Fe_3Al specimens is not known. Another unexplained feature of the data in Fig. 11 is the fact that for all six specimens, it appeared that failure occurred when the total mass gain reached approximately 25–30 mg/cm^2 of Al consumed. Obviously, adaptation of the model to accommodate ODS-Fe_3Al requires a mechanistic description of the oxidation process which is somewhat different from that for MA956HT. Nevertheless, as shown in Fig. 12 in which the oxidation lifetimes of the two types of oxidation behavior exhibited by ODS-Fe_3Al are plotted separately, if the alloy can be

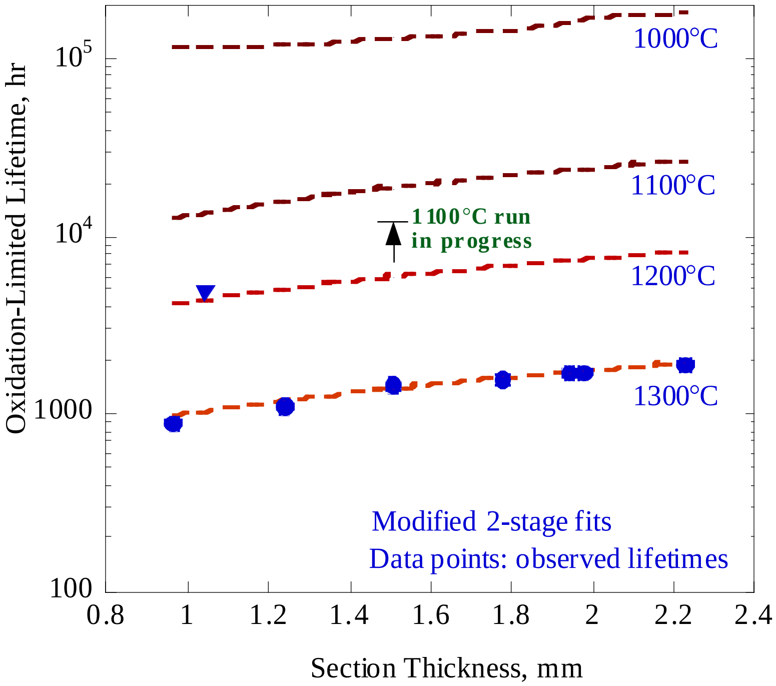

Fig. 10. Predicted lifetimes as a function of temperature. (Basis: $<\tau_{2-3}$, oxidation is parabolic, $n_2 = 0.5$; $>\tau_{2-3}$, oxidation 'linear,' $n_3 = 1.0$; k_2, k_3 from averages of data set for $n_2 = 0.5$, $n_3 = 1.0$; $f_{n3} = 0.06$; $C_{Bb} = 1.2$.)

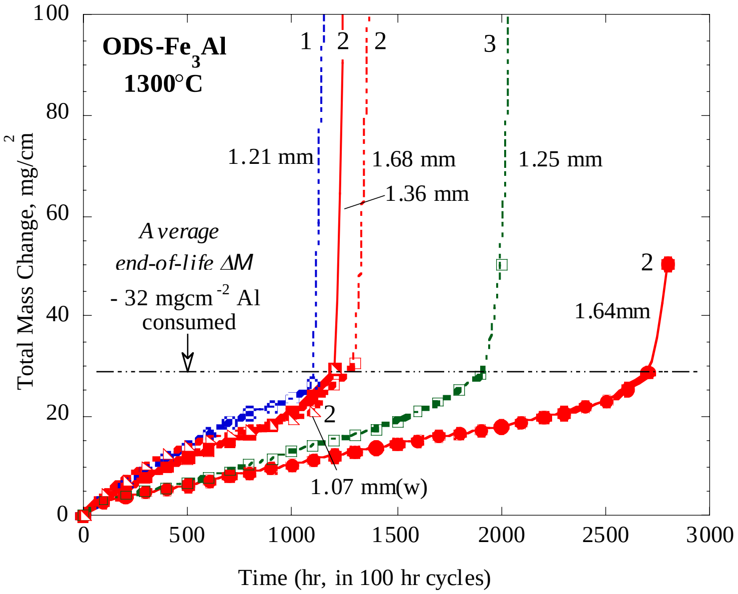

Fig. 11. Experimental data for ODS-Fe_3Al oxidized at 1300°C (2372°F) in 100-h cycles (specimens identified as Alloy 1, 2, or 3)

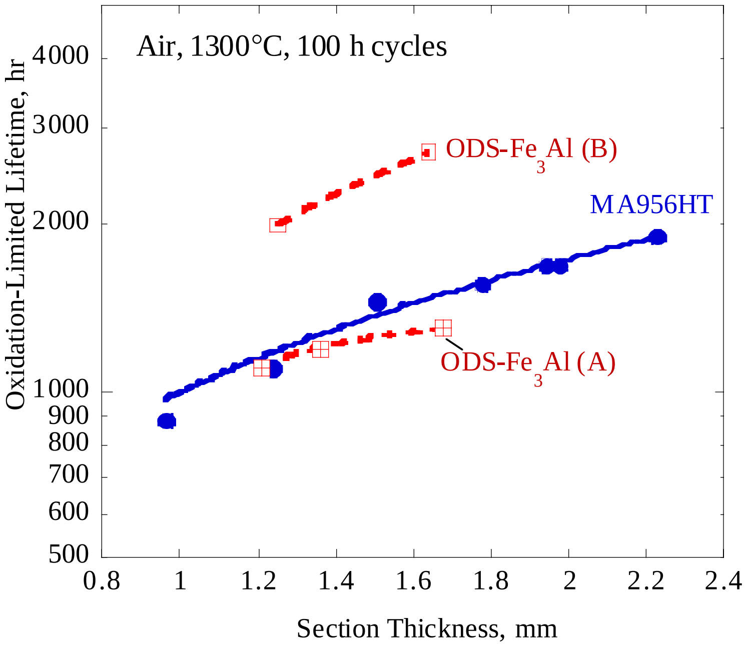

Fig. 12. Comparison of observed lifetimes of ODS-Fe_3Al and MA956HT at 1300°C (2372°F) as a function of specimen thickness. Note that ODS-Fe_3Al specimens that oxidized with low k_3 values (B) exhibited longer lifetimes than both MA956HT those ODS-Fe_3Al specimens with higher k_3 values (A).

made to perform consistently in the type B mode, the increased lifetimes (compared to ODS-FeCrAl alloys) anticipated from its large Al reservoir can be realized.

REFERENCES

1. F. Starr, A. R. White, and B. Kazimierzak, in *Materials for Advanced Power Engineering 1994*, D. Coutsouradis, et al., Eds., (Kluwer Academic Publishers, 1994) pp. 1393–1412.
2. D. J. Seery and J. Sangiovanni, "Engineering development of a coal-fired high-performance power generating system," Paper No. 1.7 in *Proc. of the Advanced Coal-Based Power and Environmental Systems'98 Conference*, Morgantown, West Virginia, July 21–23, 1998, DOE/FETC-98/1072.
3. INCO Data Sheet PP-1: Physical Properties of INCOLOY alloy MA956.
4. A. R. Jones, "Reduction in defect content of ODS alloys," *Proc. 14th Annual Conference on Fossil Energy Materials*, Knoxville, Tennessee, April 2000.
5. H. K. D. H. Bhadeshia, Materials Science and Engineering, **A223**, 64–77 (1997).
6. I. G. Wright, C. G. McKamey, and B. A. Pint, "ODS alloys for high-temperature applications," *Proc. 14th Annual Conference on Fossil Energy Materials*, Knoxville, Tennessee, April 2000.
7. W. J. Quadakkers and M. J. Bennett, Materials Science & Technology, **10**, 126–131 (1994).

8. W. J. Quadakkers and K. Bongartz, Werkstoffe und Korrosion, **45**, 232–41 (1994).
9. M. J. Bennett, H. Romary and J. B. Price, "The Oxidation Behavior of Alumina Forming Oxide Dispersion Strengthened Ferritic Alloys at 1200–1400°C," pp. 95–103 in *Heat Resistant Materials*, K. Natesan and D. J. Tillack, eds. (ASM, Materials Park, Ohio, 1991).
10. I. G. Wright, B. A. Pint, L. M. Hall, and P. F. Tortorelli, "Oxidation lifetimes: experimental results and modeling," paper presented at the European Federation of Corrosion Workshop on *Life Time Modeling of High-Temperature Corrosion Processes*," Frankfurt am Main, Germany, February 2001.
11. C. E. Lowell, C. A. Barrett, R. W. Palmer, J. V. Auping and H. B. Probst, Oxidation of Metals, **36**, 81–112 (1991).
12. I. G. Wright, V. K. Sethi, and A. J. Markworth, Wear, 186–187, 230–237 (1995).

OXIDATION RESISTANCE, FRACTURE TOUGHNESS AND CREEP STRENGTH OF Mo-Si-B ALLOYS CONTAINING α-Mo

J. H. Schneibel and D. S. Easton

Oak Ridge National Laboratory
Metals and Ceramics Division
P. O. Box 2008
Oak Ridge, TN 37831

INTRODUCTION

Silicide intermetallics can have outstanding oxidation resistance. This is evident in $MoSi_2$ which is widely used in heating elements for resistance furnaces. Its good oxidation resistance is due to the formation of a protective silica glass scale. However, $MoSi_2$ is very brittle. Its room temperature fracture toughness is only on the order of 3 MPa $m^{1/2}$ [1]. If the Si concentration is reduced below that of $MoSi_2$, phases such as Mo_5Si_3, Mo_3Si, and α-Mo (Mo solid solution) form. These phases will have a much lower oxidation resistance, but they may potentially impart a greater fracture toughness, in particular in the case of α-Mo. Two main alloy systems have been examined to date. In the first one, which was pioneered by Akinc and collaborators [2], intermetallic alloys consisting of Mo_5Si_3, the T2 phase Mo_5SiB_2, and the A15 phase Mo_3Si were investigated. These types of alloys are indicated in the schematic ternary phase diagram in Fig. 1. They exhibit excellent oxidation resistance at elevated temperatures (e.g., 1300°C). The boron additions are crucial for providing the observed oxidation resistance [3,4], as already hinted at in an early study of the ternary Mo-Si-B phase diagram by Nowotny et al. [5]. In the second system, which was pioneered by Berczik et al. [6,7], alloys consisting of α-Mo, Mo_3Si, and T2 were investigated. While these alloys are not as oxidation resistant as Mo_5Si_3-T2-Mo_3Si alloys, they do not consist exclusively of brittle phases. Depending on its volume fraction and distribution, the α-Mo can improve the room and high temperature fracture toughness significantly. Clearly, then, the optimization of Mo-Si-B alloys requires a trade-off between fracture toughness on the one hand, and oxidation resistance on the other.

Another issue is the creep resistance of these types of alloys. Akinc et al. have already shown that Mo_5Si_3-based alloys exhibit excellent creep resistance [2]. Mo_3Si and $(Cr,Mo)_3Si$ are also very strong at elevated temperatures [8,9]. Although there does not appear to be any work on the high-temperature strength of single-phase T2 to date, this compound is likely to be strong in view of its high melting point (appr. 2100°C [10]) and lack of easy slip systems. Since it is likely that the creep strength of α-Mo is lower than that of Mo_3Si and T2, the creep strength of Mo-Mo_3Si-T2 alloys is likely to depend on the α-Mo volume fraction, in particular if the α-Mo is distributed as a continuous matrix or "binder" phase. In addition, as commonly observed in creep, the grain or phase size will play an important factor—generally, the creep strength tends to increase with

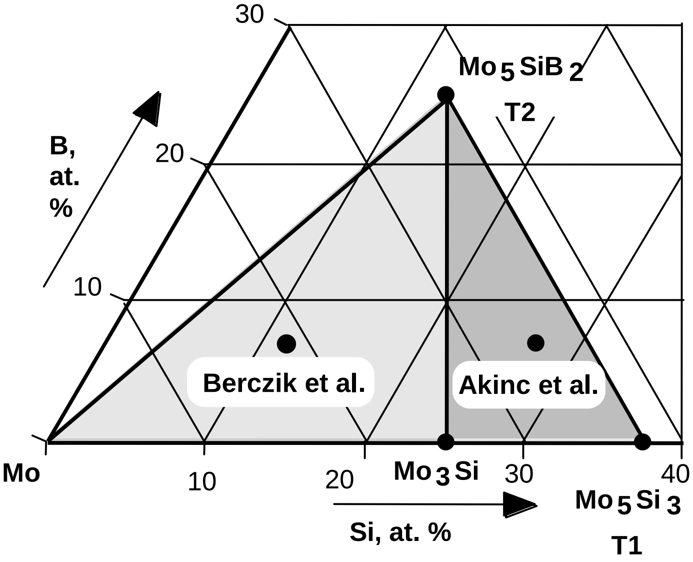

Fig. 1: Schematic illustration of the Mo-rich section of the ternary Mo-Si-B phase diagram.

increasing grain or phase size. In this paper we will summarize oxidation and fracture toughness data for Mo-Si-B alloys and illustrate the influence of alloying additions as well as microstructure on their creep strength.

increasing grain or phase size. In this paper we will summarize oxidation and fracture toughness data for Mo-Si-B alloys and illustrate the influence of alloying additions as well as microstructure on their creep strength.

EXPERIMENTAL

The alloys in this work were prepared by arc-melting of elemental starting materials in a partial pressure of argon (70 kPa) on a water-cooled copper hearth. The purity of the starting materials Mo, Si and B was 99.95, 99.99, and 99.5 wt%, respectively. Unless stated otherwise, alloy compositions will be stated in at. %. The alloys were re-melted several times in order to improve their homogeneity. Sometimes the alloys were allowed to solidify in elongated water-cooled Cu molds, in other cases they were drop-cast into cylindrical water-cooled copper molds with diameters of 12.5 or 25 mm. After casting, the alloys were usually annealed for 24 hours at 1600°C in vacuum at a pressure of approximately 10^{-4}Pa. Several as-cast alloys were crushed into powders with sizes ranging from 20 to 230 µm. They were mixed with various amounts of Mo powder (2–8 µm) and consolidated either by hot isostatic pressing in sealed Nb cans or by uniaxial hot-pressing in a graphite hot press.

Microstructural examination was carried out by optical microscopy as well as scanning electron microscopy (SEM). Metallography specimens were prepared by grinding, mechanical polishing, and etching in Murakami's etch. The phases were identified by a combination of energy dispersive spectroscopy (EDS) in an SEM and powder x-ray diffraction.

In order to assess the oxidation resistance of the Mo-Si-B alloys, screening tests were carried out. Small coupons (typically 10 × 10 × 1 mm) were weighed and annealed for 1 day in an air furnace at 1300°C. Their oxidation resistance was determined by dividing their weight change after annealing by their surface area.

Fracture toughness values were estimated from the energy dissipation during controlled crack growth of chevron-notched specimens [11].

Compression specimens with a diameter of 3 mm and a height of 6 mm were electro-discharge machined. Their creep strengths were evaluated from constant displacement rate tests carried out in a $MoSi_2$ furnace in flowing argon at temperatures ranging from 1200 to 1400°C.

RESULTS AND DISCUSSION

Oxidation Resistance

The section of the ternary Mo-Si-B phase diagram shown in Fig. 2 shows the weight losses experienced by different alloys after annealing for 1 day at 1300°C [13]. These particular alloys were tested in the as-cast condition except for one more recent alloy which was powder-metallurgically processed ("PM") by hot isostatic pressing. It should be noted that significant scatter is expected in the tests with the cast alloys since these alloys have complicated solidification paths resulting in non-equilibrium phases and macro-segregation, which are difficult to remove by annealing [10,14]. Also, alloys with less than about 40 vol. % α-Mo tended to form cracks during solidification. Nevertheless, several important points emerge from Fig. 2. First, Mo-20 Si has a poor oxidation resistance (556 mg/cm^2). Second, when the α-Mo volume fraction is kept approximately constant (i.e., as one moves, starting with Mo-20Si, upward in an approximately vertical direction), the boron concentration as well as the oxidation resistance increase. Boron additions are therefore beneficial for the oxidation resistance. Third, there is a trend for the oxidation resistance to increase as the α-Mo volume fraction decreases (i.e., as the alloy compositions in Fig. 2 move to the right). Fourth, the oxidation resistance of the PM processed alloy (5 mg/cm^2) is significantly better than that of the other alloys. While the reasons for this last result are not fully understood at the present time, the improved homogeneity and the lower incidence of cracks in the PM processed material, as compared to the cast materials, are likely to be contributing factors.

The relatively high oxidation resistance of the PM Mo-Si-B material at 1300°C does not necessarily mean that it will exhibit high oxidation resistance at intermediate temperatures (e.g., 700°C). Recent work by Natesan and Deevi [15] indicates that Mo-Si and Mo-Si-B alloys can exhibit high oxidation rates in the temperature range 500 to 700°C, indicating a "pest" reaction similar to that observed in $MoSi_2$ around 500°C. It remains to be seen to what extent the "pest" reaction can be alleviated by alloying or by pre-oxidizing at high temperatures such as 1300°C.

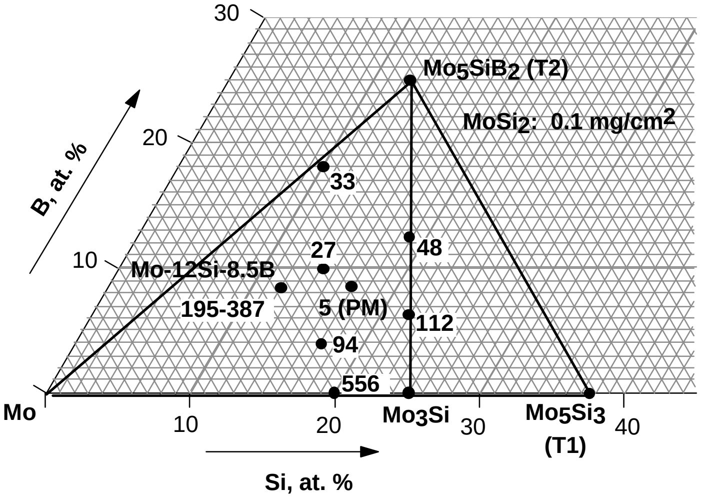

Fig. 2. Section of the ternary Mo-Si-B phase diagram indicating the alloy compositions investigated and the weight losses (in mg/cm^2) after annealing for 1 day at 1300°C in air. Except for one powder-metallurgically processed alloy ("PM"), the alloys were tested in the as-cast condition. A weight loss of 1 mg/cm^2 corresponds to a surface recession of approximately 1 μm.

Fracture Toughness

Table 1 lists the dependence of the room temperature fracture toughness, K_q, on the α-Mo volume fraction. Most of these alloys were prepared powder-metallurgically (PM). The alloy with an α-Mo volume fraction of zero is a two-phase Mo_3Si-T2 alloy (compare also the schematic phase diagram in Fig. 2). Its fracture toughness is low as would be expected from the brittle nature of Mo_3Si and T2. Table 1 shows that when the α-Mo volume fraction increases, the fracture toughness increases. Alloys with the nominal composition Mo-12Si-8.5B were fabricated by casting as well as PM. Qualitatively, the higher fracture toughness of the PM alloy as compared to the cast and annealed alloy is due to its coarser microstructure. Also, whereas the cast and annealed alloy appeared to contain discrete α-Mo particles, the PM alloy exhibited a semi-continuous α-Mo matrix. This means that propagating cracks cannot avoid the toughening α-Mo phase, and is consistent with the relatively high fracture toughness of the PM Mo-12Si-8.5B alloy.

Table 1. Room temperature fracture toughness values (determined from energy dissipation during the controlled fracture of chevron-notched specimens) of Mo-Si-B alloys with different α-Mo volume fractions.

Nominal Composition, at. %	Processing	α-Mo content, vol. %	K_q, MPa $m^{1/2}$
Mo-18.2Si-13.6B	PM	0	3.3
Mo-15.3Si-11.5B	PM	18	6.2
“	PM	18	5.8
“	PM	18	6.1
“	PM	18	7.2
Mo-12Si-8.5B	Casting	38	9.1
“	Casting	38	9.8
“	PM	38	14.0
“	PM	38	15.6

Creep Strength

Slow high-temperature compression tests with a constant crosshead displacement rate were carried out in flowing argon. The initial strain rate was 1×10^{-5} s^{-1}. A quasi-steady state flow stress (“steady-state creep strength”) was typically reached after a plastic strain of about 2%. Sometimes a gradual load drop occurred after a strain of a few percent. The creep strength was estimated as the engineering stress for a plastic strain of 2%. Note that the strength values obtained in this work are somewhat higher than those obtained in previous work [16, 17]. The reason for this is a more precise temperature measurement in the present work in which the thermocouple was inserted in a hole in the compression ram just below the specimen.

Experiments were carried out in order to determine whether the creep strength can be improved by solid solution strengthening. The cast and annealed alloy Mo-12Si-8.5B served as a base-line material. As candidate alloying elements, W and Nb (both of which are fully soluble in Mo) were chosen. In each case, 19.5 at. % of Mo were replaced by W or Nb. Whereas the Nb-containing alloy exhibited the same phases as Mo-12Si-8.5B, powder x-ray diffraction in the W-containing alloy showed an additional phase. This phase(s) has not yet been identified. Lattice parameter measurements using an internal Si standard are shown in Table 2. W additions increased the lattice parameters of the three main phases only slightly. Nb additions, on the other hand, increased the lattice parameters of all three phases significantly, as compared to the ternary Mo-12Si-8.5B alloy. The increases varied between 0.55 and 2.16% and were most significant for the T2 phase. The lattice parameter result are consistent with the Goldschmidt radii of Mo, W, and Nb which are 1.40, 1.41, and 1.47 Å, respectively.

Figure 3 compares the creep strengths of the quaternary alloys to that of Mo-12Si-8.5B. Tungsten additions cause only a modest increase in creep strength, whereas Nb almost doubles it. Both W and Nb increase the magnitude of the slopes in Fig. 3 and increase therefore the apparent activation energy for creep (see Table 3 below). Clearly, Nb additions cause pronounced solid solution creep strengthening, presumably

Table 2. Lattice parameters, in Å, for Mo-12Si-8.5B, Mo-19.5W-12Si-8.5B, and Mo-19.5Nb-12Si-8.5B.

	Mo-12Si-8.5B		+19.5W	Increase due to W, %		+19.5Nb	Increase due to Nb, %
Mo, a	3.1453		3.1490	0.12		3.1626	0.55
A15, a	4.8945		4.8952	0.01		4.9348	0.82
T2, a	6.0148		6.0352	0.34		6.1136	1.64
T2, c	11.0514		11.0677	0.15		11.2902	2.16

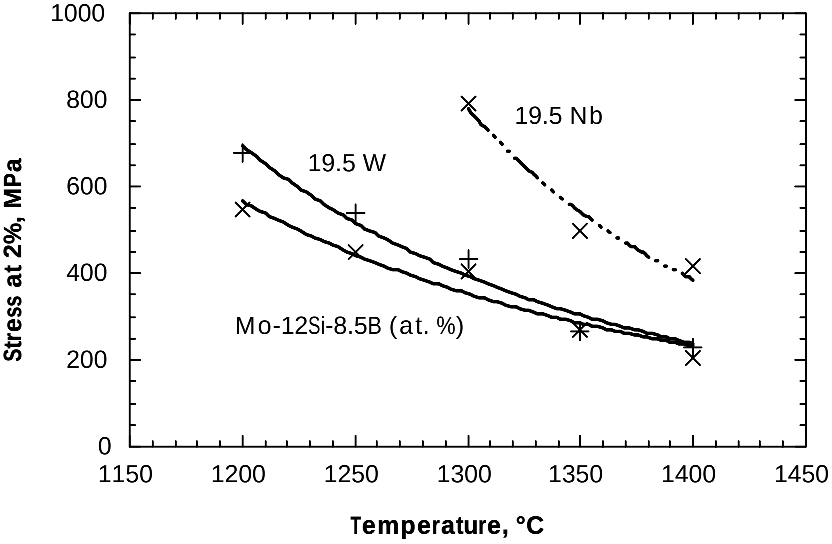

Fig. 3. Creep strength vs. temperature for Mo-12Si-8.5B, Mo-19.5W-12Si-8.5B, and Mo-19.5Nb-12Si-8.5B after annealing for 1 day at 1600°C in vacuum.

Table 3. Values of the creep parameters obtained by fitting Eq. (2) to experimental data.

A value of 2.7 was assumed for the stress exponent.

Nominal Composition, at. %	A, s^{-1}	Q, kJ/mol
Mo-12Si-8.5B	0.00019	246
Mo-19.5W-12Si-8.5B	0.0064	295
Mo-19.5Nb-12Si-8.5B	9.9	416

by a reduction in the diffusion coefficients in one or more phases in the alloy. Since the α-Mo appears to form individual particles it is not likely to control the creep rate. This suggests that either the Mo_3Si or the T2 phase (or both), which together form a continuous matrix, are responsible for the increase in creep strength. Further experiments identifying the distribution of the Nb in the three phases as well as experiments with single-phase

$(Mo,Nb)_3Si$ and/or T2 are in progress in order to clarify the pronounced influence of Nb on the creep strength of these alloys.

In order to evaluate our experiments the traditional creep equation is written as:

$$\dot{\varepsilon} = d\varepsilon / dt = A\sigma^{n} \exp(-\frac{Q}{RT}), \qquad (1)$$

where dε/dt is the strain rate, A pre-exponential factor, σ the stress, n the stress exponent, Q an apparent activation energy, R the gas constant, and T the absolute temperature. Solving Eq. (1) for the stress results in:

$$\sigma = [\frac{\dot{\varepsilon}}{A} \exp(\frac{Q}{RT})]^{1/n}. \qquad (2)$$

The unknown parameters A, Q, and n can be determined from a non-linear regression fit of Eq. (2) to Fig. 3. In order to improve the accuracy, a stress exponent value of 2.7 (which was obtained from previous tensile creep experiments [16, 17]) was used. The resulting parameters are listed in Table 2.

The creep strength is not only influenced by solid solution alloying additions, but also by the microstructure. Figure 4 shows SEM micrographs of two alloys with the same nominal composition, Mo-16.8Si-8.4B. One alloy was consolidated directly from powder crushed from an as-cast ingot [Fig. 4(a)]. The other alloy was processed from a mixture of crushed powder with the composition Mo-20Si-10B and an appropriate amount of Mo-powder [Fig. 4(b)]. The microstructure in Fig. 4(b) is clearly much coarser than that in Fig. 4(a) (note that the two micrographs have different magnifications). Not surprisingly, the creep strength of the alloy with the coarser microstructure is higher than that of the alloy with the finer one. The creep data listed in Table 4 illustrate this difference in the creep strengths. Summarizing, the creep results presented here demonstrate that the creep strength can be influenced dramatically not only by solid solution alloying, but also by microstructural manipulation.

CONCLUSIONS

Boron-containing silicides with compositions in the Mo-Mo_3Si-Mo_5SiB_2 three-phase field can be quite resistant to oxidation. When the volume fraction of the α-Mo solid solution phase is reduced, the oxidation resistance increases. However, at the same time the room temperature fracture toughness decreases. This is no surprise since both Mo_3Si and Mo_5SiB_2 are brittle phases. Controlling the properties of Mo-Si-B alloys involves therefore a trade-off between oxidation resistance on the one hand and fracture toughness on the other. Constant displacement rate compression tests at elevated temperatures show that the creep strength can be controlled by solid solution alloying and by manipulating the microstructure.

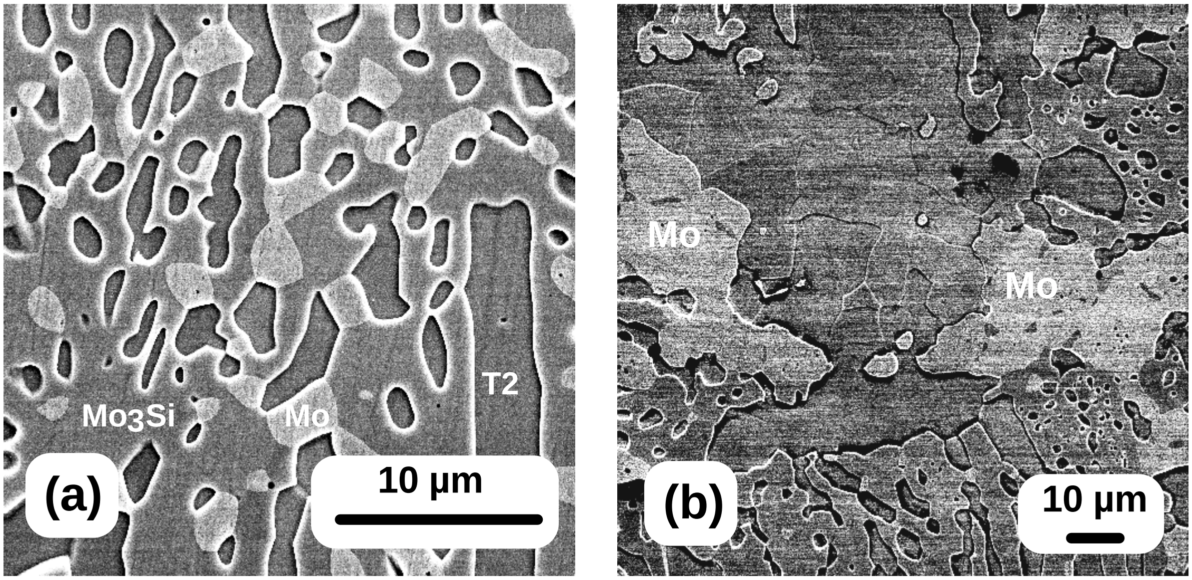

Fig. 4. SEM micrographs of polished and etched specimens prepared powder-metallurgically (a) directly from Mo-16.8Si-8.4B powder and (b) from Mo-20Si-10B powder mixed with Mo powder.

Table 4. Creep strength (engineering stress after 2% plastic strain, in MPa) of two alloys with the nominal composition Mo-16.8Si-8.4B deformed at an initial strain rate of 10^{-5} s^{-1} in argon

Temperature, °C	"Fine" microstructure [Fig. 4(a)]	"Coarse" microstructure [Fig. 4(b)]
1300	263	400
1400	104	220

ACKNOWLEDGEMENTS

This work was sponsored by the Office of Fossil Energy, Advanced Research Materials (ARM) Program, U.S. Department of Energy, under contract DE-AC05-00OR22725 with Oak Ridge National Laboratory managed by UT-Battelle, LLC.

REFERENCES

1. A. K. Vasudévan and J. Petrovic, "A comparative overview of molybdenum silicide composites," Mater. Sci. and Engng. A155 (1992) 1–17.
2. M. K. Meyer, M. J. Kramer, and M. Akinca [sic], "Compressive creep behavior of Mo_5Si_3 with the addition of boron," Intermetallics 4 (1996) 273–281.

3. M. Akinc, M. K. Meyer, M. J. Kramer, A. J. Thom, J. J. Huebsch, and B. Cook, "Boron-doped molybdenum silicides for structural applications," Intermetallics A261 (1999) 16–23.

4. M. K. Meyer, A. J. Thom, and M. Akinc, "Oxide scale formation and isothermal oxidation behavior of Mo-Si-B intermetallics at 600–1000°C," Intermetallics 7 (1999) 153–162.

5. H. Nowotny, E. Kimakopoulou, and H. Kudielka, Mh. Chem. 88 (1957) 180–192.

6. D. M. Berczik, United States Patent 5,595,616 (1997), "Method for enhancing the oxidation resistance of a molybdenum alloy, and a method of making a molybdenum alloy."

7. D. M. Berczik, United States Patent 5,693,156 (1997), "Oxidation Resistant Molybdenum Alloys."

8. I. Rosales and J. H. Schneibel, "Stoichiometry and mechanical properties of Mo_3Si," Intermetallics 8 (2000) 885–889.

9. S. V. Raj, J. D. Whittenberger, B. Zeumer, and G. Sauthoff, "Elevated temperature deformation of Cr_3Si alloyed with Mo," Intermetallics 7 (1999) 743–755.

10. C. A. Nunes, R. Sakidja, and J. H. Perepezko, "Phase stability in high temperature Mo-rich Mo-B-Si alloy," Structural Intermetallics 1997, ed. M. V. Nathal, R. Darolia, C. T. Liu, et al., (Warrendale, PA: The Minerals, Metals & Materials Society, 1997), 831–839.

11. J. H. Schneibel, M. J. Kramer, Ö. Ünal, R. N. Wright, "Processing and mechanical properties of a molybdenum silicide with the composition Mo-12Si-8.5B (at. %)," Intermetallics 9 (2001) 25–31.

13. J. H. Schneibel, C. T. Liu, D. S. Easton, and C. A. Carmichael, "Microstructure and mechanical properties of Mo-Mo_3Si-Mo_5SiB_2 silicides," Mater. Sci. Engng. A261 (1999) 78–83.

14. C. A. Nunes, R. Sakidya, Z. Dong, and J. H. Perepezko, "Liquidus projection for the Mo-rich portion of the Mo-Si-B ternary system," Intermetallics 8 (2000) 327–337.

15. K. Natesan and S. C. Deevi, "Oxidation behavior of molybdenum silicides and their composites, Intermetallics 8 (2000) 1147–1158.

16. J. H. Schneibel and H. T. Lin, "Processing and properties of molybdenum silicide intermetallics containing boron," in "Fossil Energy Program Annual Progress Report for April 1999 Through March 2000," R. R. Judkins, Program Manager, Oak Ridge National Laboratory, July 2000.

17. J. H. Schneibel and H. T. Lin, "Creep properties of molybdenum silicide intermetallics containing boron," submitted to Materials at High Temperatures.

BISMUTH OXIDE SOLID ELECTROLYTE OXYGEN SEPARATION MEMBRANES

S. D. Nunn and E. A. Payzant
Oak Ridge National Laboratory
P. O. Box 2008
Oak Ridge, TN 37831-6087

INTRODUCTION

Bi_2O_3 at elevated temperatures and various compounds of Bi_2O_3 form very efficient oxygen ion conducting solid electrolytes.[1] The high temperature polymorph of Bi_2O_3, δ-Bi_2O_3, has exceptionally high ionic conductivity, but is subject to cracking due to the volume changes associated with phase transformation during cyclic heating and cooling. Doped β-Bi_2O_3 exhibits oxygen ion conductivity that is much higher than yttria-stabilized ZrO_2 (YSZ) up to the maximum operating temperature of about 800°C.[2] The β-phase of Bi_2O_3 is formed by partial substitution for the bismuth atoms by divalent alkaline earth ions such as calcium, strontium, and barium. The general chemical formula for β-Bi_2O_3 is $Bi_{(1-x)}M_xO_{(3-x)/2}$, where M = Ca, Sr, or Ba. The conductivity increases by nearly ten-fold due to a phase change in the temperature range of 560°C to 745°C, depending upon the amount and type of dopant in the composition.[2–4] Conductivity test results for samples containing various amounts of dopant were presented in previous reports.[5,6] Another Bi_2O_3-based compound, which forms a very low temperature ionic conducting material is doped $Bi_4V_2O_{11}$.[7–9] By doping with divalent metals such as Co, Cu, and Zn, an ionic conducting compound can be formed that has the general chemical formula: $Bi_2V_{1-x}Me_xO_{5.5-1.5x}$, where Me is the divalent metal dopant. These compounds are generically referred to as BiMeVOx. In the present report, test results are given for a number of Bi_2O_3 compounds that were evaluated for ionic conductivity and oxygen ion flux rate.

EVALUATION OF MIXED-PHASE CONDUCTORS

Bi_2O_3 compositions containing varying amounts of the alkaline earth oxides CaO and SrO were prepared by normal ceramic processing methods as described in a previous report.[6] The compositions that were prepared are listed in Table 1. Some of these compositions are outside the β-Bi_2O_3 solid solution range. Those compositions with less than 22 mol % CaO or less than 8 mol % SrO are in a two-phase region of the corresponding phase diagram and contain both undoped Bi_2O_3 and the doped β-Bi_2O_3 phase. As with the single phase β-Bi_2O_3 compositions, a thermally induced phase transformation is observed for these two-phase compounds. The temperature at which the transformation is complete is shown in Table 1, which also lists the conductivity measured after the transformation. It can be clearly seen from the data in Table 1 that the two-phase compositions exhibit the highest conductivity values of all the

Table 1. Composition and properties of Bi_2O_3 compounds doped with various amounts of CaO and SrO additives.

Composition, mol %		Transformation Temperature, ºC	Conductivity after Transformation, S/cm
89.25 Bi_2O_3	10.75 CaO	715	1.211
84 Bi_2O_3	16 CaO	710	1.011
78 Bi_2O_3	22 CaO	755	0.930
72 Bi_2O_3	28 CaO	765	0.673
91.5 Bi_2O_3	8.5 SrO	745	1.352
88 Bi_2O_3	12 SrO	740	1.203
82 Bi_2O_3	18 SrO	680	0.644
72 Bi_2O_3	28 SrO	725	0.429
58 Bi_2O_3	42 SrO	645	0.104

compositions that were evaluated. A comparison of the conductivity of the various compositions as a function of temperature is shown in the Arrhenius plots in Figs. 1 and 2. The effect of the phase transformation is seen as the steep increase in conductivity at the transformation temperature.

Although a poor conductor at low temperatures, it is known that the undoped Bi_2O_3 phase has very high conductivity at elevated temperatures when it has undergone a reversible phase transformation from the monoclinic α-Bi_2O_3 phase to the cubic δ-Bi_2O_3 phase. However, the volume change that is associated with the transformation can cause severe damage when the material is repeatedly cycled through the transformation temperature, making it impractical for use in an ionic conducting device. This volume change damage was not observed in the mixed-phase conductors, even though, depending upon the composition, a portion or all of the material transforms to the δ-Bi_2O_3 phase at elevated temperatures. To better understand the relationship between the β-Bi_2O_3 phase and the δ-Bi_2O_3 phase, samples were examined by neutron diffraction analysis at high temperature using Oak Ridge National Laboratory's High Flux Isotope Reactor (HFIR). Samples were also examined by high temperature x-ray diffraction analysis (XRD).

The cubic crystal structure of δ-Bi_2O_3 is shown in Fig. 3. It is a defect fluorite structure with disordered occupancy of the cation sites and disordered vacancies on the oxygen sites. The vertical axis in the figure is the 111 axis of the cubic structure. An illustration of the high temperature rhombohedral crystal structure of β-Bi_2O_3 is shown in Fig. 4, where the vertical axis is the 001 crystallographic direction. The rhombohedral β-phase structure is composed of layers of the defect-fluorite δ-phase structure, but with the partially doped layers sandwiched between two exclusively bismuth-occupied layers. Although the divalent alkaline earth ions can be expected to increase the number of oxygen defects in the structure, the most oxygen-deficient positions are located in the vicinity of the bismuth-occupied layers. Only a relatively minor rearrangement of the dopant ions and the oxygen defects is required to

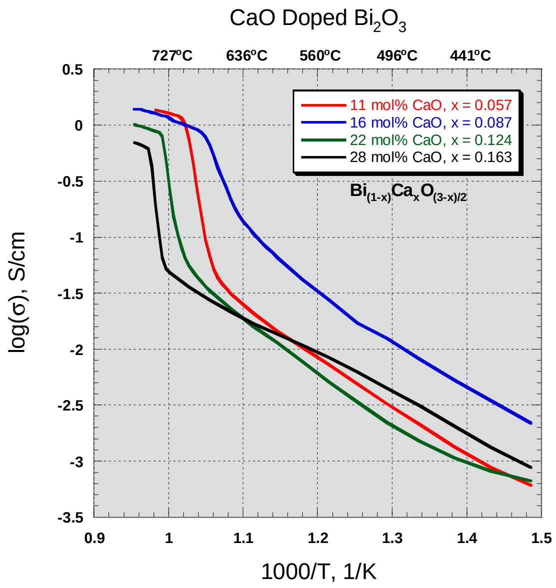

Fig. 1. The measured conductivity as a function of temperature for the CaO-doped Bi_2O_3 compositions.

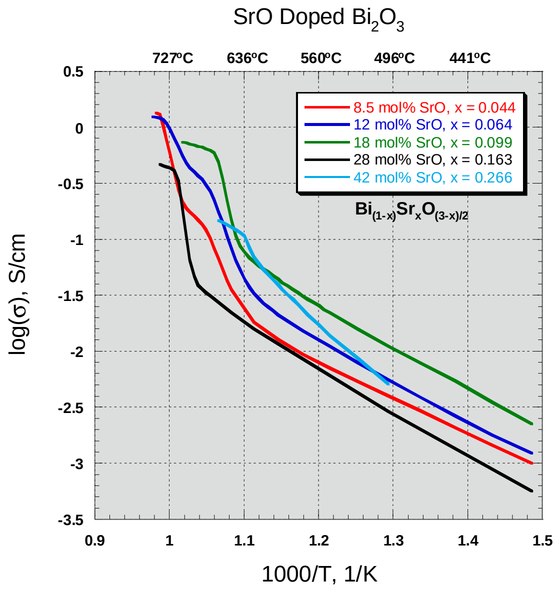

Fig. 2. The measured conductivity as a function of temperature for the SrO-doped Bi_2O_3 compositions.

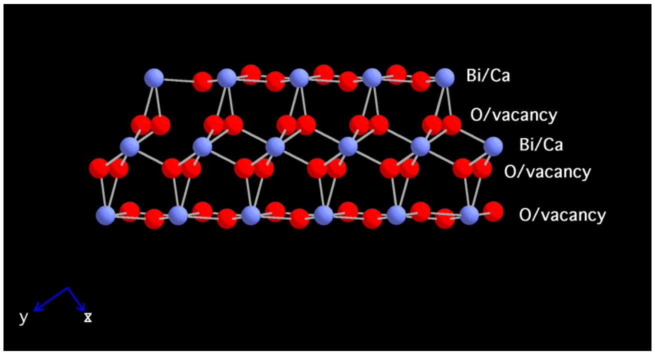

111 ↑

Fig. 3. The crystal structure of δ-Bi_2O_3 as determined by neutron and x-ray diffraction analysis.

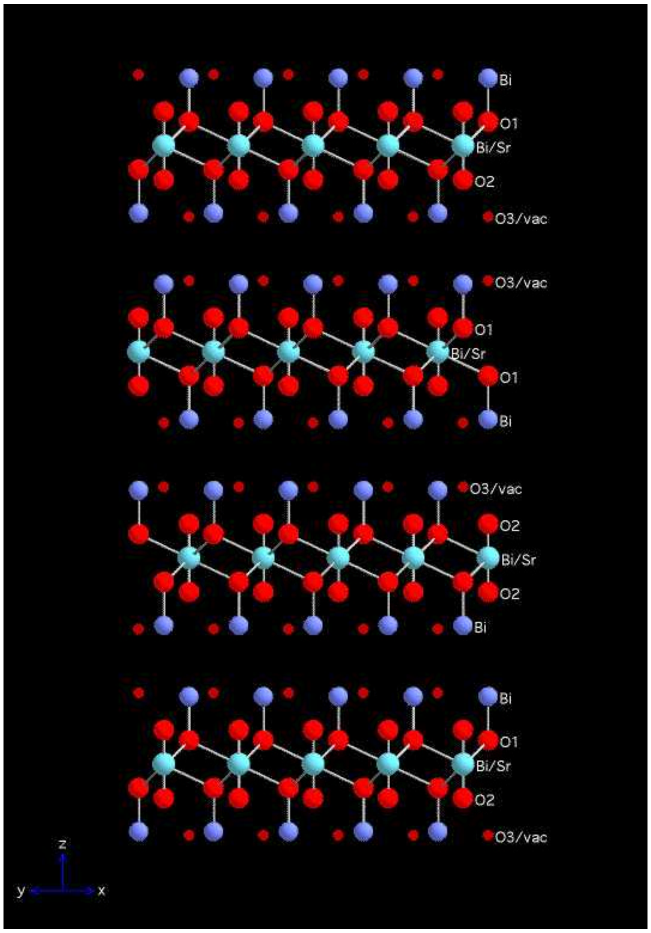

001 ↑

Fig. 4. The crystal structure of β-Bi_2O_3 as determined by neutron and x-ray diffraction analysis.

transform between the rhombohedral and the cubic phases. This may help explain the excellent conductivity properties and physical stability of the mixed-phase compositions.

LOW TEMPERATURE IONIC CONDUCTOR COMPOUNDS

Another Bi_2O_3-based compound, which forms a very low temperature ionic conducting material is doped $Bi_4V_2O_{11}$.[7–9] By doping with divalent metals such as Co, Cu, and Zn, an ionic conducting compound can be formed that has the general chemical formula: $Bi_2V_{1-x}Me_xO_{5.5-1.5x}$, where Me is the divalent metal dopant. These compounds are generically referred to as BiMeVOx. The compound $Bi_2V_{0.9}Cu_{0.1}O_{5.35}$ was prepared using the same ceramic processing methods that were used to make the mixed-phase compositions. The conductivity of $Bi_2V_{0.9}Cu_{0.1}O_{5.35}$ was measured as a function of temperature and the results are plotted in Fig. 5 along with the conductivity curves of two of the mixed-phase compositions for comparison. The conductivity of $Bi_2V_{0.9}Cu_{0.1}O_{5.35}$ increases steadily with temperature and is significantly higher than the mixed-phase materials at very low temperatures. However, the conductivity of the mixed-phase compounds is much higher at elevated temperatures. The choice of ionic conducting compounds for use in a specific application may depend in large part on the maximum use temperature that is anticipated.

OXYGEN FLUX TEST APPARATUS

A new oxygen flux test apparatus was designed and built to measure the amount of oxygen that can be transported through a Bi_2O_3-based solid electrolyte membrane. The apparatus is based on forming an oxygen concentration cell, which can be described as follows:

$$O_2\ (\text{High } P_{O2}\ (\text{cathode}))\ |\ Ag\ |\ Bi_2O_3\text{-based electrolyte}|\ Ag\ |\ O_2\ (\text{Low } P_{O2}\ (\text{anode})).$$

If the conductivity of the electrolyte is purely ionic, then the *emf* of the cell is given by the following equation:

$$EMF = \frac{RT}{4F}\ln\left(\frac{P_{O_2(cathode)}}{P_{O_2(anode)}}\right),$$

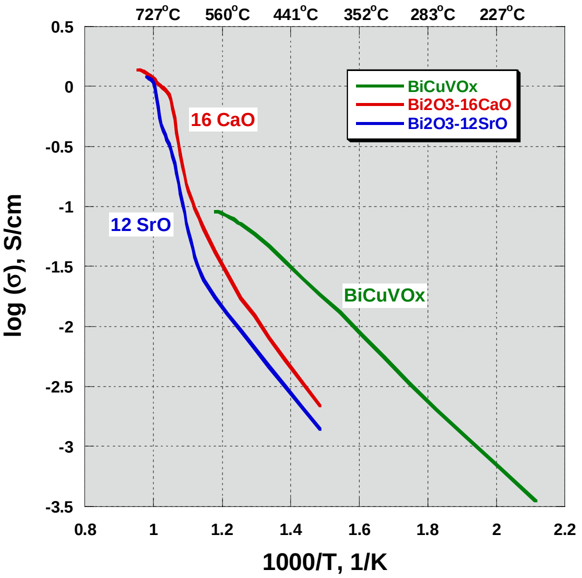

Fig. 5. A comparison of the conductivity of BiCuVOx and two alkaline-earth-doped Bi_2O_3 compounds as a function of temperature.

where *R* is the gas constant, *T* is the absolute temperature, and *F* is the Faraday constant. Additionally, if the conductivity, *σ*, and thickness, *t*, of the electrolyte are known, then the oxygen flux can be calculated as follows:

$$J_{O_2} = \frac{RT\sigma}{4Ft}\ln\left(\frac{P_{O_2(cathode)}}{P_{O2(anode)}}\right).$$

The test cell can also be run in an oxygen pumping mode, that is, an *emf* can be applied across the solid electrolyte membrane to drive oxygen from the cathode side to the anode.

The oxygen concentration cell within the test apparatus was formed using a series of concentrically nested refractory tubes made of Al_2O_3. This is shown schematically in Fig. 6. Silver electrodes were applied to each face of a disk-shaped solid electrolyte sample. Compressed gold o-rings were used to isolate the two faces of the sample. Other tubes carry the cathode and anode gasses to the surface of the sample and out of the test cell. A central tube on each side holds a thermocouple near the face of the sample and also carries a platinum wire to make electrical connection to the electroded surface. The entire assembly was placed in a tube furnace to heat the sample for testing.

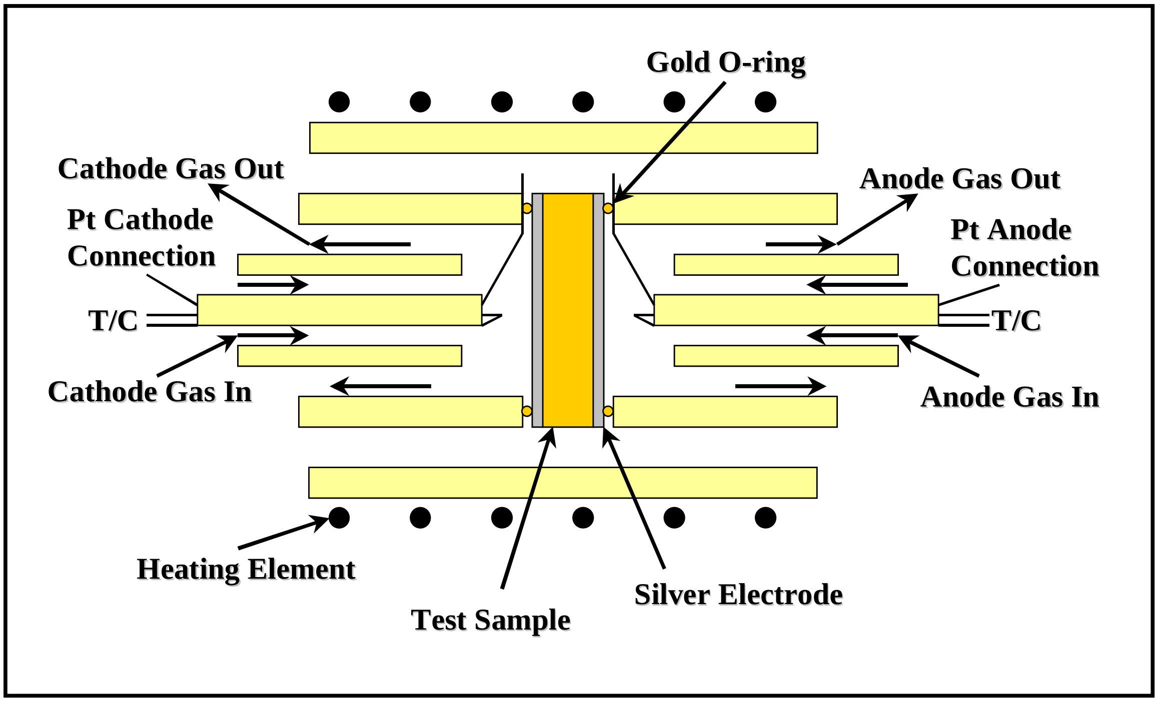

Fig. 6. A schematic diagram of the central portion of the oxygen flux test apparatus.

Oxygen flux measurements were made on samples that were approximately 13 mm in diameter and about 2 mm thick. Silver ink was painted on the two faces of the sample and fired on at 700°C. A gas flow rate of 0.3 L/min. was established on both sides of the sample. The partial pressure of oxygen on the cathode side of the test cell was 1 (pure O_2) and on the anode side the oxygen partial pressure was 98 ppm. The exhaust gas from the anode side was run through an oxygen analyzer to determine the oxygen content, which would included any oxygen that was transported through the solid electrolyte. An example of typical test data for the pumping tests is shown in Fig. 7. The oxygen concentration increases with increasing applied voltage and also with increasing temperature, as would be expected from the conductivity measurements. The large increase in oxygen concentration that is shown in the figure at 731°C compared to the lower temperatures corresponds to the phase transformation in the solid electrolyte, which substantially increases the conductivity.

Knowing the flow rate of gas to the anode side of the test cell and the active surface area of the membrane, the oxygen concentration data can be transformed to a measurement of oxygen flux through the membrane. The oxygen flux for the test data shown in Fig. 7 is plotted in Fig. 8, where the effect of driving voltage and the temperature dependence of conductivity are clearly seen.

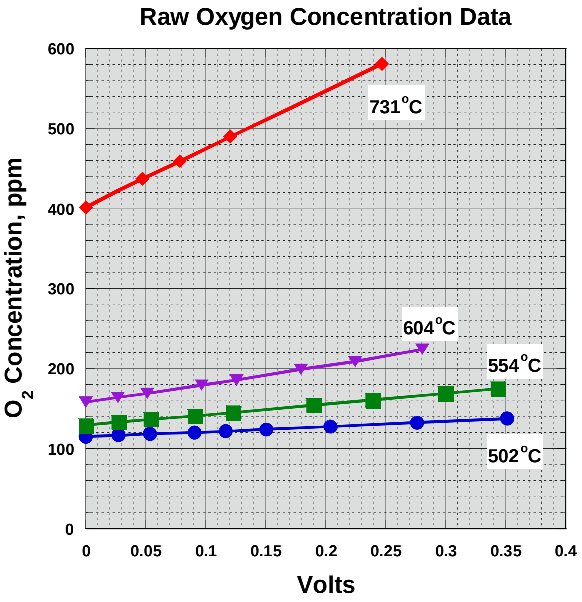

Fig. 7. The oxygen concentration as a function of the applied cell voltage at several temperatures for the composition Bi_2O_3–18 mol % SrO.

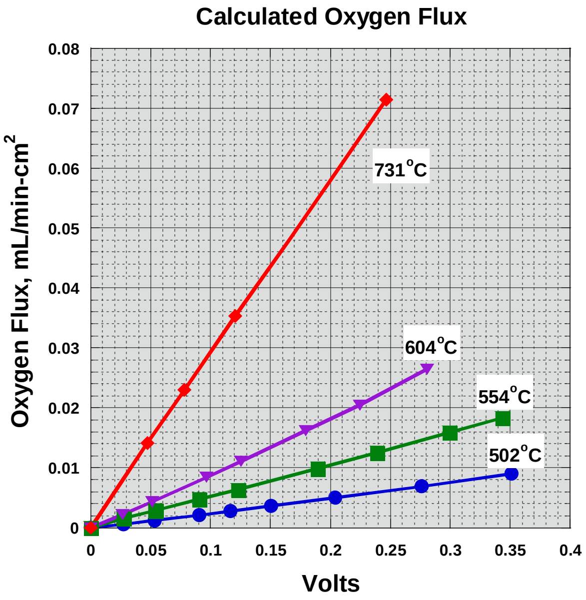

Fig. 8. The calculated oxygen flux as a function of the applied cell voltage at several temperatures for the composition Bi_2O_3–18 mol % SrO.

These oxygen flux tests should be considered preliminary in nature at this point. The complexity of the flux test apparatus and of the various instruments involved in making the measurements will require considerably more experimentation and cross-checking to be certain of the results that are being seen. However, the oxygen flux results for the samples that were tested show the relationships that would be expected based on theory and on conductivity data.

CONCLUSIONS

Bi_2O_3 compositions containing mixed-phases were prepared and evaluated for ionic conductivity. These mixed-phase compositions showed excellent conductivity values, as high as 1.35 S/cm at 745°C. Neutron diffraction analysis and x-ray diffraction analysis were used to determine the crystallographic structural relationships between the cubic δ-Bi_2O_3 phase and the rhombohedral β-Bi_2O_3 phase in these compounds. A very low temperature ionic conducting compound, $Bi_2V_{0.9}Cu_{0.1}O_{5.35}$, was prepared and the conductivity was compared to previous results. The new compound had significantly higher conductivity at low temperatures, but much lower conductivity at temperatures above about 600°C. An oxygen flux test apparatus was built and preliminary tests were conducted on the mixed-phase compounds to determine the rate of oxygen pumping under the influence of an electric field. The results show increased oxygen flux with increasing applied voltage. Also, there was an increase in the oxygen flux at a given voltage when the temperature was increased, in agreement with the conductivity measurements.

ACKNOWLEDGEMENTS

Research sponsored by the Office of Fossil Energy, Advanced Research and Technology Development Materials Program, U.S. Department of Energy under contract number DE-AC05-00OR22725 with UT-Battelle, LLC.

REFERENCES

1. N. M. Sammes, G. A. Tompsett, H. Nafe, and F. Aldinger, “Bismuth Based Oxide Electrolytes–Structure and Ionic Conductivity,” *J. Eur. Ceram. Soc.*, **19** (1999) 1801–1826.
2. T. Takahashi, H. Iwahara, and Y. Nagai, “High Oxide Ion conduction in Sintered Bi_2O_3 Containing SrO, CaO or La_2O_3,” *J. Appl. Electrochem.* **2** (1972) 97–104.
3. J. C. Boivin and D. J. Thomas, “Structural Investigations On Bismuth-Based Mixed Oxides,” *Solid State Ionics* **3/4** (1981) 457–462.
4. P. Conflant, J. C. Boivin, G. Nowogrocki, and D. Thomas, “High Temperature X-ray Structural Study of the Anionic Conductor $Bi_{0.844}Ba_{0.156}O_{1.422}$,” *Solid State Ionics* **9&10** (1983) 925–928.

5. S. D. Nunn and E. A. Payzant, “Bismuth Oxide Solid Electrolyte Oxygen Separation Membranes,” Fossil Energy Program Annual Progress Report, April 1, 1998–March 31, 1999.
6. S. D. Nunn and E. A. Payzant, “Bismuth Oxide Solid Electrolyte Oxygen Separation Membranes,” Fossil Energy Program Annual Progress Report, April 1, 1999–March 31, 2000.
7. F. Abraham, J. C. Boivin, G Mairesse, and G Nowogrocki, “The BIMEVOX Series: A New Family of High Performance Oxide Ion Conductors,” *Solid State Ionics* **40/41** (1990) 934–937.
8. K. Reiselhuber, G. Dorner, and M. W. Breiter, “Studies of BICUVOX.10 by Conductivity Measurements and Differential Thermal Analysis,” *Electrochimica Acta*. **38** [7] (1993) 969–973.
9. J. C. Boivin, C. Pirovano, G. Nowogrocki, G. Mairesse, Ph. Labrune, and G. Lagrange, “Electrode-Electrolyte BIMEVOX System for Moderate Temperature Oxygen Separation,” *Solid State Ionics* **113–115** (1998) 639–651.

DEVELOPMENT OF NOVEL ACTIVATED CARBON COMPOSITES

Tim Burchell, Rod Judkins, Alex Gabbard, Omats Omatete and Mike Rogers
Metals and Ceramics Division
Oak Ridge National Laboratory
1 Bethel Valley Road
Oak Ridge, TN 37831-6088

INTRODUCTION

There is a great need for a versatile (i.e., applicable to a wide range of process conditions), effective, and regenerable CO_2 separation and capture device that is cost effective, produces minimal waste, and is readily adaptable to a variety of carbon sequestration schemes. Separation and capture of CO_2 has been identified in numerous forums as a critical issue for sequestration of carbon as a carbon emission mitigation option. An innovative concept using an activated carbon adsorbent called a carbon fiber composite molecular sieve (CFCMS) is being investigated at the Oak Ridge National Laboratory (ORNL) and at other laboratories around the world. The CFCMS has distinct adsorption-capacity and adsorption-kinetics advantages over conventional granular activated carbons.

The CFCMS is a monolithic carbon adsorbent material composed of petroleum-derived isotropic pitch carbon fibers and phenolic-resin-derived carbon binder. The material was developed jointly by ORNL and the University of Kentucky Center for Applied Energy Research. High micropore volumes (0.5–1.0 cm^3/g) and BET surface areas (1000–2000 m^2/g) are routinely attained in this material. In addition, the monoliths have an open structure that allows the free flow of fluids through the material (see Fig. 1). The CFCMS has been shown to be highly efficacious in the adsorption of polar molecules and for some flat nonpolar molecules, such as CO_2 (variants of the CFCMS have an affinity for other nonpolar molecules, such as CH_4).

Moreover, the continuous nature of the monolith's structure imparts electrical conductivity to the material. Advantage has been taken of this property by ORNL to develop a novel desorption process, which has been named "electrical swing adsorption" (ESA). On saturation of the CFCMS with, for example, CO_2, immediate desorption of perhaps 90 to 95% of the adsorbed gas can be accomplished by application of a low voltage across the adsorbent. There are many important operational implications of this desorption process. The system pressure and temperature do not have to be altered as in other parametric swing processes such as pressure swing adsorption (PSA) or thermal swing adsorption (TSA). The ESA process is extremely fast in comparison to PSA and TSA. It is an inherently low energy process compared to PSA and TSA. All of these features suggest a great deal of system and operational simplicity and indicate that CFCMS and the ESA technique may be the basis of a new unit operation system for energy and environmentally relevant separations.

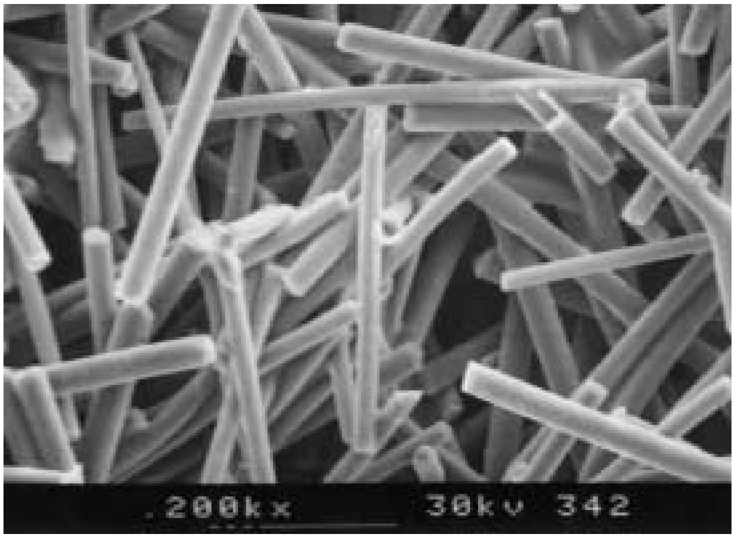

Fig. 1. Micrograph of the CFCMS showing the open structure of the material.

The manufacture of CFCMS, characterizations of its pore structure, and its physical properties, as well as adsorption data for CO_2 are reported here. The novel ESA process is discussed, and breakthrough experimental data are presented. The experimental ESA system that is being used to acquire process-relevant separation data is described, and experimental data demonstrating the efficacy of the material under a variety of system conditions are presented.

OBJECTIVE

The objective of the work described here was to demonstrate the performance potential of CFCMS for CO_2 separation and capture. This broad objective imposed the condition for the development of a novel processing as well as the need for a test system with broad flexibility for simulation of systems of interest. It was not intended that this work would result in an optimized material for any specific system application. Rather, it was intended that this work would establish the feasibility of CFCMS as an adsorbent and would help to define further work on material optimization and system integration.

This work was also intended to develop all processing parameters required to consistently produce CFCMS and to identify or develop the necessary characterization methods required to demonstrate consistency of quality. Furthermore, there was a need to develop a laboratory test system that could be used to simulate conditions of systems of interest in a carbon sequestration scenario.

APPROACH AND TECHNOLOGY DESCRIPTION

The CFCMS material utilized in this work was manufactured via the slurry process [1,2] outlined in Fig. 2. Isotropic-pitch-derived carbon fibers are mixed with powdered phenolic resin and water to form a

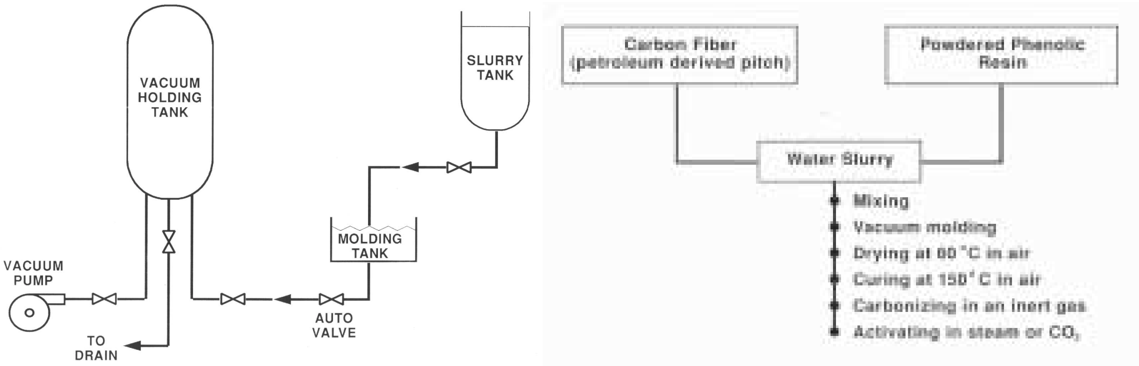

Fig.2. Schematic diagram of the slurry molding apparatus (left) and the synthesis route (right) for the CFCMS.

slurry. The slurry is transferred to a molding tank, and the water is drawn through a screen under vacuum. A schematic diagram of the molding apparatus is also shown in Fig. 2. The resultant green artifact is dried in air at 60°C and stripped from the mold screen. The composite is cured at ≈ 150°C prior to carbonization at 650°C in an inert gas. The final synthesis stage involves activation of the composite in moisture saturated He or in dry CO_2.

The thermal conductivity of CFCMS was determined by using the thermal flash technique. A sample was illuminated on one face with a laser, and the temperature of the other face was monitored with an infrared detector. The thermal diffusivity was calculated from the thermal transient; and the thermal conductivity was then determined from Eq. (1):

$$K = \alpha \cdot \rho \cdot C_p \ , \tag{1}$$

where α is the thermal diffusivity at the test temperature, ρ is the bulk density, and C_p is the specific heat at the test temperature.

Pore structure characterization of CFCMS was conducted with a Quantichrome Autosorb-1 instrument to measure N_2 adsorption isotherms at 77 K. Parameters such as the BET surface area, Dubinin-Astakhov (DA) and Dubinin-Radushkevich (DR) micropore size and micropore volume, and the t-method micropore volume are determined from the isotherms. Meso- and macro-pore size distributions were obtained by using mercury intrusion analysis, optical microscopy, and scanning electron microscopy (SEM) examination.

A gas flow loop was constructed to determine and verify the performance characteristics of the CFCMS. A general view of the loop is shown in Fig.3. The gas flow loop has a capacity of about 50 L/h and can be operated up to 1000 psi. The gas flow loop is highly instrumented and provides a wealth of

Fig. 3. General view of the gas flow loop.

data for determination of adsorption capacity and adsorption kinetics as well as data that are helping to elucidate the mechanisms of adsorption and desorption associated with CFCMS.

In these experiments, certified gas mixtures are typically used although the system has the capability to mix pure gases to produce desired mixtures for separation.

A side stream is led from the loop and passes through an adsorption (Fig. 4) containing the activated CFCMS. Copper head ring connectors are attached at each end of the CFCMS, and electrical connections are led to a low-voltage (0–8 V DC) power supply. Gas pressure, temperature, and flow rates in the loop and adsorption cell are monitored and recorded. A sample of the cell outlet gas is led to a mass spectrometer or gas detector so that gas concentrations in the exit may be detected. The ESA subsystem of the loop imparts the ability to stimulate desorption of CO_2 from the CFCMS sample.

RESULTS AND DISCUSSION

STRUCTURE

The macrostructure and porosity of CFCMS are illustrated in Fig. 5. The carbon fibers are bonded at their contact points creating an open and permeable structure. Macroscopic voids in the structure are approximately 50–250 μm. Fiber lengths are 50–1000 μm, and diameters are 12–16 μm. The N_2 isotherm for CFCMS in Fig. 6 exhibits the characteristics of a Type I isotherm (i.e., typical of a microporous solid).

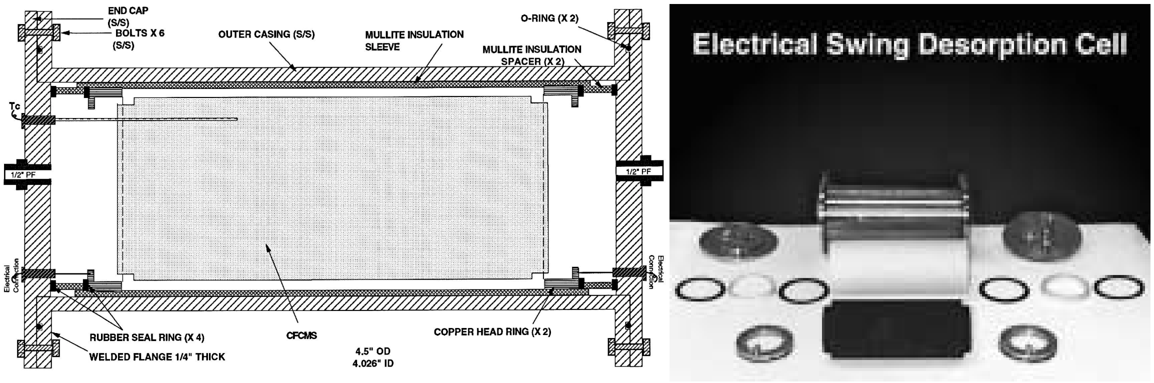

Fig. 4. Adsorption cell schematic (left) and exploded view of components (right).

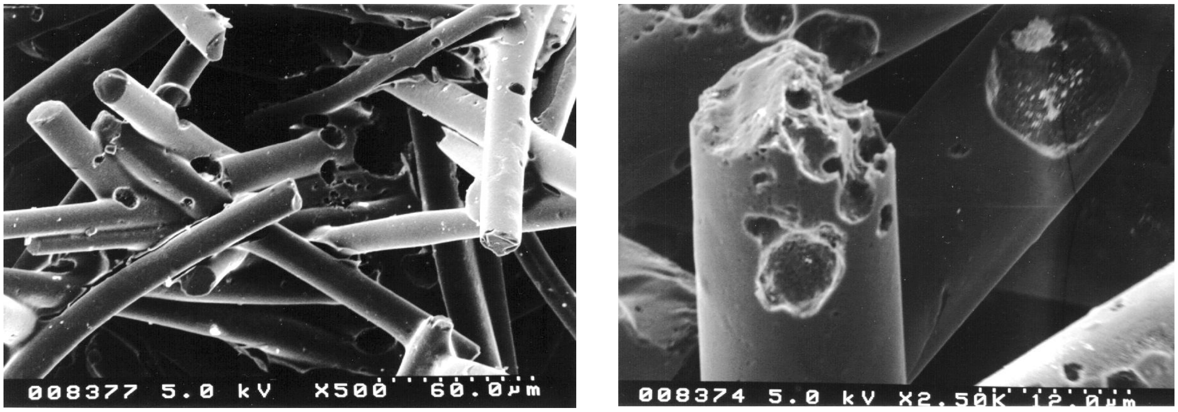

Fig. 5. The microstructure of activated CFCMS (left) and a scanning electron micrograph of an activated carbon fiber from a CFCMS sample.

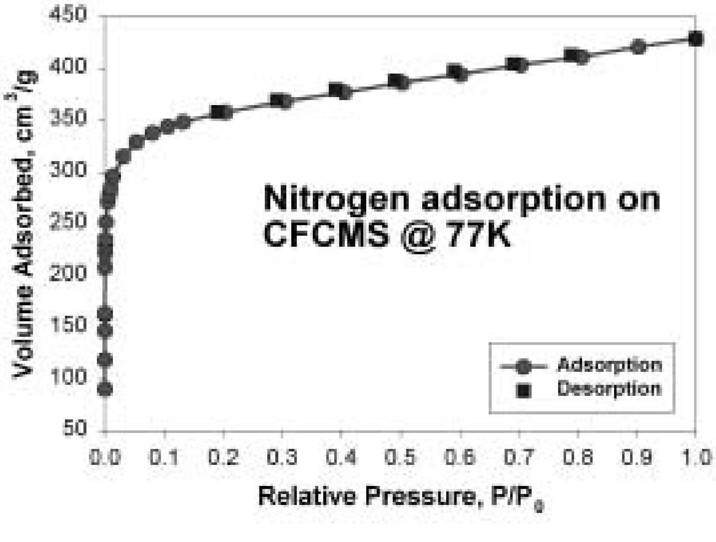

Fig. 6. Type I isotherm of CFCMS, which is indicative of a microporous solid.

THERMAL CONDUCTIVITY

The thermal conductivity of CFCMS monoliths (Fig. 7) is several times higher than that of packed beds of conventional granular or powdered activated carbon. Typically, the thermal conductivity of CFCMS is anisotropic, the value parallel to the fibers being three to four times greater than that perpendicular to the fibers [2]. The thermal conductivity of an adsorbent has significance in gas-separation and storage applications, where large temperature gradients can be established during adsorption and desorption cycles. These temperature gradients can increase the process cycle time and hence reduce the overall efficiency of the separation process. Therefore, the increased thermal conductivity of CFCMS gives it a distinct advantage over existing activated carbons.

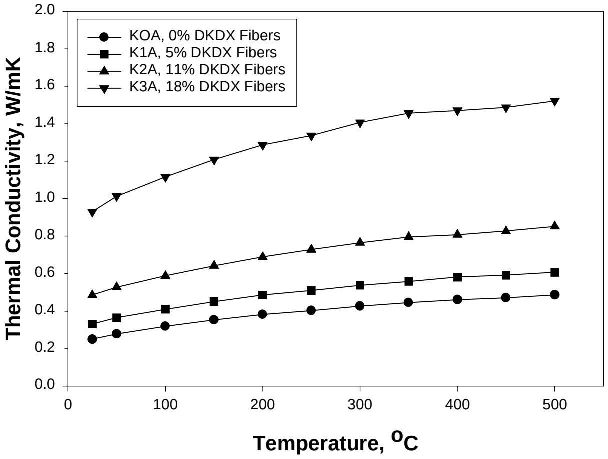

Fig. 7. Thermal conductivity of typical CFCMS samples.

In addition to being thermally conductive, the CFCMS monoliths are, by virtue of their continuous carbon skeleton, electrically conductive. This feature offers the potential of a separation system based on electrically induced desorption [1,2].

MICROPORE CHARACTERIZATION DATA

Micropore structure data determined from nitrogen adsorption isotherms on steam activated CFCMS with bulk densities in the range of 0.15 to 0.30 g/cm^3 are reported in Table 1. Similar data for higher-density CFCMS samples (0.4 to 0.8 g/cm^3) activated with CO_2 are reported in Table 2.

The data in Tables 1 and 2 clearly demonstrate that CFCMS can be activated to high BET surface areas and micropore volumes and that for a given burn-off the surface area and micropore volume are larger for the CO_2-activated CFCMS. Moreover, these data suggest an ability to tailor the microstructure of CFCMS and thus its adsorbent characteristics.

Table 1. Micropore characterization data for steam activated CFCMS at different burn-off levels

Burn-off (%)	BET surface area (m^2/g)	Micropore pore volume [t-method] (cm^3/g)	Mean DA micropore radius (nm)
9	512	0.21	0.68
18	1152	0.40	0.71
27	1962	0.65	0.75
36	1367	0.41	0.79

Table 2. Micropore characterization data for CO_2 activated CFCMS at different burn-off levels

Burn-off (%)	BET surface area (m^2/g)	DR micropore pore volume (cm^3/g)	Mean DR micropore radius (nm)
18	961	0.36	1.60
38	1608	0.60	2.00
56	2552	0.88	2.61
66	2660	0.92	2.73

ADSORPTION AND SEPARATION DATA

High-pressure adsorption isotherms for CO_2 and CH_4 are given for two samples of activated CFCMS in Fig. 8. The data in Fig. 8 suggest that CFCMS might provide an effective medium for the separation of CO_2 from gas mixtures containing CO_2 and CH_4. A breakthrough apparatus [1] was used to evaluate the suitability of CFCMS for this separation. A typical breakthrough plot for a CO_2/CH_4 mixture is shown in Fig. 9. The specimen was initially heated by the passage of a low-voltage electric current through the material and the desorbed gases were driven out by a He purge. The input gas was then switched to a 2:1 mixture of CO_2/CH_4 at a flow rate of 0.33 slpm. The outlet stream He concentration is seen to decrease to zero, and the CH_4 concentration increases rapidly (i.e., CH_4 breakthrough occurs). Adsorption of CO_2 occurs and therefore the concentration of CO_2 in the outlet gas stream remains low for a period of some 5 or 6 min, whereupon CO_2 breakthrough occurs. Adsorption capacity depends on the adsorbate temperature and partial pressure, but at ambient temperature and about 5 to 7 psig, the adsorption capacity of CFCMS is about 10 L of CO_2 per liter (bulk volume) of the CFCMS. The sample can be regenerated quickly and without any apparent temperature rise [1] by the passage of a low-voltage electric current.

The electrical regeneration of the CFCMS monolith is also illustrated in the H_2/H_2S breakthrough plot in Fig. 9. The breakthrough of the Ar and H_2 (not shown in Fig. 9) is almost instantaneous. However, the H_2S is adsorbed on the CFCMS and does not break through for 18 min (Fig. 9). When the CFCMS is totally saturated with H_2S (at about 42 minutes) the feed gas flow is stopped and an electrical voltage is

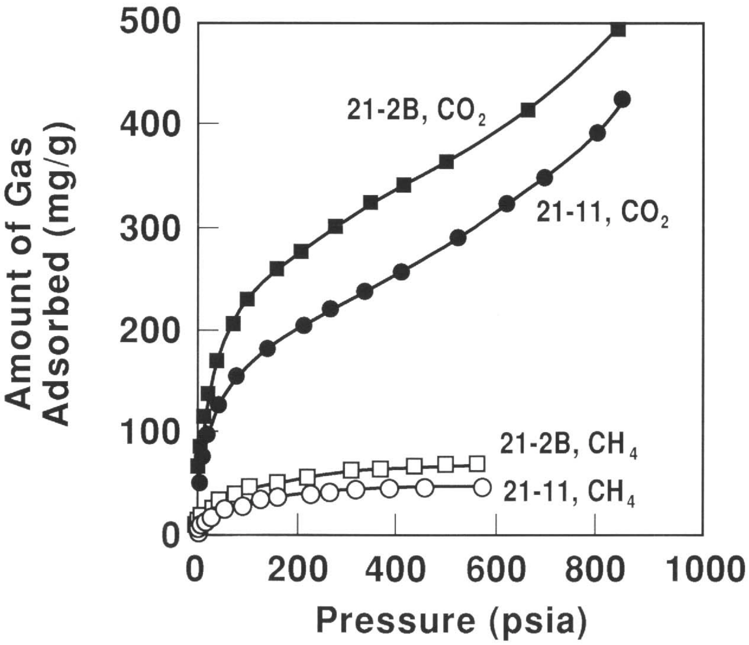

Fig. 8. High-pressure isotherms at 25°C of CO_2 and CH_4 for CFCMS monoliths.

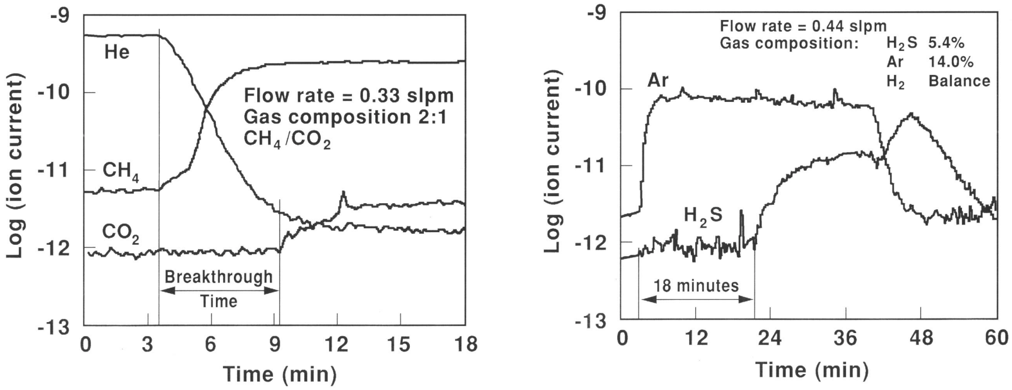

Fig. 9. A typical room temperature CO_2/CH_4 breakthrough plot (left) for a CFCMS sample with 9% burn-off and a typical H_2S breakthrough plot for a CFCMS monolith with18% burnoff.

applied to the sample. The H_2S is immediately desorbed from the CFCMS, as indicated by the rapid rise in H_2S concentration in the outlet gas stream. Complete desorption occurs over a period of 18 min, at which time the sample is completely regenerated.

The combination of CFCMS adsorbent monoliths and the passage of a low voltage electrical current provides the basis for a new unit operation separation system wherein the regeneration of the adsorbent CFCMS is achieved by electrical swing rather than by pressure or thermal swing.

ELECTRICAL SWING ADSORPTION

Figure 10 shows three adsorption/desorption cycles. In the first and second cycles (A and B in Fig. 10), desorption is caused by the combined effect of an applied voltage (1 v DC) and a He purge gas. In the third cycle (C in Fig. 10), desorption is caused only by the application of a He purge gas. It is evident from A, B, and C in Fig. 10 that desorption of the adsorbed CO_2 (regeneration) can be rapidly induced by the application of a direct current voltage. This is the basis of the ESA process. Bonding the fibers together with a carbon derived from a phenolic resin creates a continuous electrical circuit. The attractive forces, static electrical forces, or perhaps van der Waals forces between the carbon and the adsorbate are disrupted or perhaps reversed in polarity by the electric current. As a result, the adsorbed gases are released or repulsed from the micropore surfaces and desorption occurs.

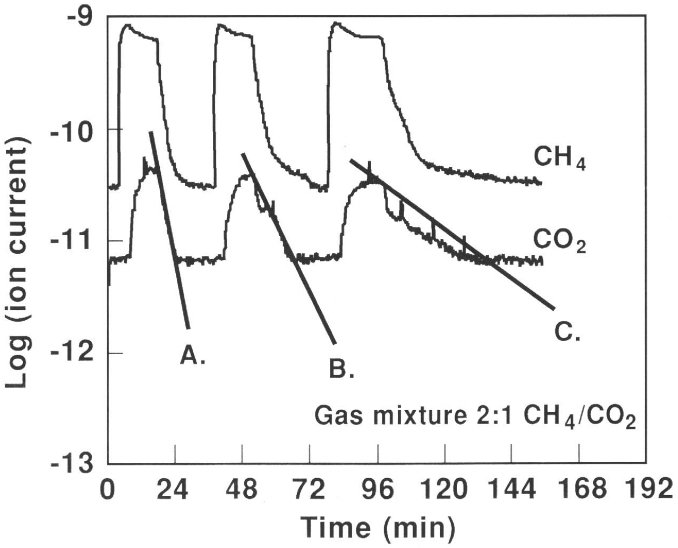

Fig. 10. CO_2/CH_4 breakthrough plots for a CFCMS sample with 10% burn-off, showing the benefit of electrically enhanced desorption: A. 1 volt, He purge @ 0.4 slpm, B. 1 volt, He purge @ 0.06 slpm, and C. 0 volts, He purge @ 0.06 slpm.

In the ORNL tests, most of the adsorbed gas is released in the first few seconds of current flow, followed by a slower, probably diffusion-controlled release of the balance of the gas. There is no indication of gross thermal heating of the mass of carbon during the initial rapid desorption phase. Current must be allowed to flow for several minutes to cause heating of the mass of carbon. Any ohmic heating during this phase is obviously offset by the cooling on desorption of the gas. To a first approximation, the energy requirement for desorption of a gas from CFCMS is equal to the heat of adsorption of that gas. ORNL researchers have suggested that the kinetics of desorption are such that it may be desirable in an operating system to limit the desorption phase to the initial rapid desorption. This would minimize cycle time but would have some impact on individual cycle adsorption capacity. In an adsorption-desorption cycle, the CFCMS would be saturated with CO_2 during the adsorption phase and approximately 80% of the CO_2 would be desorbed during the desorption phase, and then the cycle would be repeated. Such an approach would maximize the kinetics of the desorption phase and would minimize any ohmic heating of the CFCMS. On desorption of most (90 to 95%) of an adsorbed gas, continued electrical current flow causes heating of the monolith. This is shown in Fig. 11 where, in the absence of an adsorbed gas, the carbon is readily heated. However, as discussed previously [1], when an adsorbed gas is present on the CFCMS, the temperature is not observed to rise until virtually all of the adsorbed gas is desorbed.

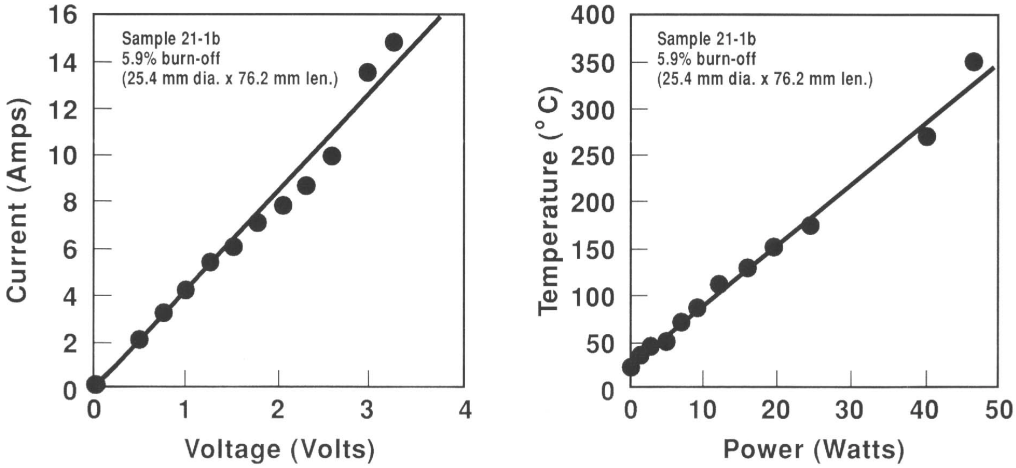

Fig. 11. The voltage-current relationship (left) and resistive heating curve (right) for a CFCMS monolith (18% burn-off, 2.5-cm diameter and 7.5-cm length).

ESA TEST PROGRAMS

The new experimental gas flow loop and ESA test system were described in Section 3 of this paper. A more comprehensive description of the gas flow loop and ESA cell can be found elsewhere [3].

The experimental program currently being pursued in the gas flow loop/ESA system includes the separation of CO_2 from natural gas, the separation of CO_2 from gas turbine exhaust streams, the removal of impurities from H_2-rich gas mixtures, and fuel and oxidant processing for fuel cell applications.

These test programs, complemented by earlier tests, are demonstrating the versatility of CFCMS over a wide range of process conditions. The CFCMS can reduce the concentration of CO_2 in air from its nominal value of about 350 ppm to much less than 50 ppm, and it can remove essentially all the CO_2 from natural gas containing about 33 % CO_2 by volume.

CONCLUSIONS

A novel carbon-fiber-based adsorbent monolith has been developed at ORNL. The adsorbent monolith referred to as CFCMS, shows considerable promise for the separation of gas mixtures, especially the removal of CO_2. The monolithic material has numerous advantages over conventional powdered and granular activated carbons. For example, CFCMS is more robust and does not settle or suffer attrition during use. Thus, the formation of channels such as those that develop in packed granular beds cannot form. Moreover, the continuous carbon structure of the monoliths imparts improved thermal conductivity and makes the monoliths electrically conductive. The principle of an ESA system based upon the electrical conductivity of CFCMS and its gas-adsorption properties has been demonstrated. The efficacy of CFCMS for separating CO_2 from CH_4 and other gas mixtures has been demonstrated. A new ESA test apparatus has been constructed at ORNL, and a test program aimed at further developing CFCMS-ESA for gas separation is currently being pursued.

REFERENCES

1. T. D. Burchell, R. R. Judkins, M. R. Rogers, and A. M. Williams, *CARBON* Vol. 35, No. 9, pp. 1279–1294 (1997).
2. T. D. Burchell, Porous Carbon Fiber-Carbon Binder Composites, Chapter 6 of *Carbon Materials for Advanced Technologies*, T. D. Burchell, Editor, pp. 169–203, Pergamon, 1999.
3. T. D. Burchell, in *Fossil Energy Program Annual Progress Report for April 1997 Through March 1998*. **ORNL-6943**, (1998), pp. 45–50.

ACKNOWLEDGMENTS

Research sponsored by the U.S. Department of Energy, Office of Fossil Energy, Advanced Research Materials Program under contract DE-AC05-00OR22725 with UT-Battelle, LLC, at Oak Ridge National Laboratory.

THE INFLUENCE OF BORON AND SILICON IN IMPROVING THE OXIDATION RESISTANCE OF Mo_5Si_3

P. F. Tortorelli, B. A. Pint, K. L. More, A. J. Thom,* and M. Akinc*
Oak Ridge National Laboratory
Oak Ridge, Tennessee 37831-6156
***Ames Laboratory and Iowa State University**
Ames, Iowa 50011

INTRODUCTION

Silicides can provide exceptional high-temperature corrosion resistance under oxidizing and sulfidizing conditions characteristic of many fossil energy environments and thus are potential candidate materials for protective coatings. It was previously reported that the addition of boron to Mo_5Si_3 results in substantial improvement in high-temperature oxidation resistance.[1,2] Using similar alloys based on the Mo_3Si-T1-T2 and $MoSi_2$-T1-MoB phase regions as well as Mo_5Si_3 without B, this boron effect was investigated under thermal cycling conditions (1200°C, oxygen, 1-h cycles). The ongoing objective of this work is to develop a better understanding of the effects of boron, silicon, and phase distribution on oxidation behavior of Mo-Si-B systems, particularly in the context of what we know regarding high-temperature environmental reactions of Si-based materials and multiphase alloys. This information can then be used as input into the design of Mo-Si systems for high-temperature applications in advanced fossil energy systems

EXPERIMENTAL APPROACH

Four Mo-Si-B alloys and undoped Mo_3Si_5, produced at Ames Laboratory, were oxidized (see Fig. 1 and Table 1). Molybdenum disilicide ($MoSi_2$) was also examined for comparison as it typically shows excellent oxidation resistance at temperatures greater than 800°C.[3] Automated cyclic oxidation exposures were conducted in dry, flowing O_2 at 1200°C using a cycle consisting of 60 min at temperature and 10 min out of the furnace. Specimens were attached to alumina rods with Pt-Rh wires and mass changes were measured after 1, 5, 20, 40, 60, 80, and 100 cycles and then every 100 cycles using a Mettler model AG245 balance.

After oxidation, selected specimens were examined by optical and backscattered electron imaging of polished cross sections as well as by electron probe microprobe analysis (EPMA). In two cases, scanning transmission electron microscopy (STEM) was used to image cross-sectional specimens fabricated using the focused ion beam (FIB) technique.[4]

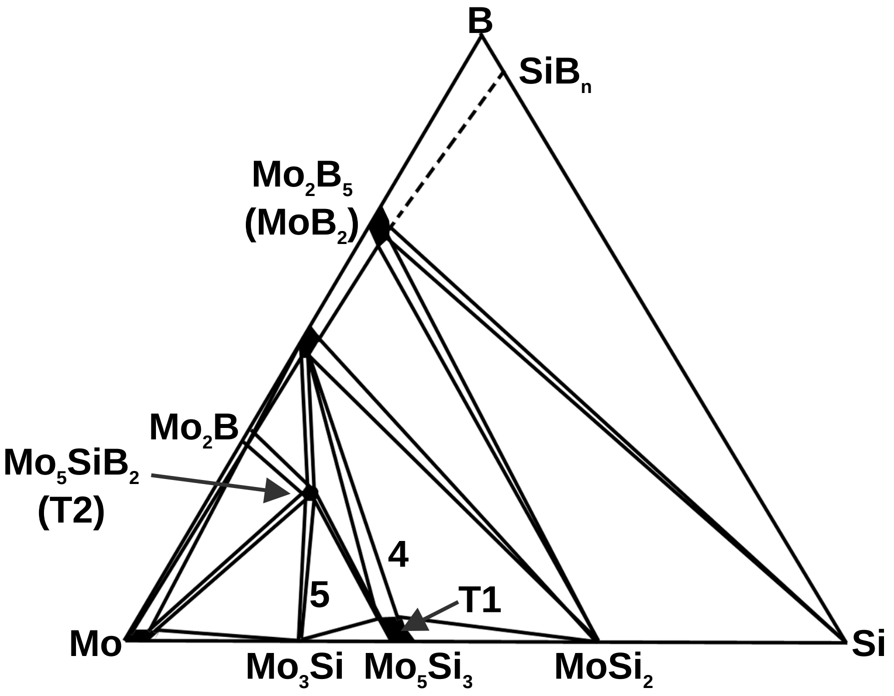

Fig. 1. A schematic Mo-Si-B phase diagram based on Nowotny et al., 1957. The numbers 4 and 5 show the compositions of the alloys so designated in Table 1.

Table 1. Compositions studied

Alloy	Phase(s)
1	Mo_5Si_3
2	$Mo_5Si_3B_x$ (T1)
3	$Mo_5Si_3B_x$ (T1)
4	T1, MoB, $MoSi_2$
5	T1, Mo_5SiB_2 (T2), Mo_3Si
6	$MoSi_2$

RESULTS

The mass changes measured for $MoSi_2$, Mo_3Si_5, and the Mo_3Si_5-B alloys under cyclic oxidation conditions at 1200°C are shown in Fig. 2. There was a clear differentiation in oxidation behavior among the different compositions. The multiphase alloys (4 and 5, see Table 1) showed substantially better cyclic oxidation resistance than the T1 and Mo_5Si_3 compositions. Of alloys 4 and 5, the T1-MoB-$MoSi_2$ composition performed significantly better under the cyclic oxidation conditions (Fig. 3). It showed an initial mass loss but then a slow mass gain comparable to $MoSi_2$. In contrast, the T1-T2-Mo_3Si (alloy 5) showed a greater initial mass loss followed by a less rapid, but continuing decrease in mass. Thus, it is not

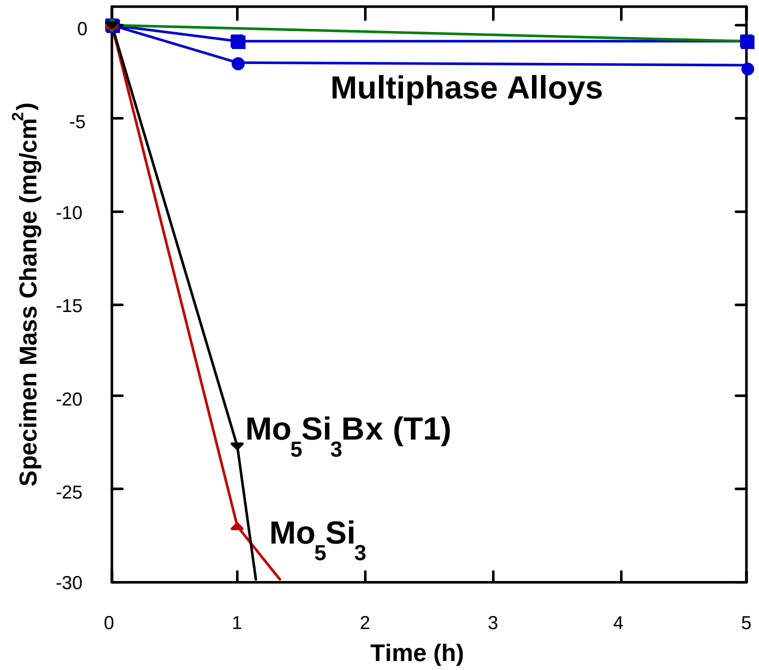

Fig. 2. Specimen mass change versus time for oxidation at 1200°C in dry air.

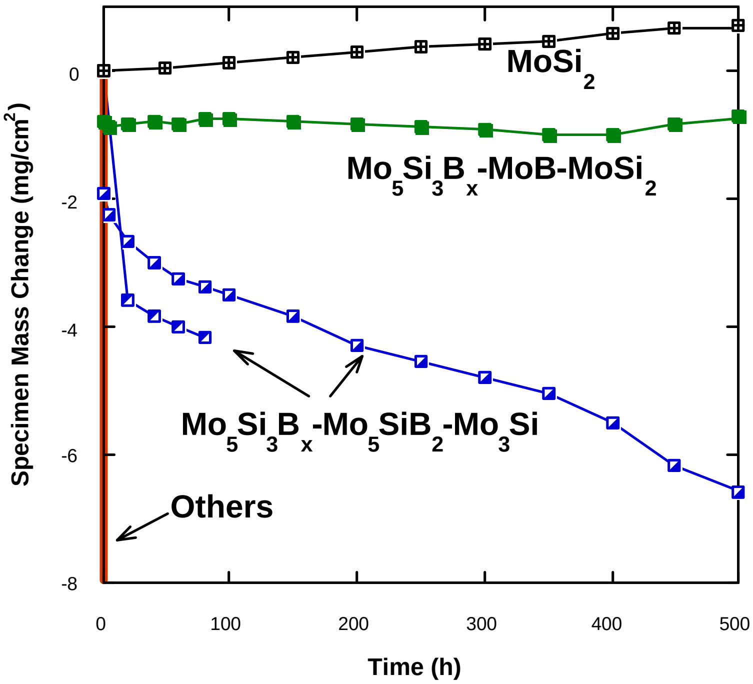

Fig. 3. Specimen mass change versus time for oxidation at 1200°C in dry air.

only the presence of boron but also the multi-phase structure of the Mo-Si-B alloys that leads to improved oxidation resistance under these conditions.

Imaging of polished cross sections of MoSi$_2$, T1-MoB-MoSi$_2$, and T1-T2-Mo$_3$Si clearly showed increasing oxidative degradation, respectively and thus was consistent with the gravimetric results. As shown in Fig. 4, the MoSi$_2$ formed a thin crystalline silica layer (as determined by transmission electron microscopy) that provided oxidation protection throughout the 500 1-h thermal cycles at 1200°C. The T1-MoB-MoSi$_2$ showed a substantially nonuniform thicker reaction product after similar exposure (Fig. 4b).

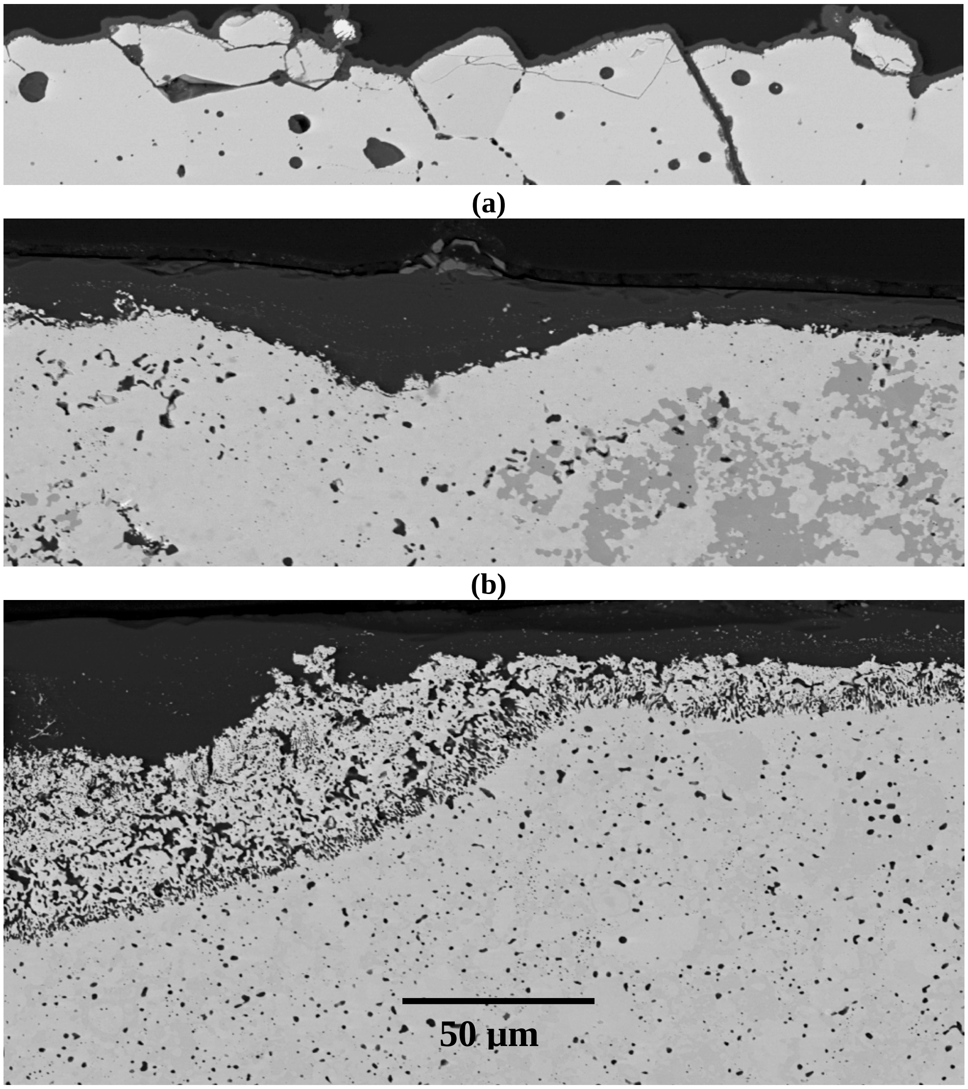

(a)

(b)

(c)

Fig. 4. Polished cross sections of specimens exposed for 500 h (500 cycles) at 1200°C in flowing air. (a) MoSi$_2$ (b) Mo$_5$Si$_3$B$_x$-MoB-MoSi$_2$ (c) Mo$_5$Si$_3$B$_x$-MoSiB$_2$-Mo$_2$Si

Scanning transmission electron microscopy of a cross section revealed a thin silica layer under a thicker glassy zone (Fig. 5). The development of this underlying silica, presumably promoted by the initial preferential oxidation of Mo and B (leading to Si enrichment), can explain the protective behavior (low oxidation rate) observed after approximately 150 h (Fig. 3).

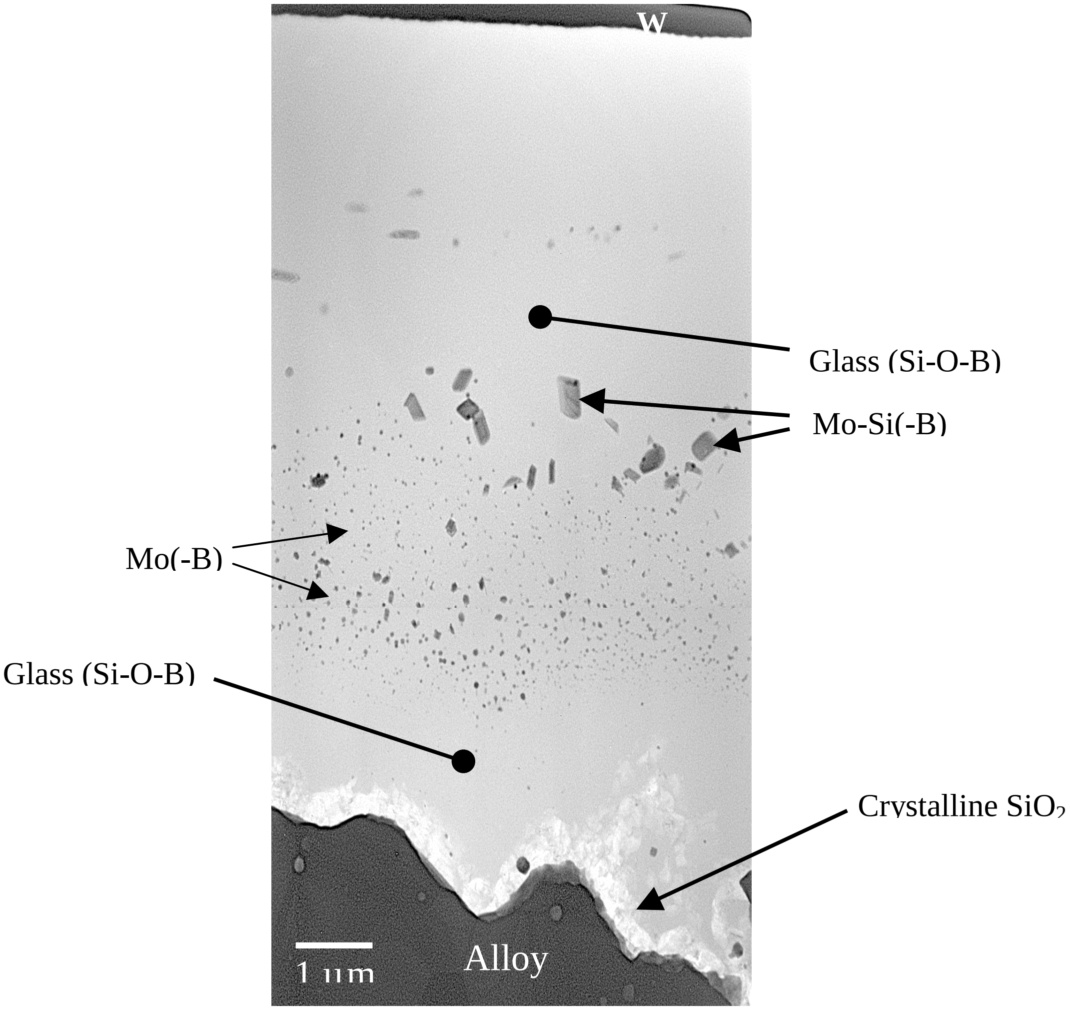

Fig. 5. Scanning transmission electron micrograph of reaction product on $Mo_5Si_3B_x$-MoB-$MoSi_2$ after 500 h (500 cycles) at 1200°C in dry air. (Tungsten coating protects surface during FIB milling.)

A continuous silica layer did not form on the T1-T2-Mo_3Si alloy (Fig. 4c). Rather, a thick outer glassy layer accompanied by substantial subsurface (internal) oxidation to form dispersed SiO_2 was observed (Fig. 6). Such reactions are to be expected when there is not sufficient Si available to form a continuous protective film of silica. The T1-T2-Mo_3Si phase assemblage (Fig.1) does not contain a phase with sufficient Si so as to act as a source for the development of protective silica under oxidizing

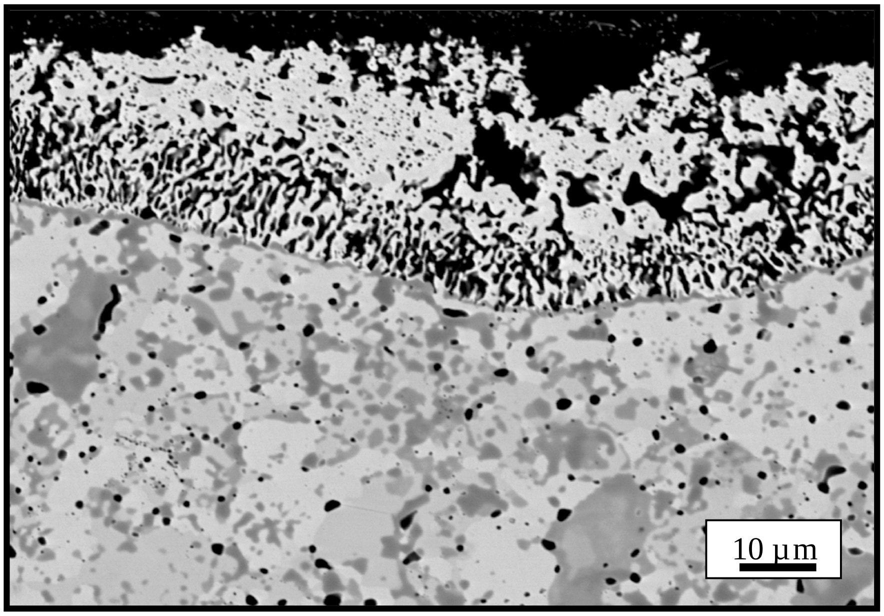

Fig. 6. Backscattered electron micrograph of $Mo_5Si_3B_x$-$MoSiB_2$-Mo_3Si after 500 h (500 cycles) at 1200°C in dry air.

conditions. In contrast, the $MoSi_2$ phase of the alloy 4 composition (Table 1) can act in this manner. Therefore, the present results indicate that Si content, and its distribution in the alloy, is also an important consideration in determining the oxidation resistance of these Mo-Si-B compositions.

SUMMARY

Using Mo-Si-B alloys based on the Mo_3Si-T1-T2 and $MoSi_2$-T1-MoB phase regions as well as Mo_5Si_3 without B, the boron effect was demonstrated under thermal cycling conditions (1200°C, oxygen, 1-h cycles). Scanning and transmission electron microscopy showed that boron not only helped by promoting rapid glass formation even in the presence of thermal cycling but by changing the phase distribution. Furthermore, the amount of Si was critically important in setting a phase assemblage that more readily promoted the formation of a protective silica-containing product, thus improving oxidation resistance.

REFERENCES

1. M.K. Meyer and M. Akinc, *J. Am. Ceram. Soc.*, 79 (1996) 938–944.
2. M.K. Meyer and M. Akinc, *J. Am. Ceram. Soc.*, 79 (1996) 2763–66.
3. G. H. Meier and F.S. Pettit, *Mater. Sci. Eng. A*, 153 (1992) 548–60.

DEVELOPMENT OF MODIFIED ALLOY 803 WITH IMPROVED CREEP-RESISTANCE ABOVE 800°C

P. J. Maziasz and R. W. Swindeman (ORNL)
M. A. Harper and G. D. Smith (Special Metals Corp.)

INTRODUCTION

The objective of this Cooperative Research and Development Agreement (CRADA) project between Special Metals Corp. (formerly INCO Alloys International) and ORNL is to develop a modified version of alloy 803 with significantly improved creep-resistance at 650–800°C. INCOLOY 803 (Fe-25Cr-35Ni alloy) was developed in the mid-1990's as a higher-performance alternative to alloys 800H (Fe-20Cr-30Ni alloy) and 800HT [1]. ORNL had previously developed a unique scientific alloy development method based on precise design and control of fine carbides for high-temperature strength and increased matrix phase stability for very long-term aging resistance [2–4]. ORNL had used this methodology to develop high-temperature, ultrafine precipitate-strengthened (HT-UPS) versions of type 316 austenitic stainless steel and 800H austenitic stainless alloys with dramatically improved creep-resistance at 700–800°C in the late 1980's and early 1990's [3,4]. Therefore, this CRADA project was defined to combine these technologies and work together in order to develop a modified alloy 803 with significantly improved creep-resistance for advanced steam heat-exchanger tubing applications in fossil power plants. Another application that has evolved during this CRADA project is the need for much more oxidation/corrosion- and creep-resistant metal foils compared to type 347 austenitic stainless steel (Fe-17Cr-10Ni steel) for advanced microturbine recuperator (compact heat-exchanger) applications. High-temperature properties of modified alloy 803 foils indicate that it can be considered as a high-performance and yet cost-effective alternative to type 347 stainless steel for this application [5,6].

TECHNICAL PROGRESS

This CRADA project began in February of 1999, and was scheduled to last for 4 years. The overall plan was to go through several rounds of alloy development, with oxidation/corrosion as well as high-temperature mechanical properties screening. Alloy development included minor alloying additions or changes to design and control microstructure, as well as appropriately modified processing to further enhance the performance boost. The project to this point (about 2.5 years) has involved cost-share (funds-in plus in-kind funds) of greater than 1:1 relative to DOE Fossil Energy program funds.

The CRADA began with the specification of 6 compositional modifications of alloy 803, and 6 VIM heats were melted at Special Metals, and then hot-rolled into plate that was sent to ORNL for further processing. Heats will be designated by a number, indicating the 1st, 2nd, or 3rd alloying iteration, and a letter (A-F) to designate the particular alloy within that round. A second round of 3 alloys were melted based on alloys 1B and 1C of the first round, and then a third set of alloys was made based on alloy 2A. The hot-bands were hot-rolled and then cold-rolled and solution-annealed at several different temperatures at ORNL into 0.13 inch thick plate. The material was then sent to Special Metals, who made and tested oxidation/corrosion, tensile and creep-rupture specimens to screen the alloys. As part of a related effort on another program (EERE/DPG Advanced Microturbines), a portion of some of the better alloys was further processed into 0.004 inch thick foil, and specimens were laser-cut for creep-rupture testing at ORNL.

The base composition of standard alloy 803 is 25Cr-35Ni-1Mn-0.6Ti-0.5Al-0.7Si-0.07C (bal. Fe). Modifications were made to this composition that totaled less than 5 wt. of minor alloying element additions or changes. Tensile testing indicated that all of the 1st round alloys were somewhat weaker than the standard alloy 803 at 21–900°C, but the modified alloys 1B and 1C had significantly better creep-rupture life at 816°C and 10 ksi, and their performance boost was even further enhanced by careful changes the thermo-mechanical processing (Fig. 1). Similar modified processing had only a small effect

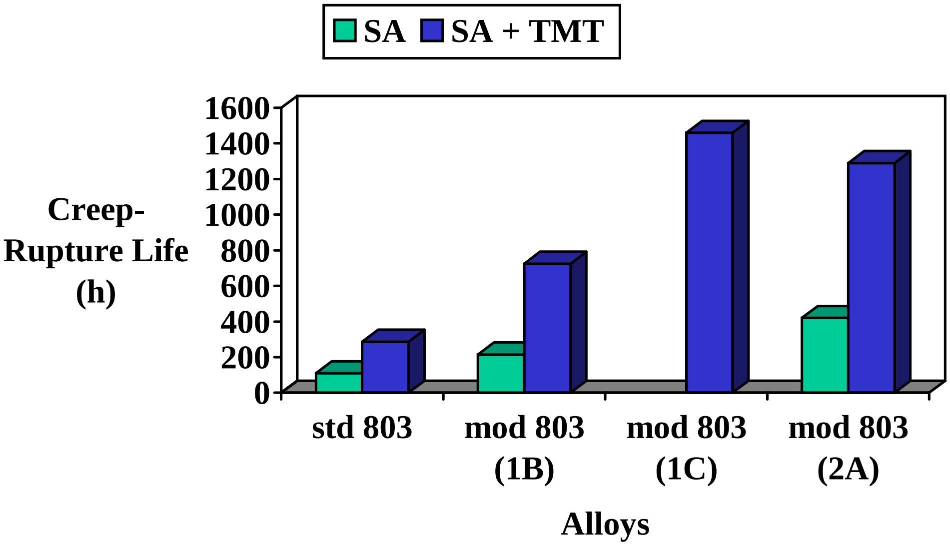

Fig. 1. Creep rupture life (h) at 816°C and 10 ksi for specimens of standard or modified 803 alloys processed into plate and tested in either the solution-annealed (SA) or a SA plus thermomechanical treatment (TMT) condition. Both alloy modification and processing modification boost the performance relative to the standard alloy.

on improving the creep-rupture of the standard alloy 803. Metallography revealed that the modified 1st round alloys all had as-processed grain sizes in the 10–40 μm range, and analytical electron microscopy revealed that alloys 1B and 1C best satisfied the initial microstructural design target of austenite plus a small or minimum dispersion of MC carbides with no $M_{23}C_6$ (truly stabilized). A series of oxidation, carburization and sulfidation screening tests revealed similar or slightly less resistance of the modified alloys relative to standard alloy 803.

Alloys 2A, 2B and 2C were developed based on further additions to alloys 1B and 1C. Alloy 2A showed a larger improvement in creep-rupture resistance at 816°C and 10 ksi in the SA processing condition relative to alloy 1B or the standard 803, and a thermomechanical processing boost similar to alloy 1C (Fig. 2). The oxidation/corrosion behavior of the 2nd round alloys was similar to or better than

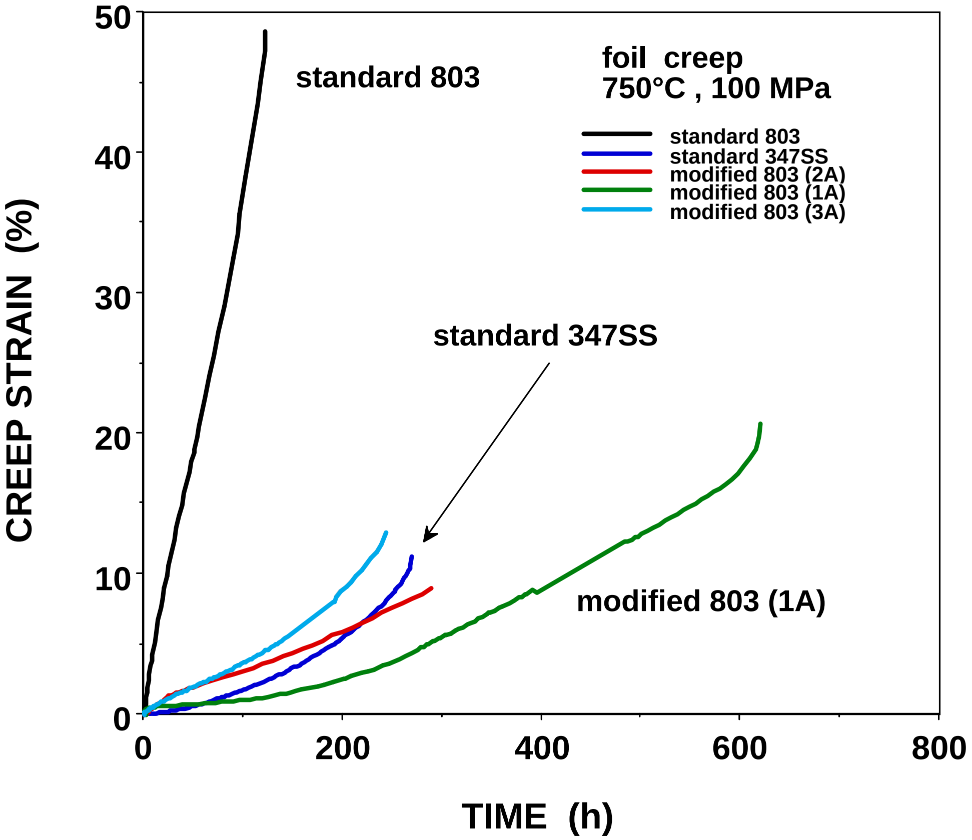

Fig. 2. Creep strain versus time plots for creep-rupture tests at 750°C and 14.5 ksi of 0.004 inch thick foils of 347 stainless steel and various heats of alloy 803. Alloy designations here are a little different than in-text, with 1A=1B, 3A=1C, but 2A=2A. While the standard 803 has much less creep-resistant than 347 stainless steel, alloy 1B has significantly better creep-resistance.

the first round alloys. A 3rd and final round of alloys was produced based on alloys 2A and 2B, and these have been processed, and will be tested shortly. Sulfidation screening reveals that the 3rd round alloys show a significant improvement in resistance relative to standard 803.

Finally, creep-rupture testing at 750°C and 14.5 ksi to screen foils of the modified 803 alloys was also done at ORNL to compare them to type 347 stainless steel for advanced microturbine recuperator applications. The standard alloy 803 was significantly weaker than 347 stainless steel, and alloy 1B was much better, while alloys 1C and 2A are similar to 347 stainless steel. For microturbine recuperator applications, the modified 803 (1B) stainless alloy is attractive because it has much better oxidation/corrosion resistance that 347 stainless steel (due to more Cr), and has a lower coefficient of thermal expansion. For this application, modified alloy 803 is much less costly than alloy 625, which has been the high-performance alternate material considered for this application previously [7].

REFERENCES

1. P. Ganesan, J. A. Plyburn, and C. S. Tassen, “INCOLOY Alloy 803, a Cost Effective Alloy for High Temperature Service,” pp. 191–198 in *Heat-Resistant Materials II*, eds. K. Natesan, P. Ganesan and G. Lai, ASM-International, Materials Park, OH (1995).
2. P. J. Maziasz, “Developing and Austenitic Stainless Steel for Improved Performance in Advanced Fossil Power Facilities,” *Journal of Metals*, 41 (July 1989) 14–20.
3. R. W. Swindeman and P. J. Maziasz, “The Mechanical and Microstructural Stability of Austenitic Stainless Steels Strengthened by MC-Forming Elements,” pp. 33–42 in *Creep: Characterization, Damage and Life Assessment*, ASM-International, Materials Park, OH (1992).
4. R. W. Swindeman and P. J. Maziasz, “The Effect of MC Forming Additions and 10% Cold Work on the High Temperature Strength of 20Cr-30Ni-Fe Alloys,” pp.251–259 in *Heat-Resistant Materials*, eds. K. Natesan and D. J. Tillack, ASM-International, Materials Park, OH (1991).
5. M. A. Harper, G. D. Smith, P. J. Maziasz, and R. W. Swindeman, “Materials Selection for High Temperature Metal Recuperators,” paper to be published in proceedings of ASME Turbo Expo 2001, to be held June 4–7, 2001 in New Orleans, LA.
6. P. J. Maziasz and R. W. Swindeman, “Selecting and Developing Advanced Alloys for Creep-Resistance for Microturbine Recuperator Applications,” paper to be published in proceedings of ASME Turbo Expo 2001, to be held June 4–7, 2001 in New Orleans, LA.
7. M. E. Ward, “Primary Surface Recuperator Durability and Applications,” Turbomachinery Technology Seminar paper TTS006/395, Solar Turbines, Inc. San Diego, CA, 1995.

FABRICATION TECHNOLOGIES FOR FUEL CELL APPLICATIONS

M. L. Santella, R. R. Judkins, and V. K. Sikka
Oak Ridge National Laboratory
Oak Ridge, TN 37831

INTRODUCTION

Fuel cells are continuously-fueled batteries that offer considerable potential as efficient, flexible, clean devices for production of electrical energy. There are four major types of fuel cells, but of these, solid oxide fuel cells (SOFCs) require the highest operating temperatures (600–1000°C) and represent the most efficient way to generate power from fossil fuels. The SOFC relies primarily on hydrogen as a fuel gas which is obtained by decomposing (reforming) natural gas or other fuel gas through a thermocatalytic process.

Research and development activities for SOFC materials are very active. However, the optimum materials based on current understanding are well defined. Yttria-stabilized zirconia (YSZ) is the preferred electrolyte material because of its high ionic conductivity, low electronic conductivity, and good chemical stability under normal operating conditions. Cathode materials must have the catalytic activity necessary to dissociate oxygen molecules, high electronic conductivity, and high oxidation resistance. Commonly used cathode materials are noble metals such as platinum and silver, and certain ABO_3 oxides such as $LaMnO_3$. Anode materials must have high electronic conductivity and high resistance to reducing conditions. Nickel and cermets of Ni+YSZ are commonly used for anodes. Other important components are interconnects that link adjacent cells together electrically and separate fuel and oxidizing gases, and the support structures for containment of cell stacks and the distribution of fuel, oxidizing and exhaust gases.

The operating conditions of SOFC units create an exceptionally harsh environment for the containment material. The containment and gas distribution system must simultaneously withstand the high temperatures (900–1000°C maximum), and the relatively unique combination of oxidizing and reducing conditions. Conventional austenitic alloys are commonly used for these components because they have acceptable resistance to either the oxidizing or reducing conditions in the desired temperature range. However, service experience indicates many austenitic alloys deteriorate more rapidly in the combined SOFC conditions than they would deteriorate independently in either of the individual oxidizing or reducing environments. The rapid deterioration of the containment is a major concern in limiting the SOFC unit life. Consequently, there is strong interest in identifying and constructing containments from alternate alloys.

Preliminary testing indicates that Fe_3Al alloys are much more resistant to the SOFC operating conditions than austenitic alloys such as stainless steels. Further evaluations of the performance and fabrication of SOFC containments from Fe_3Al alloys are being done under this task.

Materials and Experimental Details

The composition of the alloy made for this study is given in Table 1. An ingot of the alloy was prepared by air melting under a cover of Ar and poured into a 3.5-in.-diameter graphite mold. The ingot was subsequently extruded at 1100°C into a bar with a cross section of 2 in. × ¾ in. Pieces of the extrusion were prepared for subsequent hot rolling by grinding the surfaces to remove defects from the casting and extrusion processes. The extrusion coupons were reheated to 1100°C and then hot rolled to a thickness of 0.01 in. The thickness reductions taken during this sequence were on the order of 20%, with three cross rolling passes to increase the width of the rolled material. After each rolling pass the coupons were reheated for 5 min in a furnace held at 1100°C.

Table 1. Analyzed composition of Fe_3Al alloy

	Heat #17838, analyzed composition				
	Fe	**Al**	**C**	**Cr**	**Zr**
Weight %	Bal.	16.0	0.014	3.62	1.06
Atomic %	Bal.	28.3	0.06	3.30	0.6

At this point the surfaces of the rolled sheets were again cleaned and the sheets were reheated to 1000°C and hot rolled to a thickness of 0.02 in. These sheets were cleaned again and finished to a hot rolled thickness of 0.01 in. The sheets were annealed at 700°C for stress relieving and then quenched in an oil bath. Lastly, they were given a small reduction by cold rolling to flatten. A photograph of the finished sheets is shown in Fig. 1. The finished sheets were approximately 5-in.-wide × 0.0085-in.-thick.

A portion of this sheet material is being used to determine the welding characteristics of the alloy. Two heat treatments and two cleaning methods were used to prepare coupons for welding. The heat treatments were a stress relief treatment of 1 h at 700°C and a recrystallization treatment of 1 h at 850°C. Prior to welding, surface oxides were removed from the sheet coupons either by grinding or by a chemical cleaning procedure. The chemical cleaning consisted of immersion for 5–10 min in a saturated aqueous solution of iron chloride, $FeCl_3$, that was heated to about 80°C. The appearance of the Fe_3Al alloy after chemical cleaning is shown in Fig. 2. Chemical cleaning was very effective for removal of the surface oxide, but it also reduced the thickness of sheets by an additional 0.001–0.002 in.

Full penetration welds were made on the sheets using either gas-tungsten-arc welding (GTAW) or laser welding (LBW). Both types of welds used Ar gas shielding on the front and back sides of the sheet

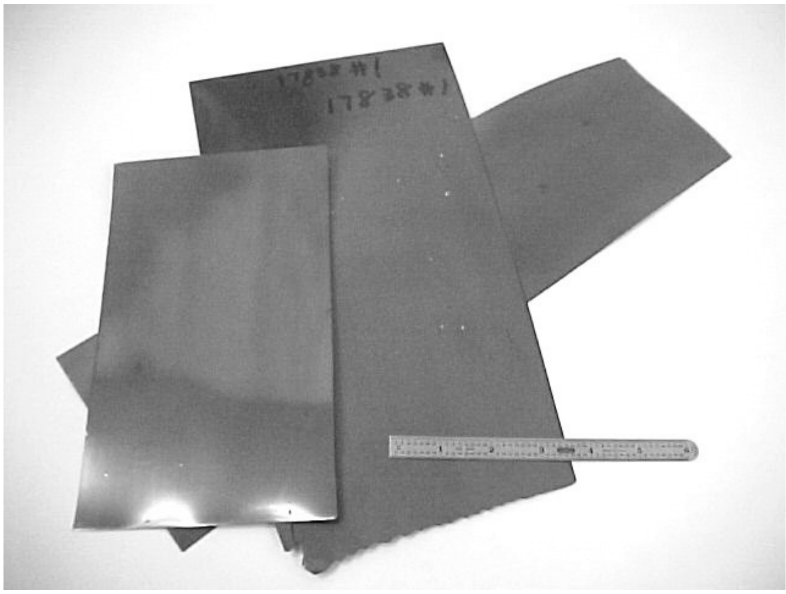

Fig. 1. Fe_3Al alloy sheets after final cold rolling.

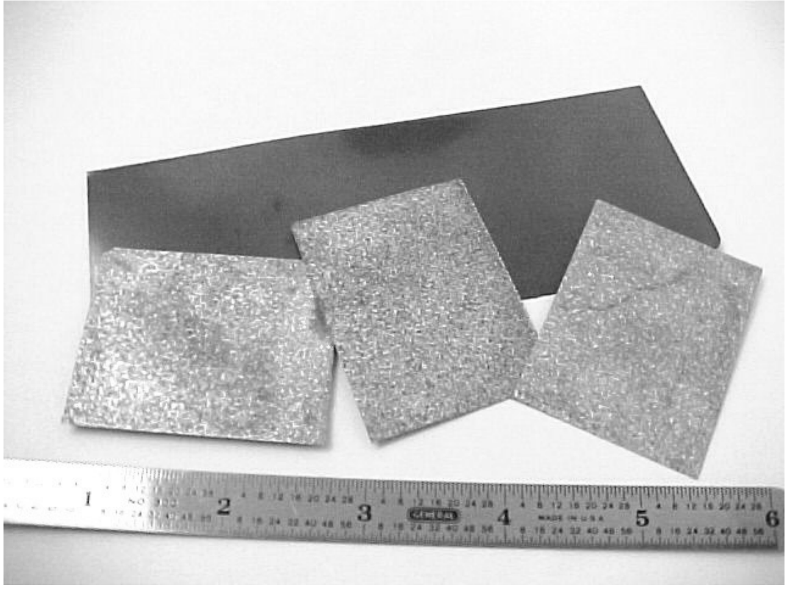

Fig. 2. Appearance of Fe_3Al alloy sheets before and after cleaning in $FeCl_3$ solution.

specimens. In both cases, the sheets were moderately restrained in stainless steel fixtures to maintain the position of the sheet specimens relative to the welding sources. No preheat or post heat was applied to either type of weld. The GTA welding was done at 2–5 A using an arc gap of 0.04 in. at a welding speed of 10 in./min. Laser welding was done with a continuous wave Nd-YAG laser operated at ~200 watts using a welding speed of 10 in./min. The LBW source was adjusted for sharp focus at the sheet specimens surfaces with a lens angle of 20° from vertical. A sheet specimen containing a LBW is shown in Fig. 3.

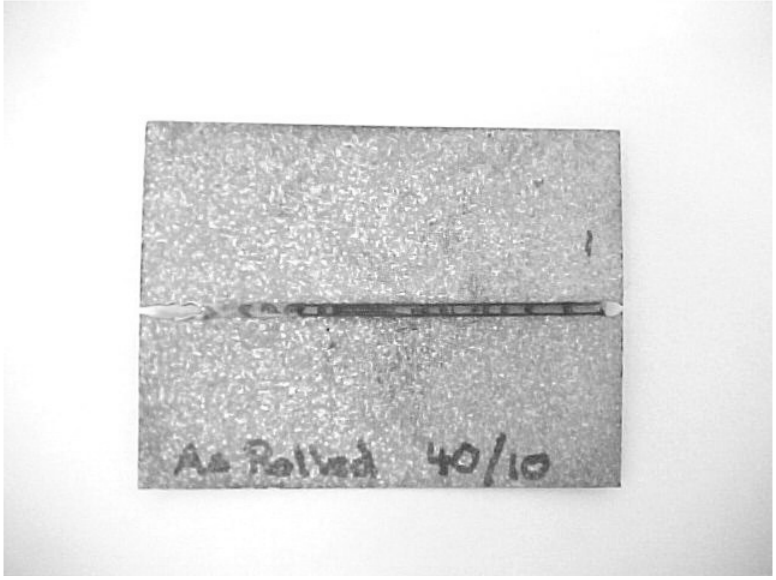

Fig. 3. Fe_3Al sheet specimen containing a laser weld bead. The specimen width is 2 in.

Specimens from the welds are examined metallographically. Also, thermodynamic analysis using the ThermoCalc® is being used to predict the microsegregation patterns of alloying elements in the weld fusion zones.

RESULTS AND DISCUSSION

Initial GTA welding on as-cold-finished sheet specimens suggested that crack-free welds can be made on this Fe_3Al alloy. Examination of the as-welded surfaces at low magnification indicated that no centerline cracks or transverse cracks developed in these specimens. Welding produced considerable distortion of the specimens because of the relatively high thermal expansion of the Fe_3Al alloys. The stresses associated with this distortion did not contribute to cracking, but the distortion did complicate preparation of metallographic specimens. Metallographic specimens were prepared to view the welds from the perspective of the sheet surfaces. However, distortion adjacent to the weld beads coupled with the thinness of the sheets prevented the preparation of specimens in which good overall views of weld, heat-affected zones, and base metal could be examined. Nevertheless, some microscopic examination of GTA welds was possible.

The microstructure near the fusion line of a GTA weld made on the cold-finished sheet is shown in Fig. 4. A distinct microsegregation pattern developed in the fusion zone, and epitaxial growth of grains at the fusion line into the fusion zone is clearly visible. The grain structure in the heat-affected zone was somewhat different than that of the base metal. Grains in the heat-affected zone have undergone growth.

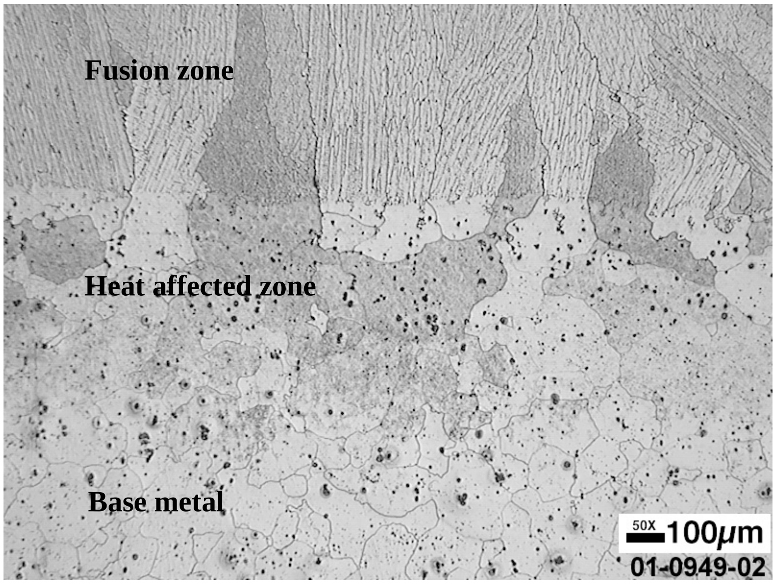

Fig. 4. Microstructure near fusion line of GTA weld in Fe_3Al alloy sheet.

Also, the contrast in heat-affected zone grains is different suggesting that precipitation or redistribution of phases occurred in this region.

Details of the microstructure at the fusion line are shown in Fig. 5. The microsegregation pattern produced by the non-equilibrium solidification conditions associated with welding is evident. The darker etching features occur in the interdendritic regions of the solidification microstructure. The fusion line boundary between melted and unmelted alloy is clear, and an isolated pocket of melted material slightly removed from the fusion line (liquation) is also visible. The liquation is probably associated with a precipitate phase in the base metal, and under certain circumstances could be a concern for producing cracks during welding.

A comparison of microstructures in the base metal and the heat-affected zone is shown in Fig. 6. The base metal clearly contains a large number of second-phase particles. In addition to these large particles the metal in the heat-affected zone also contains a distribution of much finer precipitates. The finer particles must either be precipitates that already existed in the base metal and were coarsened by local heating during welding, or they are particles that precipitated during the welding process. Additional study will be required to determine the exact nature and possible influence of these particles.

Thermodynamic modeling (ThermoCalc®) is being used to assist in the analysis of the microsegregation in the weld fusion zones by describing alloy element redistribution during the solidification process. The effects of alloy element redistribution on the freezing temperature range of the Fe_3Al alloy are shown in Fig. 7 where equilibrium conditions are compared to those of a Scheil (non-

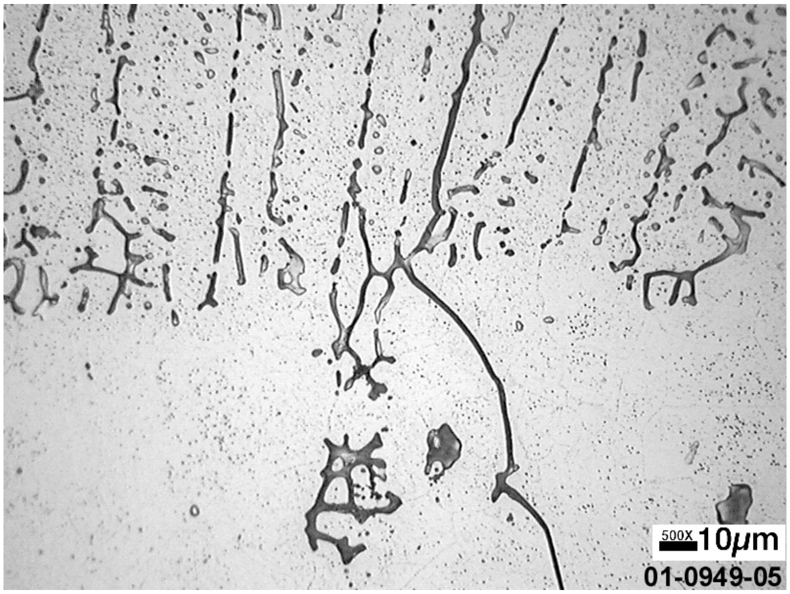

Fig. 5. Details of weld microstructure at fusion line.

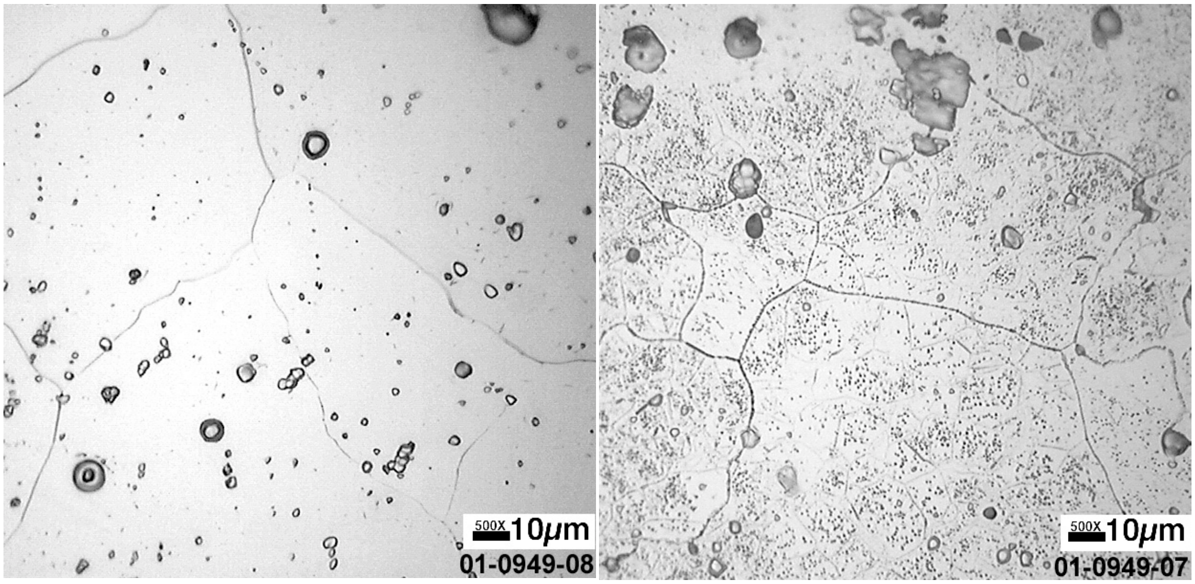

Fig.6. Microstructure of Fe_3Al alloy sheet in the base metal (left) and heat-affected zone (right).

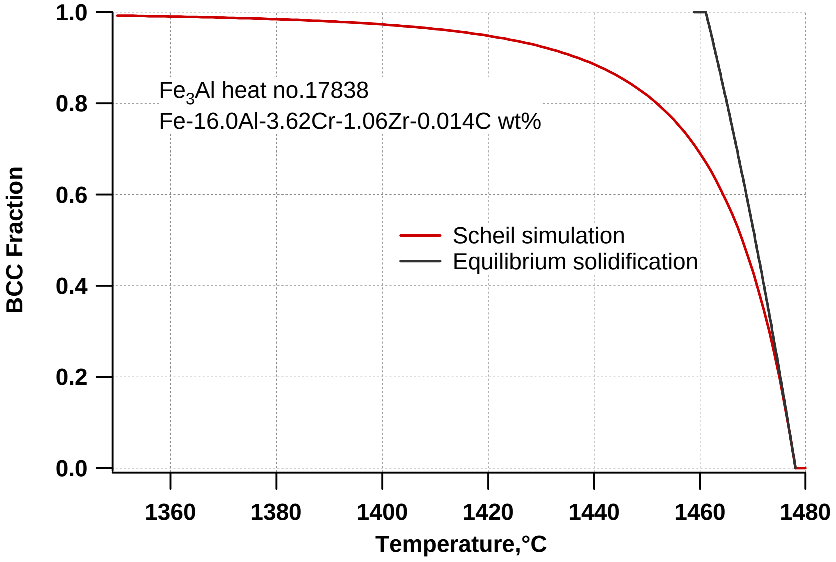

Fig. 7. Effect of microsegregation during solidification on the freezing temperature range of Fe_3Al alloy.

equilibrium) analysis. The equilibrium conditions assume that there is complete diffusion of alloying elements in both the liquid phase and the solid (BCC) phase during solidification. For the equilibrium conditions, the predicted freezing temperature range is 1478–1461°C. The Scheil simulation assumes that the composition of the solid phase that is forming at any temperature is given by that of the solidus line, but that there is no diffusion in the solid. In contrast, complete diffusion in the liquid phase is assumed. The overall effect of the Scheil assumptions is to enrich the liquid phase with alloying elements and to make it stable over a wider temperature range than would exist for equilibrium conditions. The freezing temperature range predicted by the Scheil analysis, 1478–1104°C, is much larger than the equilibrium freezing temperature range.

The Scheil conditions predict the overall trend of microsegregation pattern that is typically observed in welds and cast alloys. However, the Scheil analysis represents a limiting condition because usually some diffusion of alloying elements will occur in the solid phase during solidification. In general, the alloy element redistribution patterns predicted by the Scheil analysis more closely represent actual conditions than does the assumption of equilibrium conditions. A comparison of Al microsegregation for either equilibrium or Scheil conditions is shown in Fig. 8. Because complete diffusion is assumed for equilibrium conditions, the Al concentration is predicted to be the same everywhere in the microstructure, 16 wt%. In contrast, imposing the non-equilibrium Scheil assumptions results in a microsegregation pattern where Al can vary from 14.3 wt% at the start of solidification (corresponding to dendrite cores) to

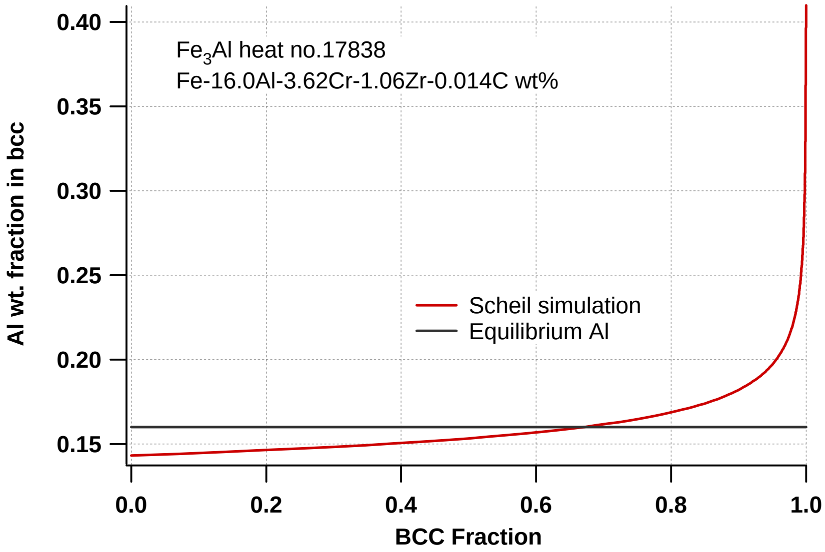

Fig. 8. Comparison of the Al microsegregation pattern in Fe_3Al for assumptions of equilibrium solidification and solidification under Scheil assumptions.

39.3 wt% at the end of solidification (corresponding to the interdendritic regions). Actually, the Scheil analysis also predicts that a small amount of the compound $FeAl_2$ forms during the final stages of solidification as the fraction of solid BCC phase approaches unity. Examination of the weld fusion zone microstructure in Fig. 5 suggests that this phase may actually be present. Analysis of microsegregation will continue and eventually it will be correlated with metallographic analyses of weld microstructures. The microsegregation in the weld fusion zones is important because it will influence the ease with which this Fe_3Al alloy can be welded, as well as the mechanical and corrosion properties of the welds.

SUMMARY

An Fe_3Al alloy was fabricated into 0.01-in.-thick sheets by hot extruding and then rolling an air-melted ingot. Coupons taken from the sheets were used to evaluate the welding characteristics of the alloy. The initial evaluation indicates that satisfactory welds can be made in the sheets by either gas-tungsten-arc welding or by laser welding. Some coupons were chemically cleaned in an aqueous solution of $FeCl_3$ prior to welding, but there was no clear advantage of this method over grinding to remove surface oxides. Thermodynamic modeling was used to predict the microsegregation pattern of Al in this multi-component alloying system. Predictions indicate that microsegregation significantly enlarges the freezing range of the alloy, and causes substantial variations of Al concentration in the weld fusion zone microstructures.

LOW-COST MANUFACTURING OF FUEL CELLS

T. R. Armstrong, B. L. Armstrong, M. E. Forrest, P. G. Engleman, D. C. Harper,
C. A. Walls, and C. A. Blue

INTRODUCTION

Solid oxide fuel cells (SOFC) have been under development for more than 30 years and are on the verge of commercialization. The projected initial costs for the fuel cell stack are approximately $1000/kW while the allowable fuel cell installed cost ranges from $700/kW to more than $1500/kW, depending on the market segment and size[1]. The largest contributors to the cost of the SOFC stack are materials costs, the fabrication method, and heat-treatment (sintering) time. When and if low-cost materials and fabrication methods are used, the amount of time required for heat-treatment becomes the dominate factor in the cost of the fuel cell.

A new method has been developed for densifing coatings on both planar and tubular metallic and ceramic supports. This process called high-density-infrared (HDI) transient-liquid coating (TLC) process has been developed to produce wear- and corrosion-resistant coatings on a variety of surfaces that are of commercial interest [2,3]. Infrared technology is used in a wide range of industrial applications. It is used in the electronics industry for drying solder resists, in food processing for browning and sterilization, in finishing for stoving and curing, in textiles for drying and sealing, in plastics for softening, in printing for drying, and in engineering for preheating and shrink fitting [4]. These types of equipment for the above applications are typically limited to 537 to 760°C.

Infrared heating has many advantages over other heating techniques. Infrared heating provides (1) an inherently clean non-contact heating method; (2) rapid response energy fluxes capable of heating rates in excess of 500°C/s (state-of-the-art equipment provides excellent spatial and tempered control which allows sample-only heating uni-directionally over large areas), (3) rapid power level changes [no thermal mass (plasma lamp)], and (4) rapid cooling rates due to the “cold wall” nature of the process in which only the sample is heated. The plasma lamp technology provides controllable temperature gradient processing due to flux densities of up to 3500 W/cm^2. Thus, infrared provides a versatile and flexible answer to heat transfer problems throughout the industrial spectrum [4] and it has recently been used to sinter YSZ on an anode support with the complete cycle time (heat-up, sintering, cool down) being reduced to less than 5 minutes. It is the purpose of this paper to briefly discuss this work.

HIGH DENSITY INFRARED (HDI) PROCESS

The HDI process utilizes a unique technology to produce extremely high-power densities of up to 3.5 kW/cm^2 with a single lamp, which is currently the most powerful one in the world (Fig. 1). Instead of

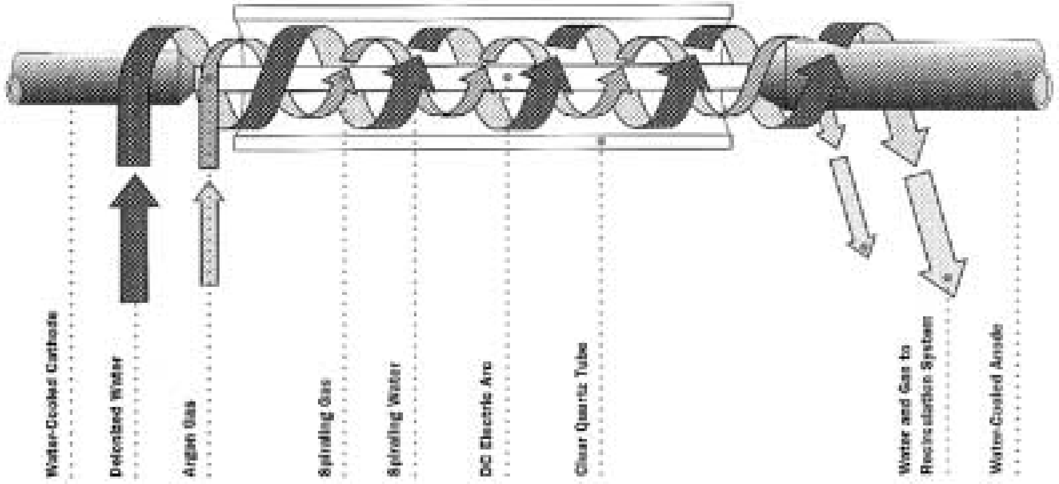

Fig. 1. Schematic of a high-power density plasma-arc lamp and the principles of operation.

using an electrically heated resistive element to produce radiant energy, a controlled and contained plasma is utilized.

The lamp consists of a 3.175-cm-diam quartz tube, which can be 10.16, 20.32, or 38.1 cm long. The lamp is sealed at the ends where the cathode and anode are located. Deionized water mixed with argon or nitrogen gas enters at the cathode side through high-velocity jets impinging at a given angle. Due to the high velocities and pressure, the de-ionized water is impelled to the wall of the quartz tube and spirals down the length of the tube in a uniform 2- to 3-mm-thick film. This water film serves two purposes: (1) to cool the quartz wall and (2) to remove any tungsten particulate that may be expelled from the electrodes. The gas moves in a spiral fashion through the center of the tube, and a capacitive circuit initiates the plasma. The plasma, which has a temperature in excess of 10,000 K, is stable and produces a radiant spectrum from 0.2 to 1.4 microns. The spectrum is primarily in the infrared (0.78 to 1.00 µm), although substantial energy is released in the visible wavelength, similar to the appearance of natural sunlight in energy distribution and color rendition. In contrast, the spectrum at a CO_2 laser with wavelengths near 10.6 microns is absorbed with much lower efficiency. The powder coatings discussed here are highly absorbing because the open areas act like black bodies.

The lamp has a typical life of approximately 1200 hours, and failure occurs in the anodes and cathode, which are inexpensive and can be changed in approximately 15 min. Furthermore, the lamp has a consistent spectral output independent of lamp life and power level. The lamp is typically configured with a reflector to produce a line focus or an area of uniform irradiance.

The HDI lamp is mounted on a large six-axis robotic manipulator. A state-of-the-art PC based robotic controller is utilized for precise lamp movement. This controller is capable of using computer-aided drawing data files of large parts to generate instructions to manipulate the source over a complicated geometry in a predetermined systematic way.

Test sample processing is performed in an environmentally controlled box, which has a quartz window cover to permit processing of materials in a controlled atmosphere. The infrared reflector has a focal length that extends through the quartz and onto the material being processed. A lathe to rotate parts while heat treating or fusing coatings is also included in the processing facility. Another feature of the plasma lamp for this facility is a water window. This water window device passes a thin film of water over the quartz glass covering the elliptical reflector. This feature protects the lamp when operating in harsh environments. This widow has a 3-mm water film that continuously cools the lamp quartz window. The water clings to the quartz window due to surface tension and stream momentum. The water is introduced on one side of the lamp across an air knife and removed on the opposite side through a vacuum orifice. This water window, show in Fig. 2, protects the lamp from harmful effluent and hot-spalled material.

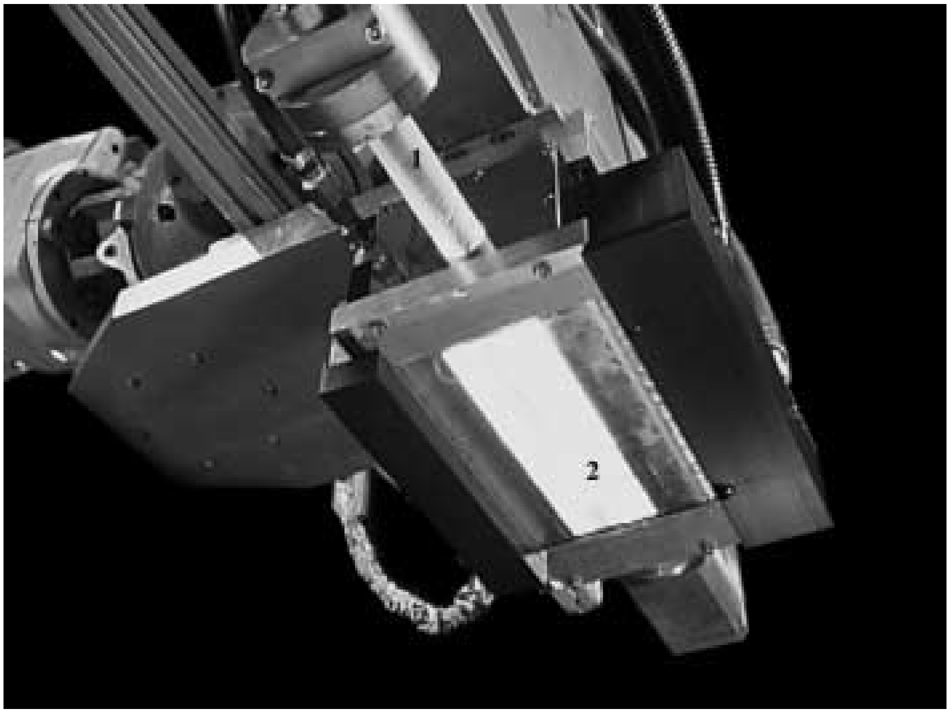

Fig. 2. Infrared plasma-arc lamp showing (1) internal and (2) external water walls.

A new method has been developed for densifing coatings on both planar and tubular metallic and ceramic supports. This process called high-density-infrared (HDI) transient-liquid coating (TLC) process has been developed to produce wear- and corrosion-resistant coatings on a variety of surfaces that are of commercial interest. The use of the HDIC process for fuel cell materials has only been in development for a short period and is still in the early development stages. The HDIC process, however, shows potential for use to rapidly sinter YSZ. Two separate experimental approaches have been taken, liquid and solid-state sintering, for densification of the YSZ. Initial experimentation utilized pre-densified NiO substrates with screen printed YSZ on the surface for liquid-phase densification. Lamp powers were varied from 800–2700 watts/cm^2 in an effort to fuse the YSZ while not melting the underlying NiO. Thermal shock issues were eliminated by preheating the specimens with a defocused beam to temperatures in excess of 1100°C in seven minutes followed by a high heat flux scan, 1800–2000 watt/cm^2. This process was successful in fusing the YSZ without melting the underlying NiO but continuous coatings have not been obtained. The solid-state sintering approach however has shown substantial success. A similar preheat cycle is performed as in the liquid phase approach but instead of a high power scan, a defocused beam at approximately 250 watts/cm^2 is utilized to solid-state sinter the film. Though only a limited number of experiments have been performed, continuous films have been sintered with only small, less than one micron, pores observable. Refinement of the sintering times and temperatures should allow for production of fully dense films in less than 8 minutes.

RESULTS AND DISCUSSION

The use of the HDIC process for fuel cell materials has only been in development for a short period and is still in the early development stages. The HDIC process, however, shows potential for use to rapidly sinter YSZ. Two separate experimental approaches have been taken, liquid and solid-state sintering, for densification of the YSZ. Initial experimentation utilized pre-densified NiO substrates with screen printed YSZ on the surface for liquid-phase densification. Lamp powers were varied from 800–2700 watts/cm^2 in an effort to fuse the YSZ while not melting the underlying NiO. Thermal shock issues were eliminated by preheating the specimens with a defocused beam to temperatures in excess of 1100°C in seven minutes followed by a high heat flux scan, 1800–2000 watt/cm^2. This process was successful in fusing the YSZ without melting the underlying NiO but continuous coatings have not been obtained. The solid-state sintering approach however has shown substantial success. A similar preheat cycle is performed as in the liquid phase approach but instead of a high power scan, a defocused beam at approximately 250 watts/cm^2 is utilized to solid-state sinter the film. Though only a limited number of experiments have been performed, continuous films have been sintered with only small, less than one micron, pores observable. Refinement of the sintering times and temperatures should allow for production of fully dense films in less than 8 minutes. SEM micros are shown in Fig. 3.

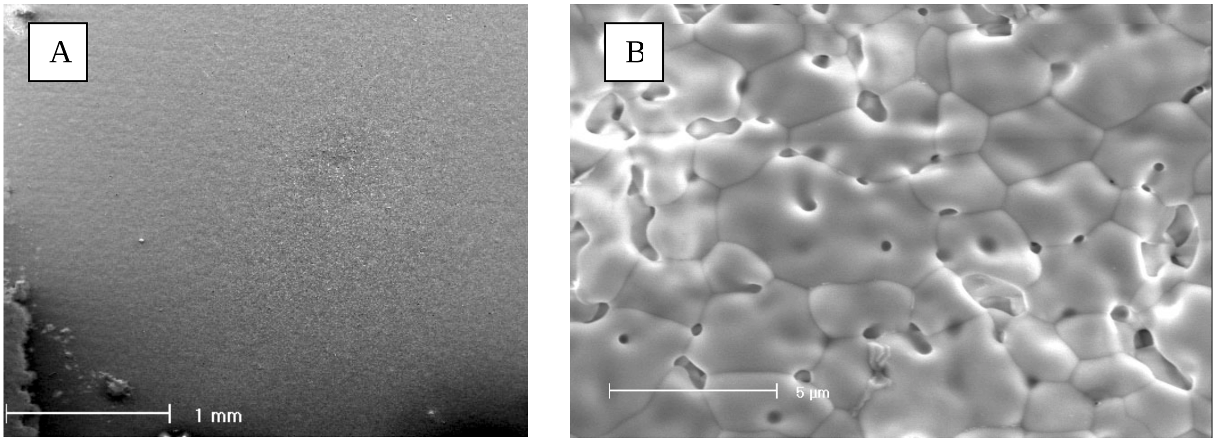

Fig. 3. A SEM of the surface of the YSZ after the high density infrared sintering process (A), and a high magnification SEM of the surface of the YSZ after the high density infrared sintering process showing almost 95% densification (B).

REFERENCES

1. Fuel Cell Fundamentals, Training Consultants, Inc., (2000).
2. C. A. Blue, V. K. Sikka, E. K. Ohriner, P. G. Engleman, and D. C. Harper, JOM-e, **52** [1] (2000).
3. N. C. Cox and D. E. McGee, Industrial Heating, **4** 46–48 (1989).
4. H. Bischof, “The Answer is Electrical Infrared,” *J. Microwave Power and Electron. Energy*, **25** (1) 47–52 (1990).

EVALUATION OF METALLIC HOT-GAS FILTERS

P. F. Tortorelli, C. G. McKamey, E. Lara-Curzio, B. A. Pint, and I. G. Wright
Oak Ridge National Laboratory
Oak Ridge, Tennessee 37831

INTRODUCTION

Hot-gas filtration is a key enabling technology for turbine-based power generation using coal-derived gases from integrated gasification combined cycles (IGCC) and pressurized fluidized bed combustors (PFBCs). Particle removal from hot gases produced by coal gasification or combustion is vital to achieving the efficiency and emission goals offered by such advanced systems as the gas turbine must be protected from degradation by erosion, corrosion, or deposition associated with the entrained species. Hot-gas filters offer a promising method of providing such protection if the reliability and durability of such devices can be assured.

Materials used in hot-gas filters are required to withstand prolonged exposure to corrosive, high-temperature gaseous environments as well as to condensable vapors and solid species, some of which may have the potential for localized interaction with the filter material after extended times. The gas streams may be oxidizing (PFBCs) or reducing, in which the sulfur species are largely in the form of H_2S (in the case of the product gas from IGCC processes or from carbonizers). Degradation of metallic filter elements has been observed under oxidizing, sulfidizing, and/or carburizing conditions and acts as a driving force for the development of ceramic hot-gas filters, particularly for the higher temperatures associated with advanced gasification and combustion designs. However, iron aluminides can also be considered for such applications because they offer the reliability advantages of metallic filters and typically have good to exceptional high-temperature corrosion resistance in a variety of sulfur-bearing environments relevant to coal-derived energy production.[1–3]

This project involves the evaluation of metallic hot gas filters in the field as well as in their as-processed conditions. Most of the analyses are of iron-alminide filters manufactured by Pall Corporation (Cortland, New York), but filters elements of other alloys are occasionally examined for comparison purposes. Through such analyses, the corrosion resistance and reliability of metallic hot-gas filters, particularly those fabricated from iron aluminides, will be determined for various environments representative of working coal-fired plants of relevance to advanced fossil systems.

SUMMARY OF ACTIVITES

In the past twelve months, filters exposed at the Wabash River gasification plant (West Terre Haute, Indiana) and the Wilsonville (Alabama) demonstration project have been evaluated. In addition, o-ring specimens cut from as-manufactured filter elements provided by Pall Corporation and exposed on the downstream (cleaned-gas) side of the filter system at the Wabash Rive plant were examined.

Typically, as-processed and field-exposed filter elements are cut into o-rings, which, along with the specimens exposed as such, are qualitatively checked for permeability and then are mechanically tested by internal pressurizatiion.[4] Following mechanical testing, the fracture surfaces and polished cross sections are evaluated by optical metallography, scanning electron microscopy, and electron microprobe analysis. Auger electron spectroscopy is used to help analyze the alumina films formed on the as-processed filters by preoxidation.

Results from the last year include the following findings and issues (details and conclusions to date have yet to be fully discussed and cleared with the parties involved):

- occasional low-temperature degradation of filter elements and of filter materials exposed on the clean-gas side
- little environmental degradation of the first iron-aluminide filter exposed at Wilsonville
- beneficial effect of the preoxidation treatment under a variety of conditions
- variations in the nature of alumina films formed by preoxidation
- high-temperature limit of iron-aluminide filters based on oxidation lifetime considerations
- effects of filter cleaning procedures during downtime

REFERENCES

1. J. H. DeVan, pp. 107–15 in *Oxidation of Intermetallics*, T. Grobstein and J. Doychak, Editors, The Minerals, Metals, and Materials Society, Warrendale, PA, 1989.
2. F. Gesmundo, D. Pocci, O. Tassa, F. Viani, and A. DiGianfrancesco, pp. 1657–67 in *Materials for Advanced Power Engineering*, D. Cousouradis and et al., Editors, Kluwer Academic Publishers, 1994.
3. K. Natesan and P. F. Tortorelli, pp. 265–80 in *Nickel and Iron Aluminides: Processing, Properties, and Applications*, S. C. Deevi, et al., Editors, ASM International: Materials Park, OH, 1997.
4. P. F. Tortorelli, C. G. McKamey, E. Lara-Curzio, and R. R. Judkins, paper 99-GT-268 in Proc. International Gas Turbine and Aeroengine Congress & Exhibition, ASME International, New York, 1999.

HYDROGEN MEMBRANE PROCESSING, ANALYSIS AND CHARACTERIZATION

Timothy R. Armstrong, Beth L. Armstrong, P. F. Becher, R. D. Carneim,
M. K. Ferber, C.-H. Hsueh, and H. T. Lin

INTRODUCTION

Inorganic membranes provide superior thermal and chemical stability when compared to commercially available organic membranes. Inorganic membranes may be classified as metallic, ceramic, or hybrids such as a cermet. This program will only be concerned with developing mixed conducting (protonic-electronic) ceramic membranes. Potential applications of protonic conducting ceramic membranes are extensive and varied, and include hydrogen production, aromatic upgrading, H_2S removal, alkane coupling, alkane dehydrogenation, and butane to isobutylene conversion. Ceramic membranes could be used to improve the efficiency and performance of a wide range of “Vision 21” fossil energy systems. Gas separation and purification are among the most important applications of such devices.

Dense ceramic membranes are very promising candidates for commercial hydrogen separation applications. Hydrogen may be incorporated as defects in oxides, and it is easily ionized to protons (H^+). Protons exhibit relatively high mobilities in oxides and in high concentration give rise to protonic conductivity. Proton conductors can be used in hydrogen pumps, sensors, electrochemical reactors and fuel cells. The primary advantage of dense membranes is their “infinite” selectivity—hydrogen is the only chemical species that is transported through the membrane (Fig. 1). Thus, the separation product is essentially 100% pure hydrogen. The membrane consists of a solid electrolyte material offering mixed protonic/electronic conductivity. The electronic conductivity is small. The driving force for proton transport is an externally applied voltage, so that external circuitry and porous, conductive electrodes are required.

The development of solid hydrogen separation membranes and materials is a critical issue for DOE and the gas industry. At present hydrogen separation membranes utilizing Pd or a microporous membrane are under development. However, recent calculations show that there is not enough Pd in the world to support commercialization of Pd based membranes. The microporous membranes, on the other hand, cannot operate above 600°C due to limitations of the system, thereby prohibiting their use in hot coal gas streams. There is an immediate need for a new technology (e.g., materials, membrane design, fabrication methods) to be developed.

Project Objectives

The objectives of this project are to develop: (1) novel designs for compact hydrogen separation membranes, (2) model the designs to determine manufacturing feasibility, (3) fabricate 1 or 2 novel

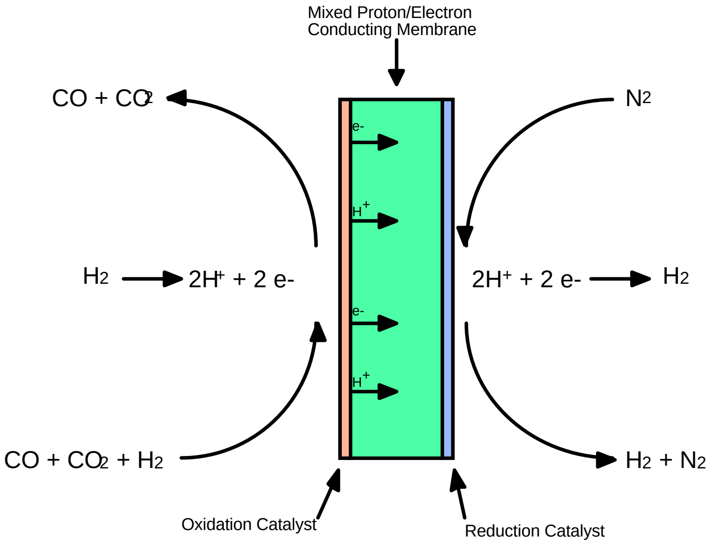

Fig. 1. Schematic showing anodic and cathodic reactions in dense ceramic H_2 separation membrane.

membranes for testing, (4) develop reliability models for asymmetric membranes, (5) evaluate constrained sintering of asymmetric membranes (6) characterize materials developed by Eltron using state-of-the-art x-ray diffraction, neutron scattering analysis, and for mechanical properties and (7) determine the optimal method for synthesis of mixed protonic-electronic conductors.

RESULTS AND DISCUSSION

Materials Synthesis and Analysis

A test plan was developed for this task to determine the appropriate method of synthesis for doped $BACeO_3$. A determination was made by Eltron Research and ORNL that the initial compositions would be chosen from:

$Ba (Ce_{1-X} Y_X)O_3$ where x is varied from 0 to 0.4 and

$(Ba_X Sr_{1-X}) Ce_{0.8}Y_{0.2}O_3$ where x is varied from 0.2 to 0.8.

Two test plans were developed. The first involves investigating the appropriate method of synthesizing a standard composition in the family listed to determine the method results in a powder of uniform composition, that is flowable, and can easily be sintered without the addition of post-synthesis processing. The synthesis methods chosen for investigation in this study included: combustion synthesis, coprecipitation, solid-state reaction, and spray pyrolysis. These methods were chosen because they were commercially available and any technology developed could easily be transferred to industry to rapidly produce large quantities of power. The second plan involves procuring and testing powders from commercial vendors to determine power characteristics (particle size, surface area), composition, and ease of processing and sintering. We are presently obtaining quotes on a standard composition from several vendors and anticipate beginning this work in the 3rd quarter.

Initial studies will focus on determining the proper stoichiometry (x) in $(Ba,Sr)_xCe_{0.8}Y_{0.2}O_3$ so that the powders will have minimal reactivity with humidity and CO_2. All powders in this study will be evaluated primarily on how well they can be processed into the desired green body whether it be a pressed tube or cast sheet and how well they sintered to full density.

ORNL evaluated the stability of $BaCeO_3$ with Y and Zr additions in CO_2 to verify their phase stability. Powdered samples prepared by combustion synthesis were analyzed by high-temperature x-ray diffraction under flowing CO_2 to determine the temperature at which $BaCO_3$ forms. In all the samples containing Y, $BaCO_3$ formed at 1050°C. In samples containing >15mole % ZrO_2, no traces of $BaCO_3$ were detected.

Membrane Design

ORNL has been designing novel monolithic gas separation membranes to separate oxygen from air. These sample membranes may be useful for separating hydrogen from mixed gas streams. This task will look at those membranes, attempt to develop new designs, and evaluate the feasibility of manufacturing these membranes. These membrane designs will be shared with Eltron Research and Coors. A consultant on the Coors team, James Stephan, is an expert in materials manufacturing and will be able to determine if these membranes can be produced using low-cost, high-volume manufacturing methods already available.

Mechanical and Thermal Property Characterization of Porous Membrane Materials

A test plan was developed for this task to support the evaluation of the mechanical reliability of the membrane materials. It consists of three major components the first of which will evaluate the influence of temperature and stressing rate on fracture strengths in four-point flexure and the applied flexure stress on time to failure in air of individual membrane compositions, Table 1. These tests will assess not only the strengths and strength distributions but also any effects of temperature and environment on failure due to slow crack growth. Based on these results, the influence of reducing/oxidizing environments and water vapor on time-to-failure responses will be characterized for the more promising compositions. Results for fracture toughness and Young’s modulus as a function of temperature and thermal expansion coefficients will be required in both the reliability analysis and the analysis of internal stress that can develop within the materials and influence densification and reliability.

Table 1. Outline of Test Plan

Fracture strength in four-point flexure in air		**Purpose**
Test Temperature, °C	22 600 800 1000	Range of stressing rates and temperatures used to assess potential of strength degradation due to slow crack growth or creep. This data also used to select 2 temperatures to evaluate flexure strength distributions for reliability analysis.
Stressing rate, MPa/s	30 0.03	
Time to failure		**Purpose**
Test Temperature °C	22 600 800 1000	Develop applied stress-temperature time-to-failure (long-term survivability) envelope in air. Use results to select materials for evaluating effects of partial pressure of oxygen, water vapor content.
Applied Stress	Selected based on above fracture strength data	
Fracture toughness and Young's modulus measurements		**Purpose**
Test Temperature, °C	Selected based on above results	Provide additional input data for reliability and stress analysis
Thermal expansion coefficients		**Purpose**
Environment	Air Reducing	Provide additional input data for reliability and stress analysis

The preliminary plan calls for the characterization of the following potential compositions:

$Ba\,(Ce_{1-X}\,Y_X)O_3$ where x is varied from 0 to 0.4 and
$(Ba_X\,Sr_{1-X})\,Ce_{0.8}Y_{0.2}O_3$ where x is varied from 0.2 to 0.8.

Modeling

ORNL completed development of the mathematical equations and codes to model constrained sintering of asymmetric membranes consisting of either: (1) a 2-layer membrane with a thin dense film supported on a thick porous substrate or (2) a 3-layer membrane with a thin dense film sandwiched between a thick porous substrate and a porous catalytic layer.

It is noted that the electrolyte film and the electrode substrate sinter at different rates causing stresses to develop in association with this differential shrinkage. These stresses may cause sintering damage, such as delamination or cracking of the film or warping of the bi-layer. It is also noted that materials are susceptible to viscoelastic deformation during sintering, such that stresses induced by differential shrinkage can be partially relaxed by viscoelastic deformation. Hence, the stresses in the system are controlled by both the rate of stress development and the rate of stress relaxation. Also, the sintering rate can be affected by the presence of stresses (1–4)**.** Specifically, when the substrate has a lower sintering shrinkage rate than the film, the film is subjected to in-plane tension, which, in turn, results in retardation of film densification. Models have been developed to analyze the constrained sintering behavior of a thin film on a substrate (1–4). A rigid (i.e., non-sintering) substrate, however, has often been assumed in order to simplify the analyses (1–3). A recent model (4) was developed to account for shrinkage in both the film and the support. This model, however, predicted the stresses in the system based on the constrained sintering behavior of the film on the substrate. A model capable of predicting both the film's constrained sintering behavior and stresses is still lacking. The purpose of the present study is to predict both the constrained sintering behavior of the film on a sintering substrate and the stresses that result due to the differential shrinkage between the film and the substrate.

The model was tested using existing data on a typical fuel cell system (yttria stabilized zirconia and Ni-zirocnia cermet) and found to give very good results. The data required to test the model on $BaCeO_3$ will require 2 quarters to collect. Researchers at ORNL plan to initially model a 2-layer system. In this system the sintering rate of the porous layer varied such that in one case the rate will be controlled by additions of a fugitive phase and in a second by coarsening the $BaCeO_3$. In both cases, the thin membrane will be between 10 and 20 microns thick and sinter to full density at 1400°C (2 h). Its sintering properties will not be altered. This model will allow the team to determine the stresses that exist in the membrane after sintering as a function of the thickness of the layers, their elastic properties, and sintering rates.

REFERENCES

1. G. W. Scherer and T. J. Garino, *J. Am. Ceram. Soc.*, **68,** 216 (1985).
2. C. H. Hsueh, *Scrip. Metall.*, **19,** 1213 (1985).
3. T. J. Garino and H. K. Bowen, *J. Am. Ceram. Soc.*, **73,** 251 (1990).
4. P. Z. Cai, D. J. Green, and G. L. Messing, *J. Am. Ceram. Soc.*, **80,** 1940 (1997).

TESTBED FOR INORGANIC MEMBRANE GAS SEPARATION

L. D.Trowbridge

INTRODUCTION

As part of a larger activity, ORNL's Chemical Technology Division is to construct and operate a test bed for lab-scale evaluation of inorganic membranes which are designed to separate hydrogen from hydrogen/hydrocarbon gas streams. The inorganic membranes to be tested are those developed under a different portion of this overall effort by the Inorganic Membrane Technology Laboratory (IMTL) located at East Tennessee Technology Park (ETTP) in Oak Ridge, TN. ORNL's experimental role is to test IMTL's membranes using flammable gas mixtures, first using surrogate binary gas mixtures (e.g., H_2 + CH_4 or H_2 + C_2H_6) but later using gas mixtures generated by a lab-scale catalytic cracker to be obtained from Phillips Petroleum.

The gas membranes to be tested take the form of tubes. The test bed is intended to hold one short section of such a tube; full scale application will involve many longer, parallel tubes. The goal of this work is to determine the capability of specialized inorganic membranes for separating hydrogen from hydrocarbon streams. Realistic gas separation measurements will yield separations that incorporate a number of inherent inefficiencies that can be fairly well characterized and predicted from gas transport measurements. To be able to predict performance under conditions other than the specific ones examined experimentally, it is necessary to make the appropriate measurements allowing one to factor out these known, predictable inefficiencies so as to reveal the inherent ideal separation efficiency of the membrane.

Gas separation efficiency is generally interpreted by the equation:

$$(\alpha - 1) = E_p\, E_m\, E_c\, E_b\, (\alpha^* - 1)$$

In this equation, α is the actual separation factor, a function of the concentrations of the components in the two product streams. E_p is the back pressure correction factor (the ratio of the pressure drop across the membrane to the high-side pressure). E_m is the mixing efficiency, a function of the flow and composition-dependent gas transport parameters, such as the diffusivity and viscosity of the gases. E_c is the cut correction factor, a function of the fraction of the gas directed through the membrane. These factors can be calculated from measurable experimental parameters.

Two variables in the above equation which have not been mentioned are E_b, the membrane (i.e., barrier) efficiency, and α^*, the ideal separation factor. Separation relying purely on the relative velocity of gas molecules, so-called Knudsen flow (from whence the term "Knudsen membrane" derives), has an α^*

equal to the ratio of the average molecular velocities. A design variation on this is the “molecular sieve” membrane, with pores sufficiently small that it relies on both the molecular velocities plus the effect of different molecular sizes to improve separation of light, small molecules over larger heavy ones. If the pore size distribution is known, the ideal separation factor for this type membrane can also be estimated. For these two membrane designs, α^* can be readily calculated, leaving E_b as the ultimate parameter to be determined from the experiment.

A third design strategy, the “surface flow” membrane, involves transport via surface condensation, surface diffusion, and re-evaporation of the more condensable component. Its ideal separation factor is not as well defined, and the experimental parameters to be determined are the combined factor “$E_b (\alpha^* - 1)$.”

All this was mentioned to indicate that the design of a test bed for membrane gas separation must measure those physical parameters (temperature, concentrations, flow rates, pressures and pressure differences) with sufficient accuracy to retain adequate accuracy of the desired parameters, namely the membrane efficiency and ideal separation factors.

EXPERIMENTAL

The membrane separation theory discussed above was used to determine those parameters which need to be measured and controlled, and to determine the necessary accuracy of those measurements. That done, more detailed considerations in apparatus design included the techniques chosen for achieving those measurements and the safety of the system.

A simplified schematic of the system design is shown in Fig. 1. The system will utilize pre-mixed gases as a supply, separating them in a single pass through the membrane. Figure 2 shows a photograph of a membrane holder mounted in its thermostatted oven. Pressures are monitored in each stream (P) as is the pressure difference between the two separated stream (ΔP). Pressure is controlled in each stream by back-pressure regulators (BPR). The total flow in the system is controlled upstream of the membrane by a flow controller (FC) and measured downstream in each stream by flow meters (FM). Each stream (or a side-stream thereof) passes through a thermal conductivity detector (TCD) to determine composition. Downstream of the TCDs, the two streams are mixed and then diluted below the flammability limit with a controlled flow of nitrogen and exhausted to the laboratory hood. Flows, pressures, temperatures and concentrations are measured and recorded by an on-line data acquisition system. As a more definitive back-up to the composition measurements made by the TCDs, samples will also be taken for analysis by gas chromatography.

The primary control on the flammability of the gases is the dilution of the exhaust stream to below its flammability limit. Control on the degree of dilution is set by the flow controllers (FC) on the source gas

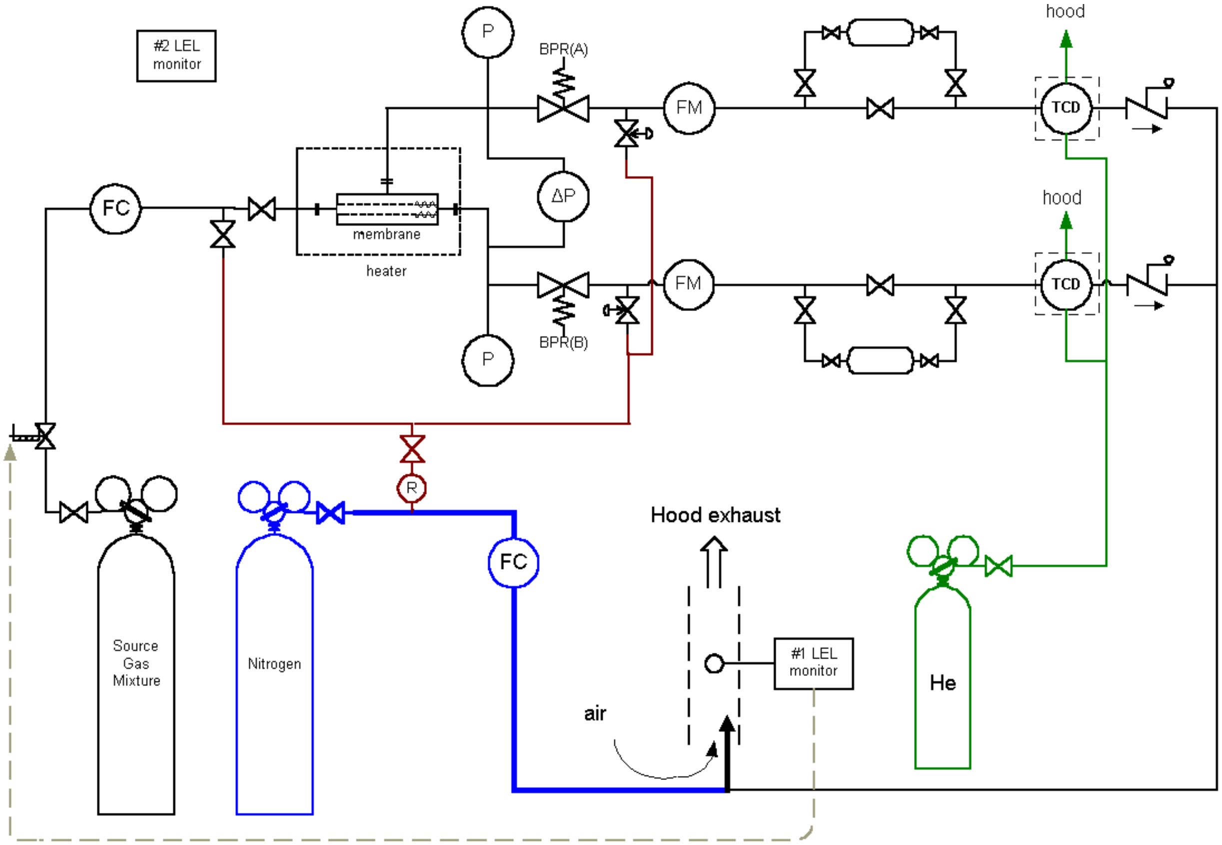

Fig. 1. Schematic of membrane test apparatus showing major operational elements only.

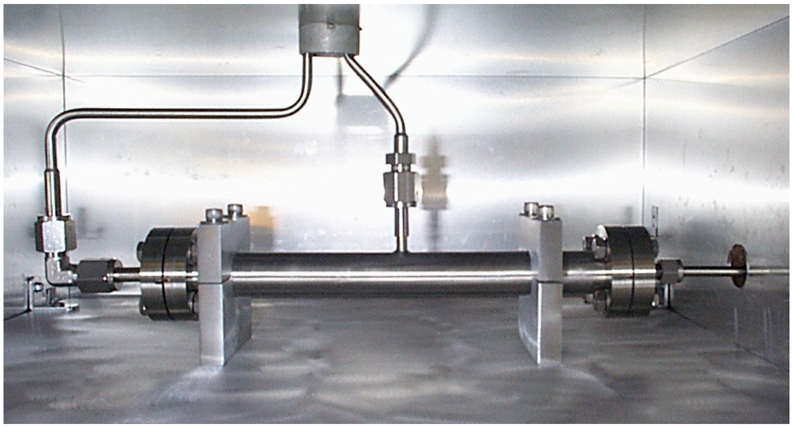

Fig. 2. Membrane holder mounted in oven.

stream and the nitrogen stream. To verify that the gas is indeed below the flammability limit, an LEL (lower explosion limit) device monitors the exhaust stream continuously. A second LEL device monitors the general atmosphere in the vicinity of the apparatus. Safety approvals for operating this system have been obtained.

PROGRESS

The IMTL-designed and manufactured membranes, though by no means identical to those used in the gaseous diffusion uranium enrichment plants, are descended from those types of membranes. As such, these membranes are at present considered classificated materials, so lab security is a consideration. Security modifications to the laboratory have been completed, and the security plan for the work prepared and approved. A Knudsen-type membrane has been fabricated by IMTL and is available for use, but has not been brought to the lab yet so as not to prematurely invoke the security measures.

The apparatus described here has been assembled and has undergone some component testing and integrated flow testing. This testing was underway when funding was interrupted at the beginning of FY 2001. Consequently, no activity took place during the first half of FY2001. Activity is now resuming (as of April 2001) with the release of FY2001 funds.

CONCLUSIONS

During the last half of FY 2000, an experimental system was designed and constructed for purpose of testing inorganic membranes for the separation of hydrogen/light hydrocarbon gas mixtures. Construction was substantially complete, and component and integrated testing was partially accomplished by the end of FY2000. Safety and security arrangements are in place to allow operation of the test bed.

Planned future activities include complete apparatus testing, installing the IMTL Knudsen membrane initially, and other or improved designs as they become available. Membranes will be tested first on binary gas mixtures (e.g., $H_2 + CH_4$; $H_2 + C_2H_6$; $H_2 + C_2H_4$). Ultimately, we intend to obtain a lab-scale catalytic cracking unit and test separation of more complex gas mixtures.

REFERENCES

R. A. Ebel and L. P. Pasquier, “Design of a Gaseous Diffusion Stage,” NUCLEAR ENGINEERING-PART XXIII, AIChE Symposium Series, 123(68) p 107 (1972).

R. L. Hoglund, J. Schacter, and E. von Halle, “Diffusion Separation Methods,” ENCYCLOPEDIA OFCHEMICAL TECHNOLOGY, vol 7, 3rd Edition, J. C. Wiley and Sons (1979).

BIOMINERALIZATION FOR CARBON SEQUESTRATION

T. J. Phelps and R. J. Lauf
Oak Ridge National Laboratory

INTRODUCTION

The purpose of this research is to develop an understanding of the mechanisms by which iron-reducing and carbonate-precipitating microorganisms sequester carbon dioxide into solid carbonate mineral phases and to use this knowledge to design biological processes to capture carbon dioxide from fossil fuel plants while stabilizing fly ash wastes. This research will develop a scenario by which fly ash is stabilized into carbonate solid conglomerates that could potentially be useful as fill materials or road construction aggregates. We envision an open system whereby ash collection ponds would be colonized with calcareous microorganisms capable of producing calcite, aragonite, and iron carbonates such as siderite. These carbonates would be formed in situ, at the surface by photosynthetic algae and at depth by anaerobic carbonate producing bacteria. Results to date demonstrate that iron-reducing bacteria indeed convert CO_2 into sparingly soluble carbonate minerals such as calcite and siderite using metal containing fly ash and lime. Biological carbonate mineral formation using fly ash and lime materials indicated that bacteria may complement the capture of carbon dioxide from fossil fuel plants while potentially stabilizing fly ash wastes and bind the fly ash into solid materials. In essence, the proposed research adds a depth factor on the previous concepts of algal ponding. First, it would remove carbon from the atmosphere and immobilize it into a stable mineral phase. Second, it could turn waste ash into a useful product. Third, it could at the very least stabilize the ash to reduce the leaching of metals into the environment. Fourth, the process could be combined with a waste treatment strategy in which the carbonate forming microbes would use waste products from agriculture or food processing to supply energy for microbial growth. This would constitute energy plexing by combining multiple diverse waste streams into new products.

The proposed concept of ponds for the precipitation of low quality aggregates is an early example of energy-plexing; combining known diverse energy processes into a close-proximity constructive product line. We envision an energy-plex gaining advantage from alkaline ecosystems based on the algal ponds of the Great Salt Lake (GSL) during its low period of the 1970s. While the surface of the lake was algal rich there was complex biogeochemical processing occurring in the waters, facilitating the production of carbonate-rich deposits. We propose adding the carbonate precipitating aspects of high ionic strength microbial cultures with biogeochemically robust anaerobic microorganisms that precipitate carbonates in the water and sediments.

Recently, we demonstrated that partial pressures of CO_2 and ionic species composition of aqueous media exhibit profound influences on the type of minerals precipitated in anaerobic microbial cultures. Minerals precipitated under a nitrogen atmosphere were predominantly magnetite. In the presence of 20% headspace CO_2, a mixture of magnetite and iron rich carbonates such as siderite was formed. XRD analysis of these minerals formed by the psychrophilic marine bacterial isolate PV-4 grown at 14°C is shown in Fig. 1 in addition to results from an inoculated control. Precipitates formed from aqueous solutions containing carbonates, calcium, magnesium, and iron include: calcite ($CaCO_3$), aragonite ($CaCO_3$), dolomite [$CaMg(CO_3)_2$], and siderite ($FeCO_3$). The most abundant carbonate minerals in sediments are calcite and dolomite, followed by siderite and ankerite (an Fe- and Mn-bearing member of the dolomite group) plus some magnesite ($MgCO_3$).

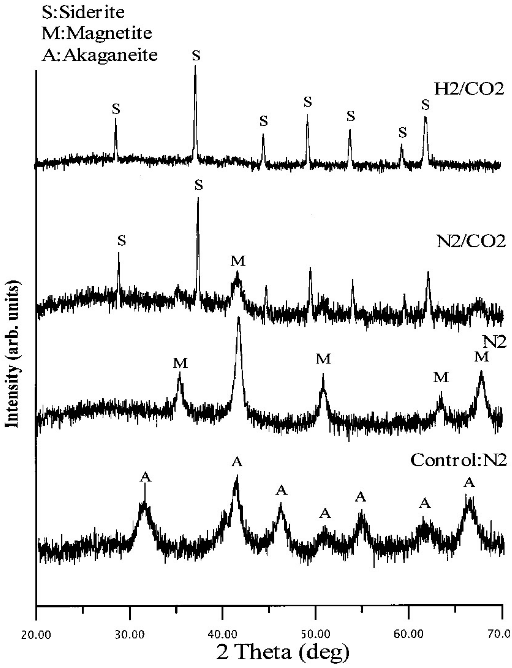

Fig. 1. XRD analysis of precipitates formed by culture PV-4 under the different atmospheres.

In our research biological conversion of CO_2 into rock-like, sparingly soluble carbonate minerals, such as calcium carbonate ($CaCO_3$) and siderite ($FeCO_3$) has been studied using bacteria in conjunction with low-value products such as lime, metal containing fly ash and iron oxides. For these preliminary experiments representatives of our psychrophilic (from Pacific Ocean sediments and Alaskan tundra), mesophilic (from lake and estuary sediments), and thermophilic (from deep subsurface) metal reducing bacteria were used to show proof of principle carbonate-rock precipitation by microbially facilitated mechanisms. These metal reducing bacteria, at the partial pressure of CO_2 and ionic species composition used, exhibited profound influence on the type of minerals in these anaerobic cultures. Minerals precipitated under a nitrogen atmosphere were predominantly magnetite (Fig. 1). In the presence of 20% headspace CO_2, a mixture of magnetite, siderite, and calcite were formed (Fig. 2). Magnetite and siderite formation was observed in these anaerobic cultures incubated at pH = 6.9–8.8 and Eh < –200 mV. In all cultures examined to date, as the pCO_2 increased, there was a shift from metal oxides to carbonate solids.

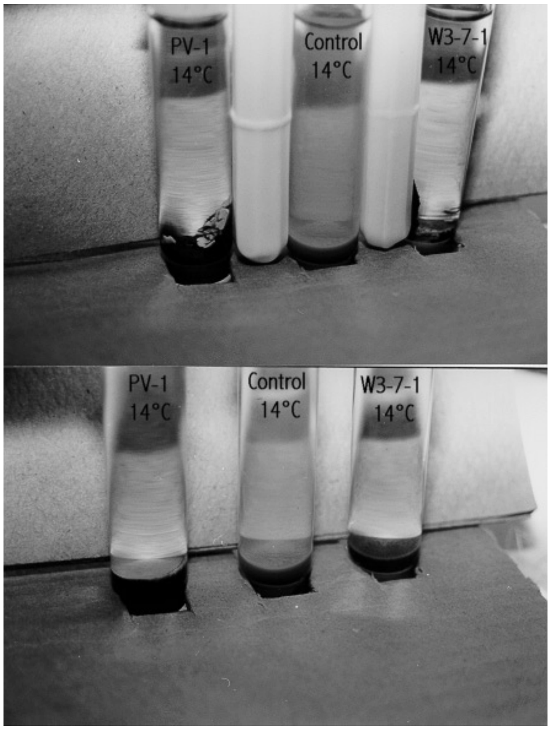

Fig. 2. Carbonate rock formed by culture PV-4 in the presence of 20% headspace CO_2.

Metal reducing bacteria were added to solutions in order to precipitate calcium carbonate minerals on fly ash and lime. Metal reducing bacteria applied to fly ash plus lime showed that bacteria precipitated calcium carbonate on fly ash (Fig. 3). Biological and inorganic conditions may affect the surfaces of the lime and fly ash enough to allow dissolution and precipitation to take place at a significant rate. Calcium carbonate, such as rhombohedral calcite ($CaCO_3$), was precipitated with lime and fly ash particulates after the inoculation of thermophilic iron reducing bacteria, TOR-39 (Fig. 3c,d). No calcium carbonate was precipitated without organisms (Fig. 3a,b). Calcification was observed in psychrophilic, mesophilic, and thermophilic cultures incubated at pH 7.4–8.5 and Eh < –200 mV. Calcium and iron carbonate are

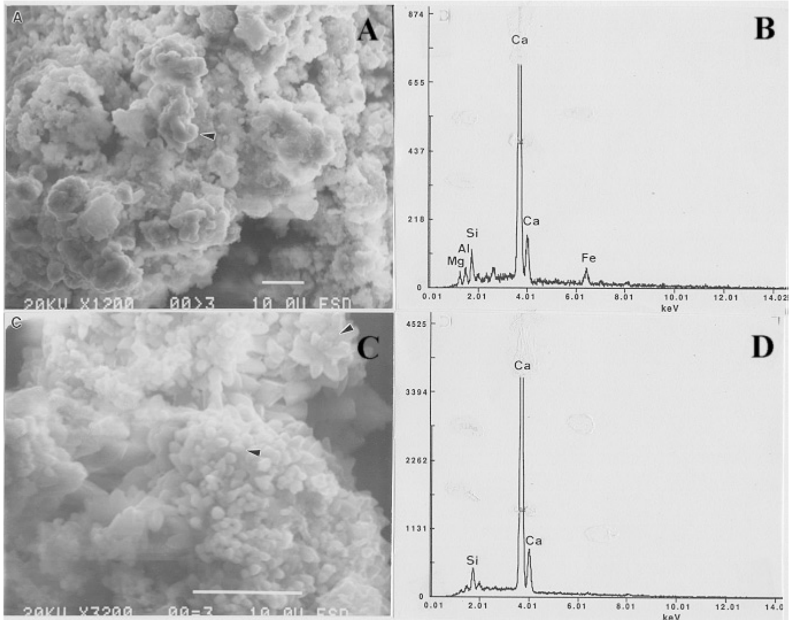

Fig. 3. SEM/EDX analysis of fly ash plus lime used for microbial precipitation of carbonate minerals under a H_2-CO_2 atmosphere (A and B: without bacteria; C and D: with bacteria).

microbially precipitated and mineralized by altering local Eh conditions, pH conditions, or both and likely creating conditions of supersaturation with respect to a mineral phase.

Mineral rich fly ash, rejected dust from cement kilns and non-regulated agricultural wastes or food processing wastes are often trucked and land filled at total disposal costs (including transportation) often exceeding $50 per ton while carbon dioxide is liberated to the atmosphere. While previous strategies dealt with these as separate issues we intend to energyplex them into useful product lines in high ionic strength deep algal ponds. The high ionic strength would be provided by the fly ash (along with residual sulfate from the sulfur in the coal) and/or reject kiln dust. Carbon dioxide from the plant would be bubbled through the deep alkaline pond. Agricultural wastes could provide additional energy into the pond. While the algae are precipitating (sequestering) carbon at the pond surface, the anaerobic bacteria fed by the organics in the wastes precipitate additional carbonates in the sediments. Within our labs different cultures of these bacteria produce siderite pellets in 5% salts at temperatures from 4°C to 75°C within days. Importantly, they also reduce other metals including chromium, manganese, calcium, uranium, and cobalt. The product of our proposed process could therefore be hydrated multi-metal limestone-like aggregates suitable for road fill materials or other uses.

Assuming ponds of 8 m (25 ft) depth with residence times of weeks we hypothesize a set of ponds (5–8) each being 12–25 acres in size could easily handle 10,000 tons of ash per day (ash from >40,000 tons of coal per day). We hypothesize sequestering 1/3 of the approximately 20,000 tons of carbon dioxide bubbled through the ponds each day as some will surely escape. Sequestration mechanisms would include algal precipitation, anaerobic microbial sequestration and abiotic geochemical precipitation. To the mixture of ash, agricultural wastes, water and bubbled carbon dioxide we could readily add hundreds of tons of waste cement kiln dust per day enhancing the bio- and geo-chemical precipitation sequestration efficiency. Accordingly we would estimate sequestering a small fraction of a pound of carbon per cubic ft of pond each day (one pound per day per 10 cubic ft of pond). Such an efficiency would represent approximately 10% of the efficiency of our microbial cultures observed in the laboratory in the absence of significant abiotic geochemical precipitation. By circulating warm process waters and heating the deeper portions of the ponds to 30–45°C the biogeochemical sequestration rates would dramatically increase. Using the same conservative assumptions field sequestration may represent less than 1% of the metabolic efficiency of our lab cultures. Therefore, use of warm recirculating waters to heat the ponds could accelerate rates of sequestration and/or require less land for the biogeochemical sequestration.

Accordingly, we will have used several waste streams to create a new product line. While most of the cost advantage represents offsets from disposal costs (fly ash, and ag wastes) the aggregate will have value and further offset excavation/mining/calcining costs of fill materials costing $4–15 per ton. Even with bulk discounts and close proximity the disposal costs from the waste streams would be >$35/ton. Added to the value of the product this process could represent a value gain of >$40/ton but more likely represent a gains of $10–20 ton of aggregate or a net value gain of approximately $2–5 per ton of sequestered carbon. Consequently, the objective of the proposed research is to develop an understanding of the microbially mediated processes that can add a depth component to the previous art of algal ponding as a mechanism of stabilizing fly ash while sequestering carbon.

TECHNICAL PROGRESS

Work in FY 2000 included experiments directed toward proof of principle using cultures in serum vials. Strains of carbonate producing microorganisms (freshwater, brackish, and marine) were evaluated by culturing them with selected sources of metal ions and providing them with carbon dioxide in bicarbonate buffered media, a N_2/CO_2 atmosphere, and a H_2/CO_2 atmosphere to determine the kinetics of carbonate mineralization. Psychrotolerant (PV-1, W3-6-1), mesophlic (BrY), and thermophilic (C1, TOR-39) iron-reducing bacteria were used to examine the reduction of amorphous iron(III) oxyhydroxide in the presence of N_2, N_2/CO_2, H_2, and H_2/CO_2 headspace gases as well as in HCO_3– buffered medium under N_2 conditions. Magnetite was dominant under a N_2 and H_2 atmosphere and siderite was dominant under a H_2/CO_2 (80:20, V:V) atmosphere. A mixture of magnetite and siderite were formed in the presence of N_2/CO_2 headspace. In a HCO_3– buffered medium with lactate, amorphous iron oxyhydroxide was extensively reduced with increasing HCO_3– concentration, and the crystalline phases were dominated by siderite. Results of this study showed that the atmosphere, chemical milieu, and species of bacteria affected the extent of iron reduction as well as the mineralogy and morphology of the crystalline phases. These results have significant implications for biomineralization processes in both natural and manipulated environments.

The work also evaluated the mineral products so formed in terms of crystalline phases, particle size, strength, etc. for comparison to naturally formed analogues. The TEM replica (Fig. 4d,e) showed that siderite particles formed by TOR 39 using a medium buffered 90 mM $NaHCO_3$ were globules with diameters between 3 and 5 mm. Siderite globules formed by TOR-39 showed that the surface structure appears to be composed of flakes of crystals rather than a single rhombohedral crystal formed by Geobacter metallireducens. The magnetite particles formed by TOR-39 coexisted with siderite and have diamond shapes with edge lengths <0.3 mm. The TEM replica showed that siderite formed by BrY under a H_2/CO_2 atmosphere were disk-like crystals having diameters between 2 and 3 mm and thickness <0.4 (Fig. 4c). The SEM photograph showed that rhombohedral siderite crystals (Fig. 4b) formed by the psychrotolerant Fe(III)-reducing bacterium, PV-4, are similar to siderite formed by GS-15 and found in natural samples. However, siderite globule (Fig. 4a) formed by the W3-7-1 cultures was different from siderite formed by PV-4 and GS-15.

In parallel to the development tasks, basic scientific studies were undertaken to understand the biochemistry of carbonate and iron mineralization (with the ultimate goal of improving the production of minerals and/or tolerance for environmental variations) and to determine the effect of a carbonate binder phase on leaching of trace metals from the ash. Chemical and X-ray powder diffraction analysis support that the metals such as Co, Cr, Ni could be directly incorporated into the magnetite and siderite crystal structure. It is unclear how iron minerals nucleated and grew, and how trace metals are incorporated into iron minerals during the biomineralization by microorganisms. Although the exact mechanism is currently unknown, TOR-39 appears to have caused the formation of trace metal-incorporated magnetite and siderite by enhancing Fe3+ and other metal reduction via organic carbon oxidation. TOR-39 isolated from deep subsurface have the ability to reduce Fe(III) and other heavy metals such as Cr(VI), Mn(IV), and Co(III) from solution and produce nanometer-sized particles of magnetite outside of the cell. The solid phase conversion of amorphous iron hydroxides is in accordance with the strong sorption of metals to amorphous iron hydroxide. The reduced cations (Cr3+ and Co2+) by microorganisms, and other metals (Co2+ and Ni2+) added as reduced forms are easily adsorbed on iron oxides in alkaline media and can also be incorporated in iron oxide structure during the crystallization. These adsorbed trace metals

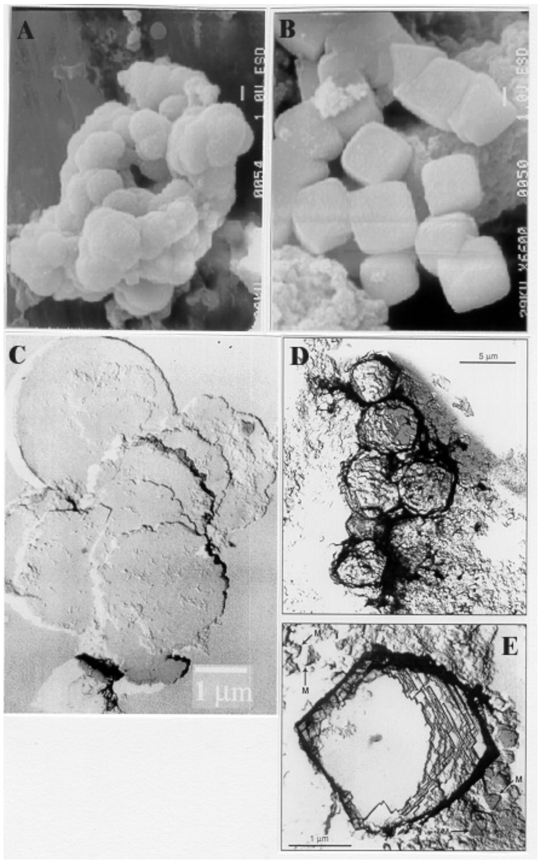

Fig. 4. SEM and TEM photomicrographs of biologically-facilitated siderite precipitates

will be incorporated into magnetite and then become a part of the crystals as magnetite crystal growth continues.

Efforts in late FY 2000 also included selecting the best microbial strains that most effectively produce carbonates and culturing them with actual fly ash samples to determine whether they can utilize calcium, magnesium, manganese or iron from the ash and continue to build carbonate minerals productively. Biological conversion of CO_2 into sparingly soluble carbonate minerals such as calcite ($CaCO_3$) and siderite ($FeCO_3$) has been studied using iron-reducing bacteria in conjunction with metal containing fly ash and lime. Psychrotolerant (PV-1), mesophlic (BrY), and thermophilic (TOR-39, C1) iron-reducing bacteria were not only selected according to their growth and carbonate mineral formation rate but also by the rate, extent and size of products produced (Table 1). These organisms were used to examine biogeochemical processes such as dissolution and mineralization using fly ash in the presence of N_2, N_2/CO_2, and H_2/CO_2 headspace gases as well as in HCO_3– buffered media (30–210 mM). Chemical analysis of culture media after incubation revealed that the leaching of Ca and Fe from fly ash was significantly reduced in the presence of a H_2/CO_2 atmosphere and in HCO_3– buffered media (>140 mM).

Table 1. Microbial isolates chosen for current and ongoing investigations at ORNL

Organisms	Growth condition	Source	Growth rate	Carbonate mineral formation rate	Potential minerals
TOR-39	Thermophilic	Deep subsurface	Very fast	Very fast	Magnetite Siderite, Maghemite, Uraninite, Sergeevite, Calcite
C1	Thermophilic	Deep subsurface	Very fast	Very Fast	Magnetite, Siderite, Maghemite
BrY	Mesophilic	Estuaries	Fast	Fast	Magnetite, Siderite
PV-4	Psychrotolerant	Near hydrothermal vent	Fast	Fast	Magnetite, Siderite, Calcite

This effect was a consequence of microbial metal reduction and the precipitation of siderite in the presence of appropriate electron donors such as lactate and glucose. Iron-reducing bacteria applied to fly ash plus lime also precipitated calcium carbonate onto fly ash particulates in HCO_3– buffered media (>140 mM). The precipitation is likely facilitated by the organisms altering local Eh, pH, and nucleation conditions. Biological carbonate mineral formation using fly ash and lime materials indicated that bacteria may complement the capture of carbon dioxide from fossil fuel plants while potentially stabilizing fly ash wastes. Mineralogical and chemical characterization of fly ashes from several different sources (Table 2) was completed in early FY 2001 that identified iron- and Ca-rich ashes.

Table 2. Fly ash and lime currently investigated at ORNL

Material	pH	SiO_2	Al_2O_3	Fe_2O_3	CaO	MgO	Mineralogy
ORNL Steam Plant Ash, Oak Ridge, TN	7.7	34.4	19.1	15.2	1.8	0.4	Mullite ($Al_6Si_3O_{15}$), Quartz (SiO_2)
TVA Bull Run Ash, Oak Ridge, TN	6.4	48.1	24.4	8.4	1.6	0.9	Mullite ($Al_6Si_3O_{15}$), Quartz (SiO_2)
TVA Johnsonville Ash, Chattanooga, TN	8.4	44.9	20.9	24.7	2.5	1.1	Mullite ($Al_6Si_3O_{15}$), Maghemite (Fe_2O_3), Quartz (SiO_2)
Springerville Ash, Joseph city, AZ	11.4	45.9	19.1	2.9	15.0	0.9	Mullite ($Al_6Si_3O_{15}$), Portlandite [$Ca(OH)_2$], Quartz (SiO_2)
ORNL Inhouse Lime	11.7	8.9	1.5	0.7	44.8	22.9	Calcite ($CaCO_3$), Quartz (SiO_2)

The first six months of FY 2001 was highlighted by the acceptance of one paper and the submission of a second manuscript with preparation of four more. In addition we presented five poster presentations at national meetings, and those are in addition to the three presented in FY 2000. Lauf and Phelps were hosted by TVA in Chattanooga, TN for a workshop where we discussed potential collaborations. TVA appears quite interested in DOE-TVA collaborations and proposed potential matching funds from EPRI along with use of TVA sites. Lauf and Phelps also presented two invited talks at the Western Region Ash Group meeting in Denver, CO., in October, 2000:

PUBLICATIONS

Zhang C., J. Horita, D. R. Cole, A. V. Palumbo, and T. J. Phelps. 2001. Temperature-dependent oxygen and carbon isotope fractionations of biogenic siderite. Geochim. Cosmochim. Acta. (In press.)

Roh, Y., R. J. Lauf, A. D. McMillan, C. Zhang, C. J. Rawn, J. Bai, T. J. Phelps. 2001. Microbial Synthesis and the Characterization of Metal-Substituted Magnetites. Solid State Communications (In Press)

Roh, Y., T. J. Phelps, A. D. McMillan, and R. J. Lauf. 2001. Utilization of Biomineralization Processes with Fly Ash for Carbon Sequestration. Proceeding of First National Conference on Carbon Sequestration, Washington, DC, on May 14–17, 2001. (In Press)

Roh, Y., C.-L. Zhang, R. J. Lauf, H. Vali, C. S. Romanek, and T. J. Phelps. 2000. Chemical and microbiological factors on iron mineral formation. In Preparation for Chemical Geology.

Roh, Y., G. Li, H. Huang, T. J. Phelps., and J. Zhou. Metal reduction and mineral formation by thermophilic Fe(III)-reducing bacteria from deep subsurface environments. In preparation for Applied Environmental Microbiology.

Roh, Y., J. Zhou, R. Stapleton, G. Li, C. Zhang, A. V. Palumbo, T. J. Phelps. 2001. Iron reduction by extremophiles: geochemical and environmental implications. In: C. Zhang, J. D. Coates (eds.), The Biogeochemistry of Iron Cycling in the Environments, Kluwer Academic Press. In Preparation.

ABSTRACTS

Roh, Y., A. D. McMillan, C. Zhang, C. J. Rawn, R. J. Lauf, T. J. Phelps. 2001. Microbial synthesis of metal-substituted magnetite nanoparticles using thermophilic Fe(III)-reducing bacteria. The Clay Minerals Society Meeting, June 2001, Madison, WI

Roh, Y., H. Vali, R. D. Stapleton, T. J. Phelps, J. Zhou. 2001. Single-domain magnetite formation by a psychrotolerant iron-reducing bacterium. American Society for Microbiology Meeting, May 2001, Orlando, FL.

Roh, Y., A. McMillan, R. Lauf, T. Phelps. 2001. Utilization of biomineralization processes with fly ash for carbon sequestration. National Conference on Carbon Sequestration, May 2001, Washington, DC.

Zhou. J., Y. Roh, R. Stapleton, G. Li, H. Huang, A. Palumbo, T. Phelps, C. Zhang, A. Murray, J. Tiedje. 2000. Iron reduction by extremophiles. American Geophysical Union, Dec. 2001 San Francisco, CA.

Phelps, T. J. 2000. Life and times of microorganisms in deep subsurface environments. American Geophysical Union Meeting, December 15–19, San Francisco, CA (Invited talk).

Roh, Y., A. McMillan, R. Lauf, T. Phelps. 2000. Utilization of biomineralization processes for carbon sequestration. American Geophysical Union Meeting, Dec. 2001, San Francisco, CA.

Phelps, T. J. 2000. Applied microbiology for the coal ash environment. Western Region Ash Group Fall Meeting. Nov. 2000, Denver, CO.

Roh, Y., T. J. Phelps, J. Zhou, C. Zhang. 2000. Metal reduction and mineral formation by iron-reducing bacteria. Soil Science Society of America Meeting, Nov. 2000, Minneapolis, MN. (Invited talk).

Roh, Y., G. Li, H. Huang, T. J. Phelps, J. Zhou. 2000. Metal Reduction and Mineral Formation by Thermophilic Fe(III)-Reducing Bacteria from Deep Subsurface Environments. American Society for Microbiology Meeting, May 2000, Los Angeles, CA.

Zhou, J., Heidelberg, J., Li, G., Roh, Y., Huang, H., Murray, A., Liu, S., Stapleton, R., Qiu, Q., Fraser, C., Palumbo, A., Phelps, T., Lies, D., Nealson, K., and Tieje, J. M. 1999. Ecological, physiological and genomic diversity of metal reducing bacteria. 7th Conference on Genomics, Nov. 2000, Arlington, VA.

Roh, Y., R. D. Stapleton, C.-L. Zhang, A.V. Palumbo, J.-Z. Zhou, and T.J. Phelps. 1999. Chemical and Mineralogical Characterization of Iron Carbonate Formed by Psychrophilic, Mesophilic, and Thermophilic Bacteria. The 4th Int. Sym. on Subsurface Microbiology, August 1999, Vail, CO.

PATENT PENDING

Lauf, R. J., T. J. Phelps, C. Zhang, and Y. Roh. 1999. Mixed oxide nanoparticles and method of making. Patent Pending (U.S. Patent Application Serial No. 09/428,376).

APPLICATION OF NATURAL AND INTRODUCED TRACERS FOR OPTIMIZING VALUE-ADDED SEQUESTRATION TECHNOLOGIES

G. R. Moline and D. R. Cole

INTRODUCTION

This project is one element of an interdisciplinary public-private partnership, GEO-SEQ, that was established to develop and deliver the enabling technology and information needed to accelerate application of safe and cost-effective methods for geologic sequestration of carbon dioxide. The goal of this project is to provide methods that utilize the power of natural and introduced tracers to decipher the fate and transport of CO_2 injected into the subsurface. The resulting data will be used to calibrate and validate predictive models used for (1) estimating CO_2 residence time, reservoir storage capacity, and storage mechanisms; (2) testing injection scenarios for process optimization; and (3) assessing the potential leakage of CO_2 from the reservoir. This work directly addresses a key objective of the overall GEO-SEQ project: to increase confidence in and the safety of geologic sequestration by identifying and demonstrating cost effective and innovative monitoring technologies to track migration of carbon dioxide and its reaction products in geologic formations. Secondarily, this work will contribute to the following GEO-SEQ objectives: to lower the cost of geologic sequestration by developing innovative optimization methods for sequestration technologies with collateral economic benefits such as enhanced oil recovery (EOR), enhanced gas recovery (EGR) and enhanced coal-bed methane production; to assist operators and developers in selecting the best sequestration sites by developing a set of screening criteria and siting guidelines; and to enhance performance assessment methods to predict and verify that long term sequestration practices are safe, effective and do not introduce any unintended environmental problems.

EXPERIMENTAL APPROACH

Our basic approach is to utilize a combination of natural and applied gas tracers to delineate the subsurface movement of injected CO_2. The injected CO_2 will undergo a number of mass transfer processes as it interacts with the subsurface materials (e.g., rock, brine, hydrocarbons). These processes can enhance the reservoir's capacity for long-term storage of CO_2 and are, thus, important for both predicting and optimizing the effectiveness of geological sequestration of CO_2.

As the injected CO_2 interacts with the subsurface its isotopic signature changes, making it an obvious natural tracer if: (1) the injection gas stream can be isotopically characterized, (2) the isotopic changes are significant enough to be detected during transport, and (3) the changes can be interpreted in the presence of multiple carbon sinks and sources in the subsurface. The first condition is straightforward, but the second and third are unknown and require laboratory testing to determine the feasibility of use of the injected CO_2 mixture as a tracer without incorporating additional tracers into the gas injection stream.

Through careful selection based on their physical and chemical properties, a combined suite of applied tracers can act as a surrogate for the injected CO_2, providing information about the mass transfer processes involving CO_2 by their differential transport behaviors. Two types of information are necessary in order to understand and quantify the fate and transport of CO_2 in the subsurface: (1) the hydrologic characteristics of the formation, which control the movement of fluids and gases (e.g., advective velocity, dispersion, molecular diffusion into stagnant pores), and (2) chemical interactions with fluids and solids along the transport pathway, which control the storage of constituents contained in those fluids and gases (e.g., sorption onto minerals, partitioning into hydrocarbons, partitioning between reservoir fluid and gas phases).

Our approach is to conduct batch reactor and flow-through column tests using a range of reservoir materials and temperature/pressure conditions to measure CO_2 isotopic changes and to evaluate a suite of applied tracers and to quantify mass transfer coefficients relative to reservoir conditions (e.g., porosity, mineralogy, water saturation, hydrocarbon saturation, temperature, pressure). Initial experiments have focused on the interaction of CO_2 with reservoir materials in order to determine the magnitude of the types and magnitude of those interactions which, in turn, guide the selection of appropriate tracers to act as surrogates for the CO_2. Additionally, the need to design and construct a column flow-through apparatus has put the initiation of the applied tracer experiments later in the schedule. The natural and applied tracers are being tested separately to determine their respective transport behaviors. Later, we will combine them in flow-through column tests and determine correlations between the CO_2 and applied tracers. These experiments will provide a basis for designing and interpreting the results of a pilot field-scale CO_2 injection test. They will also provide key parameters for reservoir modeling and geophysical data interpretation being conducted by others on the project team.

In the flow-through column studies, we will use two methods to evaluate the reservoir hydrologic properties and the impact of various transport and mass transfer processes. These methods are illustrated using the results of previous experimental work.

(1) Co-injection of multiple tracers: The use of multiple tracers having different physical and chemical characteristics enables the separation of simultaneously occurring processes. This is illustrated in Fig. 1 from earlier experiments where three solute tracers were co-injected into a weathered highly-fractured rock core. Matrix diffusion results in a separation of the tracer breakthrough curves due to differences in the tracer diffusion coefficients, while sorption results in a separation due to differences in

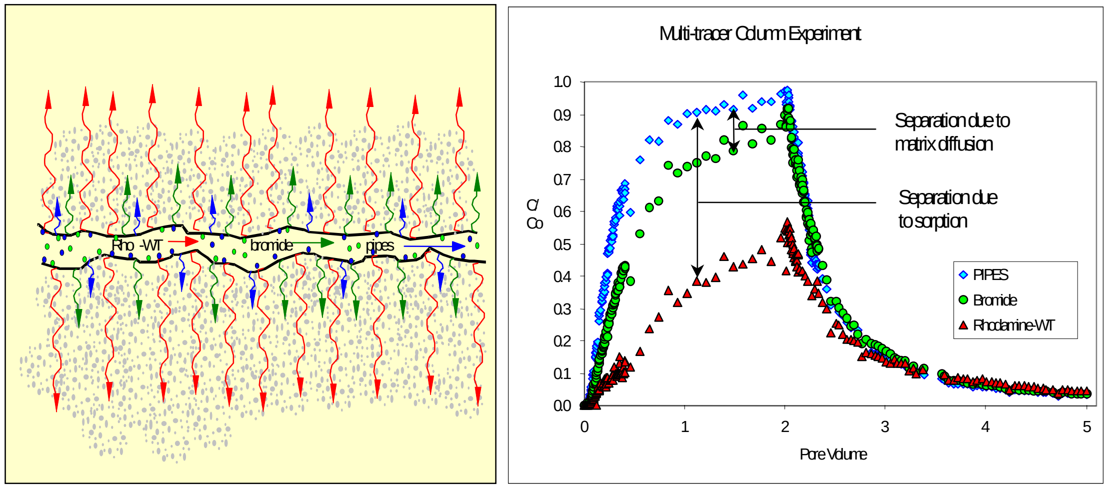

Fig. 1. Multi-tracer experiment showing breakthrough curve separation due to matrix diffusion and sorption.

reactivity of the tracers. This method has also been used in other studies to measure fluid saturation (partitioning into gas phases) and nonaqueous phase saturation (partitioning into an oil phase).

(2) Chemical waveforms: The use of periodic injection concentration rather than the standard pulse or continuous concentration injection methods has been shown to provide a better resolution of key hydrologic parameters and better detection of the tracer signal in the presence of high background concentrations or noise. Figures 2 and 3 show the results of previous numerical and column experiments designed to test the sensitivity of the output signal (concentration measured at an observation point) to frequency and dispersion coefficient, an important but difficult parameter to quantify.

Figure 2 shows breakthrough curves from 1D numerical simulations where the dispersion coefficient (Ez) has been varied for each of four frequencies. Simulations have also been done to evaluate the sensitivity to linear and nonlinear sorption and to dispersion in 3D.

In Fig. 3, breakthrough curves from 1D column experiments are compared with the analytical solution for several frequencies. sodium salicylate solution was pumped at constant flow rate but oscillating concentration through a long 1/16-in. tube. Breakthrough curves were constructed from high-frequency fluorimetry measurements of the column outflow and compared to analytical solutions for an ideal tube of the same dimensions assuming Taylor dispersion. The measured and predicted curves are a very good match and demonstrate the validity of the numerical model and predicted sensitivity.

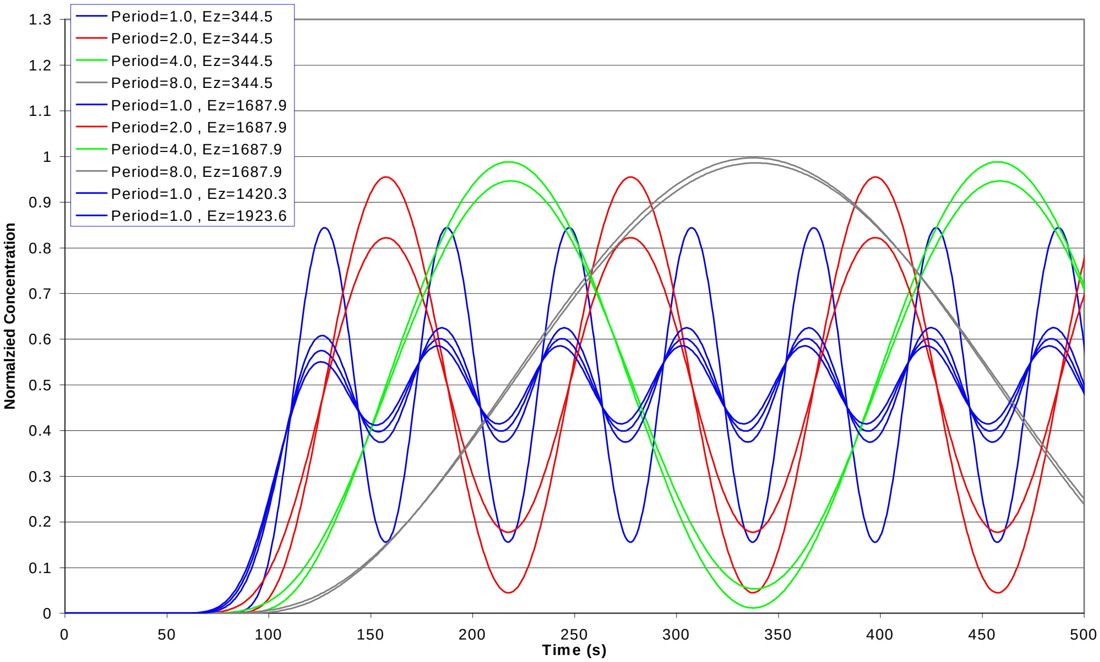

Fig. 2. Numerical simulations for 1D dispersion showing sensitivity of the output wave to frequency and dispersion coefficient.

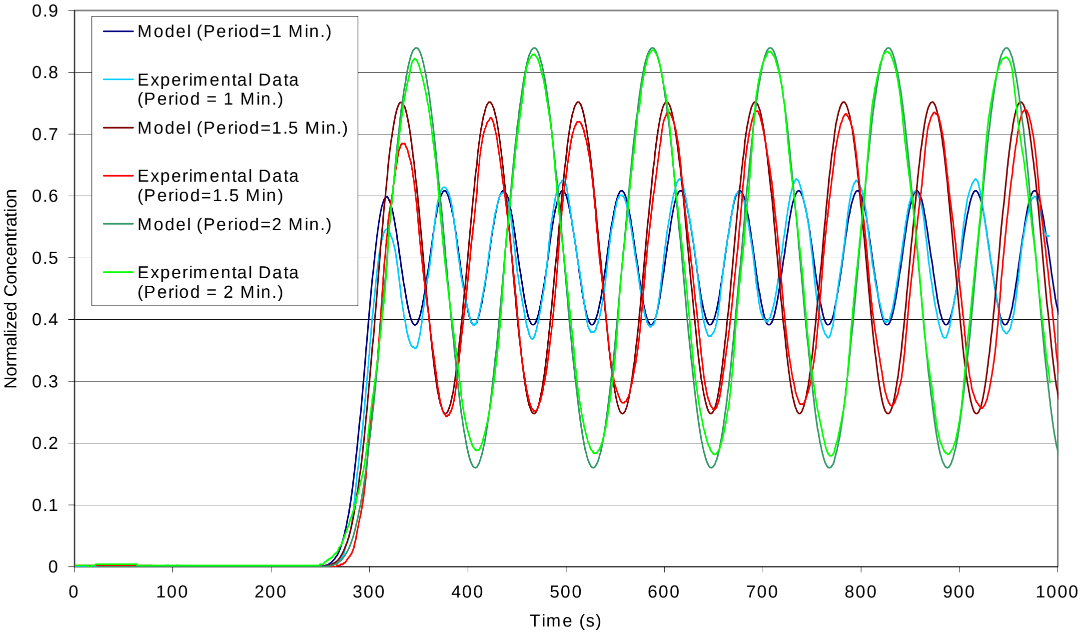

Fig. 3. Comparison of experimental results with analytical solutions for 1D dispersion in a long thin tube.

DISCUSSION OF CURRENT ACTIVITIES

Efforts this year have focused on two areas: batch-reactor (static) isotopic tracer experiments to evaluate the partitioning behavior of CO_2 in the presence of common reservoir materials; and design and construction of the flow-through experimental apparatus and selection of tracers for dynamic multi-tracer experiments.

Isotopic Tracers:

Initial efforts involved reacting CO_2 with organic-rich diatomaceous cores obtained from the Lost Hills reservoir to evaluate the partitioning behavior of CO_2 in the presence of commonly-occurring reservoir materials. In order to use the stable isotope compositions of carbon and oxygen in CO_2 as effective tracers during the injection tests we need to understand how these isotopes partition as a consequence of different process pathways (e.g., mineral reactions; sorption; aqueous dissolution). Initial investigations focused on one important isotopic partitioning pathway, that of CO_2 interacting with hydrocarbon-saturated rock (an EOR injection scenario) in static mode. Four samples were selected from the Lost Hills cores. Approximately 1.5 gms from each core were disaggregated, loaded into a two zone reaction vessel and reacted with a small quantity (2.33E–5 moles, ~0.001gms) of dry CO_2 (initial $\delta^{13}C_{PDB} = 50.4\%$ and $\delta^{18}O_{PDB} = -13.47\%$). CO_2 was also loaded into a fifth vessel (control) containing no core sample to measure possible partitioning between CO_2 and the vessel walls. These systems were allowed to react for 72 hours at $25^{o}C$. A small aliquot of CO_2 was isolated from the solid in the upper portion of each vessel and analyzed isotopically.

The CO_2 from the control vessel showed no isotopic variation from the starting composition. Without exception, the CO_2 sampled in the presence of the solid was isotopically enriched in both carbon and oxygen relative to CO_2 lost to the solid (possibly sorption). CO_2 reacted with sandy diatomites was heavier in $\delta^{13}C$ by between 3.5 and 4% relative to “fixed” CO_2, whereas enrichments of between 6.3 and nearly 7% were observed for CO_2 reacted with diatomite. The $\delta^{18}O$ enrichments in CO_2 relative to “fixed” CO_2 were similar in magnitude regardless of lithology–roughly 17 to 20%. The magnitude of the carbon isotope partitioning is comparable to what others have observed for CO_2 interaction with aqueous solutions. The preliminary conclusion to draw here is that a light isotopic component of CO_2 may be retained in the reservoir leading to progressively heavier isotopic CO_2 farther down the flow path.

More effort is needed to quantify how these isotopes fractionate as a function of temperature, PCO_2, surface area, hydrocarbon composition, mineral composition, solid to volatile mass ratios, presence of H_2O, and ultimately, flow rate. To begin to assess the magnitude of carbon isotope change in CO_2 as it reacts with potential reservoir phases, model calculations were conducted. These calculations assumed reaction in a closed system where CO_2 is allowed to interact with at varying portions with either a HCO_3^-

bearing brine, calcite or hydrocarbon-rich rock (HC; Lost Hills) of unspecified composition. Equilibrium isotope fractionation is assumed in all calculations except one set where we applied experimental sorption isotope partition data obtained using the Lost Hills core. Calculations were conducted for 20 and 100°C except for the sorption process which was based on our 20°C data. The initial carbon isotope value ($\delta^{13}C_{PDB}$) of the CO_2 was set at–35‰, typical for CO_2 generated from coal-burning power plants. The initial carbon isotope values for the HCO_3^- fluid and calcite were set at –5 and 0‰, respectively, and are typical of what is observed in carbonate-hosted brine reservoirs. The HC carbon isotope value (–23‰) is based on what we measured for the Lost Hills core.

The results of these calculations are shown in Fig. 4, where the $\delta^{13}C_{PDB}$ values for CO_2 are plotted against the atomic % carbon ratio between CO_2 and the interacting phase of interest (i.e., HCO_3^-, calcite, HC). In a simplistic way, one can think of the extreme left-hand side of the figure as the injection point for the CO_2, which undergoes reaction with progressively more and more of a particular carbon source during transport through the reservoir (left to right across the figure). In all cases the carbon isotope values of CO_2 become less negative through reactions with either aqueous HCO_3^-, calcite or HC. The carbon isotope trajectory is determined by temperature that fixes the fractionation factor between CO_2 and

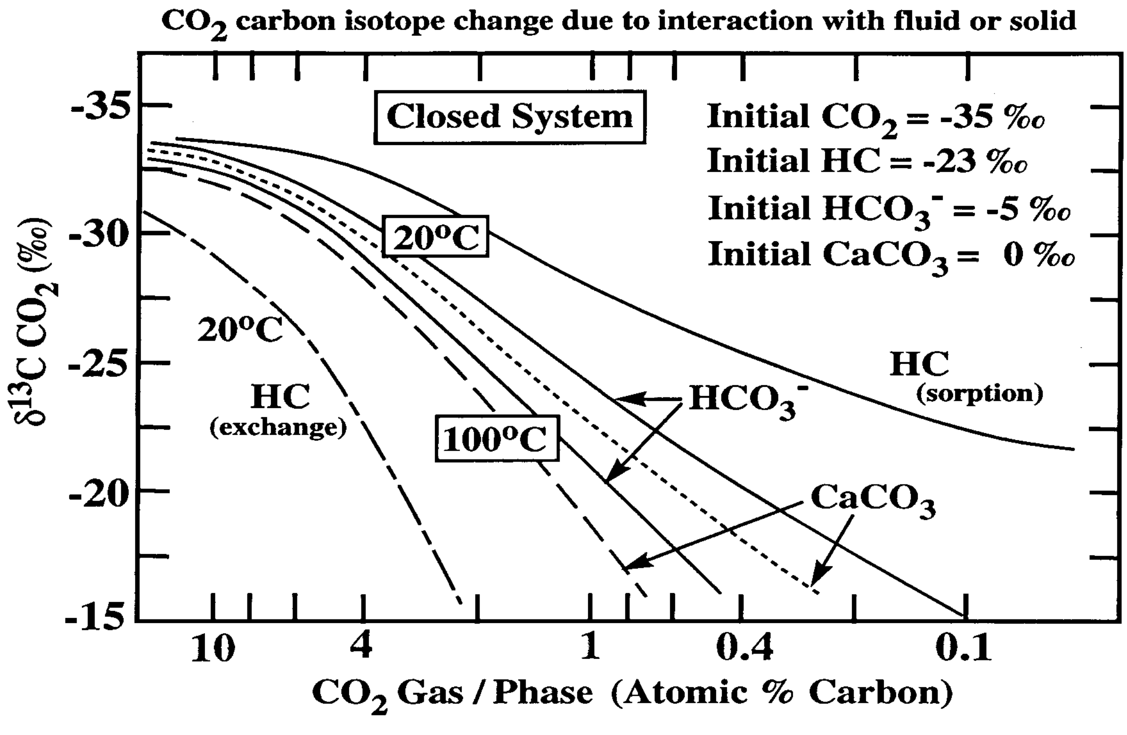

Fig. 4. Changes in CO_2 isotopic composition due to interaction with fluids and solids. Movement along the x-axis from left to right can be considered analogous to changes during subsurface transport.

any coexisting phase and the relative proportion of carbon in CO_2 to the carbon in the interacting phase. All of the cases shown are for binary systems (e.g., CO_2–calcite; CO_2–HCO_3^-). However, carbon isotope trajectories for CO_2 interacting with both HCO_3^- and calcite would lie between the respective binary curves for any given temperature scenario. Note that the carbon isotope trajectories for CO_2 interacting with HC-bearing rock vary considerably depending on whether the process is controlled by equilibrium isotope exchange or sorption; the latter being perhaps more realistic for low temperatures involving CO_2 injection into EOR or CBM systems.

We have since expanded the types of geological materials to include quartz, calcite and montmorillonite. We also examined the isotope partitioning between CO_2 and crude oil provided by Chevron from Lost Hills. The focus here was to demonstrate whether or not the isotopic behavior was reproducible and reversible, and to assess the impact hydrocarbons have on the isotopic behavior. To accomplish this we used isotopically different CO_2 gases ($\delta^{13}C$ = +50.4 vs –40.7‰; $\delta^{18}O$ = –13.5 vs –17.5‰), reacted with these materials for different lengths of time (3, 5, 7 days) at slightly different PCO_2 levels (0.003 to 0.0055 MPa) . Steady state partitioning for both carbon and oxygen isotopes was generally reached after 5 days. In all cases the “free” CO_2 was isotopically enriched in ^{13}C and ^{18}O relative to gas sorbed onto the solids. The magnitude of the partitioning for oxygen always exceeded that of carbon by roughly a factor of 2–3. The carbon isotope partitioning was greatest between CO_2 and the oil (7–10‰) followed in order by montmorillonite (7–8‰), Lost Hills core (4–7‰), calcite (2–3‰), and finally quartz (1–2‰). The order of partitioning was somewhat different for oxygen isotopes: greatest in the Lost Hills core (20–35‰), followed by montmorillonite (22–27‰), Lost Hills crude oil (7–13‰), calcite (6–12‰), and finally quartz (2–3‰). These preliminary results clearly indicate that hydrocarbons and clay may have a profound effect on the isotope compositions of CO_2 injected into the subsurface.

Four Argonne Premium coal samples have been obtained for use in both CO_2–CH_4 sorption-desorption and isotope partitioning experiments. These four coals are a medium volatile bituminous (#1, Upper Freeport seam, PA), a sub-bituminous (#2, Wyodak-Anderson seam, WY), a low volatile bitiminous (#5, Pocahontas No. 3 seam, VA), and a high volatile bitumonous (#7, Lewiston-Stockton seam, WV). Tests completed to date include scanning electron microspcopy (SEM), grain size analysis, and N_2 BET surface area measurements.

Applied Tracers:

The applied tracer work has focused on two areas: the selection of an appropriate suite of tracers for monitoring the fate and transport of injected CO_2 in the subsurface, and design and construction of a flow-through column apparatus that will allow evaluation of the tracer transport behavior under a variety of pressure and temperature conditions and in the presence of a variety of reservoir materials. Because the ultimate goal is to apply these tracers to a pilot-scale field injection test, some important criteria were considered. These criteria include: (a) low to zero concentration in the subsurface; (b) detectable at very low concentrations (parts per trillion or less); (c) stable under reservoir conditions; (d) environmentally safe; (e) subject to some of the same mass transfer processes as the injected CO_2; and (f) amenable to analysis using a single sample and a single method for the entire suite. This last criterion is important in simplifying the analyses, reducing analytical time and costs, and making in-field analysis possible.

After evaluating the results of published laboratory and field tracer studies, we have selected a suite of gas tracers that appear to have the physical and chemical properties that would make them appropriate for field use for tracking injected CO_2. Based on published studies, we have selected SF_6 and a suite of perfluorocarbons for our initial column studies. These tracers hold good promise for this application, as they meet most of the selection criteria. They've been used in previous deep subsurface applications and so their behavior is documented under some reservoir conditions. These gases are all detectable using a gas chromatograph equipped with and electron capture device (ECD), thus the potential is there for analysis of the entire suite of tracers in a single analysis. Further, these gases have an extremely low detection limit (in the ppt range), they are relatively inert, and they have low to zero background concentrations in the subsurface. The latter is an advantage over some of the noble gases such as He and Ar, where natural background levels could be significant thereby lowering the effective detection limit.

Additionally, we have selected a basic design for a flow-through column apparatus that will allow us to test the relative interactions of the gas tracers with a variety of reservoir materials and under a range of pressure and temperature conditions appropriate for proposed injection scenarios (Fig. 5). A similar

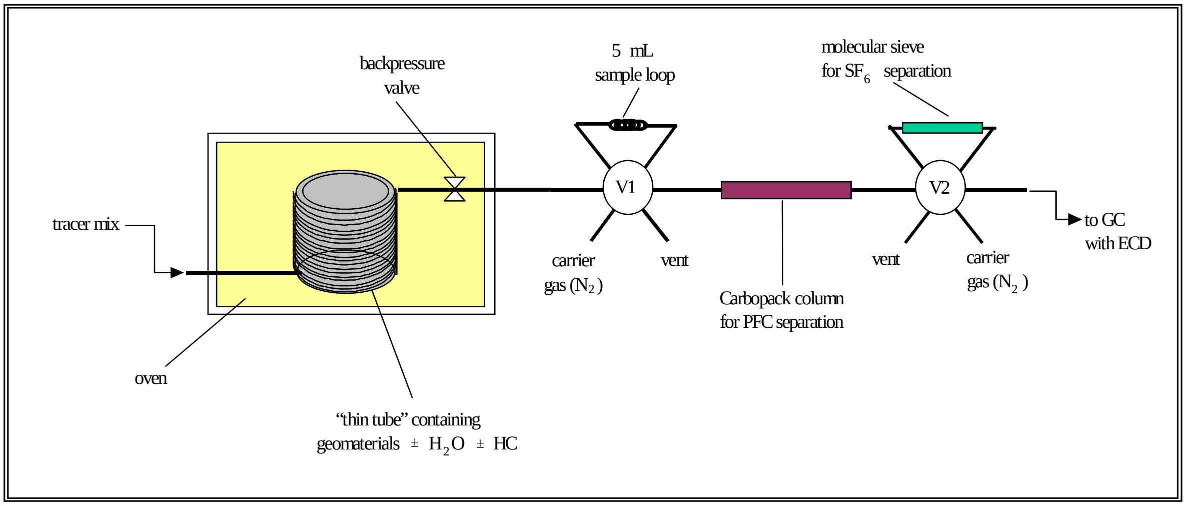

Fig. 5. Flow-through column apparatus for testing tracer/geomaterial interactions under varying conditions.

system has been used by researchers at the Institute for Energy Technology in Norway (Galdiga and Greibrokk, 1997; Dugstad et al., 1992). The system contains two elements: a reactor cell and a detection device. The reactor cell consists of a long, thin column which will be packed with a variety of reservoir materials (the same materials used in the batch reactor experiments) which is installed in an oven. The outlet side of the column has a back-pressure valve to allow control of the injected gas tracer mix as it flows through the column. Thus, tracer interactions can be studied under a variety of pressure and temperature conditions.

The detector device is a gas chromatograph equipped with an ECD and a dual-column setup that allows both the SF_6 and the perfluorocarbons to be analyzed in a single injection. The dual columns are required because the perfluorocarbons will foul up the molecular sieve column used to separate the SF_6 from other background gases. By passing the gas mixture through a Carbopack™ column, the perfluorocarbons will be stripped out and the remaining gases can be shunted through the molecular sieve using a 6-way valve, allowing SF_6 separation. The molecular sieve can then be bypassed and the perfluorocarbons analyzed as they elute from the Carbopack™ column. A second 6-way valve is used to capture 5-ml samples for analysis, and between samplings the outlet gas stream can be vented as waste. This method makes online automated analysis in the field possible.

Eventually, co-injection of tracers and CO_2 will be included in the dynamic experiments to allow direct comparison of the CO_2 and tracer transport behaviors under identical conditions. Results of these studies will be the basis for final determination of the tracers to be used for a field-scale CO_2 injection test and evaluation of the results of that test.

MANUSCRIPTS SUBMITTED

Blencoe, J. G., Cole, D. R., Horita, J. and Moline, G. R. (2001) Experimental geochemical studies relevant to carbon sequestration. First National Conference on Carbon Sequestration, Sponsored by NETL, May 15–17, 2001, Washington, DC, 14 p.

REFERENCES

Dugstad, O., T. Bjornstad, and I. A. Hundere, 1992. Construction of a slim-tube equipment for gas tracer evaluation at simulated reservoir conditions. Appl. Radiat. Isot., vol.43 (4), pp.527–535.

Galdiga, C. U., and T. Griebrokk, 1997. Simultaneous determination of trace amounts of sulphur hexafluoride and cyclic perflourocarbons in reservoir samples by gas chromatography. Chromatographia, vol.46 (7/8), pp.440–443.

ENHANCING CARBON SEQUESTRATION AND RECLAMATION OF DEGRADED LANDS WITH FOSSIL-FUEL COMBUSTION BYPRODUCTS

John F. McCarthy,[1] James E. Amonette,[2] and F. Blaine Metting[2]
[1]Oak Ridge National Laboratory; [2]Pacific Northwest National Laboratory

INTRODUCTION

This project, FEAA049, is supported by the U.S. Department of Energy (DOE) National Energy Technology Laboratory, Morgantown, WV; Sarah Forbes, Program Manager). The project is coordinated with the DOE Center for Research on Enhancing Carbon Sequestration in Terrestrial Ecosystems (CSiTE), which currently emphasizes research on forest, prairie, and agricultural lands. The NETL project leverages these activities by expanding CSiTE's research to include lands that have been disturbed by mining, highway construction, or poor management practices. Our approach focuses on amendments with solid byproducts from fossil-fuel combustion, paper production, and biological waste-treatment facilities. The primary goal is to identify and quantify the key factors leading to successful C sequestration and reclamation of degraded lands. The results will be summarized in a set of guidelines containing practical information about matching amendment combinations to land types and optimum site-management practices. A scientific evaluation of existing field sites where such amendments have been applied will provide the basis for the guidelines. Results from the available literature will be combined with additional new measurements of properties at these sites including (1) the extent and nature of the sequestered C, (2) microbial communities and their influence on greenhouse-gas emissions, and (3) redox, alkalinity, toxic metals, and key soil physical properties. Long-term field studies will also be designed and site(s) recommended for the demonstration and further optimization of this approach. Specific tasks will focus on determining how percolating dissolved organic carbon can enhance the mass of soil organic carbon sequestered in deep soil horizons, assaying for populations of denitrifying bacteria, comparing the results to DOE/CSiTE measurements, and evaluating management practices to optimize this sequestration strategy.

GOALS AND TECHNICAL APPROACH

The **goals of this project** encompass both scientific and technology transfer components:

Scientific Goal: Identify optimal selection and delivery strategies to maximize the contribution of amendments to carbon sequestration.

Technology Transfer Goal: Foster interactions between the scientific and user communities to maximize the application of new knowledge and approaches for enhancing terrestrial C sequestration through optimal utilization of fossil energy by-products and management of degraded lands.

Our **research strategy** addresses these challenges through a combination of *evaluation* and *technology transfer* focused on existing field sites of opportunity.

Our strategy to achieve the *Scientific Goal of optimizing C sequestration* has two parts.

1. *Evaluate Existing Experimental Sites:* Because of the diversity and extent of previous amendment studies and the long times needed to determine success or failure from a C-sequestration perspective, we are evaluating a number of existing sites where flyash and biosolids amendments have already been applied. These experimental sites were selected to represent different levels of amendments, different types of fly ash (alkaline and acid), and different ages since treatment. Data obtained from these experimental manipulations were not originally designed to explore the potential for C-sequestration, and we are supplementing existing information with additional measurements of key parameters such as the depth distribution and amounts and types of organic and inorganic C present, emission of greenhouse gases, and changes in nitrogen cycling microbial communities. This new information is being correlated with amendment treatment parameters and other soil properties to identify the most favorable (and detrimental) combinations of soils, fossil-fuel combustion byproducts, and management practices.

2. *Design Experiments to Test and Demonstrate C Sequestration:* The second part of our strategy will be to design a limited set of experiments at one or two sites that focus on the deep incorporation of specific amendments (fly ash and FGD products, in combination with other sources of organic C such as biosolids, pulp and paper byproducts) to enhance sequestration of C. The(se) site(s) would be selected to represent typical degraded lands (e.g., mine reclamation sites, degraded agricultural lands) near existing coal combustion plants where transportation costs and associated CO_2 emissions associated with application of coal-combustion byproducts and other amendments would be minimized. The results of this research would not be known for several years and would require support beyond the current 2-year term of the proposed work to be fully successful.

The *Technology and Information Transfer* component of this project communicates to industry stakeholders the practical value of new knowledge and innovative technical approaches to land management and fossil energy by-product use. The principal tool to be used will be interactive, or hands-on workshops that bring industry, FETC and CSiTE researchers together to communicate new information and discuss its applicability to regional and site-specific problems. This task will leverage parallel activities and partnerships established by CSiTE, including its Scientific Research Council, which is currently being organized and will include DOE-FE and industry representation. Building on a successful workshop held in October 2000, with representatives from the fossil energy industry and DOE, an interactive hands-on workshop is planned to address site-specific issues in land use and by-product utilization. This workshop is currently scheduled for November 2001 in Lexington, KY. The results of the

Technology and Information Transfer activities will be summarized as a technical report with recommendations for future research and transfer.

TECHNICAL PROGRESS

Scientific Component

The effect of organic amendments on the soil organic carbon (SOC) concentrations of reclaimed mine lands was examined at the Powel River Site in Wise, County, VA. Two experiments had been implemented at that coal mining experimental site by collaborators at Virginia Tech University. In both cases, limestone-dominated mine spoils were supplemented with organic amendments, as well as control plots without organic supplements. One set of experiments was begun in 1982, thus providing us with information on the effects over a 19-year period. The second experiment was begun in 1989, thus providing a temporal contrast in treatment effects.

The plots that were sampled in the 1982 experiments were selected to make the following comparisons on the types and rates of biosolid additions

- Sawdust versus sewage sludge
- 2 sludge rates (224 versus 56 Mg/ha)
- Control (inorganic fertilization)

The 1989 experiment used only one type of organic amendment, municipal sewage sludge, over a large (several hectare) area, as well as smaller dose-rate plots. The following comparisons were made on the effects of rates of biosolid additions:

- “regular” rate, 1.5X rate, and untreated control
- Compare wet (poorly drained) versus dry (well-drained) sites

Soil development and SOC profiles over 1-m depth were assessed by digging pits using a backhoe, which was required due to the presence of a large fraction of large rocks imbedded in the fine soil material. Analyses of the soil genesis and depth distribution of SOC have been completed. Analyses of other soil parameters (particle size, CEC, extractable metals, etc.) are in progress.

As expected, these mine soils are very rocky, ranging from 40 to 80% coarse fragments in all horizons described. The fine earth fraction (<2mm) is also relatively coarse with a sandy loam texture. All mine soils described had well-developed horizonation with clear A horizons and moderately well developed transitional AC horizons. The AC horizons in several of the 1982 pedons contained moderate structure and could possibly warrant description as weak B horizons (Bw). In the1982 experiment, soils receiving high amounts of either biosolids or sawdust contained A horizons that were darker than the control soils, and/or contained AC horizons with “browner” coloration. The wetter soil described in area D also exhibited distinct redoximorphic features due to what appears to be aquic soil conditions. Rooting was generally common to a depth of 35 to 50 cm in most soils observed, but was limited by densic (Cd) layers in several pedons. When compared with earlier soil descriptions from these same experimental areas, the mine soils observed are clearly progressing down a pedogenic pathway of continued darkening of the AC horizon and overall strengthening of structure grade in their A horizons.

The soil profile observed in the high biosolids rate plot is shown. Note the development of a distinct A horizon in the top 15-cm, with transition to an AC transition horizon. Note also the large number of large coarse fragments.

The changes in the SOC concentrations were evaluated. First, the temporal changes in the SOC in upper 15-cm was evaluated in the 1982 experiment, based on data collected in previous sampling. Clear effect of biosolids application, especially for the biosolids, compared to sawdust, treatment. Percent organic matter was determined by the Walkley-Black wet oxidation method.

Treatment	1982*	1983*	1984*	1987**	1998***	2001
	----------------------------% OM---------------------------					
CONTROL	1.0	2.0	2.2	3.2	3.9	4.2
Sawdust (112 Mg/ha)	7.4	9.3	8.5	7.3	4.3	3.3
Biosolids (56 Mg/ha)	3.2	5.1	4.8	7.9	4.4	5.9
Biosolids (224 Mg/ha)	6.0	6.7	6.4	7.1	nd	6.5

*Roberts, J. A. 1986. Mine soil genesis and tall fescue nutrient status as a function of overburden type and cultural amendment. M.S. Thesis, Virginia Polytechnic Institute and State University.

**Haering, K., W. L. Daniels, J. Torbert, and J. Burger. 1990. The effects of controlled overburden placement on topsoil substitute quality and bond release. Phase III. Final report for OSM Cooperative Agreement HQ51-GR87-10022. Department of Crop and Soil Environmental Sciences and Department of Forestry, Virginia Polytechnic Institute and State University.

***Bendfeldt, E.S. 1999. Dynamics and characterization of soil organic matter on mine soils 16 years after amendment with topsoil, sawdust, and sewage sludge. (nd = not determined)

The previous sampling at this site had been limited to only the surface soil, and had not considered the potential vertical movement of SOC through the soil profile. In considering C-sequestration, movement of SOC into deeper horizons would not only result in a greater total mass of carbon being sequestered, but because SOC buried in deeper horizons is generally considered to be less available for microbial degradation, that deeper SOC would be expected to represent long-term sequestration. To give a relative estimate of the total mass of SOC sequestered in the entire soil profile, the SOC concentration in each soil horizon (mass of carbon per mass of soil) was multiplied by the thickness of that horizon. Assuming some unit surface area, and assuming that the bulk density of the soils were equal between plots and with depth, this calculation would provide a comparison of the depth integrated measure of the mass of SOC in the different treatments. Note that the bulk density may not be constant, and differences in the bulk density are currently being analyzed. However, the patterns in the figure below illustrate the effects of treatments on C-sequestration in soil at these sites. SOC appears to have penetrated more deeply and to a higher mass content in the low-biosolids treatment, compared to the high-biosolids plots. This may be related to differences in the soil pH. These data are being analyzed, but the high-biosolids treatment is likely to result in higher soil pH, and SOC adsorption is known to decrease under more alkaline conditions. The high SOC level observed in the control plot for the C horizon may be related to possible background positive analytical errors in the Wakley-Black method due to the presence of certain mineral oxides. Ongoing analyses of extractable metal content should permit corrections for any such errors.

Analyses of the soil samples are continuing to provide data on other key soil parameters such as particle size, cation exchange capacity, etc. These data are critical to final interpretation of the SOC patterns and their implications concerning the effect of these treatments on the mass of SOC sequestered in these reclaimed mine lands.

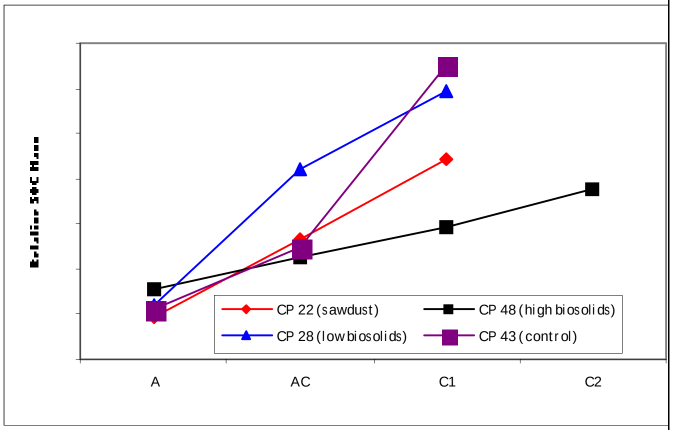

The cumulative mass of SOC though the 1-m deep soil profile of the 1982 experiment is estimated as a preliminary comparison of the different treatments on the depth distribution of SOC. The horizontal axis is the soil horizon designation (the surface soil is on the left, and deeper horizons on the right) Because the bulk density of the soil is not currently known, the mass of SOC is not quantified in the y-axis.

Several other degraded mine land field sites that received experimental treatments of flyash or biosolids amendments will also be samples, with special emphasis on obtaining information on the downward penetration of the organic matter or carbonate alkalinity to depth. Sites and treatments being examined include several experimental mine reclamation site in northern West Virginia. These sites contrast with the neutral-to-alkaline Powell River site in that flyash, rather than organic, amendments were placed over strongly acidic coal refuse. Because pH is know to be an important master variable controlling the extent of SOC adsorption to mineral surfaces, the comparison of the two field sites should provide important contrasts that will help delimit conditions favoring carbon sequestration in soil. Additional field sites will be analyzed in ongoing research.

Technology and Information Transfer Component

An organizational meeting was held on October 24, 2000 to discuss the technical scope and objectives, venue and approach for a regional "hands on" workshop in terrestrial carbon sequestration. The workshop was intended to facilitate partnerships among energy producers, land owners, the biomass and biofuels industry, and the terrestrial carbon sequestration research community by engaging stakeholders in a discussion of scientific and technical objectives for research in terrestrial carbon sequestration. This is to include identification of potential sites and experimental approaches for long-term field research focused on the use of fossil energy by-products and other amendments for reclamation of degraded lands and enhanced carbon sequestration. This workshop is planned for November 2001.

ENHANCED PRACTICAL PHOTOSYNTHESIS CARBON DIOXIDE MITIGATION

J. D. Muhs

INTRODUCTION

The project's purpose is to demonstrate that low-risk methods of Carbon Dioxide mitigation based on using existing biological organisms in an optimal way are capable of significant Carbon Dioxide uptake and offer a valid near-term solution for the Carbon Dioxide sequestration problem. Specifically, we will demonstrate the technical and economic feasibility of using an "optimized" enhanced photosynthesis system that (a) separates and uses various spectral regions of direct, non-diffuse sunlight to maximize cyanobacteria growth, (b) directly decreases Carbon Dioxide concentrations in the emissions of fossil generation unites, especially those in the Midwest for which ocean-based sequestration is not likely to be feasible, (c) reduce the required space needed (compared to other biological techniques) by a factor of 20, and (d) simultaneously produce enough electrical energy to partially self-power the entire sequestration system.

The approach for this project for FY 2001 begins with designing a hybrid solar photosynthetic CO_2 control system within 12 months.

Design the Lighting System: Preliminary estimates show that a hybrid solar photosynthetic CO_2 control system could potentially sequester CO_2 at a cost of \$5–8 per ton, which exceeds DOE's target of \$10 per ton. The key is the low cost of the power source to sequester CO_2, namely solar power. Clearly, better utilization of solar energy has a substantial economic gain that is realized in this application.

The results of an initial evaluation suggest that light collection and delivery losses in the proposed solar lighting system will be approximately 40%. This is due to the fact that once inside the bioreactor, light losses along its length are desirable. Losses cause fibers to emit light (glow like a linear fluorescent lamp). The estimated photon flux rate that is effectively used to achieve maximum photosynthetic efficiency is therefore 1200 μE m^{-2} s^{-1}.

For mesophilic cyanobacteria whose preferred photosynthetic flux rate is 60 μE m^{-2} s^{-1}, early estimates suggest that approximately 15 large-core fibers 5 mm in diameter, 6 m in length, and spaced 20 cm apart will deliver adequate lighting to achieve the desired spatial redistribution of 1 m^2 of direct sunlight into ~20 m^2 of vertically-stacked enclosed cyanobacteria growth area, i.e., $(0.60)(\mu E\ m^{-2}\ s^{-1})/20\ m^2 = 60\ \mu E s^{-1}$.

An optimization of the required size/configuration of a hypothetical hybrid solar photobioreactor based on an initial design is beyond the scope of this discussion and is the subject of one of our proposed tasks. However, we anticipate the size of the solar collector will likely be significantly larger than those designed for building applications because the space being illuminated is directly below the collector/receiver, minimal lateral light transport is required, and the overall spatial illumination requirements are conducive to such an arrangement. For the sake of comparative analyses, we assume that when in full production late this decade, the overall cost of the light delivery and power generation system will remain at ~\$1,000/m^2 of collected sunlight though the proportional component cost will shift.

Based on initial calculations, the proposed system applied to a 500 MW facility will provide 889,000 metric tons of sequestered CO_2, 505,000 metric tons of biomass, and 647,000 metric tons of regenerated O_2 per year, and require 10.2 MW of power to operate the system. Assuming a plant lifetime of 30 years and the previous example parameters, we first estimated an 8.8% auxiliary load for electric lighting, pumping, and dewatering at an average cost of \$0.035 per kW-h, a labor cost of \$1 per ton (mostly for hauling the dry biomass) and a comparable production price of a similar sized ESP (scaled by a factor of five (5) for the solar collectors), yields a maximum cost of \$15–\$16 per ton of CO_2 removed. The breakdown costs, per unit ton of CO_2 removed assuming no cost of capital, are \$4.50 capital cost, \$10 for operating costs, and \$1–\$2 for associated operating labor.

However, if no auxiliary lighting is used (as is the case in this project), the potential long term cost drops to only \$5–\$8 per ton including only \$1.50 per ton for power consumption because of the high level of self-generated (photovoltaic) power. Finally, while these numbers are only estimates, they are consistent with prior assumptions. The calculations for cost also do not include any potential revenue from the sale or use of the biomass, which would further reduce overall costs.

In addition, an operational photobioreactor will require power to run the auxiliary systems, including the harvesting and nutrient delivery systems. The use of photovoltaics will supply more than a quarter of the energy required to run all systems during the day when the loads are greatest.

Calculations based on earlier studies by Hirata et al. and Ohtaguchi et al. indicated that a little more than 1,000,000 m^2 bioreactor surface would be required to reduce the CO^2 emission of a typical 500 MW coal-fired generation unit by 25%. This translates into 257 acres of water surface area for a high-density raceway type reactor. Using the design of Bayless et al., incorporating the novel solar collection technology described herein, the required area decreases to 11.7 acres. In a more practical scenario that considers roof-top collector/receiver packing densities and other factors, the required space would likely increase to 15 acres. An enclosed reactor of this size may be formidable to site and construct, but is certainly manageable compared to siting and operating a 257 acre pond near a power plant, which would create numerous groundwater contamination concerns. Further, an enclosed reactor has a number of options for delivery of the CO_2, including as raw flue gas. Bubbling flue gas through a 257 acre pond would be illegal, as the ground level contamination would be pose extreme health threats to the area.

Therefore, a raceway reactor would require CO_2 separation before utilization, eliminating virtually any energy advantage of a bioreactor in CO_2 control.

Compared to previous attempts to develop similar solar-enhanced photobioreactors incorporating fresnel lenses and fiber optic bundles, the anticipated cost per delivered lumen (2.8 cents vs 20 cents) also represents a seven-fold improvement in the cost of sunlight utilization not including the added benefit of electrical power generation. Thus, the primary advantages are enhanced sunlight utilization and less power consumption.

Non-photosynthetic carbon sequestration is a significant net energy loss. Separation of CO_2 from the flue gas either requires refrigeration or mechanical action. The sequestration (compression or pumping) of the separated CO_2 also requires significant energy.

All totaled, CO_2 sequestration by non-photosynthetic means will require 25–40% of the power generated by a host utility compared to 2–5% for the hybrid solar photobioreactor. That means more fossil fuel will have to be burned to produce the same net power output before sequestration. This also has direct implications on the environment. Because more fuel must be burned to power the sequestration systems, more associated pollutants will be released, including ozone forming NO_x, mercury, PM.2.5 and other particulates. Only a system utilizing solar energy to produce biomass, as described in this project, will require minimal power generation to minimize CO_2 emissions and does not produce significant harmful emissions.

Compared to a utility-scale PV system of the same size that generates ~5 MW (peak) at a cost of $\$3–5/W_p$, the proposed system will remove carbon from approximately 125 MW (peak) fossil-based generated power using a net load of 10 MW. The estimated cost of proposed photobioreactor system is $3,000.00. Considering the size of the facility (54,000 m^2), this equates to an approximate two-fold improvement in cost, i.e. $[(\$3{,}300/m^2 \times 54{,}000\ m^2)/(125\ MW – 10\ MW)] = \$1.54/Wp$ of cleaned fossil-based power produced. As such, separation and use of different portions of the solar spectrum for different purposes improves the overall cost and performance of solar energy used at power plants. In addition to this advantage, biomass has inherent value beyond that of carbon sequestration. It can be used as a feedstock, agricultural supplement, food supplement, or in pharmacological uses. Third, coal must remain a viable fuel to maintain fuel diversity. Without coal, the long term (20+ years) price of electrical power will escalate at a dangerous rate, especially with regards to national economic growth. This system provides a critical component in the portfolio of carbon management techniques that will allow coal to remain viable (note, not favorable, just viable.)

DISCUSSIONS OF CURRENT ACTIVITIES

We are currently designing the solar collector and fiber optic lighting system for this project. Early prototype components are pictured below.

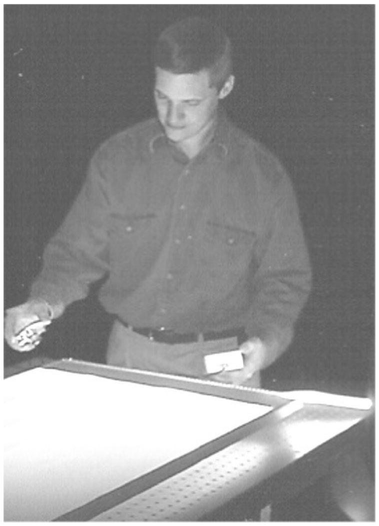

Fiber optic lighting system for lab-scale bioreactor.

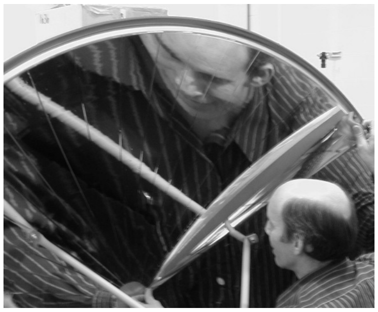

Primary mirror being coated.

Tracking system for collector.

ESTIMATION OF CARBON CREDITS IN CARBON DIOXIDE SEQUESTRATION ACTIVITIES

K. Thomas Klasson and Brian H. Davison
Oak Ridge National Laboratory, P.O. Box 2008-6226, Oak Ridge, TN 37831

INTRODUCTION

The United States may soon be focusing national attention on processes and activities that mitigate the release of CO_2 to the atmosphere and, in some cases may remove CO_2 from the atmosphere. As we invest national resources to these ends, it is important to evaluate options and invest wisely. How can we apply consistent standards to evaluate and compare various CO_2 sequestration technologies? A standard methodology that considers all the carbon impacts is needed. This would be useful for policy makers to understand the range of options and for technology developers and investors to guide investment decisions. It would also serve as a source of information for calculations or estimations of carbon credits in a future credit trading system.

Decisions on national policy and strategy for carbon management must take into account a variety of factors dealing with economic, environmental, and social impacts. Several of these issues are already pursued from a global perspective.

Traditional carbon accounting methods follow the approach for emissions accounting that is proposed by the Intergovernmental Panel on Climate Change (IPCC). Similar national accounting methods could be developed for carbon sequestration activities. These methods account only for the annual carbon emission reduction represented by sequestration activities. Carbon emissions that relate to energy use, transportation, raw materials, etc., to accomplish the sequestration are accounted for by other industries on a national basis. However, in order to compare different sequestration technologies, a more complete assessment methodology must be developed to assist in future decision-making processes. For example, if the operators of a coal-fired steam plant are considering implementation of either an off-gas CO_2 scrubbing technique or an algal pond strategy to reduce CO_2 emissions in order to get favorable treatment from a regulatory agency, the evaluation approach may be considerably different from the national accounting approach—especially if these sequestration technologies are moderate in size and do not significantly influence, on an individual basis, the national accounting calculations. Even if a national accounting strategy were used on a very localized zone, no clear method exists by which sequestration technologies should be compared regarding their effectiveness in achieving long-term sequestration. For example, is a method that sequesters CO_2 for an average of 200 years twice as good as one that sequesters it for 100 years?

Ideally, we would like to evaluate each sequestration technology based on the global impact on atmospheric CO_2 levels or on global warming. This, however, may not be a practical method for many activities. It is likely that short-term or more-limiting activities, not globally implemented, will not significantly alter the result predicted by global modeling efforts. Thus, we should develop a more generic approach that would be less labor intensive and yet provide some indication of technology benefits.

OBJECTIVE

Our objective was to develop a general methodology for evaluation of carbon sequestration technologies. We wanted to provide a method that was quantitative but that was structured to give qualitative robust comparisons despite changes in detailed method parameters—that is, it does not matter what “grade” a sequestration technology gets, but a “better” technology should always get a better grade.

The performance objective for a sequestration technology is not necessarily zero emission of CO_2 but rather a reduction compared with the baseline of current practice. To make sure that all carbon aspects are considered, care must be taken to ensure that there are no hidden emissions when making an alteration from the baseline. The fundamental question underlying an analysis of merit of a process or alteration of a process is as follows:

How much CO_2 is generated as a result of the operation (or change) of this process, and what is its ultimate fate?

Both inputs and outputs must be considered to obtain a total picture. When we speak of carbon sequestration, we refer to all greenhouse gas sequestration measured in carbon dioxide or carbon equivalence (CE). The carbon dioxide equivalence is also called the Global Warming Potential (GWP). A complete list of GWP values has been prepared by IPCC [1].

APPROACH

To address our objective, we have developed and elaborated on the following concepts:

- All resources used in a sequestration activity should be reviewed by estimating the amount of greenhouse gas emissions for which they historically are responsible. We have done this by introducing a quantifier we term *Full-Cycle Carbon Emissions* (FCCE), which is tied to the resource.
- The future fate of sequestered carbon should be included in technology evaluations. We have addressed this by introducing a variable called *Time-Adjusted Value of Carbon Sequestration* (TVCS) to weigh potential future releases of carbon, escaping the sequestered form.

- The *Figure of Merit* of a sequestration technology should address the entire life cycle of an activity. The figures of merit we have developed relate the investment made (carbon release during the construction phase) to the lifetime sequestration capacity of the activity. To account for carbon flows that occur during different times of an activity, we incorporate the *Time Value of Carbon Flows*.

The methodology we suggest does not rely on global atmospheric modeling efforts and can be expanded to include financial, social, and long-term environmental aspects of a sequestration technology implementation.

REFERENCE

1. *Climate Change 1995—The Science of Climate Change*, ed. Houton, J. T., Meira Filho, L. G., Callander, B. A., Harris, N., Kattenberg, A., and Maskell, K., Cambridge University Press, pp. 21–22 (1996).

METHANE HYDRATES IN SEAFLOOR SEDIMENTS

Olivia R. West, David R. Riestenberg, Scott McCallum, and Tommy J. Phelps

INTRODUCTION

The purpose of this project is to obtain thermodynamic stability conditions for methane hydrates in seafloor sedimentary materials. The data gathered are applicable to several technology areas concerning natural gas hydrate deposits including resource assessment, gas production, and mechanical stability of hydrate-rich sediments. Thermodynamic stability data are essential to resource assessment where these values are integrated with subsurface thermal and pressure gradients to delineate hydrate stability fields in seafloor or permafrost deposits (e.g., Collett, 1998). Stability data are also needed for evaluating the impact of climactic and oceanographic changes on natural gas hydrate deposits, particularly when there is a concern for their decomposition and resultant impacts on seafloor stability and the global climate (Kvenvolden, 1999).

An extensive thermodynamic and kinetic database exists for simple mixtures of methane or natural gas components and water, including hydrate inhibitors such as salts and alcohols (e.g., Sloan, 1990). However, thermodynamic and kinetic data are still lacking for natural gas hydrates in sedimentary environments where the effects of capillary pressure, pore water chemistry, and sediment/solid surfaces must be considered (Clennell et al., 1999). Among these factors, the effects of salinity have been experimentally determined (Dickens and Quinby-Hunt, 1994) and theoretically modeled (Dickens and Quinby-Hunt, 1997). Other pore water constituents (e.g., dissolved and suspended organic matter, pH) have not been investigated. The effects of capillary pressure have been modeled by Clarke et al. (1999) and Henry et al. (1999). Clark et al.'s model compared reasonably well with experimental measurements made by Handa and Stupin (1992) in 70-Å-radius silica gel pores. However, data for pore sizes more representative of sedimentary materials do not exist. The few published works on sediment/surface effects have conflicting results. For example, Cha et al. (1988) showed improved natural gas hydrate stability in bentonite/water suspensions, while Englezos and Hall (1994) found no enhanced effect. Clearly, there is a need for more experimental data that will establish the degree to which chemical and physical properties of sediment surfaces can affect the thermodynamic stability of methane hydrates. This need is addressed by the experiments reported here.

EXPERIMENTAL SYSTEM AND RESULTS

Experiments were conducted in the ORNL Seafloor Process Simulator (SPS, Fig. 1, Phelps et al, 2001) which consists of a 31.75-cm internal diameter, 91.4-cm long high-pressure vessel (max. pressure = 3000 psi) in an explosion-proof temperature-controlled chamber (2 to 10ºC). It is constructed of corrosion resistant Hastelloy C-22, and has numerous access ports for instrumentation and 4 sapphire windows for visual observation into the vessel. The vessel is equipped with gas delivery lines which allow vessel pressurization either through a gas diffuser near the bottom of the vessel, or through the top lid of the vessel (see Fig. 2). Vessel pressure is measured using a piezoelectric transducer (Precise Sensors, model 9112) with a working range of 0–20 Mpa (0–2900 psi). Internal fluid temperatures are measured using 3 Omega (Stamford, CT USA) type K thermocouples with Hastelloy sheaths calibrated to +/- 0.2°C.

Fig. 1. Photograph of the ORNL Seafloor Process Simulator facility showing the high-pressure vessel and temperature-controlled chamber.

Hydrates are formed in the vessel by actively bubbling methane gas through a porous disc at the bottom of a 4.8 cm x 60 cm glass column (see Fig. 2). The glass column was used for better visualization of hydrate formation in sedimentary materials. Furthermore, bubbling of methane within the glass column allowed better mixing whenever hydrates were formed in colloidal suspensions. Prior to bubbling, the vessel was filled with 55-57 L of water leaving about 15-20 L of gas headspace remaining (see Fig. 2). Plastic spacer disks were placed in the vessel to lower the gas headspace to about 5 liters, reducing the amount of gas needed to pressurize the vessel. The glass column was filled either with fine silica sand and water, or with a colloidal suspension (bentonite or silica at 34 g/L). The vessel was then pressurized with

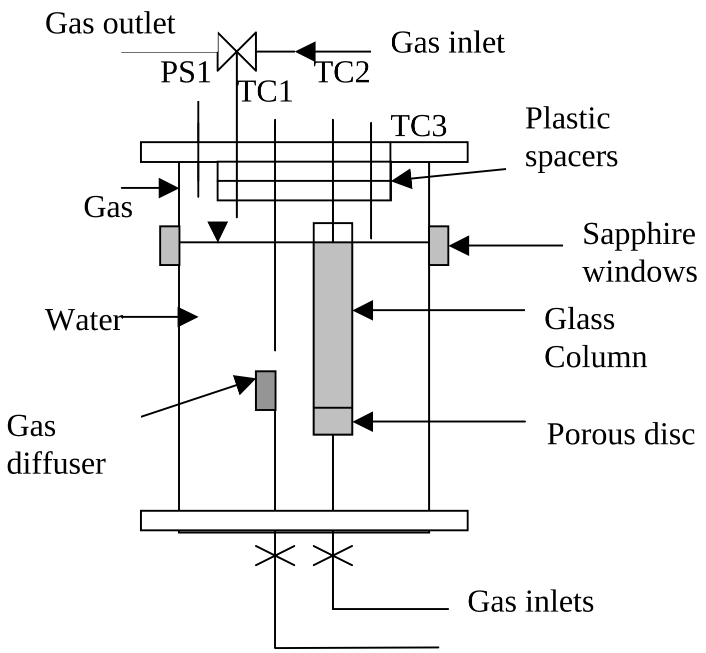

Fig. 2. Schematic of experimental set-up for methane hydrate experiments in the ORNL SPS. PS1 is pressure transducer; TC1-3 are thermocouples.

99.9% pure methane gas to about 500 psi and cooled to ~5°C for at least 12 hours to allow the system to equilibrate outside the bulk hydrate pressure and temperature formation conditions.

After the temperature of the vessel was equilibrated, two methods were used for forming hydrates. In the first method, methane gas was injected through the porous disc of the glass column with the vessel vent closed such that vessel pressure increased with time. In the second method used for later experiments, the vessel was pressurized to ~1000 psi with methane gas through the top of the vessel. Methane gas was then injected into the vessel through the glass column's porous disc at a rate of 500 sccm. During gas injection, the vessel vent was left open while a back pressure regulator installed on the gas outlet line was set to maintain vessel pressure at ~1000 psi. Prior to hydrate formation, methane gas bubbles would rise and burst at the gas/suspension/sediment interface. Eventually, these gas bubbles no longer burst and begin to accumulate (Fig. 3); the stability of these gas bubbles is attributed to the formation of a hydrate shell on the surface of the bubble. In the colloidal suspensions (see Fig. 3b), colloidal material appeared to be trapped within the interstices of the hydrate-encrusted bubbles. The accumulation of these bubbles often registered an increase in temperature as shown in Fig. 4. After 2–3 inches of hydrate-encrusted bubbles accumulate in the glass column, the gas flow through the column was stopped. The vessel pressure was then adjusted to a pre-selected experimental pressure by injecting or removing gas through the top lid of the vessel.

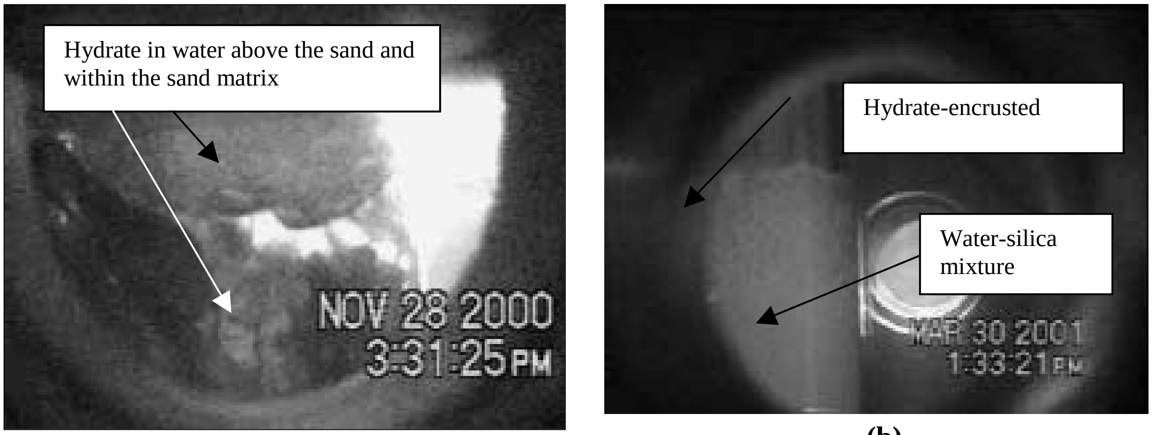

(a) (b)

Fig. 3. Hydrate formation in (a) a sandy matrix, and (b) in a colloidal silica-water suspension. Photographs taken through the sapphire windows of the SPS.

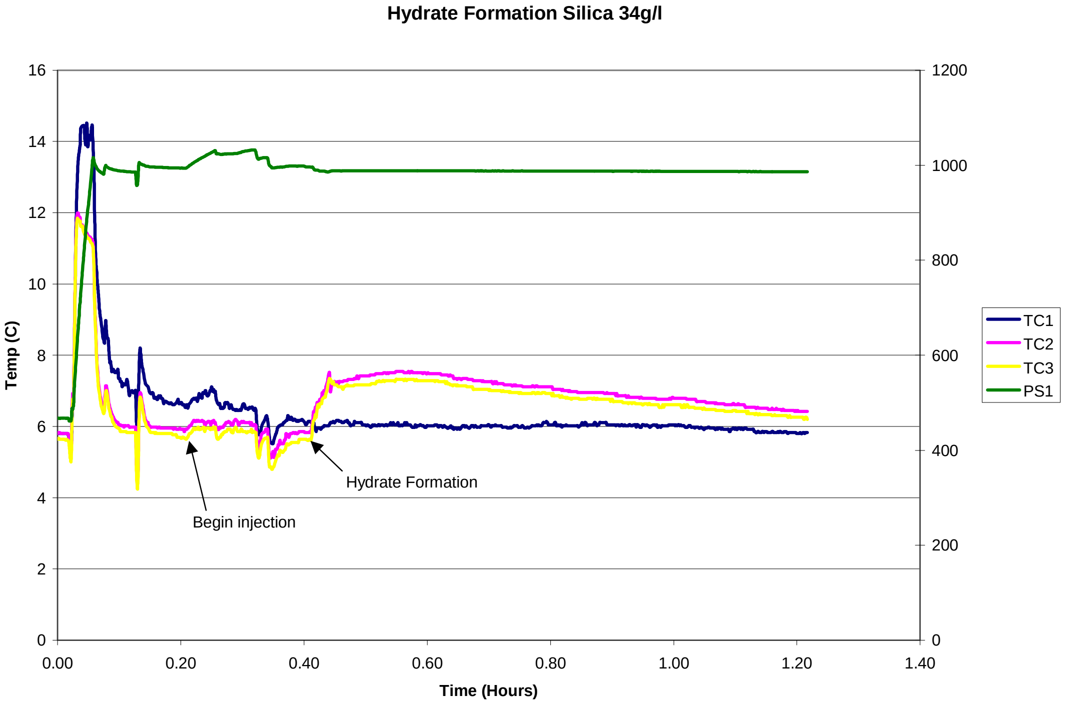

Fig. 4. Temperature and pressure measurements during hydrate formation in a silica-water suspension. PS1–vessel pressure, TC1–gas/headspace temperature, TC2 and TC3–hydrate zone temperature.

Hydrate dissociation conditions were measured by warming the vessel after a mass of hydrates was produced as described above. Warming was achieved by turning off the cold room refrigeration system. The average rate of temperature increase in the vessel was either 0.5 to 1C/h when the cold room door was left closed, or 2C/h when the cold room door was left open. Three thermocouples were located within the vessel: one was located within the vessel headspace, while two were positioned right at the gas/sediment/suspension interface in the glass column (see Fig. 2). Because hydrate-encrusted methane bubbles accumulated at this interface, the thermocouples at this location were intended to measure temperatures within the hydrate zone. As the vessel was warmed and the gas temperature rose, one or both thermocouples in the hydrate zone would plateau for a period of time (see Fig. 5); this "flatlining" was taken as an indication of hydrate dissociation and the absorption of latent heat. During warming, pressure within the vessel would stay relatively constant, increasing by less than 100 psi for the duration of the dissociation experiment. The "flatline" temperature and corresponding pressure were taken as the hydrate dissociation pressure/temperature conditions.

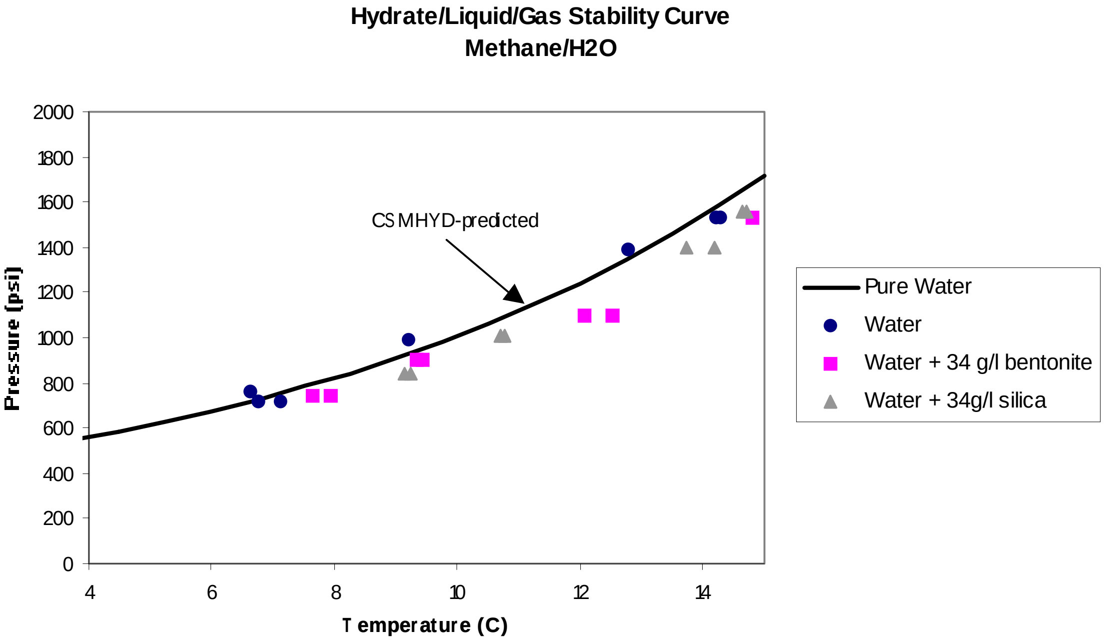

Fig. 5. Effect of colloidal sedimentary particles on the stability of methane hydrates. P-T line for pure water obtained using CSMHYD (Sloan, 1990); data points obtained from experiments in the ORNL SPS.

Based on experimental results to date, the stability of methane hydrates appear to be affected by the presence of colloidal sedimentary materials (see Fig. 5). For example, the measured hydrate dissociation temperatures in the silica suspension were 13.7 and 14.2C at 1400 psi, compared to 12.8C measured in water alone. In addition, similar behavior was observed for both the colloidal silica and bentonite experiments. These results are significant because hydrates are typically found in sandy matrices with high percentages of fine grained silt and clay (Booth et al., 1996). The measurements conducted in the fine sand did not show any significant differences from water (experimental data not shown); this result is not surprising given capillary pressures in a fine sand may not be high enough to impose a significant effect.

Further experimental work is being conducted to determine the effects of carbonate particles and natural organic matter on methane hydrate thermodynamics. Efforts are also underway to determine the underlying mechanisms for the apparent increase in hydrate stability in the presence of sedimentary materials.

PUBLICATIONS

Phelps, T. J.; Peters, D. J.; Marshall, S. L.; West, O. R.; Liang, L.; Blencoe, J. G.; Alexiades, V.; Jacobs, G. K. 2001. "A new experimental facility for investigating the formation and properties of gas hydrates under simulated seafloor conditions," Rev. Sci. Instrum., 72, 1514–1521.

Riestenberg, D.; West, O. R.; McKinney, M.; Liang, L.; Phelps, T. J. 2000. "Effects of sediment grain size and mineralogy on methane hydrate stability under simulated seafloor conditions," American Geophysical Union Fall Meeting, 2000, San Francisco, CA.

REFERENCES

Booth, J. S.; Rowe, M. M.; Fischer, K. M. 1996. "Offshore gas hydrate sample database with an overview and preliminary analysis," U.S. Geological Survey, Open-File Report 96–272.

Cha, S. B.; Ouar, H.; Wildeman, T. R. and Sloan, E. D. 1988. "A third-surface effect on hydrate formation," J. Phys. Chem. 92, 6492–6494.

Clarke, M. A.; Pooladi-Darvish, M.; Bishnoi, P. R. 1999. "A method to predict equilibrium conditions of gas hydrate formation in porous media," Ind. Eng. Chem., 38, 2485–2490.

Clennell, M. B.; Hovland, M.; Booth, J. S.; Henry, P. and Winters, W. J. 1999. Formation of natural gas hydrates in marine sediments, 1. Conceptual model of gas hydrate growth conditioned by host sediment properties," Journal of Geophysical Research, Vol. 104, No. B10, 22, 985–23,003.

Collett, T. S. 1998. Methane Hydrate: An Unlimited Energy Resource? JNOC-TRC, Japan.

Dickens, G. R.; Quinby-Hunt, M. S. 1994. "Methane hydrate stability in seawater," Geophysical Research Letters, 21, 2115–2118.

Dickens, G. R.; Quinby-Hunt, M. S. 1997. "Methane hydrate stability in pore water: A simple theoretical approach for geophysical applications, " Journal of geophysical research, Vol. 102, No. B1, 773–783.

Handa, Y.; Stupin, D. 1992. “Thermodynamic properties and dissociation characteristics of methane and propane hydrates in 70-A-radius silica gel pores,” J. Phys. Chem. 96, 8599–8603.

Henry, P.; Thomas, M.; Clennell, M. B. 1999. “Formation of natural gas hydrates in marine sediments, 2. Thermodynamic calculations of stability conditions in porous sediments,” Journal of Geophysical Research. 104, 23,005–23,002.

Kvenvolden, K. 1999. Potential effects of gas hydrate on human welfare. Proc. Natl. Acad. Sci USA, 96, 3420–3426.

ENVIRONMENTAL ANALYSIS SUPPORT

R. L. Miller

Activities in environmental analysis support included assistance to the National Energy Technology Laboratory (NETL) at Morgantown and Pittsburgh in reviewing and preparing documents required by the National Environmental Policy Act (NEPA) for projects selected for the Clean Coal Technology (CCT) Program and for the Low Emission Boiler System (LEBS) Program. An important activity for the CCT Program was the preparation of an Environmental Impact Statement (EIS) for a project to demonstrate the integration of a direct ironmaking process with the production of electricity at Geneva Steel's existing plant in Vineyard, Utah. An important activity for the LEBS Program was the preparation of an EIS for integrated coal-fired technologies for electric power generation at the proof-of-concept scale adjacent to the Turris Coal Company's existing underground coal mine near Elkhart, Illinois.

ENVIRONMENTAL SUPPORT TO THE CLEAN COAL TECHNOLOGY PROGRAM

Work for the National Energy Technology Laboratory (NETL) during this period included the preparation of an Environmental Impact Statement (EIS) to evaluate the potential environmental effects associated with constructing and operating a project selected by DOE under the Clean Coal Technology (CCT) Program. The project would demonstrate the integration of a direct ironmaking process with the production of electricity using coal in an efficient and environmentally responsible manner. Direct ironmaking eliminates the intermediate step of producing coke from coal. The EIS will be used by DOE in making a decision on whether or not to provide cost-shared funding to design, construct, and demonstrate the HIsmelt (High Intensity smelting) technology proposed by the CPICOR Management Company at Geneva Steel's existing plant in Vineyard, Utah. CPICOR is an acronym for Clean Power from Integrated Coal/Ore Reduction. The site is located immediately west of Orem, Utah, about 5 miles northwest of Provo, Utah, and about 35 miles south-southeast of Salt Lake City. The proposed project would be demonstrated during a 2- to 4-year period starting in February 2004.

The overall objective of the project is to demonstrate the feasibility of the HIsmelt technology at a size large enough to allow the ironmaking industry to make decisions regarding commercialization of the technology. The new HIsmelt facility would use iron ore and coal to produce about 3,300 tons of molten iron per day. Consequently, the existing blast furnace No. 3 would be placed in standby status (i.e., it would not operate whenever the HIsmelt facility is operating), while blast furnaces No. 1 and No. 2 would be available to continue in operation without modification. Offgas from the HIsmelt facility would be used as a fuel in the existing boilers to produce steam for in-plant use by Geneva Steel and to generate electricity using a combination of new and existing turbines. Most of the electricity would be used for internal process needs at the Geneva Steel plant, and the remainder would be available for export to the existing power grid. Following a successful demonstration of the proposed project, it is anticipated that the existing coke ovens at the plant would not be replaced as they reach the end of their useful life. The project is expected to provide Geneva Steel and offsite consumers with a low-cost, efficient, and environmentally sound source of additional electric generating capacity.

The HIsmelt technology produces molten iron directly from iron ore and coal in a single integrated operation, which eliminates the intermediate step of producing coke from coal. Iron ore, coal, fluxes (i.e., limestone, dolomite, lime, and dolime) and oxygen-enriched hot air are injected into a closed molten-bath reactor. The metal bath is the primary reaction medium in which carbon from the coal reduces iron ore to iron. The fluxes keep the materials molten in the reactor. Molten iron that collects in the bottom of the bath is continuously tapped from the reactor vessel to maintain a constant level of iron inside the vessel. Slag (the molten by-product generated from coal ash, fluxes, iron oxide, and other impurities) is tapped periodically and used to coat and control the internal cooling system and reduce heat loss.

The reactor vessel is aligned vertically in the HIsmelt technology. The coal is injected into the bath where carbon in the coal dissolves rapidly. The dissolved carbon reacts with oxygen from the injected iron ore to form carbon monoxide and iron. The high-temperature reactions release large quantities of buoyant coal gases (e.g., carbon monoxide and hydrogen) that create a large liquid fountain as they entrain and propel droplets of slag and molten iron upward into the post-combustion zone of the vessel. The result is strong mixing within the metal bath, which provides thermal uniformity. Because the iron reduction reaction in the molten bath is endothermic, additional heat must be generated and returned to the bath to sustain the reduction process and maintain an acceptable hot metal temperature. This additional heat is generated in the post-combustion zone by combusting the carbon monoxide and hydrogen released from the bath with oxygen-enriched hot air blast (2,200°F) that is injected down through piping from the top of the vessel. This reaction heats the metal and slag droplets in the post-combustion zone which, in turn, heat the bath after gravity returns them to the bath. Oxygen enrichment of the hot air blast increases the productivity of the process. Reacted gases, mainly nitrogen, carbon dioxide, carbon monoxide, hydrogen, and water vapor exit the vessel. After scrubbing the reacted gases, the cleaned gases can be combusted to generate electricity. The cleaned gases can also be used to pre-heat and partially pre-reduce the incoming iron ore.

The HIsmelt process possesses several advantages over conventional processes. Because it uses a high-temperature reactor vessel (up to 5,000°F) and eliminates the intermediate step of producing coke from coal, many of the air emissions and solid waste streams associated with traditional coke plant operations are eliminated. The high temperature breaks down and destroys hydrocarbons (e.g., toluene, benzene, and phenols) to minimize hazardous air pollutants typically emitted by coke ovens at temperatures less than 2,800°F. Because the high temperature of the reactor vessel exceeds the threshold for condensation of alkalis, problems in blast furnaces associated with alkaline iron ores and coals from the western United States are eliminated. The process is responsive to short-term operational problems because it can be shut down rapidly and easily restarted. Process efficiency is improved by capturing and recycling particulate matter.

Work on the EIS has included the initial evaluation of environmental issues that could result from construction and operation of the proposed project. During the scoping process at the beginning of work on the EIS, local residents were encouraged to express their concerns about potential effects. The issue of most concern was the potential impact to air quality from the proposed project's emissions. Other concerns that were expressed during the scoping process were the proposed project's use of coal; potential effects of the project on human health; potential impacts of the project on the water quality of the nearby Utah Lake; potential effects on wetlands; transportation, handling, and use of hazardous materials; issues associated with emergency preparedness and response; changes in the types and number of jobs associated with the proposed project; a possible decline in housing values; and potential visual impacts. The public input obtained during the scoping process was used to add to the list of issues requiring assessment. Issues are analyzed in the EIS in accordance with their level of importance. The most detailed analyses focus on issues associated with air quality impacts.

In addition to the proposed project, the no-action alternative (including two reasonably foreseeable scenarios) is being considered in the EIS. Under the no-action alternative, DOE would not provide funding to demonstrate the integration of the HIsmelt direct ironmaking process with the production of electricity. In the absence of DOE funding, there are two options that Geneva Steel could reasonably pursue: (1) Geneva Steel could continue to operate the blast furnaces using the existing coke ovens and importing coke, as needed; and (2) Geneva Steel could modernize the existing blast furnaces to lessen the requirements for coke and install new cokemaking facilities with state-of-the-art pollution controls that are needed to comply with the National Emissions Standards for Hazardous Air Pollutants.

ENVIRONMENTAL SUPPORT TO THE LOW EMISSION BOILER SYSTEM PROGRAM

Work for the National Energy Technology Laboratory (NETL) during this period included the preparation of an Environmental Impact Statement (EIS) to evaluate the potential environmental effects associated with constructing and demonstrating a new coal-fired Low Emission Boiler System (LEBS) for electric power generation at the proof-of-concept scale. The EIS will be used by DOE in making a decision on whether or not to provide cost-shared funding to design, construct, and demonstrate the integrated technologies proposed by a team headed by DB Riley, a private sector participant in the LEBS Program. The goal of the LEBS Program is to provide the U.S. power industry with a reliable, economic, highly efficient, and environmentally preferred alternative to current coal utilization technologies.

The proposed project would demonstrate the technologies using a new 86-MW coal-fired power plant to be built adjacent to an existing underground coal mine owned and operated by Turris Coal Company, a member of the project team. The site is situated in central Illinois, about 2 miles southeast of the town of Elkhart and about 17 miles northeast of Springfield. The project would incorporate the following technologies: (1) a slagging combustor, which is U-shaped to increase the combustion reaction time; (2) low oxides of nitrogen (low-NO_x) burners, staged combustion, and coal reburning (injecting about 10–15% of the coal higher in the combustor) for NO_x control during combustion, in combination with a selective catalytic reduction (SCR) post-combustion NO_x control system; (3) a wet limestone scrubbing system for sulfur dioxide (SO_2) capture; and (4) an electrostatic precipitator for particulate removal from the flue gas. The technologies are expected to capture at least 96% of SO_2 emissions, decrease NO_x emissions by 85%, and remove 99.8% of particulate matter.

The proposed project would be demonstrated during a 6-month period in late 2003 and early 2004. The facility would be fueled with coal from the adjacent mine, and electricity generated by the facility would be provided to the mine and to the local power grid. The captured SO_2 would be converted to commercial-grade gypsum, which would be marketed as feedstock for wallboard production. Bottom ash from coal combustion would be marketed for commercial applications such as a road base or construction material.

Potential impacts to environmental resources, including air quality, groundwater, and land availability, that could result from construction and operation of the proposed project were analyzed. Key findings include that emissions from the proposed facility would not exceed National Ambient Air Quality Standards (NAAQS) or Prevention of Significant Deterioration (PSD) increments. For the latter set of standards, the emissions would be less than 20% of the allowable degradation. The contribution of emissions from the proposed facility to acidic deposition and to global climate change is expected to be negligible.

Initial results indicate that the aquifer may be capable of supporting the additional requirements of groundwater withdrawal during facility operation, but declines in groundwater levels may occur in nearby water supply wells, including the village of Elkhart municipal water well, located approximately 1 mile west of the proposed site. In addition, the relatively large additional consumption could degrade water quality in the aquifer, resulting in increased total dissolved solids, heavy metals, and dissolved minerals. However, the effects of drawdown and groundwater quality degradation can be mitigated somewhat by using multiple wells for groundwater withdrawal with sufficient separation from the village of Elkhart well. In addition, the use of field drainage runoff that passes through the Turris property is being pursued as a mitigation measure that could supplement groundwater withdrawal.

With the construction of a new coal combustion waste disposal area at the adjacent mine, sufficient disposal capacity would be available to accommodate all solid wastes generated by the proposed facility during its 30-year commercial operation, even if no bottom ash or gypsum were sold or used. If the proposed waste disposal area is not constructed, the Turris Coal Company would have other options to dispose of the material, including (1) reducing the current level of coal combustion ash received from offsite customers, and (2) transporting solid waste off the site to a permitted landfill.

Impacts to other resource areas would be minor. Flooding at the site is not anticipated, and floodplain encroachment would not occur. There are no significant wetland resources near the proposed site. No appreciable impacts on terrestrial or aquatic ecosystems are expected. There are no historic or archaeological resources known to occur on the project site. Construction and operation of the proposed facility are anticipated to have only minimal impacts on socioeconomic factors in the surrounding area, and no environmental justice impacts are expected. With respect to aesthetic resources, construction of the proposed project would produce slight short-term visual impacts, but visual characteristics would not differ appreciably over the long term from those at the site now. No appreciable impacts are expected with regard to noise, traffic, land use, and human health including worker safety.

ADVANCED COMPUTATIONAL TOOLS FOR 3-D SEISMIC DATA FUSION

D. B. Reister, E. M. Oblow, J. Barhen, and J. B. DuBose, Jr.

The objective of this effort is to develop and test advanced computational tools for data fusion in 3-D seismic analysis. Research focuses on one task: application of novel global optimization methods to residual statics in seismic imaging. During the period covered by this report, we have completed the task. This report will have one section.

1. GLOBAL OPTIMIZATION

Since the objective function that is used to estimate surface-consistent residual statics can have many local maxima, a global optimization method is required to find the optimum values for the residual statics. As reported in several recent papers, we had developed a new method (TRUST) for solving global optimization problems and had demonstrated it was superior to all competing methods for a standard set of nonconvex benchmark problems. The residual statics problem can be very large with hundreds or thousands of parameters and large global optimization problems are much harder to solve than small problems. To solve the very challenging residual statics problem, we have made major improvements to TRUST (Stochastic Pijavskij Tunneling) and we have made several significant advances in the mathematical description of the residual statics problem (derivation of two novel stack power bounds and disaggregation of the original problem into a large number of small problems). Using the enhanced version of TRUST, we have performed extensive simulations on a realistic sample problem that had been artificially created by large static disruptions. Our simulations have demonstrated that TRUST can reach many plausible distinct "solutions" that could not be discovered by more conventional approaches.

During the period covered by this report, we have had a paper published by the leading journal in the field (**Geophysics**) and received a patent.

2. PUBLICATION

Reister, D., J. Barhen, J. DuBose, and E. Oblow. Global Optimization to Maximize Stack Energy, **Geophysics**, 66, 320–326 (2001).

3. PATENT

D. B. Reister, J. Barhen, and E. M. Oblow, "Method for using global optimization to the estimation of surface-consistent residual statics" Patent Number: 6,188,964 B1.

Date of Patent: February 13, 2001.

NATURAL GAS AND OIL TECHNOLOGY PARTNERSHIP SUPPORT

T. W. Schmidt

PARTNERSHIP SUPPORT

The Natural Gas and Oil Technology Partnership expedites development and transfer of advanced technologies through technical interactions and collaborations between nine national laboratories and the petroleum industry (majors, independents, service companies), and universities.

The Partnership combines the expertise, equipment, facilities, and technologies of the U.S. Department of Energy's national laboratories with those of the US petroleum industry. The laboratories utilize unique capabilities developed through energy and defense research and development, including electronics, instrumentation, materials, computer hardware and software, engineering, systems analysis, physics, and expert systems. Industry contributes specialized knowledge and resources and prioritizes Partnership activities.

The areas of technology are as follows:

- **Diagnostics and Imaging Technology** addresses cutting-edge geophysical methods for improved reservoir characterization with a focus on improved borehole hardware and computational efforts for seismic processing and other exploration issues. The Partnership catalyzed formation of a 25-company collaboration, which has become the industry focal point for this technology.
- **Oil and Gas Recovery Technology** addresses a broad range of technologies aimed at improving production from existing fields and with specific emphasis on assisting independent producers. The industry interface is an Industry Review Panel consisting of more than 20 individuals representing independents, majors, and the service companies.
- **Drilling, Completion, and Stimulation Technology** aims at better access to the reservoir through improved drilling and completion technologies. Currently, the laboratories participate in several joint industry projects fostered by two industry organizations: the Drilling Engineering Association (DEA) and the Completion engineering Association (CEA).
- **Environmental Technology** addresses new technologies that are needed to produce more oil and gas from mature domestic sources while safeguarding the environment. Key issues to be addressed include:
  - – produced water
  - – stationary source emissions
  - – risk assessment

  - tank bottoms and sludge
  - naturally occurring radioactive material (NORM)
  - soil remediation
  - vapor recovery
  - offshore structure decontamination and dismantlement (D&D)
  - drilling wastes.
- **Downstream Technology** is a new area of technology that was funded under the NGOTP for the first time in Fiscal Year 1999. Projects were funded in the areas of bioprocessing of heavy oils and the monitoring of $PM_{2.5}$ particulate.
- **Ultra-Clean Fuels Technology** is a new area of technology that is being coordinated under the NGOTP for the first time in fiscal year 2000. Eight new projects have been funded in fiscal year 2001. These projects were selected based on industry needs from a technology roadmap prepared with the help of the petroleum industry.

FUNDAMENTAL CHEMISTRY OF HEAVY OIL

W. V. Steele

INTRODUCTION

Catalytic hydroprocessing continues to be the core method for upgrading of feedstocks with high aromatic content. European environmental organizations have already established standards in this area and the US is expected to follow in the near future. The reduction of aromatics in heavy petroleum upgrading will require careful management of hydrogen during hydroprocessing. Effective hydrogen management requires an understanding of the relationship between the distribution of the hydrogenated products in the process streams and the conditions of their formation, i.e., temperature and pressure.

To counteract the adverse effects of carbon rejection methods, refiners have the option of hydrogen-addition (hydroprocessing) methods. However, hydroprocessing consumes large quantities of hydrogen. As refineries reconfigure to produce the new “clean fuels” (“reformulated fuels,” i.e., those with oxygenates present), hydrogen shortages are occurring, and new sources of supply are required. The addition of oxygenates to gasoline means that less octane is required from the reformer, lowering the severity of the operation and the amount of hydrogen formed. Also, the mandated reduction of aromatics content by the U.S. government in the 1990 Clean Air Act Amendments has resulted in a further reduction of reformer operating severity, hence, severely reducing hydrogen production. Other contributions to the problem in managing hydrogen result from mandated lower gasoline temperature endpoints and reduced sulfur levels. Hence, the use of hydrogen exactly where it will “do the most good” is paramount. Overhydrogenation will have to be minimized.

DISCUSSION OF CURRENT ACTIVITIES

Background

Worldwide demand for petroleum products continues to expand as the nations develop. However, if the demand is analyzed in terms of the three major classes of petroleum cuts: light products such as gasolines; petrochemical feedstocks, middle distillates such as jet fuels and diesels; and heavy products such as fuel-oils and lubricants; then there has been a drastic shift in emphasis toward the light end. Whereas in 1972 both the light products and the middle distillates accounted for approximately 30% by mass of the market, by 1990 they had each risen to approximately 36% of the market. Analysts believe that by the turn of the century the light products will have 38%, the middle distillates 40%, leaving only 22% for the 1973 major component the heavy-ends.

Whether it is an East Coast refinery importing crude oil from Nigeria, or a U.S. Gulf Coast refinery importing crude oil from Saudi Arabia, or even a U.S. West Coast refinery operating on Alaskan North Slope crude, over the last decade or more for which records are available (1986–96), the quality of the crude oil processed by refineries has declined. If the decline in the quality of crude processed in U.S. refineries is denoted in terms of the API gravity, the gravity has decreased by an average of 0.15° per year in the decade 1986–95.[1] Furthermore, the decline appears to have accelerated back to the rate applicable in the early 1990's. Measured as a five-year average (1989–93), the API gravity had declined by 0.22° per year. After leveling at 31.3° for the next four years, in 1996 it was back on the line pointing to a value of 30.5° for the API gravity in the year 2000. As the API gravity of crude oil falls, the aromatic content (carbon content) increases and the correlations derived for the light crudes begin to breakdown. The failure of the correlations is well documented in the literature. New or revised correlations are necessary for continued high thermal efficiency in the refining of present and future crudes.

Within the petroleum industry, catalytic hydroprocessing continues to be the core method for upgrading of feedstocks with high aromatic content, as well as for heteroatom removal through HDS and HDN. Meetings such as the 3-day symposium "Recent Advances in Heteroatom Removal" presented at the Division of Petroleum Chemistry meeting as part of the ACS biannual meeting held in Dallas March 1998 demonstrate the extensive interest by the petroleum and catalysis industries in this area. In a review of fuel-quality specification for transportation fuels, Touvelle et al. of Exxon Research and Engineering discussed trends in the regulation of aromatics in fuels. Although benzene content is carefully scrutinized, the total aromatics content is not regulated specifically in the US. In contrast, European environmental organizations have already established standards in this area and the US is expected to follow in the near future.

The reduction of aromatics in petroleum and particularly in heavy petroleum will require careful management of hydrogen during hydroprocessing. Effective hydrogen management requires an understanding of the relationship between the distribution of the hydrogenated products in the process streams and the conditions of their formation, i.e., temperature and pressure. To meet this need a dual-track approach involving both state-of-the-art property measurement and advanced Ab Initio computations is proposed.

The property measurement program previously funded by DOE Fossil Energy in Oklahoma has accumulated extensive results for partially hydrogenated two, three and four-ring aromatics. The majority of these results have not been published; particularly those which allow calculation of hydroaromatic distributions under processing conditions. Ab Initio computational coding is in its infancy in this area. Accurate atomistic modeling of hydroaromatic systems will use the codes and techniques we have developed for parallel molecular simulations on the ORNL Paragons and other parallel supercomputers.

Using our simulation capabilities, we believe we can substantially surpass the best prior efforts in realism and quantitative, predictive accuracy. These simulations will build on existing ORNL world-class efforts on simulating high temperature liquid and supercritical aqueous systems.

The experimental database and the fundamental understanding from the simulations will be brought together to develop useful models for correlating data and predicting stability under hydroprocessing conditions. The two fundamental questions to be address in this research are: (i) What are the “ideal conditions” for meeting low aromatics levels and still meet sulfur levels, smoke point etc., (ii) How does the model react to changes in the complex heterogeneous and multi-component systems (i.e., addition of a new crude oil from say Nigeria to the refinery)?

Results from this research will allow the industrial participants to lead the field in catalyst development and process condition controls in processing particularly middle distillates. It can be anticipated that severe operating conditions such as high temperatures, low space velocities, and high pressures can be mediated as the result of insights developed within the program. For example at low temperatures and high space velocities the amount of monoaromatics in the product can be higher than in the original feed. This is not unexpected since every mole of triaromatic compound that is saturated would add a mole to the diaromatics, each diaromatic compound hydrogenated would add a mole to the monoaromatic category, and as the number of rings decrease the rate of saturation should also decrease. Interaction between the various options can be simulated in the model and options such as increased catalytic activity balanced again two- or even three-stage process designs.

Progress

Work is in progress on a number of fronts within this project. An initial literature search is being performed to ascertain the relative importance of various aromatic compounds and sulfur-containing compounds in the range of heavy petroleum being imported to refineries in the U.S. Emphasis will be placed on finding the degrees of condensation and substitution of the compound types. The results of the study will be used to define the scope of the experimental work and the reaction schemes to be studied. Available literature data is being collected and process conditions defined were applicable. Properties for the majority of the species have not been published in the open literature, particularly those that allow calculation of hydroaromatic distributions under processing conditions. Hydroaromatic distributions will be derived where possible and a list of gaps in the database highlighted. This work will conclude with the reporting of sets of compounds to be studied to widen the applicability of the derived correlations.

Work is also in progress to ascertain the practicality of using the range of heavy petroleum being imported to refineries in the U.S. to produce both 5ppm sulfur gasoline and a “clean diesel” with the following specifications:

50 ppm sulfur with
lower density
lower PAH (polyaromatic hydrocarbons)
lower boiling point
and higher cetane number

than the "best" diesel being produced for the California market. Preliminary results of calculations of the conditions necessary to obtain various sulfur levels in diesel using hydrodesulfurization are given in Table 1. In the table the baseline is assumed to be the conditions (temperature/pressure/catalyst activity) required to produce 500ppm sulfur diesel.

Table 1. Conditions necessary to produce certain sulfur ppm levels in diesel

Sulfur content	Catalyst activity	Temperature F	Hydrogen pressure
Baseline 500 ppm	100%	Baseline	Baseline
350 ppm	130%	+15 F	120%
200 ppm	190%	+30 F	170%
100 ppm	300%	+ 55 F	300%
50 ppm	450%	+ 70 F	600%

To obtain the required sulfur level only one of the listed options would be required. Obviously the hydrogen pressure increase option is not realistic. Note also that the increase in temperature would mean that the amount of aromatics would increase requiring even greater hydrogen pressure to premeditate the effect.

Another option other than hydrodesulfurization to meet the sulfur level is alkylation of the sulfur-containing molecules raising the boiling point of sulfur-containing fraction and removing the sulfur in the resid. Or, the sulfur-containing compounds can be removed by selective adsorption using a catalyst containing a zero-valent transition metal. Both methods of sulfur removal are being presented by refiners at present as new technology options. Results from this research project will aid in both research areas (property measurements will give examples of boiling point of substituted benzothiophenes with both degree of substitution and actual position of substitution). Initial calculations point to several metals being particularly capable of reversible adsorption of benzothiophenes and dibenzothiophenes under very moderate reaction conditions. Further computational chemical calculation during FY2001 will expand on these initial ideas.

Finally work is also in progress on what the PI of this project calls "The 2015 Refinery" where all processes within the bounds of the refinery are as environmentally sound as possible. The 2015 refinery would for example not have any alkylation units with the associated problems of H–or H_2SO_4. Fuels would be manufactured via olefin formation and upgrading. Possibilities then increase of producing “zero sulfur” gasoline and even cleaner-burning naphthenic fuels.

REFERENCES

1. Swain, E. J., *Oil & Gas Journal*, November 10, 1997: pp. 79–82.

BIOLOGICAL UPGRADING OF PETROLEUM FEEDSTOCKS AND HEAVY OILS

Abhijeet. P. Borole

INTRODUCTION

Bioprocessing offers a practical alternative to thermochemical treatment of petroleum in certain niche areas such as sulfur and other heteroatom removal. Reduction in allowable sulfur in transportation fuels beginning 2005 has created an urgent need for a technology, which can greatly reduce the sulfur content of the fuels. Although bioprocessing provides a viable alternative to achieve this, significant fundamental issues are yet to be addressed. These issues are centered around the complexity of petroleum and the need to create biocatalysts capable of attacking the numerous compounds present in petroleum.

During the last year, we have dedicated our efforts in two different directions. One is to develop improved microbial biocatalysts for handling the broad substrate specificity as well as to achieve improvements in activity in petroleum biodesulfurization. This project is being funded by the Office of Industrial Technologies–Petroleum Industries of the Future. The other project is aimed towards the development of a technology using enzymes as biocatalysts instead of whole cells. The enzyme technology would be simpler in the application sense since it would not require an aqueous phase and would be more similar to the current technology but the operating conditions would be much milder. Currently, metal-based catalysts are used for petroleum processing. The enzyme technology would enable use of environmental friendly enzyme biocatalysts instead, allowing an energy efficient and clean operation. Fundamental research to study and understand the enzymatic reactions for petroleum compounds was initiated. This project is being conducted in collaboration with Texaco, Chevron and Phillips via a cooperative research and development agreement and it is funded by the National Petroleum Technology Office, Department of Energy.

DISCUSSION OF CURRENT ACTIVITIES

Improving activity and broadening substrate specificity for biological desulfurization.

This project involves the use of genetic engineering techniques to conduct molecular evolution of biodesulfurization enzymes. The desulfurization enzymes are being engineered into E. coli host, which will then be subjected to mutagenesis followed by screening to select clones with improved activity and specficity. This work is being conducted in collaboration with Texaco, ExxonMobil and Enchira Biotechnology Corporation. The industrial partners will be involved in developing recombinant strains, generating clones via combinatorial mutagenesis, development of analytical techniques for compounds of interest, and providing diesel and oil samples and analysis of the petroleum feedstocks before and after the treatment.

Enzymatic upgrading of heavy crudes via partial oxidation or conversion of PAHs

Enzymes, naturally occurring in aqueous environments can be adapted to work in organic media by chemical modification and genetic engineering, making them stable and active in the organic media. In our previous work we have studied oxidative reactions as model reactions, to understand the conversion of polyaromatic hydrocarbons (PAHs) using enzymes in organic media. A detailed thermodynamic analysis of the enzymatic reactions was conducted to understand the inherent limitations of the system. It was found that substrate interaction with the enzymes weakens in organic media reducing the rates of the reactions. Improvements were therefore necessary in the enzymes themselves to allow better interactions. This was conducted by chemical modification of the enzyme structure including the active site. Up to eight-fold improvements were observed in the catalytic efficiencies upon chemical modification via hydrophobic alkyl attachments at and near the active site. Due to the limitations in the available points for hydrophobic group attachment, chemical modification cannot impact the activities to the extent required for commercial applications. Therefore, alternate approach implementing use of genetic engineering was employed to allow further improvements in the enzyme activities. The development of the recombinant strains to be used for directed evolution is currently in progress. Lignin peroxidase was selected as the candidate enzyme for development, due to its high native activity towards pyrene biotransformation.

ACKNOWLEDGMENTS

The substrate specificity project is being funded by DOE-OIT. The project on PAH conversion is supported by the National Petroleum Technology Office, U.S. Department of Energy.

REFERENCES

Borole, A P, Cheng, C L, Davison, B H; Substrate partitioning as a controlling factor for enzymatic transformations in organic media, A poster presented at the ACS National Meeting in San Diego, CA, April 2001

Kuritz, T, Borole, A P, Rodriguez, M R, Davison, B H; Extracellular expression of active lignin peroxidase in the yeast pichia pastoris, a paper to be presented at the American society of Microbiology in May 2001, Orlando, FL.

REAL-TIME CHARACTERIZATION OF METALS IN GAS AND AEROSOL PHASES

Meng-Dawn Cheng (Project FWP: FEAC313)

INTRODUCTION

Oak Ridge National Laboratory (ORNL), BP Amoco, Equilon, Marathon, Phillips, Shell, and Eastman Chemicals Company are collaborating in the research and development of a field portable monitor for real-time characterization of metals emissions. Emissions of toxic metals are regulated under the Resource Conservation and Recovery Acts (RCRA). Among the 11 toxic metals and numerous compounds that bind to the metals, mercury has received unique attention lately, although hexa chromium, lead, vanadium, beryllium, etc. are known to be detrimental to human health and the environment. Measurement of the metal content has long been conducted with filter sampling and subsequent laboratory analysis using standard analytical methods such as atomic absorption, atomic emission, and/or inductively coupled plasma techniques. The turn-around time for the result can take one or more days. One serious limitation of the standard techniques is its inability to provide an alarm function for workers when an elevated level of toxic metals is present. Also, the long sampling and analytical time could also prevent researchers to gather useful data to improve the understanding of important processes (e.g., gas-particle partition) involving the metals and metallic species.

BACKGROUND

To make the metal monitor field portable, the analytical technique selected needs to be relatively simple in terms of hardware requirements—portable and low power consumption. This monitor will need to be optimized for measurement of aerosol particles. This technique we used belongs to a class of laser spectroscopic techniques called laser-induced breakdown spectroscopy. We call it laser-induced plasma spectrometry (LIPS) in this project. ORNL’s metal monitor is built on the LIPS technology with a major signal enhancement brought about by an aerosol beam technique called aerosol beam focusing (ABF). ABF technique enables active sampling of airborne particles and moves the particles to a spot on the fly through a shaped nozzle. In ABF-LIPS, airborne particulate matter or aerosol particles are sampled directly from the air and aerodynamically focused into a spot. This increases the local concentration of airborne particles at the focal spot; thereby, it increases the sensitivity of LIPS measurement. In Fig. 1, a pulsed laser beam of 532-nm is tightly focused onto the spot in the micro volume. This energy would ignite plasma on the focal spot. As the energy pulse stops the plasma decays and emits light of characteristic wavelength of and the decay time of a wavelength that is specific to the elements present in the aerosol.

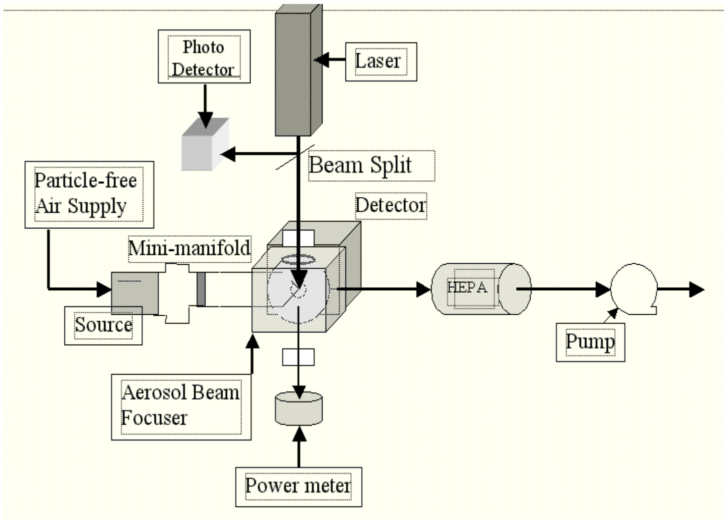

Fig. 1: Experimental Setup of ABF-LIBS at Oak Ridge National Laboratory

All material inside the plasma core would be atomized irrespective to their molecular structure. Atoms are excited. Excited atoms release visible light at their characteristic wavelengths as they return to the ground states from the plasma-excited states. The emission light generally lasts for approximately a few nanoseconds to several microseconds. The decay time of plasma emission light at a specific wavelength is species dependent and controlled by laser energy and pulse used. One can use the decay time in a time-resolved spectroscopic fashion to improve the detection sensitivity. We then collect the plasma light onto a grating spectrograph that disperses the light and images the dispersed light onto a 1024 × 256 pixel intensified charge-couple device for spectral data recording. The delay time for a specific element is chosen with the assistance of a kinetic program that was ran on-line. Once the optimal delay time is determined, the computer program will acquire the spectral data at the delay time in separate runs, account for electronics noises, perform model extraction analysis, and finally display the result. The whole process typically takes seconds to a few minutes depending on the analytes in the aerosol sample and analytical merits desired. The ABF-LIPS experimental configuration is shown in Fig. 1 above.

PROGRESS

We have been concentrating on field-testing and optimization of the prototype monitor this year. Each run of a test gave important piece(s) of performance data useful for improving and upgrading the monitor. We have been testing the monitor at an Engine Dyno Research facility located at the Y-12 National Security Complex in Oak Ridge, TN. We have collected data under various conditions during the times when the diesel engine was available for our tests. We have run the diesel engine at various load conditions from ideal conditions (no load) to up-hill with and without freights. We have also tested the analysis on exhausts from the use of different fuels–regular, sulfur-doped, and ultra-clean (zero sulfur) fuels. Metals that we have examined at these engine exhaust conditions include Na, Cr, Ca, Cu, Ni, V, and Pb. Metals-laden particles were produced by atomization, dried in a custom-made dilution manifold. Particle-filtered exhaust gas was used as the working gas driving the atomization process. Except for Cu, Ni, and V, the rest of the metals were spiked into the exhaust gas to test for the consistency and possible matrix effects of background gas. Due to the nature of the field tests and scheduling of the engine, a couple of experimental designs remain to be carried out in May and June 2001. We also are poised to conduct a pending experiment at a chemical manufacturing facility in East Tennessee. Publication-wise, we will present a paper describing the technology and some data in the upcoming annual meeting of the Air and Waste Management Association in June 2001. We have published two papers, one in the Applied Spectroscopy, and another in the Fuel Processing Technology. A third paper is to be submitted to the Journal of Aerosol Science when review is completed. An industrial CRADA with the Eastman Chemical Company was signed in June. This is a major step towards moving the technology into the commercial market. We have also been working on various issues related to commercialization.

FUTURE PROGRESS–CLOSEUP PHASE IN 2001

We will continue to analyze the data collected in the field experiments over the past few months and modify our original design of some components in the prototype monitoring system based on the analysis of collected performance data. We are again re-establishing connection through our Eastman CRADA, since our contact at Eastman left the company in February/March 2001. We are also making contact for a field-testing opportunity organized by the Florida Power and Light and University of North Dakota in the coming July.

NATURAL GAS AND OIL TECHNOLOGY PARTNERSHIP COORDINATION OF BIOPROCESSING PROJECTS

T. W. Schmidt and S. M. Robinson

The Natural Gas and Oil Technology Partnership Bioprocessing program involves projects at four national laboratories: Oak Ridge National Laboratory, Brookhaven National Laboratory, Idaho National Engineering and Environmental Laboratory, and Lawrence Livermore National Laboratory. To ensure coordination between the different projects, two meetings involving the four laboratories and their collaborating industry partners are held each year.

DISCUSSIONS OF CURRENT ACTIVITIES

During 2001, T. W. Schmidt participated in the development of the recommendations for funding of the Partnership Programs on behalf of Oak Ridge National Laboratory. In addition to existing projects in Diagnostics and Imaging Technology and Downstream Environmental Technology, T. W. Schmidt and S. M. Robinson assisted in the continued funding of the In-Well Oil and Water Separation Project, the Physical Property Measurement of Produced Water Project, and the funding of a new project to develop an ecological framework to evaluate the impacts of the releases at petroleum exploration and production sites. Other activities include program planning with the Partnership, selection of a Partnership Steering Committee, coordination of the Partnership projects in Bioprocessing of Crude Oils, coordinating all of the national laboratory participation in the Downstream Technology Area, and the development of a new technology area in Ultra-Clean Fuels through the coordination of an industry workshop and project review. New projects funded in 2001 were: Use of Ionic Solvents to Produce Clean Fuels, Application of Oak Ridge Membrane Technology to Separate Hydrogen in Refinery Streams, and Measuring Tension on Platform Mooring Ropes with Fiber-Optics

FUNDAMENTAL CHEMISTRY AND PROPERTIES OF IMPORTANT INDUSTRIAL CHEMICALS

W. V. Steele

INTRODUCTION

The purpose of the cooperative work between the Design Institute for Physical Property Data (DIPPR)® and the Thermophysical Property Group within the Chemical Technology Separations Group at ORNL is to develop thermodynamic and thermophysical property data for use in leading edge chemical technology. The property measurements are directed by the DIPPR Project Steering Committees responsible for Project 821–Pure Component Liquid-Phase Vapor Pressure Measurements and Project 871–Pure Component Ideal-Gas Enthalpies of Formation. The objective of Project 821 is to obtain precise and accurate liquid-phase vapor pressure data for selected pure components. The objective of Project 871 is to measure the enthalpies of combustion and derive the enthalpies of formation in both the condensed and the ideal-gas phases of “key” compounds that have been chosen to elucidate the enthalpy of particular atomic groupings. These group contributions can then be used to estimate data on large families of related compounds each containing that particular atomic arrangement.

DIPPR, now in its 22nd year of funded research, is the oldest of the America Institute of Chemical Engineers’ (Aichi) active Industry Technology Alliances. In 2001, DIPPR has 31 sponsors from industry and government bodies. Its purpose is to make possible, through joint sponsorship, thermophysical property data measurement, correlation, and dissemination. The objective of the Design Institute for Physical Property Data (DIPPR)® is to develop the world’s best set of critically evaluated thermophysical and environmental property data to satisfy industry needs. Data developed in DIPPR projects have become the data of choice for leading chemical process simulators and are used throughout the world. To quote from Dr. Mary Good (then Senior Vice President, Technology, AlliedSignal, Inc.):

“The US chemical process industry had a record trade surplus of $19 billion in 1991, with indications it will be close to that for 1992 demonstrating its continued global leadership position. One of the key factors contributing to this is the development and use of leading edge chemical process technology. AlliedSignal has relied heavily on the DIPPR databases in design of its chemical and polymer processes, and finds great value in sharing the costs of developing and verifying data.”

DISCUSSION OF CURRENT ACTIVITIES

BACKGROUND

DIPPR had conducted two experimental property measurement projects in Bartlesville, Oklahoma for over a decade:

- Project 821–Pure Component Liquid Vapor Pressure.
- Project 871–Determination of Pure Component Ideal Gas Heat of Formation.

DIPPR describes these projects using the words: “We use top national research facilities to carry out specific projects.”

Dipper’s Project Steering Committees recognized the Bartlesville facility, as the only remaining thermodynamics laboratory in the United States with the full range capability to obtain the type and quality of data required by the sponsors. With the transfer of senior staff and equipment from Bartlesville to the Thermophysical Property Group within the Chemical Technology Separations Group at Oak Ridge National Laboratory (ORNL) the full range capability is maintained.

The project has been setup in the CRADA form with an initial lifetime of three years. Subcommittees comprised of DIPPR Project supporters, DOE Fossil Energy staff and ORNL staff will decided at the annual AIChE/DIPPR meeting in November a list of compounds for study in the following year in each of the two Project areas. Compounds will be chosen to represent whole families containing the necessary functionalities and to facilitate extension of available databases, rather than to fulfill the specific needs of any single member company.

Project 821–Pure Component Liquid Vapor Pressure

While vapor pressures are important in themselves for characterizing chemicals, to ensure they meet specifications, to determine suitable storage conditions and to meet safety considerations, they are also required for Material Safety Data Sheets (MSDS) and other regulatory reporting such as the new OSHA process safety requirements. One of their major uses, however, is to define reference states for vapor-liquid equilibrium and activity coefficient calculations. Such calculations are requisite for the design of separation processes, particularly distillation. Vapor pressures are also used throughout chemical engineering thermodynamics to calculate a wide variety of quantities such as acentric factors, enthalpies of vaporization, and solubilities.

Under guidance of DIPPR 821 Project Steering Committee, the Thermophysical Property Group at ORNL will conduct measurements of vapor pressure for selected compounds. The vapor pressures will be determined over a wide range of temperatures and pressures utilizing the specialized equipment obtained from Bartlesville. Pressures as low as 0.01 kPa (0.75 mm Hg) can be measured accurately using an inclined piston gauge apparatus. The upper range of pressure obtained is 270 kPa in a twin ebulliometric apparatus. The vapor-pressure data are fit to a wide-range vapor pressure equation and are verified and compared with any existing measured or predicted data. Sample purities are checked and the materials are usually purified if necessary. Critical temperatures, critical volumes, liquid-phase densities, heat capacities, melting points, enthalpies of fusion, and vaporization can be measured and critical pressures derived. Stringent efforts are made to ensure thermodynamic consistency in the derived results so that the data can be used with confidence in a wide range of process development simulations.

Project 871–Determination of Pure Component Ideal Gas Heat of Formation

This project utilizes ORNL's unique capability for precise and accurate measurements of enthalpies of combustion of a wide range of organic and organometallic compounds. The evaluation of chemical plant safety has never been as important as it is today. The enthalpy of formation is the thermodynamic property most needed for evaluation of the energy hazard potential of an organic compound. A second-order group-contribution methodology for the calculation of ideal-gas thermodynamic properties has been outlined in detail in Thermochemical Kinetics.[1] However, the text lacks parameters for a number of important groups and correction terms for several important ring structures. Parameters for some structural groups were derived from data that has since been shown to be incorrect. In the absence of data, application of the methodology for the estimation of thermochemical properties for some important organic compound types is impossible. Whereas the condensed-phase enthalpy of formation of a compound is of greatest interest in the calculation of energy balances for a given chemical process, the enthalpy of formation for the ideal-gas state is of greatest interest in the general case. This single value can give sufficient information to enable estimations for a large group of compounds containing that molecular entity. In summary, the objective of this project is to expand the group-additivity method of calculation of thermodynamic properties by determining thermochemical data on compounds containing unique groups or atomic environments.

Under guidance of the DIPPR 871 Project Steering Committee, the Thermophysical Property Group at ORNL will conduct measurements of the energies of combustion and hence enthalpies of formation in both condensed and ideal-gas phases for selected compounds. Such other thermophysical property measurements as will be required to derive the ideal-gas enthalpies of formation will also be made. Stringent efforts will be made to ensure high purities of the samples studied since small levels of impurity can result in order of magnitude errors in derived enthalpies of formation.

For both Projects ORNL staff will analyze the data obtained with special regard to the development of correlations suitable for the estimation of the properties for wide families of like compounds. Additionally DIPPR and ORNL staff will develop impact statements of the results on pollution control, waste minimization, and environmental regulation and control. Results of these studies will be available to the chemical industry and the general public through the DIPPR's databases.

PROGRESS

In the reporting period the CRADA was signed and both project committees have met during the AIChE meeting in Los Angles in November 2000. Lists of possible compounds for measurements were tentatively drawn-up at those meetings and finalized after subsequent literature surveys to ensure the quantity and quality of any available data. Samples of each of the chemicals chosen for study have been obtained and purification via spinning-band distillation or (in case of solid samples) zone-refining are in progress. The property measurements are due to commence in early May 2001.

Results from earlier work completed at Bartlesville, Oklahoma have cleared full committee review and have been submitted to the *Journal of Chemical & Engineering Data* for peer review and hopefully publication in the annual DIPPR issue slated for November 2001. The titles of the 6 submissions are:

- DIPPR Project 821. Vapor Pressure of Organic Compounds of Industrial Interest. The 1995 Project Results. Vapor pressure, heat capacity, and density along the saturation line measurements for Benzenamine, butylbenzene, sec-butylbenzene, tert-butylbenzene, 2,2-dimethylbutanoic acid, tridecafluoroheptanoic acid, 2-butyl-2-ethyl-1,3-propanediol, 2,2,4-trimethyl-1,3-pentanediol and 1-chloro-2-propanol. by W. V. Steele, S. E. Knipmeyer, and A. Nguyen.
- DIPPR Project 821. Vapor Pressure of Organic Compounds of Industrial Interest. The 1996 Project Results. Vapor pressure, heat capacity, and density along the saturation line measurements for ε-caprolactam, pyrazine, 1,2-propanediol, triethylene glycol, phenylacetylene, and diphenylacetylene. by W. V. Steele, S. E. Knipmeyer, and A. Nguyen.
- DIPPR Project 821. Vapor Pressure of Organic Compounds of Industrial Interest. The 1997 Project Results. Vapor pressure, heat capacity, and density along the saturation line measurements for cyclopropane carboxylic acid, N,N-diethylethanolamine, 2,3-dihydrofuran, 5-hexen-2-one, perfluorobutanoic acid, and 2-phenylpropionaldehyde. by W. V. Steele, S. E. Knipmeyer, and A. Nguyen.
- DIPPR Project 871 Thermodynamic Properties and Ideal-Gas Enthalpies of Formation. The 1995 Project Results. Methyl benzoate, ethylbenzoate, (R)-(+)-limonene, tert-amylmethyl ether, trans-crotonaldehyde, and diethylene glycol by W. V. Steele, A. B. Cowell, R. D. Chirico, S. E. Knipmeyer, and A. Nguyen.
- DIPPR Project 871 Thermodynamic Properties and Ideal-Gas Enthalpies of Formation. The 1996 Project Results. Trans-Methyl cinnamate, α-methyl cinnamaldehyde, methyl methacrylate, 1-nonyne, trimethylacetic acid, trimethylacetic anhydride, and ethyltrimethylacetate by W. V. Steele, A. B. Cowell, S. E. Knipmeyer, and A. Nguyen.

- DIPPR Project 871 Thermodynamic Properties and Ideal-Gas Enthalpies of Formation. The 1997 Project Results. 1,4-Diisopropylbenzene, 1,2,4,5-tetraisopropylbenzene, cyclohexanone oxime, dimethyl malonate, glutaric acid and pimelic acid by W. V. Steele, A. B. Cowell, S. E. Knipmeyer, and A. Nguyen.

REFERENCE

1. S. W. Benson, *Thermochemical Kinetics* 2nd Edition; Wiley: New York, 1976.

ADVANCED TECHNIQUE FOR IMPROVING THE BIOLOGICAL QUALITY OF PETROLEUM CONTAMINATED SOILS

Arthur J. Stewart and Mac A. Callaham, Jr.

INTRODUCTION

Project FEAC317 started in May 1999 with support by the U.S. Department of Energy (Fossil Energy Program, National Petroleum Technology Office, Tulsa, OK; Nancy Comstock, Project Manager). It provides data and technical guidance to Petroleum Environmental Research Forum (PERF) project 99-01, “Ecological Evaluation for Upstream Site Remediation”, sponsored by Chevron (see http://www.perf.org/). Participants in PERF Project 99-01 currently include Chevron, Exxon, Phillips Petroleum, Texaco and BP Amoco, in addition to the Department of Energy. Two other companies are expected to formally join PERF Project 99-01 soon, and the project is likely to involve participation of the Gas Technology Institute (GTI) and the American Petroleum Institute (API). The objective of PERF Project 99-01 is, at this point, general: “. . . to develop and/or improve methods for ecological risk evaluations and assessments via the development of early exit criteria for excluding sites from ecological risk assessment, and using field surveys to determine appropriate cleanup standards for total petroleum hydrocarbons (TPH) or salts in site soils.” Project FEAC317 focuses on the following question: What types of soil amendments or biological treatments might be used to improve the biological quality of oily soils found in petroleum landfarming operations?

Petroleum landfarms are sites where waste petroleum hydrocarbons are biotreated by direct application to the ground. The materials are tilled into the soil, along with nutrients, to encourage biodegradation of the hydrocarbons by soil microbes. Soil “bulking agents” and gypsum are usually applied as well, to improve ion balance and physical properties of the soil. One problem associated with petroleum landfarming is that while lower molecular weight petroleum compounds volatize and/or are biodegraded efficiently, higher molecular weight petroleum compounds tend to biodegrade much more slowly. Thus, a consequence of continued application of petroleum hydrocarbons to landfarm soil is the gradual accumulation of high-molecular weight petroleum compounds. These materials are not very toxic, but at high concentrations they can increase soil water repellency, which can have negative effects on plant growth. As a result, bioremediated oily soils may be less productive than desired, and may not support a taxonomically or functionally diverse community of soil invertebrates. Ultimately, the concentration of petroleum hydrocarbons approaches an upper-bound permitted limit (typically 10,000 ppm as TPH). When this occurs, the landfarm can no longer be used for treating additional waste petroleum, and alternative uses for the land are then desired. It is possible that regulators would be more willing to consider alternative land-use possibilities if the soils are of demonstrably good quality with respect to their ability to support communities of plants and soil invertebrates.

DISCUSSION OF CURRENT ACTIVITIES

Previous results from work performed as part of FEAC317 demonstrated that certain organic amendments to oily soils can substantially improve the biological quality of soils, when quality is measured as earthworm survival and reproduction.[1] This finding was significant because earthworms are an important component of healthy soil ecosystems. Indeed, earthworms have been dubbed "ecosystem engineers" because their burrowing and feeding activities fundamentally alter soil systems, making resources (space and/or food) available to other soil organisms that, in the absence of earthworms, would not be available.[2] The status of earthworms as ecosystem engineers, and the use of earthworm applications in large-scale land reclamation projects in Europe led us to consider earthworms not only as a response variable, but also as a possible treatment for improving the biological quality/ecological recovery of soils in the context petroleum landfarms.[3–5]

In June 2000, Mac Callaham, a post-doctoral research associate with experience in soil invertebrate ecology, was recruited to work on FEAC317; and in October 2000, Ms. Clara Alarcon, a visiting environmental scientist from Venezuela's national petroleum company (PDVSA), worked closely with project personnel on laboratory incubation studies (at no cost to FEAC317). Callaham and Alarcon set up experiments to explore the idea that earthworms (along with an organic amendment) might be used as a treatment to improve biological quality of petroleum-contaminated soils. In these experiments, several facets of biological quality were measured including plant growth, soil microbial activity, and survival/reproduction of other taxa of soil invertebrates. In two separate experiments, we assessed the biological quality of an oily soil (from a petroleum landfarm in Rangely, Colorado), in a factorial arrangement of earthworm additions and wheat straw treatments. In these experiments, *Eisenia fetida* was used for earthworm treatments because (1) it is easily cultured in the laboratory, and (2) there is a large body of literature detailing the ecotoxicology of this species. Wheat straw (*Triticum aestivum*) was selected for the organic amendment treatment because it is a widely available and relatively inexpensive agricultural by-product that may have desirable properties in terms of stimulating microbes capable of degrading aromatic hydrocarbons.[6]

Results from these experiments show that earthworms may improve the quality of post-remediation landfarm soils. Specifically, plant performance (assessed in terms of biomass accumulation) was significantly better in cups with earthworms than in cups lacking earthworms (Fig. 1). This was true for both shoots and roots of the tall fescue (*Festuca arundinacea*) seedlings used in this experiment. Wheat straw addition had no significant effect on plant growth, but there was an interesting trend for less shoot

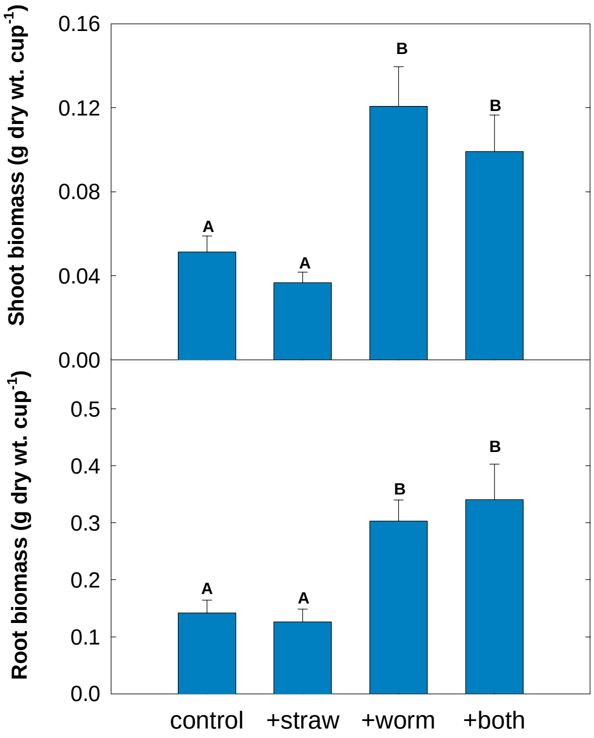

Fig. 1. Tall fescue growth in earthworm / wheat straw factorial. Bars represent mean biomass (N=5) of tall fescue shoots (top panel) and roots (bottom panel). Standard error is indicated by error bars. Bars with different letters are significantly different from one another (ANOVA, $p<0.05$). Note difference in y-axis scales.

growth in cups with wheat straw additions. A trend of this type could be due to decreased nutrient availability in cups that received wheat straw, because nitrogen and/or other nutrients may have become immobilized in the relatively recalcitrant wheat straw substrate (C/N ~75). However, the trend for less growth in straw treated cups, relative to unamended cups, was not observed for root growth in this experiment.

Soil respiration is another measure of soil biological activity/quality. We measured soil respiration in systems with and without earthworms and wheat straw, in a second factorial experiment. For this experiment, we used oily landfarm soil, a non-contaminated reference soil, and a 1:1 mixture of oily and reference soils. Experimental units for this study were 0.96–l glass jars containing 400 g soil along with earthworm and/or straw treatments (see Fig. 2). Soil respiration was assessed by sealing the jars leak-tight, incubating for 1–2 h, sampling headspace gas with a syringe, and analyzing for CO_2 content on an infrared gas analyzer. Results from this study showed that basal respiration rates for unamended (i.e. without wheat straw) landfarm soil were higher than basal respiration rates of the unamended reference soil (Fig. 3). The respiration rates for all three soils increased when wheat straw was added, but the reference soils exhibited the greatest amount of increase in respiration rate during the first 30 days of the incubation (Fig. 3). Earthworm additions increased respiration rates in all straw amended soils, but oily soils without the straw addition did not respond to the earthworm addition (Fig. 3). This result suggests that earthworms stimulated additional organic C mineralization when the organic amendment was present. However, to determine whether this additional CO_2 efflux originated from enhanced wheat straw decomposition, from endogenous soil organic matter, or a mixture of the two will require further research.

Fig. 2. Experimental units used in soil respiration earthworm/wheat straw factorial experiment. Units were constructed of 400 g dry wt equivalent soil, and depending on treatment, received 8 g chopped wheat straw, and/or 3 adult *Eisenia fetida* earthworms. Examples shown are landfarm soil without straw (left) and with straw amendment (right), both without earthworms.

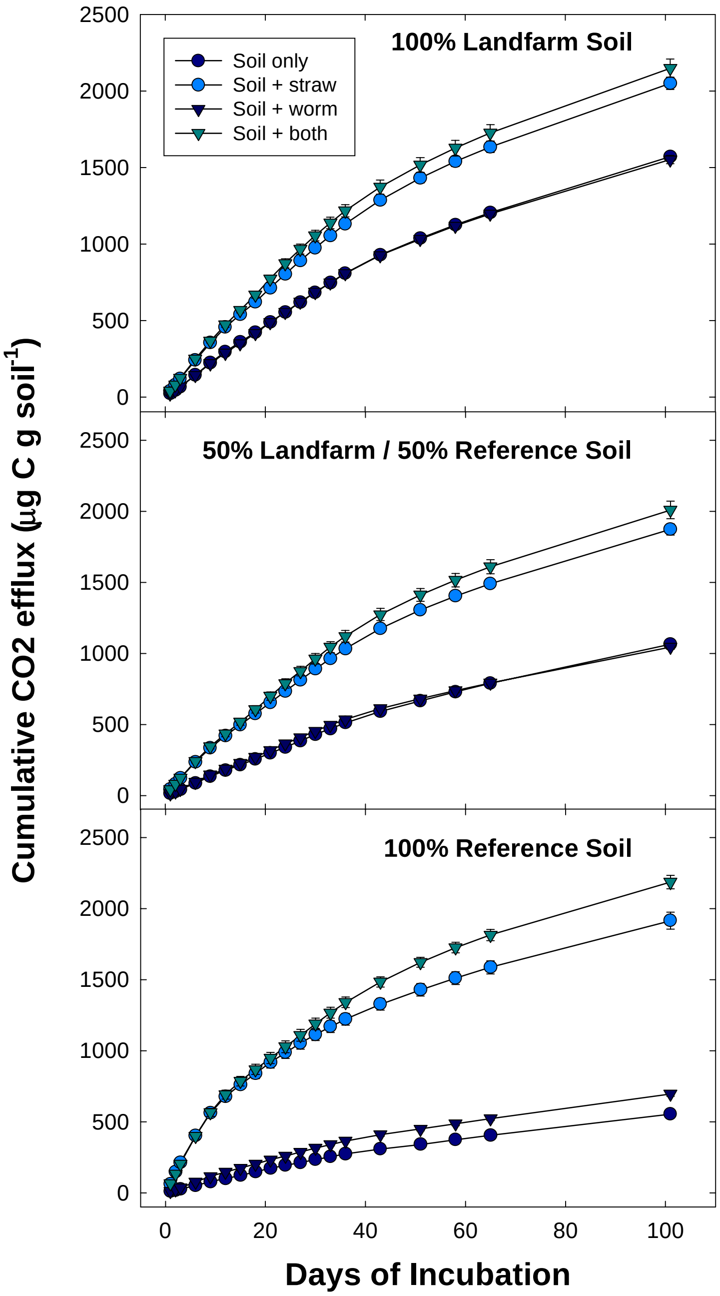

Fig. 3. Cumulative CO_2 efflux from earthworm / wheat straw factorial experiment. Symbols represent mean efflux (N=5) from experimental units of the indicated treatment. Triangles represent units with earthworms, circles represent units lacking earthworms.

One other positive influence of the wheat straw amendment was that earthworm survival, over the course of the 150-day incubation period, was substantially greater in straw-treated experimental units, regardless of soil type. Specifically, earthworm survival was zero in landfarm soils with no wheat straw, but there was 27%survival of earthworms in straw-amended landfarm soils. This result suggests that organic amendments (such as wheat straw) are critical to long-term earthworm survival in landfarm soils.

Finally, experiments presently underway will provide independent evidence for the presence or absence of a positive effect of earthworms on the biological quality of bioremediated petroleum landfarm soil. In February 2001, with FEAC317 support, Mac Callaham traveled to a soil ecotoxicology laboratory (Geo-Centers, Inc.) at Aberdeen Proving Ground in Maryland. There, he obtained laboratory cultures of other soil invertebrate organisms, and learned experimental protocols for survival and reproduction tests for these organisms. Soils from the respiration study described above, which were incubated with earthworms and/or wheat straw for 150 days, are now being used in survival and reproduction tests for the enchytraeid worm *Enchytraeus crypticus* and the collembolan *Folsomia candida*. Data from these trials will allow us to proceed with our assessment of the feasibility for using organic amendments in conjunction with earthworms as a treatment in the reclamation of petroleum landfarm soils.

REFERENCES

1. S. S. Humphries, K. D. Gwinn, and A. J. Stewart, "Effects of endophyte status of tall fescue tissues on the earthworm, *Eisenia fetida*" *Environmental Toxicology and Chemistry* (In press).
2. C. G. Jones, J. H. Lawton, and M. Shachak, "Organisms as ecosystem engineers" *Oikos* **69**:373–386 (1994).
3. S. O. Bain, K. R. Butt, and R. M. Morris, "Survival and reproduction of *Lumbricus terrestris* L. in colliery spoil and sewage sludge" *Pedobiologia* **43**:729–734 (1999).
4. K. R. Butt, J. Frederickson, and R. M. Morris, "The earthworm inoculation unit (EIU) technique, an integrated system for cultivation and soil-inoculation of earthworms" *Soil Biology and Biochemistry* **29**:251–257 (1997).
5. J. P. Curry, and D. C. F. Cotton, "Earthworms and land reclamation", pp. 215–228 in *Earthworm Ecology, From Darwin to Vermiculture,* J.E. Satchell (ed.), Chapman and Hall, London, 1983.
6. R. Martens, and F. Zaradril, "Screening of white-rot fungi for their ability to mineralize polycyclic aromatic hydrocarbons in soil" *Folia Microbiologia* **43**:97–103 (1998).

LIFE PERFORMANCE MONITORING OF SYNTHETIC FIBER MOORING ROPES USING POLYMERIC OPTICAL FIBER STRAIN SENSORS

J. D. Muhs

INTRODUCTION

The approach for the new activity for FY 2001, “Life Performance Monitoring of Synthetic Fiber Mooring Ropes Using Polymeric Optical Fiber Strain Sensors,” will be based on the proposed approaches for monitoring the performance of Synthetic Fiber Mooring Rope (SFMR). SFMR constructed from high performance polymers is an important emerging technology, which promises to enable the economical production of oil and gas in deepwater Gulf of Mexico (GOM) and elsewhere. In addition to the benefit of significant weight savings, SFMR deployment in the taut leg configuration can reduce the footprint and thus the interference with adjacent property developments. The Minerals Management Service (MMS) has not yet approved any SFMR for the GOM and is taking a cautious approach, awaiting better understanding of the issues. Future safe deployment of the SFMR will be significantly enhanced if a reliable technique can be developed to monitor the performance of the rope in service. The ultimate strain of polyester rope, including kinematic effects due to the twisted and braided architecture of the rope and stretch in response to loads, is on the order of 15 percent. Test data indicates that the strain in the rope at failure is essentially a constant independent of load path or history. Measurement of the accumulated strain in the rope should thus provide a reliable benchmark with which to estimate the remaining life and establish criteria for rope recertification or retirement.

There is currently not available any method to monitor the performance of SFMR in service except visual inspection and load cells or a gross measurement of the stretch of the mooring line. Glass fiber optics methods have been considered, but the allowable strain in glass fibers is less than 2 percent and therefore inadequate for direct measurement of the strain in the rope fiber strands. ORNL is using highly elastic polymeric optical fibers, which can potentially record tensile strains of order 10 percent, making them attractive as sensors for monitoring the strain and performance of SFMR. Further, ORNL has developed very reliable strain sensors using similar fibers with an optical-time-domain reflectometer (OTDR). Together, these technologies promise to solve the problem of strain sensing in mooring ropes and to improve the safety and reliability of deepwater oil and gas drilling operations.

The project team proposes to develop and demonstrate a reliable, robust method for monitoring strain, in service, in braided and twisted strand SFMRs. The project success criteria will be strain monitoring at 0.1% resolution in 30 foot gauge lengths, up to 10 % strain, in 1,000 foot ropes for GOM deployment. “Stretch” targets will be 0.5 % resolution in 5 foot gauge lengths, up to 15 % strain, in 2,500 foot ropes for GOM deployment. The program will be driven by the objective to develop a monitoring system, which is practical for deployment on offshore platforms. The program will coordinate closely with the damage tolerance program currently being conducted for the MMS. We are providing the following technical approach and discussions of tasks that will be performed.

Technical Approach: An OTDR measures spatial positions along an optical fiber by launching brief pulses of light into one end of the fiber and then detecting the subsequent reflections at physical interfaces inserted along the fiber. By measuring the transit time of the reflected pulses and by knowing the speed at which light travels in the optical fiber, a very accurate measure of the distance to each reflective interface can be attained. If a gauge section undergoes a strain, hence changing the interface's spatial position along the fiber, one can measure strain by measuring the change in position. An OTDR with a picosecond pulsed light source can measure distances with an accuracy of about 0.4 inches, yielding strain measurements of 0.1% over a 33 foot gauge length. Polymeric optical fibers can be used to make 10 to 30 strain measurements along a 1,000-foot mooring rope by spacing the interfaces at 33 to 100 foot intervals. A unique optical fiber coupling method will be used to insert the reflective interfaces along the length of the polymeric optical fiber, and customized software algorithms will be used to measure strain between adjacent reflective interfaces. We envision a system that—once integrated into a mooring rope—will allow platform safety engineers to readily monitor several mooring ropes in real-time to determine the time and specific location of strain values exceeding a predetermined threshold. The tasks for our proposed work are as follows.

Task 1: Development of OTDR-based fiber optic strain sensor. We will review the initial system requirements to define design parameters including response time, strain resolution/precision/accuracy, measurement frequency, acceptable gauge length, portability, and maximum/minimum strain values. We will also evaluate several available multimode polymeric optical fibers to determine their suitability for use in the system, given the design constraints. Of particular importance will be the selection of an optical fiber that is (1) compatible with high-resolution OTDR, (2) capable of withstanding required strain values, and (3) capable of transmitting the OTDR pulses over the required distance. We will also develop (1) methods of introducing low-loss partial reflectors into the optical fibers at the required spacing, (2) control algorithms to sample and process return signal information and calculate the strain values for the specified gauge lengths, and (3) a user-interface to display the strain data. This task will culminate with a lab-based feasibility demonstration that the technology is capable of achieving the desired strain measurements. Task one will be conducted principally by ORNL.

Task 2: Integration of optical fibers into the mooring rope. Task two will address integrating the optical fiber into mooring ropes of both braided and twisted strand constructions. Literature surveys, computational modeling, and experimental investigations will be conducted. .Subtasks include

(1) determining which rope element(s) should be strain monitored, (2) avoiding damage to optical fibers during deployment and field service, (3) integrating the fiber into long mooring ropes, and 4) configuring and connecting optical fibers at rope terminations. This task will also address environmental effects on the polymeric optical fiber, including sea water and extreme temperatures. This task will be led by Petroleum Composites, with significant contributions by ORNL and rope manufacturers.

Task 3: System Integration and laboratory evaluation. A systems-level laboratory evaluation will be conducted. We will test and evaluate the performance of the OTDR-based sensors with multiple reflective interfaces to measure the strain for several discrete lengths of rope. The first tests will be conducted in the lab using small rope elements (probably a single rope strand) and short gage lengths. The technique will then be applied to relatively long mooring rope specimens having several long (~33 foot) strain sensor gauge lengths. We will also test ropes which have been cut to simulate installation damage. The polymeric optical fiber may have the ability, through large strain anomalies, to assess the damage state of the rope. Long rope specimen tests will be conducted at a commercial rope testing facility. This task will involve all participants. The task leader has not been determined.

Task 4: Development of multi-rope sensor multiplexing and platform integration techniques. In task four, we will develop reliable multiplexing techniques for the OTDR-based sensor. An optical fiber switch can switch the OTDR among the polymeric optical fibers that are monitoring many ropes. Multiplexing dramatically reduces deployment cost and centralizes the monitoring function of the system. Ways to transmit the signal outside the test section via conventional glass fibers will be investigated. Termination systems and interface systems will be developed for transferring signals. This capability will provide the ability to monitor an entire length of rope from platform to the sea bed or several different ropes. The instrumentation and software to measure strains in several different ropes will be developed under this task. This capability will be demonstrated using several long-length ropes in a test in a commercial rope test facility. This task will be led by ORNL, with significant assistance by Petroleum Composites and Shell.

Task 5: Field Testing. Field demonstration of the technology is this program’s principal objective. A plan will be developed to deploy a mooring rope on a platform as a field demonstration of the feasibility of the technology. The cost of this phase must be covered by industry and may be by a single company anxious to use the technology or more likely as a Joint Industry Project. This phase is planned for year three, but every effort will be made to accelerate the program within the available resources. In addition, this task will involve writing guidelines for the use of the technology, integrating the results from this and parallel programs being sponsored by the MMS on damage tolerance. This task will be coordinated by Petroleum Composites, with the industrial partners being the major contributors.

Task 6: Project management and coordination. The project will be managed by ORNL's Jeff Muhs. Mr. Muhs leads ORNL's Photonics and Fiber Optic Applications Group and is one of the original developers of the fiber optic sensor technologies described herein. Mr. Muhs holds 10 US patents for inventions in fiber optics and related technologies, and he has successfully managed several fiber optic R&D projects of this size and duration. Dr. Jerry Williams will be responsible for coordinating with rope manufacturers, test facilities and oil companies and conducting research to accomplish the integration of the technology into the rope and laboratory and field testing. Dr. Williams is a part-time employee of the University of Houston and a consultant for Petroleum Composites. He worked for 12 years with Conoco prior to joining the Composites Engineering and Applications Center at the University of Houston where one of his responsibilities during the next year will be to work on a synthetic fiber mooring rope damage tolerance program for the Minerals Management Service. The project management plans to form an advisory group composed of oil and oil service companies and rope manufacturers to help define requirements and ensure that the capabilities developed are practical for field deployment.

DISCUSSION OF CURRENT ACTIVITIES

The funds for this project have not been received to date (May 4, 2001). To initiate this project we have had informal discussions with our subcontractors, *Petroleum Composites, Shell International Exploration and Production, Inc.*, and *Puget Sound Rope*, regarding their support of the project. We have received letters of commitment from each stating their intent to provide in-kind contributions that may include staff time, materials, travel, and use of facilities and/or equipment.

DEVELOPMENT OF A CENTRIFUGAL DOWNHOLE SEPARATOR

P. A. Taylor and K. T. Klasson

INTRODUCTION

Produced water is the largest generated waste stream by volume in the Gulf Coast region and is typically a mixture of formation and injection process water that contains oil, salts, chemicals, solids, and trace metals. In 1991, Louisiana generated over 1 billion barrels and Texas generated 7.5 billion barrels of produced water as a result of oil and gas operations. More than 250 million barrels of produced waster are discharged each year to surface waters in both Texas and Louisiana.

Two primary alternatives exist for disposal of produced water in the future: (1) improve the treatment of produced water prior to surface or subsurface disposal or (2) reduce the volumes of produced water by using downhole, or in-well, separations or reinjection. Newer technologies being considered by the industry for contaminant removal include hydrocyclones, reverse osmosis, membrane filtration, gas flotation, carbon adsorption, bioreactors, chemical oxidation, stripping/extraction, and UV oxidation. These processes are complicated and expensive, and several of these unit operations will be required to reduce the conventional, unconventional, and toxic pollutant concentrations to new discharge limits.

Therefore, emphasis should be placed on reinjection or in-well separations/recycle of produced water. Successful use of reinjection has increased in the last several years, but enhanced treatment is often required to remove oil and particulate matter to avoid damaging or plugging the rock formations. The suitability of produced water for reinjection is determined by the enhanced recovery process, the water quality, and the rock formation properties. Options for in-well separations have been evaluated but no technology has reached maturity.

This project will extend the application of remotely operated separations equipment developed for the nuclear industry to in-well recovery of oil generated by enhanced oil recovery techniques. A conceptual drawing for the process, which combines a centrifugal separator with two downhole pumps, is presented in Fig. 1. Centrifugal separators, originally developed by the Department of Energy (DOE), have been successfully used for surface treatment of produced water and wastewater generated during environmental clean-up operations.

Centrifugal separators of various sizes (from 2- to 25-cm rotor diameter) have been built and operated over the past three decades at the Savannah River Site (SRS), Argonne National Laboratory (ANL), and ORNL for use in DOE applications. These units have several characteristics that make them attractive for consideration in downhole separation of oil and produced water. These include (a) excellent phase separation; (b) reliability in remote applications with >20,000 hours of operation prior to maintenance;

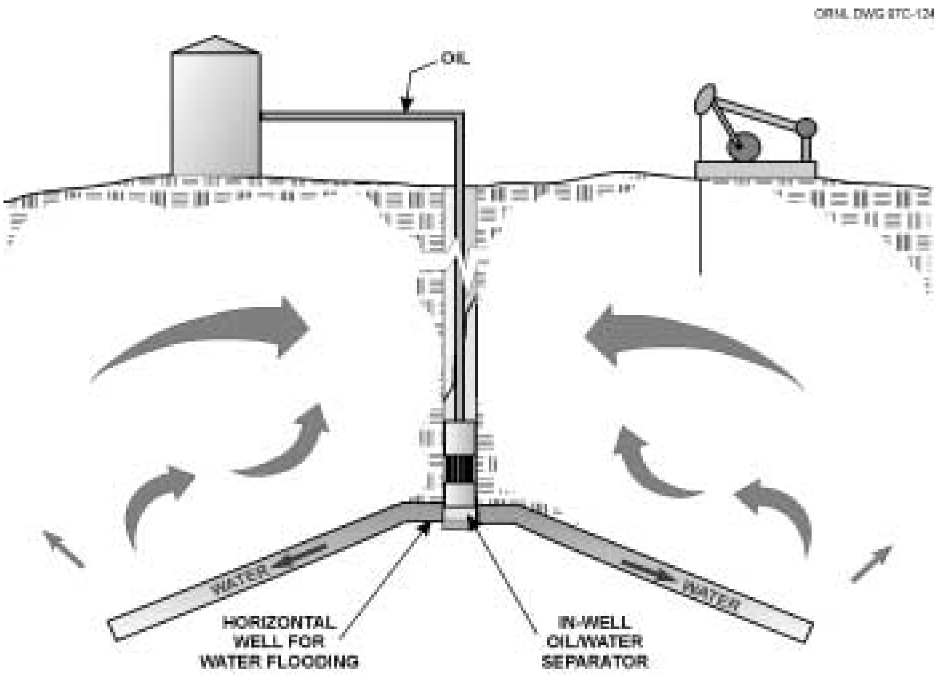

Fig. 1. A conceptual drawing for the installation of a centrifugal separator in an oil well, with the separated oil being pumped to the surface for recovery and the produced water being recycled through horizontal wells.

and (c) the ability to handle high volumetric throughput with a very low residence time. However, several modifications must be made to the design prior to successful use as a centrifugal downhole separator (CDHS). These include (a) lengthening the rotor to increase the throughput, (b) introducing the oil/water mixture directly into the bottom of the rotor to limit mixing, (c) overcoming problems associated with the accumulation of solids in the rotor, and (d) connecting the separator to downhole pumps for pumping the oil to the surface and for reinjecting the produced water. A schematic of the rotor for a centrifugal separator is shown in Fig. 2. The size of the aqueous weir can be changed to optimize the performance of the separator, depending on the properties of the oil and the ratio of water-to-oil in the feed. The oil and water discharges from the rotor are captured in collection channels in the separator housing, and drain by gravity through outlet ports back into the feed tanks.

MATERIALS AND METHODS

A model V-2 (2-inch rotor) centrifugal separator (CINC, Inc., Carson City, NV) equipped with a 1/6 HP motor is being used for the bench-scale tests. Two crude oils have been provided by a PERF industrial partner for testing. The first is a Gulf of Mexico light crude with an API gravity of 34.06°, specific gravity at 60°F of 0.8547, and a viscosity of 9.0 cP at 77°F. The second is a heavy North Sea

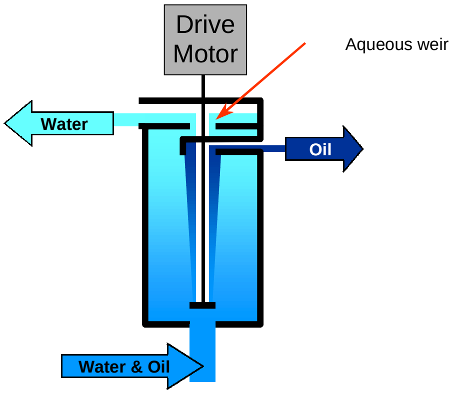

Fig. 2. Schematic drawing of the centrifugal separator rotor.

crude with an API gravity of 19.3°, specific gravity at 60°F of 0.948, and a viscosity of 400 cP at 77°F. The ASTM Standard Specification for Substitute Ocean Water (ASTM: D1141-90) is being used for the aqueous phase in the bench-scale tests with these crude oils. Most of the testing has used the light crude, based on recommendations from the industrial partners. The oil companies need to add water to the heavy crude in order the pump it to the surface, so separating water from this type of oil is not required. The tests conducted with the heavy crude do show the range of crude oils that can successfully treated using the centrifugal separator.

The separator has been tested under a variety of operating conditions. Typically, approximately 3 L each of crude oil and synthetic ocean water are used during a run, and the oil and water streams are continuously recirculated through the separator. The water and oil feed streams are mixed just before they enter the separator. Samples of oil and water from the separator are collected in API Centrifuge Tubes (12.5 mL), acidified with 0.125 mL of 1 N HCl, and centrifuged at 4500 rpm for 10 minutes. The amount of water in the oil samples is read directly from the graduations on the centrifuge tubes. The amount of oil in the water samples is determined by dissolving the oil floating on the water in two 1-mL portions of hexane, evaporating the hexane and weighing the oil residue.

In collaboration with the University of Tennessee, solids separation from an oil/water/solids mixture was tested in a hydrocyclone (Model Doxie A, Dorr-Oliver Inc., Miltford, CT) before water and oil separation was accomplished in the centrifugal separator

RESULTS

Discussions with representatives from the Petroleum Environmental Research Forum (PERF) industrial partners and the Department of Energy have resulted in the formulation of a revised set of functional criteria for use in the development of the CDHS. These functional criteria are presented in Table 1 together with the achieved results.

Table 1. Functional Criteria for Development of the CDHS

Industry supplied criteria	Achieved	Comment
Flow Rate: 2,000 to 10,000 bbl/d	15 bbl/d	The small unit used in the laboratory can be scaled in both diameter and length. The current lab-scale unit is just 2 inches in diameter and 4 inches tall. A computer program developed for design of separators will be used to scale up units.
Diameter: 6 inches for 7-inch well	2 in. D × 4 in. H	
Temperature: 100 to 180°F	75–150°F	The effect of temperature on the separation was studied using the North Sea heavy crude. Increasing the temperature improved performance.
Water-to-oil ratio: 1:10 to 10:1	1:19 to 10:1	The bench-scale separator unit has been operated through the whole regime without decrease in performance.
Gas processing: Can it be done?	Yes	Gas entrapped in the oil water does not interfere with the separation efficiency. We have studied gas levels of up to 21% (v/v).
Solids: 0–3% (sand to clay)	3% sand	3% sand was processed through the application of a hydrocyclone for solids separation followed by oil-water separation in the CDHS.
Product quality: <2000 ppm (0.2%)	<0.2%	The separation efficiency can be adjusted through replacement of the aqueous weir.
Reliability: 18 months between failure	27 mo.	The failure rate of separator units has been determined previously by DOE.

Studies performed with North Sea heavy crude oil at higher temperatures indicate that the performance of the system improves with temperature, resulting in a cleaner water stream. As is noted in Fig. 3, the viscosity of the crude oil decreased as the temperature increased. This results in an improved separation of the oil droplets from the water. Although we did not extend the studies to higher temperatures, it is likely that the trend will remain the same. The separation of water droplets from the oil was, for all practical purposes, not affected by the temperature (Fig. 4).

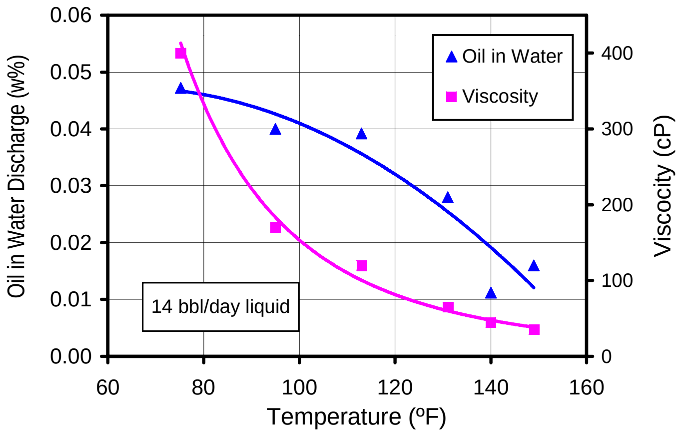

Fig. 3. Viscosity temperature dependence and results of separation of oil and water at different temperatures.

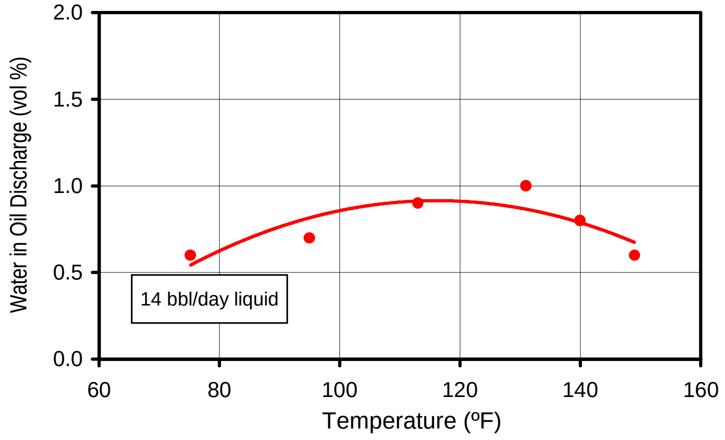

Fig. 4. Results of separation of oil and water at different temperatures.

The centrifugal separator was also operated with gas in a three-phase feed. The results indicate that gas in the inlet stream did not change the performance of the system, regardless of the gas content (Fig. 5). Thus, we are confident that entrapped gas in the oil well will not cause problems.

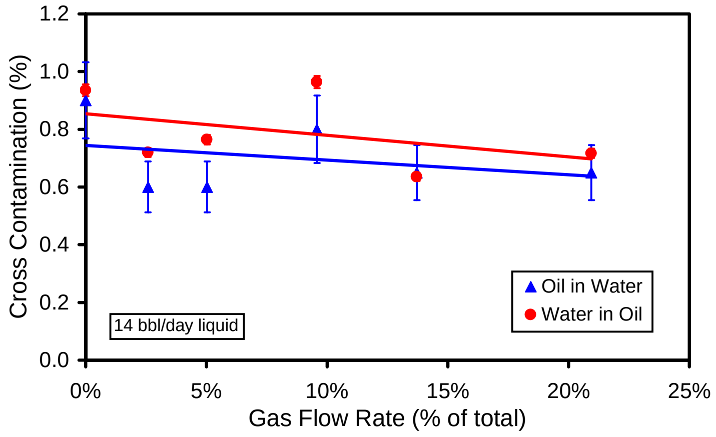

Fig. 5. Effect on oil-water separation by gas in the feed stream.

The CDHS can handle very little solids, but solids in the influent stream can be removed by coupling the separator with a hydrocyclone. Figure 6 shows the results of a stream of sand/oil/water flowing through a hydrocyclone, and then the overflow (containing oil and water) from the hydrocyclone is fed into the separator. The values next to the bottom of the bars in the left-hand side of the figure correspond to the mass flow of sand (in g/min). The values on top of the bars on the right-hand side of the figure correspond to the cross-contamination in the separator (in %). As is noted, the hydrocyclone separated out

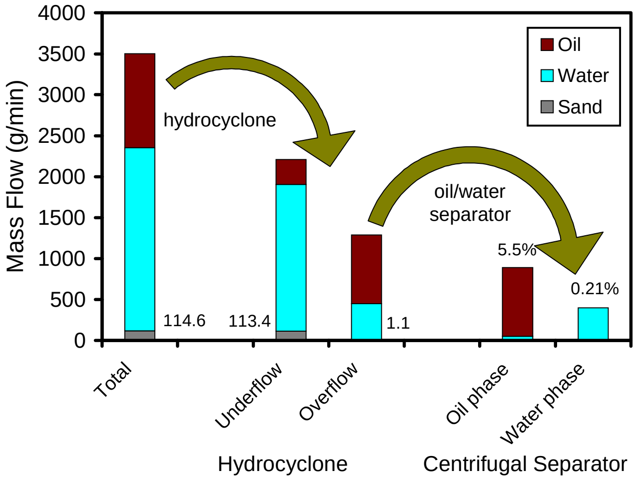

Fig. 6. Performance of a system consisting of a hydrocyclone (for solids separation) followed by separation of oil and water in a centrifugal separator.

in excess of 99% of the sand (compare 114.6 with 1.1). The subsequent processing of the stream from the hydrocyclone was able to get down to 0.21% oil in the water, while the oil stream contained 5.5% water.

SUMMARY

A centrifugal separator is currently being developed at ORNL that will extend the application of remotely operated equipment that was developed for the nuclear industry to in-well recovery of oil, with in situ recycle of produced water. A light Gulf of Mexico crude oil has been used in most of the testing.

- Water-to-oil feed ratios of 10:1 to 1:19 have been tested to date, and the separator operated efficiently for the full range of feed ratios. Air was added to the oil stream in one test to model the effect of gas in the oil. Air additions up to 20% of the feed flow rate (the maximum tested) did not have any impact on the performance of the separator.
- The separator also effectively processed a very viscous North Sea heavy crude oil. The heavy crude was used to determine the effect of higher temperatures on the performance of the separator. Increasing the temperature of the oil and water feed stream decreased the concentration of oil in the water discharge stream.
- Solids-oil-water separation from a solids/oil/water stream was accomplished in a hydrocyclone-centrifugal separator system.

OZONE TREATMENT OF SOLUBLE ORGANICS IN PRODUCED WATER

K. Thomas Klasson, David W. DePaoli, and Costas Tsouris
Oak Ridge National Laboratory

BACKGROUND

Oil production is shifting from “shallow” wells (0–650 ft water depth) to off-shore, deep-water operations (>2,600 ft.). Production from these operations is now approaching 20%. By 2007, it is projected that as much as 70% of the U.S. oil production will be from deep-water operations. The crude oil from these deep wells is more polar, thus increasing the amount of dissolved hydrocarbons in the produced water. Early data from Gulf of Mexico (GOM) wells indicate that the problem with soluble organics will increase significantly as deep-water production increases. Existing physical/chemical treatment technologies used to remove dispersed oil from produced water will not remove dissolved organics. GOM operations are rapidly moving toward design of high-capacity platforms that will require compact, low-cost, efficient treatment processes to comply with current and future water quality regulations.

This project is an extension of previous research to improve the applicability of ozonation and will help address the petroleum industry-wide problem of treating water containing soluble organics. The goal of this project is to maximize oxidation of water-soluble organics during a single-pass operation. The project investigates: (1) oxidant production by electrochemical and sonochemical methods, (2) increasing the mass transfer rate in the reactor by forming microbubbles during ozone injection into the produced water, and (3) using ultraviolet irradiation to enhance the reaction if needed. Industrial collaborators include several major petroleum companies through a joint project with the Petroleum Environmental Research Forum (PERF).

The research and demonstration program consists of three phases:

1. Laboratory testing in batch reactors to compare effectiveness of organics destruction using corona discharge ozone generation methods with hydrogen peroxide generated sonochemically and to evaluate the enhancement of destruction by UV light and micro-bubble spraying.
2. Continuous-flow studies to determine the efficacy of various contactors, the dependency of organics destruction on process variables, and scale-up issues.
3. Field testing of a prototype system in close collaboration with an industrial partner to generate performance data suitable for scale-up and economic evaluation.

INTRODUCTION

Ozone is an extremely powerful oxidant that can attack organic materials and convert them to nonhazardous products. Ozone is sparingly soluble in water. It has been determined that the main limitation in ozonation systems comes from the low mass transfer rate of ozone from the gas phase to the liquid phase. The mass transfer efficiency of ozone from the gas phase to the liquid phase depends on the mixing characteristics of the gas-liquid contactor used, the kinetics of ozone reactions in the water, and the number and size of bubbles produced. The effectiveness of ozone as an oxidant can be increased by creating a higher surface-area-to-volume ratio for the contact of ozone with the solution through the generation of smaller bubbles. A smaller bubble size results in a higher surface-to-volume ratio. In addition, smaller bubbles have higher residence times in contactors, leading to higher gas volume fractions. These findings motivated the experimental work conducted in this project.

DISCUSSION OF CURRENT ACTIVITIES

On October 7–8, 1999, the Petroleum Environmental Research Forum (PERF) steering committee reviewed the results of our research. They recommended that additional bench-scale research be conducted prior to scale-up and demonstration to answer several technical questions that remained regarding the feasibility of field application of ozonation. The scope of the continuous-flow study task was adjusted to meet those needs and the research activities shifted to two types of testing: (1) microbubble formation and (2) oxidation performance.

Several experiments have been conducted using simulated produced water and samples of actual produced water collected by our industrial partners (Company A and Company B). Microbubble formation tests involved long-term experiments to determine the impact of, and means for avoiding, possible fouling during ozonation by ferric oxide, calcium carbonate, and evaporative salt deposits. Oxidation tests were continued using laboratory-scale continuous-flow column reactors and small batch systems. The work involved multiple experiments with improved synthetic solutions to determine the effect of major process variables including gas flow rate, use of air or oxygen as the feed gas, presence of immiscible oil droplets in the water, and solution pH. No continuous experiments could be completed with actual produced water samples as the sample quantities obtained from the industrial collaborators were insufficient for continuous studies. Instead, we focused the work with actual produced water samples on batch experiments, collecting necessary data for preliminary scale-up information and cost estimation.

Several experimental systems were employed to address the effect of different variables. These systems are displayed in Table 1and Figs. 1–3.

Table 1. Experimental Systems Used in Current Studies

System	Description	Variables Studied or Type of Experiments
Batch	Sealed glass bottles (60 and 160 mL) with Teflon-lined caps (see Fig. 1)	These bottles are charged with water samples, ozone (O_3) or oxygen (O_2), and kept at a constant temperature. Acid is injected, and the gas phase is sampled for CO_2. The liquid phase is extracted with perchloroethylene (PCE). The extractable organics are determined via infrared absorption at a wavelength of 3.4 µm. The water-phase is injected into a gas chromatograph (GC) for analysis of acetic, propionic, and butyric acids. Variables Studied: O_3–produced water ratio O_3 versus O_2 treatment PH Produced water variability Effect of hydrogen peroxide (H_2O_2) addition
Small Columns	Continuous-flow counter-current column reactors. One with a 25.4-mm internal diameter. Gas (O_3 or O_2) was supplied through bubble diffusers at the bottom of column. Simulated produced water was fed from the top of the column (see Fig. 3). Typical working volume was 200–350 mL liquid in columns.	The gas feed and gas effluent were continuously monitored for ozone concentration. Periodically, the effluent gas was collected in gas sample bags and analyzed for CO_2. The feed and effluent liquid streams were sampled and the samples were analyzed for total extractable organics via PCE-IR or hexane-fluorometry. **Variables Studied:** Fouling Removal via flotation O_3/O_2 versus O_3/air mixtures for oxidation Gas-liquid flow ratio PH
Large Columns	Two continuous gas-flow column with 105- and 150-mm internal diameter. Air was supplied from the bottom through bubble diffusers. Equipped with automatic cleaning mechanism for the gas diffusers to correct fauling problems. (see Fig. 2). Typical working volumes were 4.2 and 15 L.	Long term studies to demonstrate a technique for automatic cleaning of gas diffusers. **Variables Studied:** Flow rate Diffuser flushing with fresh or salt water. Bubble-size measurement

Fig. 1. Photo of the type of reactor used in small batch experiments(160 mL).

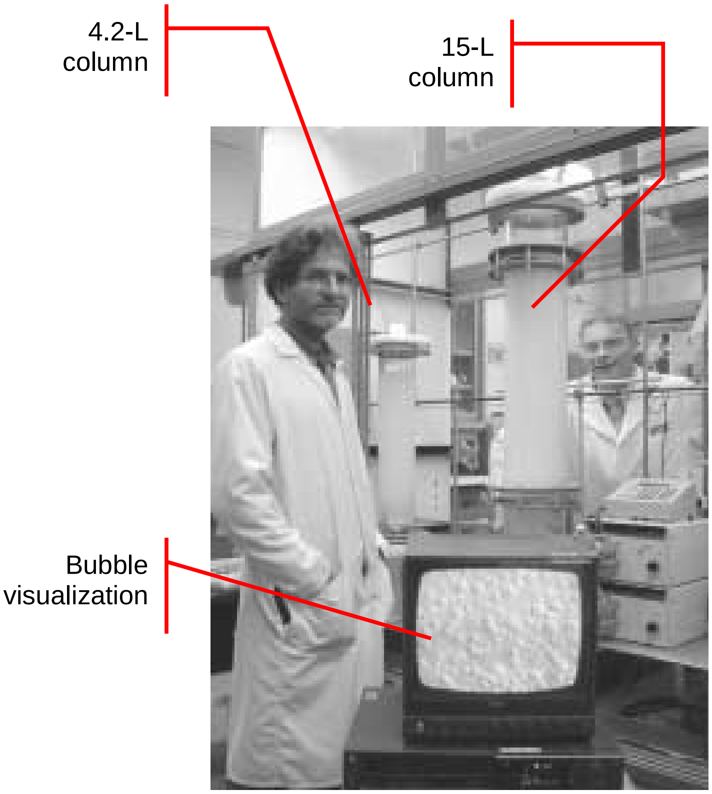

Fig. 2. Photo of the type of reactors used in large-scale column experiments.

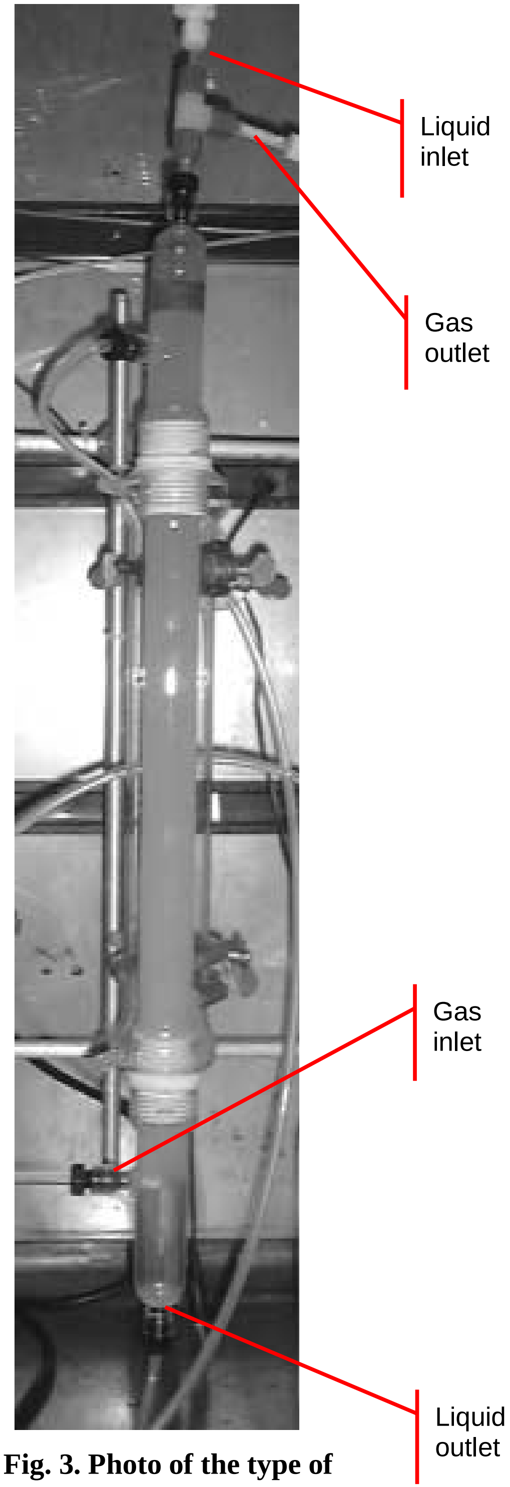

Fig. 3. Photo of the type of reactor used in small column, continuous-flow experiments (350 mL).

RESULTS

Batch Experiments

Stock solutions of samples were made from produced water provided by two oil companies (Company A and Company B). The original produced water from these companies came in 1-L bottles and was refrigerated during storage. Visual inspection showed that at the top of each bottle there was a layer of organic and inorganic particles. Three stock solutions were made from the solution of each source. The first sample was labeled “clear” and was taken from the bottom of the bottles. Care was taken to avoid particles in the water. The second sample was termed “cloudy”. It was taken approximately 2 cm underneath the top layer of the bottle and included particles. The third sample was also taken from the cloudy area but was then filtered through a 0.2-μm-pore filter and was thus called the “filtered” sample.

All batch experiments were conducted using 160-mL bottles without adjusting the pH of the produced water. Results showed that the concentration of PCE extractables in untreated samples was 62.9 ppm for the clear, 317.1 ppm for the cloudy samples, and 26.2 ppm for the filtered from Company A. These concentrations, however, were different for a different set of similar stock solutions prepared at a different time. For example, a second set of stock solutions that was prepared had PCE extractables corresponding to 40.5±5 ppm for the clear, 118.8±5 ppm for the cloudy samples, and 16.7±5 ppm for the filtered. Clearly, there is a great deal of variation in the produced water.

Although there was a significant difference among the initial concentration of PCE extractables for the three types of solutions, the PCE extractables were destroyed by ozonation. A comparison of concentrations before and after ozonation is shown in Fig. 4 for cloudy, clear, and filtered samples of Company A and Company B produced water, respectively.

The quantity of carbon dioxide formed by ozonation of produced water from both companies is plotted in Fig. 5 for clear, cloudy, and filtered samples. Two notable observations from Fig. 5 are:

1. there is no clear difference in the amount of CO_2 generated among the different types of samples (i.e., clear, cloudy, and filtered) from each company, and
2. produced water from Company A consistently yielded higher amounts of carbon dioxide.

The implication of the first observation is that complete oxidation of all PCE extractables was not achieved.

A GC/MS analysis of PCE extractables in produced water from Company A, before and after ozonation, was performed (Fig. 6). The peaks represent carbon compounds present in the samples, which unfortunately could not be recognized by the mass-spectroscopy library used in this work. The top graph (before ozonation) contains more peaks than the bottom graph (after ozonation), indicating that several

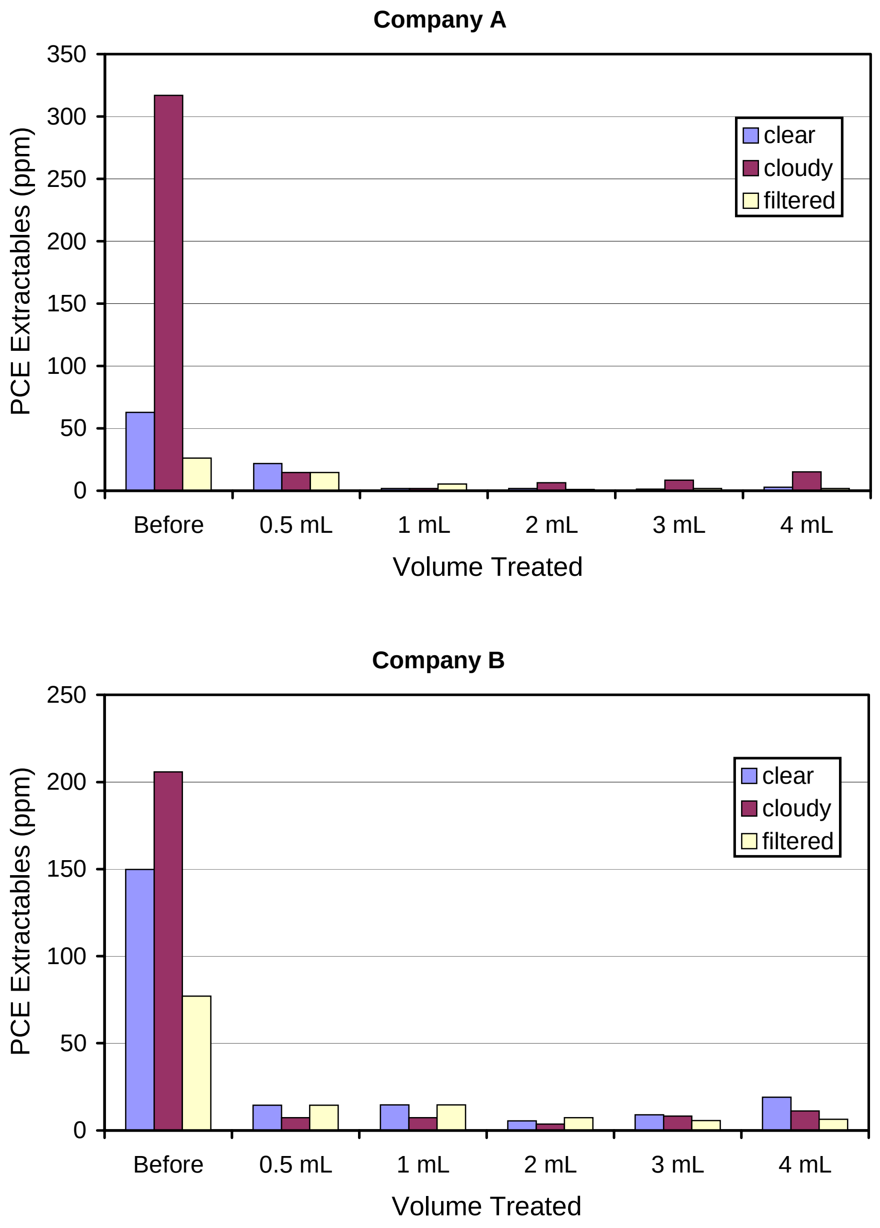

Fig. 4. Concentration of extractable organics in different fractions of produced water samples. The results show concentrations before and after treatment of the produced water. All sample volumes were treated with 160 mL O_3/O_2 mixture and O_3 concentration of approximately 40 mg/L.

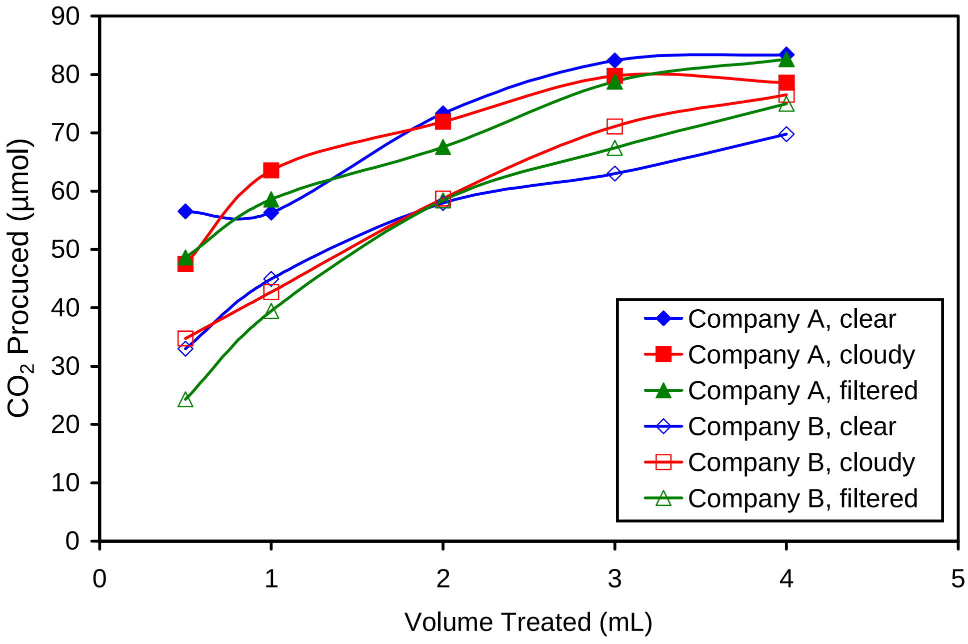

Fig. 5. Comparison of the quantity of carbon dioxide formed by ozonation of produced water from Company A and Company B.

compounds have been destroyed by ozone. Although it is demonstrated in Fig. 6 that ozonation was effective in removing organic compounds from produced water, further studies are still needed to identify both reactants and products of ozonation. Such studies are the subject of future work.

Continuous-Column Experiments

Long-term experiments of microbubble formation were conducted using synthetic saltwater containing 35 g/L sea salt, 65 g/L sodium chloride and a concentration of 30 ppm ferrous chloride that was oxidized, forming a precipitate phase. The experiments indicated that after sufficient time, depending on the gas flow rate, gas diffuser area, and solution concentration, pore fouling occurs, leading to decreased gas flow rate at constant pressure or increased gas pressure required for a given flow rate (Fig. 7). To date, fouling has been encountered only as a result of evaporative salt deposition rather than ferric oxide or calcium carbonate formation. This problem was effectively overcome by periodically flowing a small amount of water through the injectors to dissolve the salt deposits in the pores.

We have also tested larger-size equipment and continuous cleaning of bubble diffusers. The diffusers' pore size was 10–16 µm. The effect of gas flow rate and salt concentration on bubble size may be seen in Fig.8. As is noted, the bubble-size in salt water is approximately 10 times smaller than it is in fresh water.

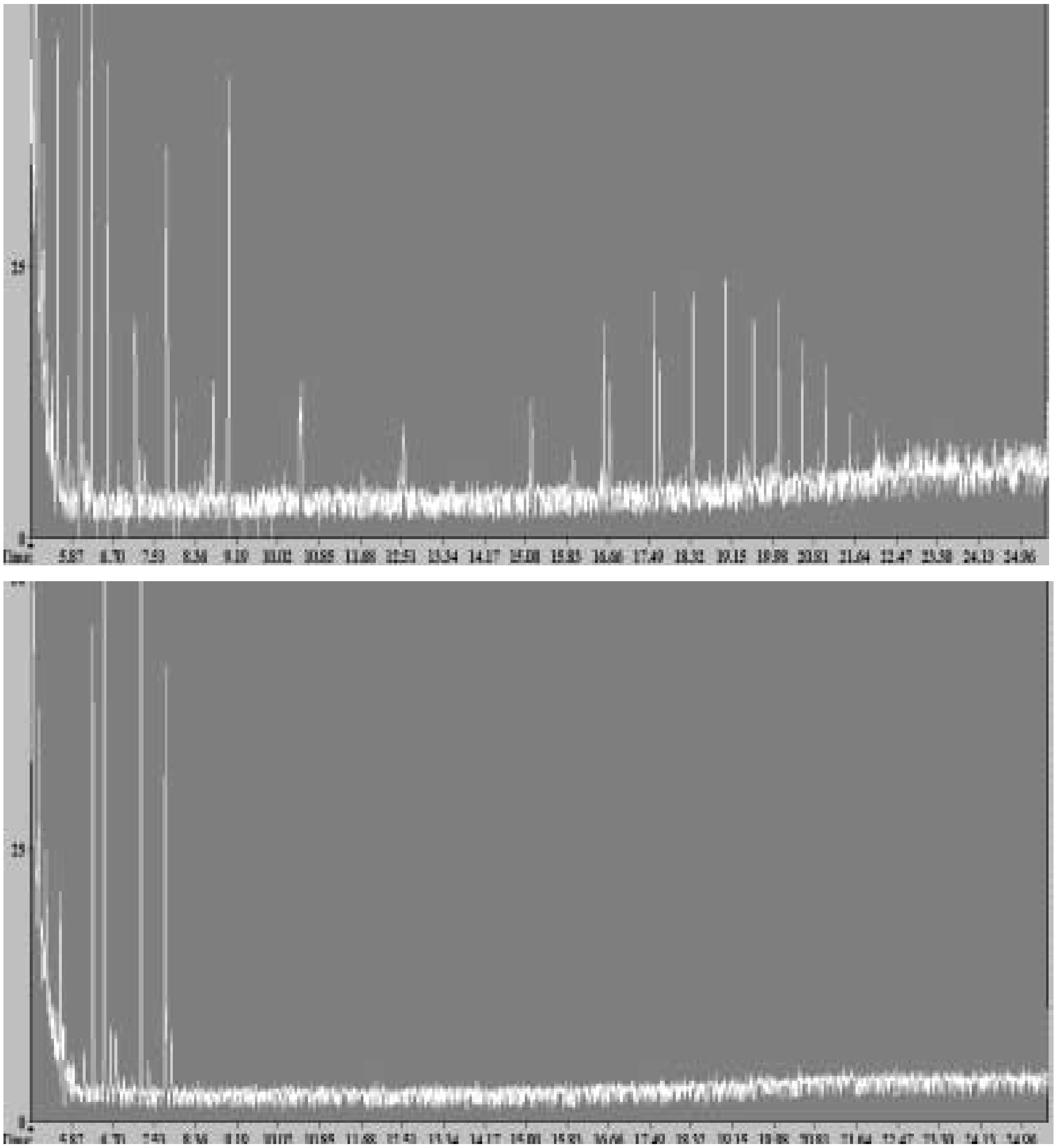

Fig. 6. GC/MS analysis of produced water from Company A before (top) and after (bottom) ozonation.

During the extended testing in the large columns, the highest flow rate was used, and every 15 min, fresh water was pumped into the gas line before the diffuser at a rate of 500 mL/min for 20 sec. After a few weeks of operation in this mode, salt water from the column was used in place of the fresh water for flushing. This method of flushing worked just as well. The system has operated for several months without problems, other than replacement of metal parts with glass parts when the flushing stream was altered to salt water.

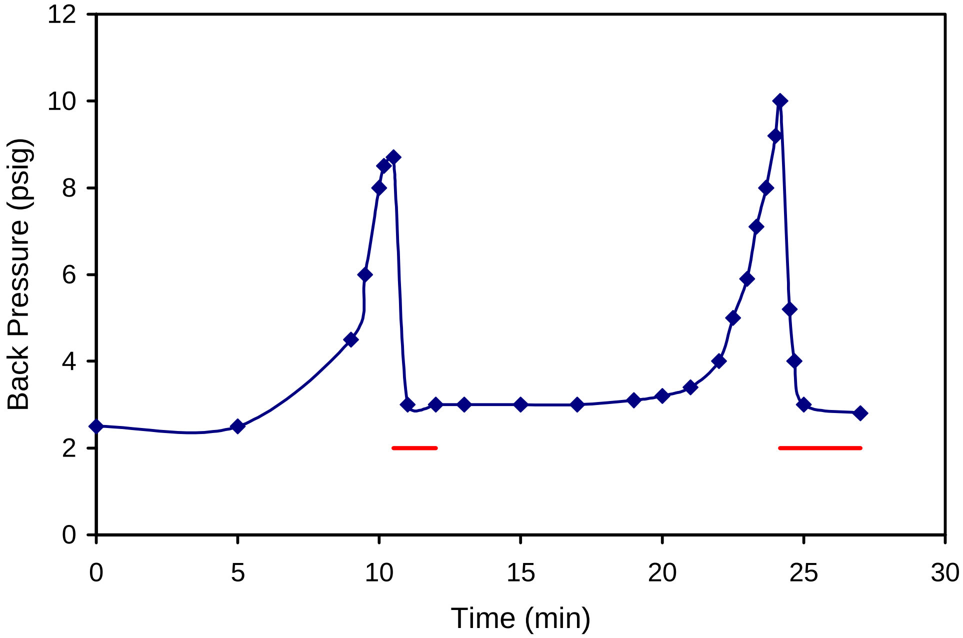

Fig. 7. Example results of salt deposition and water flush for gas flow through a porous injector. Conditions: liquid flow–10 mL/min salt water; gas flow–300 mL/min oxygen containing ozone, distilled water flush–0.3 mL/min. Horizontal bars indicate time period for water flush.

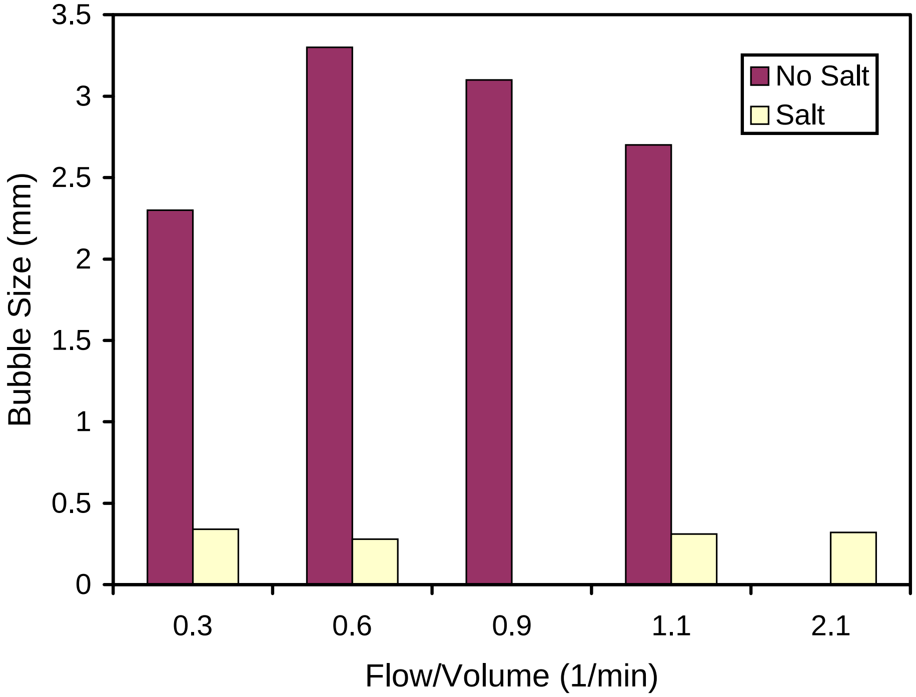

Fig. 8. Bubble size in large columns for different gas flow to contactor volume ratio.

ENVIRONMENTAL COMPLIANCE ASSISTANCE SYSTEM

S. M. DePaoli

INTRODUCTION

The Environmental Compliance Assistance System (ECAS) is a web site provided through the National Petroleum Technology Office (NPTO). This web site is targeted at the independently owned and operated oil and gas exploration and production (E&P) industry. In general, these E&P facilities are small, family-owned operations, and therefore do not have the capital to support the personnel needed to research and maintain information regarding environmental compliance issues concerned with their industry. This web site has been provided to aid these and other interested parties with regulatory information on the E&P industry; local, state, and federal contacts; waste handling/treatment/disposal options; and to direct them to other related web sites. A link to the ECAS can be found on the NPTO home page (http://www.npto.doe.gov).

ANNUAL REPORT, 2001

This NPTO funded project is tasked with updating the ECAS system that is currently on the web. The new, completed website is currently on a server at Advanced Integrated Management Services (AIMSI) (accessed through the above address). The NPTO is working on a new environmental webpage to be accessed from their main website. The ECAS website will be a link from this page, and will be incorporated when the NPTO's environmental website is complete.

A logo was designed for the ECAS website by Karen Billingsley of (AIMS) in Oak Ridge under a subcontract on this project, and is shown above. Work on creating the web site began in January 1999. A fully updated and approved web site format was completed in March 1999. The "draft" website was completed in December 1999. A formal review was held in March 2000, and formatting changes were completed on the ECAS site in April 2000. The new site now includes information regarding links to other pertinent sites; federal regulatory contacts; regulatory/legislative changes that are pending; and other links to sites within the NPTO. Information on regulations is provided through the site. Work continued in 2000 and early 2001 on updating the site's section concerning applicable treatment for wastes generated within the Oil and Gas Industry, as well as inclusion of summaries of current issues regarding environmental compliance within this industry.

Final approval for the incorporation of the website on NPTO's homepage was received in March 2001. The website is complete, and can be accessed from the NPTO's homepage at http:/www.npto.doe.gov. Updates of the current issues will be regularly reviewed and included on the website.

PHYSICAL PROPERTIES MEASUREMENTS OF PRODUCED WATER

D. A. Bostick

INTRODUCTION

ORNL, Shell, Chevron, Phillips, and Statoil are collaborating in a Petroleum and Environmental Research Forum (PERF) project to characterize water solubles in produced water. The project is aimed at reducing future production of these contaminants, thereby minimizing costs associated with their treatment. ORNL is responsible for analyzing water soluble organics (WSO) in produced water derived from Gulf of Mexico (GOM) drilling sites. WSO content is being defined through accurate measurements of equilibrium solubilities and associated thermophysical properties for deep-water crudes at ambient and high pressures and temperatures. Industrial partners provide samples of deep-water crudes and produced water, contribute to the selection of methods to characterize the water-soluble organics, compare the data with industrially obtained data from low-pressure wells, and evaluate the data for trends. Industrial partners will develop a model to predict the production of water-soluble organics as a function of crude composition and formation characteristics.

The primary tasks for FY 1999 and 2000 included: (a) devising an integrated testing plan to determine the effect of water cut, produced water pH and salinity, and crude oil properties on the type and content of WSO, (b) obtaining samples of actual crude/produced water from industrial partners, (c) characterizing WSO by methods selected by industrial partners and (d) providing data to industrial partners as it became available. These tasks will continue into 2001 as characterization data is completed for one deep-well crude and begun for a second source of deep well crude.

DISCUSSION OF CURRENT ACTIVITIES

Background

Soluble organics in produced water and the resulting refinery effluents are treatment problems for the petroleum industry. Production facilities and refineries take special efforts to meet regulatory discharge requirements for dissolved organics. These problems are expected to increase as environmental regulations become stricter and production from deepwater operations increase. Deepwater crudes are more polar, which increases the amount of dissolved hydrocarbons in the produced water and refinery effluents. Early data from GOM wells indicate that the dissolved hydrocarbons will increase significantly as deepwater production increases.

Neither the chemistry involved in the production of soluble organics in the petroleum industry, nor the impact of these compounds on total effluent toxicity, is well understood. Several industrial companies, including Shell, Chevron, Phillips, and Statoil, have developed a collaborative Petroleum Environmental Research Forum (PERF) project to characterize and evaluate water solubles aimed at reducing future production of these contaminants. The project will increase the understanding of the production of water-soluble organics, and will ultimately result in reduced production of water solubles and development of guidelines for effluent treatment. Quantitative characterization data are needed as the first step in this activity. ORNL is currently identifing WSO in produced water collected under a variety of experimental conditions. WSO from these studies are being quantitatively determined by accurate measurements of equilibrium solubilities and associated thermophysical properties.

ORNL is uniquely well suited to do research on the characterization of crude oils and water solubles, by virtue of its strong in-house concentration of equipment and expertise in high-temperature solution chemistry. In addition to a wide range of analytical instrumentation, equipment formerly under the control of the DOE NIPER program and the ORNL High-Temperature Aqueous Chemistry group is available. The Acoustic Resonance Spectrometer/Calorimeter, one of five units in the world that is on loan to ORNL from Phillips, can make ultra sensitive physicochemical property measurements. Additionally, a Vapor-Liquid Equilibria system has been made available to ORNL from Chevron. This enables ORNL to perform a full spectrum of experiments on the liquid mixtures of interest over a wide range of temperatures and pressures to simulate field conditions.

Progress

Several meetings were held among PERF members throughout FY 1999 to define the scope of this project and to systematize analytical procedures. Laboratory work began in late 1999 and has continued into FY 2001. Input from industrial partners was used to develop a detailed scope of work for sample analyses needed to support the industrial partners' development of a model for produced water contamination. Barrel quantities of crude oil were obtained from industrial partners for analyses in 2000 and 2001. An experimental work plan for their analysis was developed to insure comparability between data generated by ORNL and industrial partners.

In addition to actual crude and produced water samples, a series of laboratory-prepared water samples were planned to estimate the impact of brine parameters commonly encountered in the drilling of GOM crudes. In this case, real GOM oil would be contacted with a GOM brine simulant within the following operating ranges:

- 1–100 Atm (15–1500 psi)
- 90–200 degrees F (25–100 degrees C)
- pH 6.5 plus or minus 2 units

- water cut of 20, 50, 80 %
- 35,000–150,000 ppm TDS as chloride

Analytical results to date indicate that the TPH content in the deep-well crude was present at 50%, 42%, and 8% within C_6–C_{10}, C_{10}–C_{20}, and C_{20}–C_{28} ranges, respectively. The principal SVOCs in the deep well oil are acetophenone (0.6 g/kg) and methylnapthalene (0.4 g/kg), which represent less than 2% of the total organic content. Chemical classification by open LC protocol was used to account for the remaining 98% of the organic character in the oil. Methylene chloride-extractable material (TEM) in deep-well oil is present at 200–400 g/kg. Approximately 35% of this material can be exchanged into a hexane (HEX) matrix. The relative composition of the hexane matrix is 35% saturated hydrocarbons, 15% aromatic components, and 50% polar material. The visibly colored red-brown material is primarily present in the polar fraction. Alkaline and alkaline earth metals are the primary ICP metal components in deep well crude; their total concentration is about 17 g/kg. Several RCRA metals were detected above instrument detection limits, but not present above the EPA-defined toxicity limits.

The above crude oil was contacted with a GOM brine simulant in a Water Accumulated Fraction vessel (ASTM D6081 (Proposed Standard Practice for Aquatic Toxicity Testing of Lubricants: Sample Preparation and Results Interpretation)) to generate produced water samples under a variety of testing conditions. The total concentration of WSO observed in oil/brine simulant contacts is within the 20–30 ppm range. Identified SVOCs are 1-methylnaphthalene

(10 ppb), 2-methylnaphthalene (9 ppb), naphthalene (14 ppb) and phenol (30 ppb). Distribution of WSO within chemical classes differs significantly from that of the deep crude. Chemical fractionation of the total extractable materials suggests that 80–90% of WSO is present as polar compounds; the next largest fraction is that of aromatic materials. The visibly colored material is primarily present in the lightly yellow aromatic fraction. TEM organic matter is primarily distributed between the low and midrange carbon masses, similar to oil data.

Variation in water/oil ratio indicates that there is a slight negative trend in WSO content in all chemical fractions as the water cut increases. This effect is a combination of decreasing solubility of the C_{10}–C_{20} mass components and increasing solubility of the C_6–C_{10} carbonaceous material. Analytical results obtained in the characterization of crude oil were used in combination with data from water cut experiments to determine approximate distribution coefficients (K_d) of WSO in GOM brine as a function of % water cut and brine volume. Distribution data imply that brine is saturated with WSO for water cuts of less than 50%. The scatter in 80% water cut data indicates that the value of K_d is not only determined by the oil/brine ratio, but is also linearly dependent on the volume of brine in the contact experiment.

Variation of TDS (as salinity) does not significantly alter WSO content in produced water. However, the pH of the brine does affect TPH content. Normally, the pH of the GOM brine is buffered to a value of 7–7.5 by the presence of an oil layer. When the buffering capacity of oil is exhausted with the addition of base, the WSO content almost doubles for pH values above 7. This is primarily due to the enhanced solubility of polar organic compounds, which deprotonate at higher pH values. There is an enhanced solubility of the C_{10}–C_{20} carbon range material and a decline in C_6–C_{10} mass for pH values greater than 7.

The chemical character of WSO does not appear to be significantly dependent upon solution temperature, although the percentage mass in each carbon range is altered. The mass of WSO in the C_6–C_{10} carbon range decreases while that in the C_{10}–C_{20} range increases. Thus, the net quantity of organics in the produced water increases by 5 ppm for a 60 °C elevation in brine temperature.

Three organic acids are typically found in the produced water samples: formic, acetic, and propionic acids. Acetic acid makes up the bulk of the acid mass, present at levels similar to that of TPH (10–30 ppm). However, acid levels decrease as the brine simulant becomes more alkaline, a trend opposite that observed for hydrocarbon content. Both salinity and temperature slightly elevate organic acid concentration, particularly that of acetic acid. Less than 5% total acid in produced water is recovered in the TEM fraction; less than 1% organic acids are recovered in the HEX fraction. For 30 ppm total acid present in produced water, it is estimated that TPH content would be overestimated by less than 2 ppm if methylene chloride is used to extract WSO from produced water and by 0.5 ppm if hexane is used for solvent extraction. Assuming a constant distribution coefficient, overestimation would then increase linearly relative to total acid concentration in the produced water.

Future Progress

Analyses of the crude/produced water samples obtained in 1999 and 2000 will be completed in 2001. Data must still be acquired for oil/brine contacts at elevated pressure. Once all laboratory data is transferred to industrial partners, ORNL will assist industrial partners in the development of models to predict the production of water solubles from formation, crude, and water properties and obtain additional data required for the model in 2001–2002. ORNL will evaluate the potential impact of increased water solubles on produced water treatment methods and down-stream processing and evaluate the toxic effects of water solubles in the out years if the information obtained from the project warrants the additional activities.

IMPROVING TOOLS AND METHODS FOR ECOLOGICAL RISK ASSESSMENT AT PETROLEUM-CONTAMINATED SITES

R. A. Efroymson, W. W. Hargrove, and D. S. Jones

INTRODUCTION

This project, FEAC319, began in May of 2000 with support from the U.S. Department of Energy (Fossil Energy Program, National Petroleum Technology Office, Tulsa, OK; Dexter Sutterfield and Kathy Stirling, Project Managers; Nancy Comstock, unofficial manager). The project was intended to provide risk assessment tools and methods to the Petroleum Environmental Research Forum (PERF) project 99-13, “Expanding the Science Basis of Risk.” However, the kickoff meeting for this project occurred in February of 2001, and industry participants have not yet made commitments to this PERF project. FEAC319 has three ongoing tasks: (1) to develop a framework for Net Environmental Benefit Analysis, (2) to develop plant uptake models for chemical contaminants that are found at downstream sites, and (3) to develop or to evaluate spatial analysis models and tools for risk assessment of vegetation and wildlife. A fourth task to derive soil screening values for wildlife had no deliverables for FY2000.

Remedial activities at refinery or other downstream locations may be more expensive than necessary for two reasons. First, models for estimating ecological exposure are not readily available, so excessively conservative estimates of exposure and risk are sometimes made. Second, certain remedial actions such as soil removal and the associated destruction of habitat may result in greater risk to ecological populations or processes than the continued presence of the original, aged contamination.

Net Environmental Benefit Analysis (NEBA). NEBA attempts to answer the question: what type and scope of remediation, restoration, or natural attenuation of chemicals in environmental media would cause the least damage or most benefit to the value of the habitat? NEBA involves balancing present risk from chemical contamination with future risk from potential remedial alternatives and potential benefits from habitat alteration. Remedial alternatives include traditional methods such as excavation, and less invasive options, such as microbial bioremediation (nutrient additions and tilling), phytoremediation, natural attenuation, wetland enhancement, and planting of native species. The recolonization of areas damaged by contamination, excavation or tilling may depend on the extent of fragmentation of a landscape. The term “NEBA” was probably coined by agencies and industries evaluating options for marine oil spills. A report was published by the National Oceanographic and Atmospheric Administration in 1990 entitled *Excavation and rock washing treatment technology: net environmental benefit analysis*. In that study a group of scientists and engineers comprised of Exxon, NOAA, and State of Alaska scientists evaluated the environmental tradeoffs associated with excavating and washing hydrocarbon-contaminated sediments that were deeply buried along parts of the Alaskan shoreline affected by the

Exxon Valdez oil spill. A framework for Net Environmental Benefit Analysis, analogous to the EPA framework for ecological risk assessment, has not been developed.

Plant uptake models. A primary gap in any ecological risk assessment for terrestrial wildlife is in the quantification of chemical concentrations in wildlife foods. It is advisable to measure these concentrations at a site of concern. However, because funding or seasonal constraints may limit the number and type of measurements that may be made at a site, it is useful to have models available to estimate contaminant concentrations in plant materials and invertebrates, based on concentrations in soil, soil characteristics, and taxonomic characteristics. Elements and compounds of concern at downstream petroleum sites include: polycyclic aromatic hydrocarbons, lead, nickel, selenium, mercury, and vanadium. Published soil-plant uptake factors tend to overestimate bioaccumulation and risk when concentrations of elements in soil are high and to underestimate uptake at lower concentrations. In addition, soil and/or plant characteristics have not previously been incorporated into uptake models.

Spatial modeling. The exposure of ecological receptors to chemical contaminants has spatial dimensions. Wildlife exposure models include dietary uptake but rarely the habitat preferences that also determine exposure. Refineries, landfarms, or pipelines may be located at the center of a single habitat type (e.g., grassland), in which case the sizes of the habitat patches are important, or at the edge of two or more habitats (e.g., wetland and urban), which may have varying use by a particular species. The premise of this task is that organisms experience the environment spatially, as a patchwork. Patches may be good, as in the case of habitat for the animal, or patches may be bad, as in the case of spilled contaminants. The integrated effect of the patchwork landscape on a particular species will depend on the spatial arrangement of those patches of varying quality. Some pertinent questions are: (1) what is the role of wildlife movement and preferential uses of different habitat in determining exposure; (2) what is the role of the fragmentation of habitat in determining exposure; and/or (3) how do habitat loss and contamination interact to determine risk to wildlife? Spatial modeling will provide more realistic estimates of ecological exposure, so that fewer conservative assumptions may be used in risk assessments.

It is assumed that improved methods for ecological risk assessment should lower costs of remediation by decreasing the need for conservative assumptions in estimates of ecological exposure.

DISCUSSION OF CURRENT ACTIVITIES

Ecotoxicity benchmarks. Initial project funds were used to respond to reviewer comments on a journal article on ecotoxicity benchmarks for plants and soil invertebrates (Efroymson et al. 2000 draft) that was written under FEAC303 “Biological quality of soils containing hydrocarbons and efficacy of ecological risk reduction by bioremediation alternatives.” The article was accepted by *Environ. Toxicol. Chem.* but withdrawn after results were presented at a PERF 99-01 meeting in October 2000 and received substantial review comments from petroleum industry representatives. We plan to rewrite and to resubmit the article in FY2001.

Meetings. The project's principal investigator, Rebecca Efroymson, attended PERF 99-01, "Ecological Evaluation for Upstream Site Remediation," and 99-13 meetings in Richmond, CA in October 2000 and February 2001, respectively. She agreed to lead the ecological workgroup for PERF 99-13. She served as a peer reviewer of the EPA ecological soil screening levels in July of 2000. She attended the annual meeting of the Society of Environmental Toxicology and Chemistry meeting in Nashville, TN in November 2000.

Net Environmental Benefit Analysis. The initial focus of this task was narrowed to the development of a framework for NEBA; one petroleum industry representative indicated that such a framework would provide a useful product. We drafted part of a manuscript on this topic in October, and this task will be completed with FY01 funds. The manuscript addresses the history of NEBA, questions that are asked in NEBA, estimates of biodegradation and recovery rates, restoration under Natural Resources Damage Assessment, and a case study related to contamination of beaches from the Exxon Valdez oil spill.

Plant uptake models. To evaluate the relationship between the contaminant concentration in soil and plants, single-variable and multiple regressions were performed using SYSTAT 7.0 (SPSS 1997). Models were developed for vanadium, with soil pH as the only soil characteristic evaluated to date. A review of the literature identified seven publications containing suitable data on measurements of vanadium in soil and co-located vegetation samples. Documents included journal articles and US Geological Survey (USGS) reports. A total of 120 paired soil-plant observations were found.

Preliminary results of log-log regression analyses of soil and plant vanadium concentrations indicated that this type of model may be useful for predicting plant concentrations of vanadium. Figure 1 shows the field uptake data from the model data set and the validation data set. Also depicted in Fig. 1 is the single-variable regression based on all 120 data points in the model data set, which was statistically significant ($p < 0.001$, $r^2 = 0.25$). A multiple regression analysis of the model data including soil pH as an independent variable was also statistically significant ($p < 0.001$), and it explained more of the variance in the plant vanadium concentrations ($r^2 = 0.41$). However, closer examination of the data suggests that two distinct data sets exhibit very different relationships between the soil and plant vanadium concentrations. Three USGS reports account for 97 of the 120 paired observations. The regression of the non-USGS data was not statistically significant ($p > 0.05$), but the regression of the USGS data was significant ($p < 0.001$, $r^2 = 0.84$). The explanation for the difference between the two data sets is not yet known.

A single-variable model for lead was developed previously (BJC 1998) and was updated using funds from FEAC319. Multiple regression analyses were conducted for lead in soil and three soil characteristics (i.e., pH, percent organic matter, and cation exchange capacity). Also evaluated was the influence of soil

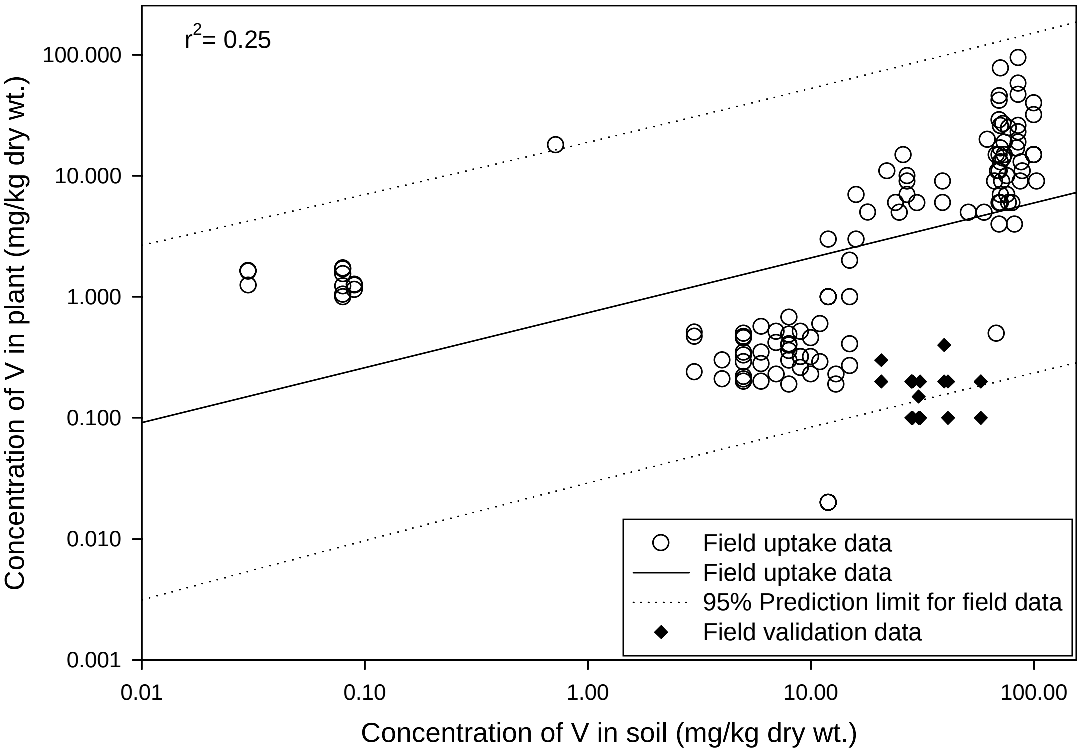

Fig. 1. Scatterplot of vanadium concentrations in vegetation versus soil. Concentrations include the model data set and the validation data set. The single-variable regression on the model data set and the 95% upper prediction limit on the regression are also depicted.

cadmium concentration on lead uptake, although cadmium is not expected at petroleum-contaminated sites. A series of two-variable models were developed, each containing soil lead concentrations and either one soil characteristic or the cadmium concentration in soil. A final multiple regression containing all three soil characteristics and soil cadmium concentrations was also developed.

Preliminary results of log-log regression analyses of soil and plant lead concentrations indicated that this model may be useful for predicting plant concentrations of lead. The single-variable regression based on all 129 data points in the data set, was statistically significant ($p < 0.001$, $r^2 = 0.40$). pH did not contribute significantly to the multiple regression ($p = 0.31$). Each of the other three tested variables did contribute significantly to the multiple regression ($p < 0.05$) when tested independently. However, only in one case, the model including percent organic matter, did the multiple regression model explain more variance in plant lead concentrations (i.e., $r^2 = 0.65$) than did the single-variable model (i.e., $r^2 = 0.40$). The model including cation exchange capacity had a multiple r^2 of 0.35, and the model including soil cadmium concentrations had a multiple r^2 of 0.36. The model including all three of these co-factors was not statistically significant ($p > 0.05$), probably because there were only 31 observations for which all three variables were available.

Petroleum industry representatives have also indicated interest in the uptake of organic chemicals by wildlife foods, and this task may shift toward organic chemicals in the future.

Spatial analysis tools and models. An initial candidate study site was the Chevron land in Port Arthur, TX. However, this option was abandoned because of sensitive regulatory negotiations occurring there. A second site that is under consideration is the Nature-Conservancy-owned Tallgrass Prairie Preserve (TPP) in Osage County, OK. Although this site is an upstream site, spatially-explicit models for studying risks at upstream sites may not differ substantially from those at downstream sites, although patches of habitat and non-habitat may occur at different scales. Spatial data are available for the TPP from the NGOTP-funded project FEAC321, "Developing an Ecological Framework to Evaluate the Impacts of Releases at Upstream Exploration and Production Sites: The Effect of Size and Distribution," a collaboration between Lawrence Livermore National Laboratory and ORNL. An additional candidate study site is a Chevron diesel pipeline spill location at the USDA Jornada Experimental Range near Las Cruces, New Mexico. However, this isolated spill may not be ideal for landscape analysis. Hyperspectral data for downstream sites may be utilized to determine habitat boundaries.

We have identified, located, and obtained two simulation tools that can be used to evaluate the spatial arrangement and juxtaposition of patches of habitat and spills, and to predict the effects of those habitat patches on particular species. The first of these is a model called Program to Assist in Tracking Critical Habitat (PATCH), written by Nathan Shoemaker at EPA Corvallis, OR. The second simulation is called Self-Avoiding Walkers (SAW), and was written by Robert Gardner of the Appalachian Ecology Lab and Eric Gustafson of the U.S. Forest Service. While both of these are individual-based models, they take different approaches to the problem.

PATCH is a spatially explicit, individual-based life history simulator designed to project populations of territorial, terrestrial vertebrate species through time. PATCH can be used for investigations involving wildlife species that are mobile habitat specialists. It must be supplied with habitat maps, specifications for habitat use (territory size and habitat affinity), vital rates (survival and reproduction), and descriptions of a species' movement behavior. Map-based outputs of PATCH include patch-by-patch descriptions of landscapes; assessments of the number, quality, and spatial orientation of breeding sites; and map-based estimates of the occupancy rate and the source-sink behavior of breeding habitat. Demographic outputs include several measures of population size as a function of time, realized survival and fecundity rates (reflecting limitations imposed by habitat quality and landscape pattern), and assessments of the occupancy rate and source-sink behavior of the breeding sites present in a landscape.

We obtained a copy of the PATCH model, written in C++, and the User's Guide (Schumaker 1998) and have it operational on a local workstation. Many of the functions of PATCH duplicate capabilities found in a standard GIS system; panning, zooming, scrolling, and displaying and querying maps. Maps can be input in a standard Sun Microsystems raster format. Dr. Schumaker, the author of the program, is willing to work with us to make changes to the code. PATCH has been used to simulate movement and reproduction of a number of species, including the original application to predict forest clear-cutting on Spotted Owl populations (Schumaker 1995). Limitations of PATCH include the following: (1) species interactions such as predation are not simulated, (2) simulated species must be territorial (3) contaminant effects can only be included as habitat suitability equivalencies.

The approach of SAW is to simulate individuals moving through a heterogeneous environment as first-order, self-avoiding walkers traversing a gridded map. Movement of the individuals is self-avoiding in that they are not allowed to return to a previously visited cell until after more than two steps. The objective of SAW-based simulations is not only to predict demographic trends in a population, but also to determine the spatial locations of important movement corridors that individuals use to move from one part of the map to another. The spatial location of contaminated sites close to or interrupting important habitat "corridors" could have deleterious effects on the demography of the population.

By simulating the release of synthetic SAWs, who have been assigned the habitat preferences and movement abilities of particular species of concern, and by keeping track of the number of times they travel through each cell in the map, movement corridors can be located within any mapped landscape. Gustafson and Gardner (1996) describe SAW, and they have used SAW to model turkeys, raccoons, and martens on various landscapes. They have also studied the effects of patch-based mortality on populations of SAWs (Gustafson and Gardner 1996). The tracks of numerous individuals can be summed to estimate colonization rates between patches. The individuals can have varying movement characteristics (i.e., sexual or age differences), and can interact with the environment (e.g., collect contaminant body burdens).

Dr. Gardner has provided us with the source code for the SAW simulation. The model is coded in FORTRAN 90, and uses a proprietary visualization package, which we do not own. We have not yet modified the code to use another, non-proprietary visualization technique.

In an additional subtask, we have obtained a list of names and locations of all 177 refineries located within the United States from Terri H. Nelson of EPA Office of Air Quality Planning and Standards. We plan to examine statistically the natural groupings of combinations of environmental conditions (soil characteristics, meteorology, elevation) occurring at refineries and to produce groups of refineries that have statistically similar environmental combinations. Initially, we will tally the occurrence of refineries within standard ecoregion divisions, including those of Bailey, Omernik and Kuchler. Distributional pie charts will show proportions of refinery sites falling into each ecoregion type.

REFERENCES

BJC (Bechtel Jacobs Company). 1998. Empirical models for the uptake of chemicals from soil by plants. ES/ER/TM-198. Oak Ridge National Laboratory, Oak Ridge, TN, USA.

Efroymson, R. A. 2000 draft. A framework for Net Environmental Benefit Analysis for remediation of petroleum-contaminated sites.

Efroymson, R. A., B. E. Sample, and M. J. Peterson. 2000 draft. Ecotoxicity benchmarks for total petroleum hydrocarbons in soil: plants and soil-dwelling invertebrates.

Gustafson, E. J., and R. H Gardner. 1996. The effect of landscape heterogeneity on the probability of patch colonization. *Ecology* 77:94–107.

Gustafson, E. J., and R. H. Gardner. 1996. Dispersal and mortality in a heterogeneous landscape matrix. Proceedings, Third International Conference/Workshop on Integrating GIS and Environmental Modeling, Santa Fe, NM, January 21–26, 1996. Santa Barbara, CA: National Center for Geographic Information and Analysis. CD and on INTERNET server.

Schumaker, N. H. 1995. Habitat connectivity and spotted owl population dynamics. Ph.D. dissertation, University of Washington, Seattle.

Schumaker, N. H. 1998. A users guide to the PATCH model. EPA/600/R-98/135, U.S. Environmental Protection Agency, National Health and Environmental Effects Research Laboratory, Western Ecology Division, Corvallis, OR.

SPSS 1997. *SYSTAT 7.0 for Windows: Statistics*. SPSS Inc., Chicago, IL. 751 pp.

DEVELOPING AN ECOLOGICAL FRAMEWORK TO EVALUATE THE IMPACTS OF RELEASES AT UPSTREAM EXPLORATION AND PRODUCTION SITES: THE EFFECT OF SIZE AND DISTRIBUTION

R. A. Efroymson, T. L. Ashwood, H. I. Jager, W. W. Hargrove, and R. A. Washington-Allen

INTRODUCTION

This project, FEAB321, began in July of 2000 with support from the U.S. Department of Energy (Fossil Energy Program, National Petroleum Technology Office, Tulsa, OK; Nancy Comstock, Project Manager). The framework and ecological modeling are collaborative research between Lawrence Livermore National Laboratory (Tina Carlsen, Principal Investigator) and Oak Ridge National Laboratory. The project has several longterm goals: (1) to develop an ecological framework for evaluating impacts of brine and/or oil spills at E&P sites, utilizing population models based on trophic transfer and patchiness of landscapes; (2) to develop early exit criteria from the ecological risk assessment process, based on size and distribution of spills in the context of potentially patchy habitat; and (3) to provide guidance for mitigation measures that may be taken by a company prior to exiting a site. The primary tasks of the past year have been (1) to choose a case study site, (2) to develop a geographic information system for serving maps of the site, and (3) to review population viability analysis models for terrestrial wildlife. Essentially, this project is intended to inject ecology into ecological risk assessment, a field that has been dominated by conservative assumptions about exposure and toxic responses. The project is will contribute to Petroleum Environmental Research Forum (PERF) project 99-01, “Ecological Evaluations for Upstream Site Remediation Programs.” Improved methods for ecological risk assessment should lower costs of remediation by decreasing the need for conservative assumptions in estimates of ecological exposure.

BACKGROUND

The exposure of ecological receptors to chemical contaminants has a spatial context. Wildlife exposure models include dietary uptake but rarely the habitat preferences that also determine exposure. The premise of this project is that organisms experience the environment spatially, as a patchwork. Patches may be good, as in the case of habitat for the animal; patches may be bad, as in the case of some spills. Areas denuded of vegetation are non-habitat for most vertebrates. The integrated effect of the patchwork landscape on a particular species will depend on the spatial arrangement of those patches of varying quality.

DISCUSSION OF CURRENT ACTIVITIES

Case study site. The subject of the case study for this project is the Tallgrass Prairie Preserve (TPP) in Pawhuska, OK. The TPP is approximately 37,000 acres of mostly intact prairie grassland with approximately 600 historic wells (about 120 in current production) and isolated spills of hydrocarbons and brine. The Nature Conservancy, which owns the site, has attempted to restore ecosystem function through controlled burns and grazing by introduced bison. Tallgrass prairie vegetation forms comprise about seven percent of oil and gas well locations in the U.S., and related plant communities such as shortgrass prairie and north mixed grass prairie comprise another thirteen percent (Fig. 1). Thus, our case study site is representative of a large fraction of upstream oil and gas locations.

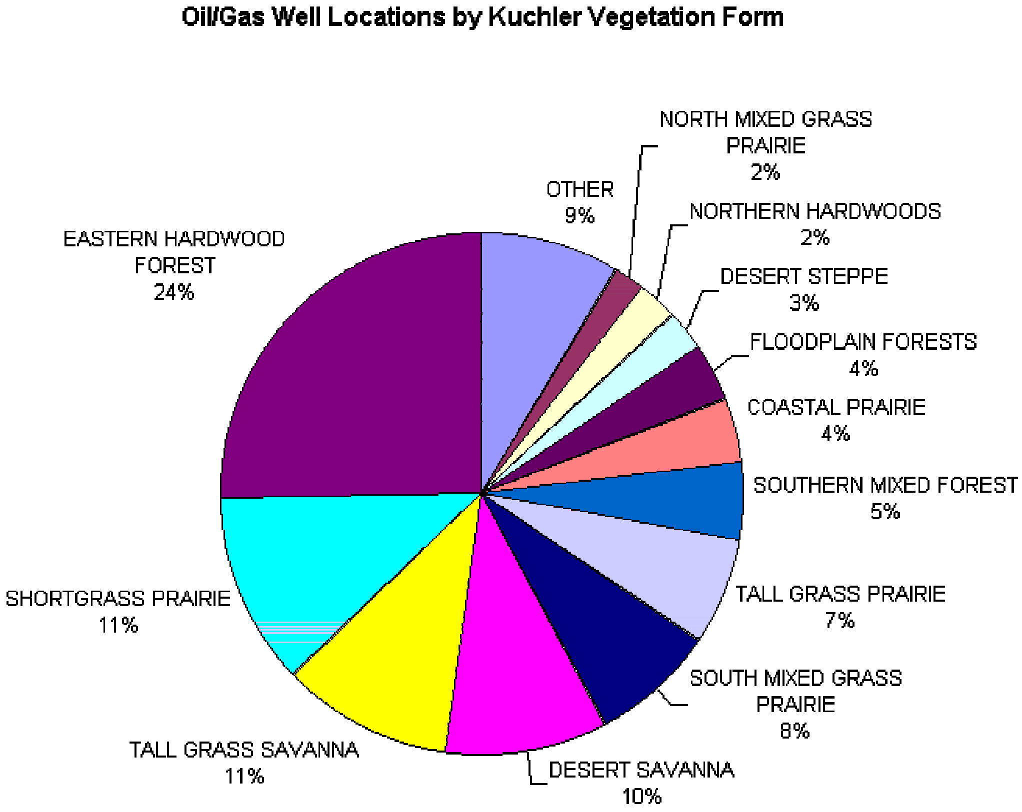

Fig. 1. Predominant vegetation forms in ¼ mile by ¼ mile cells in which productive and unproductive oil and gas wells in the U.S. are located. Data on well locations in USGS (1995), obtained from David Ferderer at USGS.

Meetings. The project's principal investigator, Rebecca Efroymson, attended PERF 99-01, "Ecological Evaluation for Upstream Site Remediation," and 99-13 "Expanding the Science Basis for Risk" meetings in Richmond, CA in October 2000 and February 2001, respectively. She also attended the DOE NGOTP project review in Tulsa, OK in January 2001. Tom Ashwood attended the International Petroleum Environmental Conference (IPEC) in Albuquerque, NM in November 2000. Robert Washington-Allen visited an additional candidate study site, a Chevron diesel pipeline spill location at the USDA Jornada Experimental Range near Las Cruces, New Mexico. However, this isolated spill of a refined product may not be ideal for an ecological modeling demonstration.

Geographic Information System. A web-based interface for the GIS was completed by researchers at Lawrence Livermore National Laboratory (LLNL). A draft data collection protocol was developed at LLNL. We obtained GIS layers (maps) from public sources, from Peter Earls at Oklahoma State University and from Kerry Sublette at the University of Tulsa. Available map layers include: (1) soil survey, (2) vegetation type, (3) digital ortho quarter quad photos (Fig. 2), (4) Landsat Multispectral Scanner data (North American Landscape Characterization data from USGS/EPA/NASA), (5) prescribed burn history (annual 1991–1999), (6) management usage and years of bison grazing, (7) bison pastures with dates opened, and (8) land ownership. The data are currently in Albers Equal-Area Projection. It has been a challenge to obtain these data layers, as there has not been a single repository of these data. These map layers will be incorporated in the GIS at LLNL as soon as metadata (i.e., information about data sources, legends, uncertainties) are developed. Airborne Visible/Infrared Imaging Spectrometer (AVIRIS) hyperspectral data have been obtained from the USGS, and these have been radiometrically corrected but not yet georectified. A Normalized Difference Vegetation Index for the years 1974, 1985, and 1992 (northern half of TPP) and 1973, 1985, and 1991 (southern half of TPP) was mapped. This index is related to plant biomass per area. A map of spill boundaries at the TPP is not yet available. These may be visible from the hyperspectral data layers (taken in July), but the digital ortho quarter quad photos were taken in February, and hence, vegetation differences in spill areas are not evident.

Population Viability Analysis and Empirical Vulnerability Analysis Review.

The purpose of the review was to evaluate models that predict population extinction for use in a model-based approach to understanding the effects of oil spills, brine spills, and natural disturbances (e.g., fire, grazing) on the grassland ecosystem. Models for Population Viability Analysis (PVA) and empirical vulnerability models can both be used to evaluate the likelihood of persistence (or extinction) of biological populations. PVA uses a dynamic population model to forecast the likelihood of persistence under prevailing environmental conditions. Empirical vulnerability models use statistical relationships to estimate the vulnerability of a population to extinction based on the characteristics of the species, the

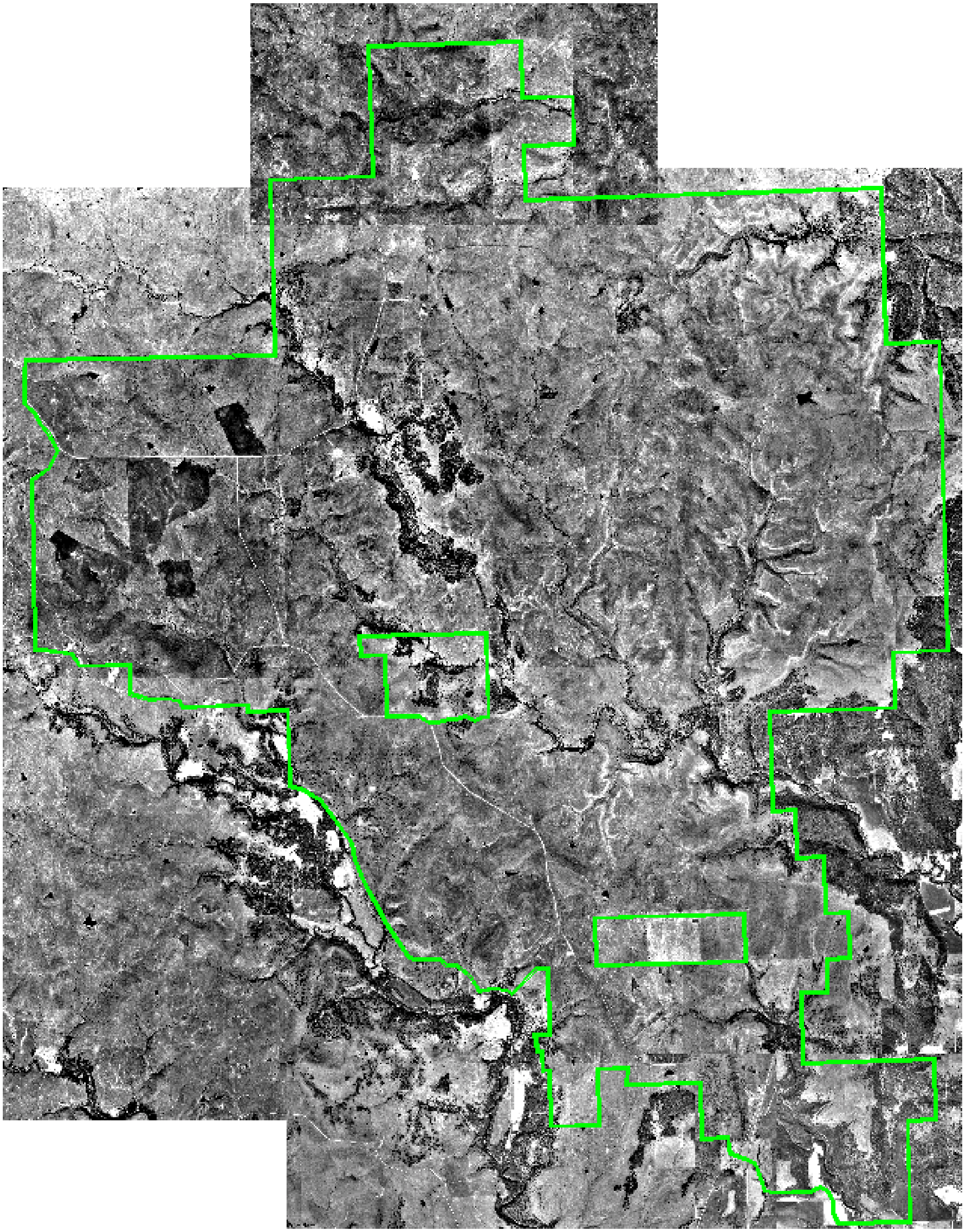

Fig. 2. Panchromatic aerial photos (Digital Ortho Quarter Quadrangles) of the Tallgrass Prairie Preserve in Pawhuska, OK. Map consists of ten photos mosaiced together. Photos provided by Peter Earls of Oklahoma State University.

particular population of interest, and its habitat. Empirical models are static and are usually used to compare risks among species or to assess communities with multiple species.

In PVA up to four categories of extinction risk are considered: (1) demographic stochasticity, (2) catastrophes, (3) environmental variation, and (4) genetic risks. Demographic stochasticity represents chance variation in population growth rate because of differences among individuals in a small population. Catastrophes are events that reduce population size or adversely influence the demographic parameters of the population. Because population size is reduced, catastrophes bring demographic stochasticity into play. Environmental variation represents the temporal variation in environment that can influence demographic parameters. This can include predictable components, such as periodic cycles, as well as stochastic (random) elements. Genetic risks to population viability result from two factors: (1) the loss of genetic variation among individuals due to small population size (and/or selection) and (2) production of homozygous individuals by inbreeding that may have lower fitness.

To develop spatial criteria for excluding petroleum exploration and production (E&P) sites from risk assessment requirements, the relationship between population risk and the size of the population and its habitat is important. Thus PVA follows the “small population paradigm” (Caughley 1994). To recommend mitigation measures for E&P sites, one must favor PVA methodology that follows the “declining population paradigm” (Caughley 1994) i.e., that evaluates restoration options by assessing the increase in population viability associated with removing agents of decline.

We summarized PVA analyses conducted for a wide range of terrestrial organisms between 1985 and 2000. Studies of modeling efforts directed at understanding the viability of terrestrial plant or animal populations were included in this review. These studies include mainly populations of birds (16) and mammals (11), but also plants (4) and other assorted taxa (2). Some standard software packages exist (e.g., RAMAS, VORTEX, or ALEX) that are able to facilitate PVA. An advantage of these packages is that they are widely available; however, they do not include mechanisms for considering social attributes of populations. Half of the PVAs reviewed are spatially explicit.

Vulnerability analysis is an alternative to PVA analysis that is particularly attractive for situations involving multiple species. This approach uses empirical models that estimate a population’s vulnerability to extinction from an array of factors, such as population size, mature body size of the species, and the amount of suitable habitat. Although few comprehensive studies exist that are relevant to grassland ecosystems, we surveyed existing vulnerability models as well as other literature that might be used to develop such a model for grasslands.

Spatial analysis tools and models. We have identified, located, and obtained two simulation tools that can be used to evaluate the spatial arrangement and juxtaposition of patches of habitat and spills, and to predict the effects of those habitat patches on particular species. The first of these is a model called

Program to Assist in Tracking Critical Habitat (PATCH), written by Nathan Schumaker at EPA Corvallis, OR (Schumaker 1995, 1998). The second simulation is called Self-Avoiding Walkers (SAW), and was written by Robert Gardner of the Appalachian Ecology Lab and Eric Gustafson of the U.S. Forest Service (Gustafson and Gardner 1996a, b).

Assessment endpoints. It is anticipated that three assessment endpoints will be chosen. These include: a plant population or community, an herbivorous population, and a population of predators. Example candidate herbivore populations include: bison, voles, rabbits, greater prairie chicken, or grasshopper sparrow. A few of the candidate predatory populations include: coyotes, badgers, or kit fox.

REFERENCES

Caughley, G., 1994. Directions in conservation biology. Journal of Animal Ecology 63, 215–244.

Gustafson, E. J., and R. H Gardner. 1996a. The effect of landscape heterogeneity on the probability of patch colonization. *Ecology* 77:94–107.

Gustafson, E. J., and R. H. Gardner. 1996b. Dispersal and mortality in a heterogeneous landscape matrix. Proceedings, Third International Conference/Workshop on Integrating GIS and Environmental Modeling, Santa Fe, NM, January 21–26, 1996. Santa Barbara, CA: National Center for Geographic Information and Analysis. CD and on INTERNET server.

Schumaker, N. H. 1995. Habitat connectivity and spotted owl population dynamics. Ph.D. dissertation, University of Washington, Seattle.

Schumaker, N. H. 1998. A users guide to the PATCH model. EPA/600/R-98/135, U.S. Environmental Protection Agency, National Health and Environmental Effects Research Laboratory, Western Ecology Division, Corvallis, OR.

U.S. Geological Survey National Oil and Gas Resource Assessment Team (USGS). 1995. 1995 National Oil and Gas Assessment: Overview of the 1995 National Assessment of Potential Additions to Technically Recoverable Resources of Oil and Gas—Onshore and State Waters of the United States. U.S. Geological Survey Circular 1118